Broadband Wireless Communication Systems: Channel Modeling and System Performance Analysis

Yuanyuan Ma

Broadband Wireless Communication Systems: Channel Modeling and System Performance Analysis

Doctoral Dissertation for the Degree *Philosophiae Doctor (PhD)* in Information and Communication Technology

University of Agder

Faculty of Engineering and Science

2011

Preface and Acknowledgements

This dissertation documents four year PhD achievements (from Jan. 29, 2007 to Jan. 28, 2011) carried out at Mobile Communications Group (MCG), Information and Communication Technology (ICT) Department of University of Agder (UiA) in Grimstad, Norway. The PhD work was funded by the Research Council of Norway (Norges Forskningsråd, NFR) through the project "Optimized Heterogeneous Multiuser MIMO Networks (OptiMO)". The dissertation mainly contributes to the wideband channel modeling and performance analysis of broadband wireless communication systems. It collects results from twelve research papers, eleven of which have been published in international journals and conferences and one will be submitted to a journal.

The completion of this dissertation would not have been possible without the help and support from many individuals. Through the years, I have become indebted to those who provided invaluable guidance and assistance during my PhD study; who encouraged me over the hard time; who accompanied and cared me in life.

First, I wish to express my thanks to my principle supervisor Prof. Matthias Pätzold. Without his efficient supervision, valuable comments, continuous support, and encouragement, this dissertation would never have become a reality. I appreciate all his contributions of time, ideas, and suggestions to make my PhD experience very creative and productive. I am thankful to my co-supervisor Prof. Frank Reichert for his great assistance. I would also like to convey my thanks to all my PhD evaluation committee members who spent their time on reading through my thesis and giving insightful comments. Their constructive feedback is very helpful for improving the quality of the manuscript. My genuine thanks also go to the MCG secretary, Mrs. Katharina Pätzold, for her immensely helps in administrative and personal matters. In addition, I would like to acknowledge supports from all staffs of ICT department. Especially, I wish to thank Mr. Gunnar Oftedahl (previous dean of the Faculty of Engineering and Science), Prof. Andreas Prinz (Head of the ICT department), and Mrs. Trine Tønnessen (PhD program coordinator of the ICT department) for their timely support and contributions to the ICT PhD programs.

My sincere gratitude goes to all the doctoral fellows at the ICT department of UiA. I am really grateful for their friendship and cares from deep inside. They made my stay in Grimstad very pleasant and I have never felt lonely in abroad because of these lovely persons. In particular, my past and present colleagues in MCG: Adrian Gutierrez, Akmal Fayziyev, Ali Chelli, Batool Talha, Bjørn Olav Hogstad, Dmitry Umansky, Gulzaib Rafiq, Nurilla Avazov, and Yi Wu, deserve my sincere thanks.

Here, I also want to take this opportunity to thank my dear friends: Chee Lim Nge, Hongzhi Jiao, Lei Jiao, Liping Mu, Martin Marie Hubert Choux, Morten Kollerup Bak, Peter Wesseh, Ram Kumar Ravikumar Santhi, Sigurd Eskeland, Xianghan Zheng, Xiaowen Guo, Xin He, Xuan Zhang, and Yi Ren. I always appreciate for their unique camaraderie, selfless cares, and every joy moment they shared with me.

My endless gratefulness goes to my beloved family: my father Cuihai Ma, my mother Baoju Guo, my sister Zixuan, and my brother Yinghao. It is my dream to get the PhD degree and it is also their dream. I know, without their cares, support, encouragement, nothing will come true. All the successes in my life belong to them. Especially, I own special thanks to my dear father, who is the first person to encourage me to start the PhD. His words "Daughter, I am proud of you" repeated many times in my mind whenever I was struggling in study and life. Thanks for the words, father! It is the last piece of words he left to me, but it will be the infinite drive in my rest life. I hope he could see this moment and be proud of me. Finally, I would like to give my profoundest thanks to my husband Meng Li for the eternal love and support during the past 13 years. Because of him, I never feel alone and scared. I know wherever I go, he will go with me.

<div align="right">

Yuanyuan Ma
May 2011
Oslo, Norway

</div>

Contents

Summary

In recent years, broadband wireless communications becomes increasingly important not only for professional applications but also for many fields in our daily routine. The reason can be explained by a large demand on high frequency utilization as well as high data rate access under high mobility environments. All these requirements, without doubt, call for intensive research efforts on how to cope with problems faced by current broadband wireless communications, e.g., limited availability of radio frequency spectrum, complex time variations in wireless fading channels, and urgent needs for good quality of service. Therefore, this dissertation is devoted to investigate broadband wireless communication systems by considering all these challenges. In particular, two goals are aimed at, which are known as wideband channel modeling and performance analysis of broadband wireless communication systems.

Wideband channel modeling, which can accurately describe the most important characteristics of wideband mobile fading channels, is essential for the design, evaluation, and optimization of broadband wireless communication systems. In the field of wideband channel modeling, the tradeoff between the prediction accuracy and simulation efficiency has to be taken into account. On one hand, channel models should be as accurate as possible. On the other hand, channel models are supposed to be simple and easy to put into use. There are several commonly used approaches to channel modeling, e.g., measurement-based channel modeling and deterministic channel modeling. Both methods are efficient in capturing the fading behavior of real-world wireless channels. However, the resulting channel models are only valid for the specific environments as those where the measurements were carried out or the ray-tracing scenario was considered. Moreover, these methods are quite time consuming with high computational cost. Alternatively, the geometry-based stochastic channel modeling approach can be employed to model wideband mobile fading channels. The most attractive feature of this method is that the derived channel models are able to predict fading behavior for various propagation environments, and meanwhile they can be easily implemented. Thus, the dissertation will complete the wideband channel modeling task by adopt the geometry-based stochastic approach.

In the dissertation, several geometry-based channel models are proposed for both outdoor and indoor propagation scenarios. The significance of the work lies in the fact that it develops channel models under more realistic propagation conditions which have seldom been considered, such as for non-isotropic scattering environ-

ments and mobile-to-mobile (M2M) fading channels. In addition, the proposed channel models remove the scarcity that proper geometry-based channel models are missing for indoor environments. The most important statistical properties of the developed channel models including their temporal autocorrelation function (ACF), the two-dimensional (2D) space cross-correlation function (CCF), and the frequency correlation function (FCF) are analyzed. Furthermore, efficient channel simulators with low realization expenditure are obtained. Finally, the validity of the proposed channel models is demonstrated by comparing their analytical channel statistics with the empirical ones measured from real world channels.

Besides the work in the field of wideband channel modeling, another part of the dissertation is dedicated to investigate the performance of SISO[1] orthogonal frequency division multiplexing (OFDM) broadband communication systems and space-time (ST) coded MIMO[2] OFDM broadband communication systems. This work provides a deep insight into the performance of a broadband mobile radio communication system over realistic wideband fading channels. Analytical expressions are derived for bit error probability (BEP) or symbol error rate (SER) of systems. In order to confirm the correctness of the theoretical results as well as to show the usefulness of the wideband channel models in the testing and analysis of a broadband communication system, SISO OFDM systems and space-time coded MIMO OFDM systems are simulated in the dissertation.

In order to improve the reliability of digital transmission over broadband wireless radio channels, a differential super-orthogonal space-time trellis code (SOSTTC) is designed for noncoherent communications, where neither the transmitter nor the receiver needs the channel state information (CSI) for decoding. In addition, a new decoding algorithm is proposed. The new algorithm has exactly the same decoding performance as the traditional one. However, it is superior from the standpoint of overall computing complexity.

---

[1]SISO stands for single-input single-output, which refers to a communication link equipped with a single antenna at both the BS and the MS.

[2]MIMO is an abbreviation for multiple-input multiple-output, which means a communication link equipped with multiple antennas at both the BS and the MS.

List of Figures

xiv

List of Tables

Abbreviations

1G	first generation
2D	two-dimensional
2G	two generation
3D	three-dimensional
3G	third generation
3GPP	third generation partnership project
4G	fourth generation
8PSK	eight phase-shift keying
ACF	autocorrelation function
AMPS	advanced mobile phone system
AOA	angle of arrival
AOD	angle of departure
AWGN	additive white Gaussian noise
BASK	binary amplitude shift keying
BEP	bit error probability
BER	bit error rate
BPSK	binary phase-shift keying
BRSM	basic Riemann sum method
BS	base station
CCF	cross-correlation function
CDMA	code division multiple access
CF	correlation function
CGD	code gain distance
CP	cyclic prefix
CSI	channel state information
DPSK	differential phase-shift keying
F2M	fixed-to-mobile
FCF	frequency correlation function
FDMA	frequency division multiple access

GMEA	generalized method of equal areas
GMEDS$_1$	generalized method of exact Doppler spread
GSM	global system for mobile communications
HiperLAN/2	high performance radio local area network
HSPA+	high-speed packet access plus
IEEE	institute of Electrical and Electronics Engineers
IFFT	inverse fast Fourier transform
IMT	international mobile telecommunications
IP	internet protocol
IS-95	Interim Standard
ISDN	integrated services digital network
ISI	inter-symbol interference
LOS	line-of-sight
LS	least-square
LTE	long term evolution
M2M	mobile-to-mobile
MCM	Monte Carlo method
MEDS	method of exact Doppler spread
MIMO	multiple-input multiple-output
MMEA	modified method of equal areas
MS	mobile station
NLOS	none light-of-sight
OFDM	orthogonal frequency division multiplexing
PDF	probability density function
PDP	power delay profile
PSD	power spectral density
PSTN	public switched telephone network
QPSK	quadrature phase-shift keying
R-MEDS	randomized method of exact Doppler spread
RMS	root mean square
SER	symbol error rate
SISO	single-input single-output
SNR	signal-to-noise ratio
SOC	sum-of-cisoids
SOS	sum-of-sinusoids
SOSTTC	super-orthogonal space-time trellis code
ST	space-time

STBC	space-time block coding
STTC	space-time trellis coding
TCAS	total access communication system
US	uncorrelated scattering
WCDMA	wideband code division multiple access
WiMAX	worldwide interoperability for microwave access
WLAN	wireless local area networks
WSSUS	wide-sense stationary uncorrelated scattering
ZF	zero-forcing

Chapter 1

Introduction

1.1   Broadband Wireless Communication Systems

Wireless communications means to exchange information between two or more parties by electromagnetic waves. The emergence of wireless communications can be traced back to 1897 when Guglielmo Marconi performed the first communication experiment between a fixed station and a ship. Since then, wireless communications has experienced exponential growth, not only from a scientific point of view but also in aspects of market size as well as impact on society. The rapid development of wireless communications occurred after the 1970s. Until now, driven by the general demand for a high data rate and high spectral efficiency, wireless communications has undergone three mature generations [26, 113, 127]. Currently, its fourth generation (4G) is in the experimental and practice stage.

The first generation (1G) wireless communications [126] is entirely based on analog technologies and provides only voice services to telephone subscribers. 1G wireless communications adopts frequency division multiple access (FDMA) techniques, where the total system bandwidth was divided into orthogonal frequency channels and allocated to different users [36, 56]. In 1G wireless communications, the most important breakthrough is to propose the concept of cellular networks in the 1970s. The system capacity was considerably increased due to the frequency reuse. Typical analog cellular communication systems include AMPS[1] [35, 170] used in United States and TCAS[2] [41] used in Europe. 1G wireless communication systems achieved far greater success than anyone had expected and many of them were still in use until the last decade. However, such systems have their own problems caused by the utilization of analogy signals, e.g., spectrum inefficiency,

---

[1] AMPS stands for advanced mobile phone system
[2] TCAS is short for total access communication system

1

voice services only, no use of encryption, and inferior call qualities. In addition, 1G communication networks cannot support roaming due to limited regional scope.

To overcome these underlying disadvantages in analogy communication systems, digital wireless communications emerged around the 1990s, which is known as the second generation (2G) wireless communications [108]. The key feature of 2G communications is that it provides non-voice services such as email and short message services. The most successful 2G standards are known as GSM[3] [16, 22] and Interim Standard 95 (IS-95) [28, 57, 65]. GSM adopts time-division multiple access [98, 101], i.e., each user occupies the overall frequency band over its assigned time slot. IS-95 is based on code division multiple access (CDMA) [11, 45, 166]. Though 2G is an indispensable revolution in the development of wireless communications, it has its limitations. Basically, 2G wireless communications is categorized as narrowband digital communications with a maximum data rate 14.4 kbps. Such low data rates cannot support real-time multimedia services as well as wireless Internet access in high-mobility environments. Moreover, the inherent incompatibilities of multiple 2G standards obstructed the process of global roaming.

All these facts motivated the evolution of wireless communications moving towards the third generation (3G) [23]. 3G wireless communications, commercially launched around 2001, was supposed to achieve the following goals. Firstly, it must be compatible with 2G networks and implement global roaming. Secondly, it is supposed to provide voice as well as high-speed multimedia data services, video calls, and mobile Internet access. Thirdly, in order to provide seamless convergence, 3G communications is required to be adapted to different types of communication networks including PSTN[4], ISDN[5], cordless, land mobile communication systems, and satellite communication systems. There are two famous standards appearing in 3G wireless communications known as wideband CDMA (WCDMA) [25] and CDMA2000 [72]. WCDMA is an outgrowth of the earlier 2G GSM standard, while CDMA2000 was developed on the basis of 2G CDMA standard IS-95. These different 3G standards became compatible within a global wireless infrastructure specified by IMT[6]-2000 in terms of various air interface and wireless mobile access technologies. With IMT-2000, global roaming was implemented for the first time. To support multimedia services, 3G standards require high data-rate transmissions, specifically, 2 Mbps for fixed environments, 384 Mbps for pedestrian, and 144 Kbps for vehicular traffic. From 3G, wireless communications started the era of mobile

---

[3]GSM shorts for global system for mobile communications

[4]PSTN is an abbreviation for public switched telephone network

[5]ISDN is known as integrated Services Digital Network

[6]IMT stands for international mobile telecommunications

broadband[7].

Now, the question is what remains for the coming 4G wireless communications. IMT-advanced, which is responsible for defining future 4G technologies, has exhibited the vision of future 4G wireless communication characteristics. 4G aims at providing a comprehensive and secure all-IP[8] based mobile broadband solution to various types of mobile devices. 4G wireless communications are expected to offer very high data rates up to approximately 100 Mbps for high mobility communications (such as from trains and cars) and 1 Gbps for low mobility communications, e.g., local wireless accesses. In addition, 4G cellular systems allow seamless connectivity and global roaming across multiple networks. In summary, by exploiting advanced 4G technologies, multimedia applications can be delivered to 4G users at anytime, anywhere with a satisfied data rate, quality of service, and security. The technical proposals, which have been submitted to the international telecommunication union as 4G candidates, are LTE[9]-advanced standardized by 3GPP[10] and 802.16m specified by IEEE[11].

In the 4G standard proposals, several physical layer transmission technologies are supposed to be applied with the goal of improving spectral efficiency, data transfer rate, and reliability, such as MIMO [70, 112], OFDM [39, 179], and space-time coding. All these fundamental 4G techniques will be addressed in the dissertation. In addition, in order to simulate, design, and evaluate 4G broadband wireless communications, accurately characterizing the fading behavior of realistic wideband mobile radio channels is necessary. Therefore, a large part of the dissertation is devoted to model and analyze wideband mobile fading channels.

1.2 Modeling of Broadband Mobile Radio Channels

As highlighted in Section 1.1, a precise description of the wideband channel fading behavior is indispensable for designing efficient broadband wireless communication systems as well as for assessing their system performance. Hence, this section is devoted to review some basic concepts of fading and describe existing important approaches for channel modeling.

---

[7]Broadband is defined as having instantaneous bandwidths larger than 1 MHz and supporting date-rates higher than 1.5 Mbps.

[8]IP is known as internet protocol

[9]LTE is an acronym for long term evolution

[10]3GPP stands for third generation partnership project

[11]IEEE shorts for Institute of Electrical and Electronics Engineers.

1.2.1   Mobile Radio Propagation

Fading is defined as the loss of the signal power at the receiver caused by the variations of mobile radio channels. In general, fading can be roughly classified into large-scale fading and small-scale fading.

Large-scale fading is known as the gradual deduction of the received signal power introduced by relatively large traveling distances between the base station (BS) and the mobile station (MS). The predominant effects involved in large-scale fading include path loss and shadowing. Pass loss manifests itself as the attenuation of an electromagnetic wave during its propagation through free space. Shadowing describes the phenomenon that the main signal propagation between the BS and the MS is obscured by a large obstacle such as tall building, trees, and dense woods.

Whereas small-scale fading refers to the rapid fluctuations of the received signal power over short propagation distances (around a few wavelengths) or short periods of time (on the order of seconds), which exists due to the multipath channel behavior. Multipath is a propagation phenomenon that electromagnetic plane waves reach the receive antenna by more than one path caused by reflection, diffraction, and scattering from buildings, trees, and other obstacles.

The overall magnitude of received signals can be entirely described by the superposition of the two scales of mobile signal variations. Large-scale fading is very important for the network level system design since it has strong influence on the cell convergence, outage, and handovers. Small-scale fading plays an important role in link level system performance analyses such as the BEP and the SER. Concerning the fact that this dissertation only focuses on the downlink physical layer aspects of broadband wireless communication systems, the attention of the dissertation is restricted to model small-scale (multipath) fading for wideband mobile fading channels.

In contrast to traditional narrowband mobile fading channels, wideband channels consider the propagation delay differences caused by various propagation paths. The impact of the multipath effect in wideband mobile fading channels can be interpreted in two different ways. In the frequency domain, the time-variant transfer function of the underlying channel is no longer constant over the entire transmission bandwidth. This is known as the frequency selectivity of the channel. In the time domain, different with narrowband channels, the time-variant impulse response of wideband channels is not a delta function. Instead, it contains a series of delta functions, each of which represents a time-variant impulse response at a specific propagation delay. As a consequence, a signal arriving at the MS has a longer duration than the originally transmitted one. Such a phenomenon is called time dispersion.

1.2.2 Basic Channel Modeling Approaches

Modeling mobile fading channels is of critical importance for the design, evaluation, and optimization of wireless communication systems. Numerous works have been reported in this field within the past ten years. The proposed channel models can be categorized in various manners. A potential way of classifying these models is by the type of the underlying considered channels, e.g., narrowband models vs. wideband models, time-variant models vs. time-invariant models, 2D propagation environment models vs. three-dimensional (3D) propagation environment models and so on. The other popular way is to distinguish channel models according to the employed modeling approach. Channel models divided by this manner can be categorized into two classes, i.e., analytical models and physical models.

Analytical models directly characterize the time-variant impulse responses or transfer functions of the channels without considering wave propagations. In most cases, analytical models are described by means of a channel covariance matrix or a specific coupling matrix and steering/eigenvectors. Analytical models, on the other hand, provide limited insight into propagation characteristics of mobile radio channels. Additionally, these models greatly depend on measurements, such as bandwidth, antenna configuration, and aperture of arrays. Physical models characterize mobile fading channels by some physical parameters, e.g., complex amplitudes, angle of arrival, and angle of departure. Compared with analytical models, physical models are capable of reproducing radio propagations. The other advantage of physical models is that they are independent of antenna configurations and system bandwidth. So far, several well known approaches exist in the literature for the purpose of developing physical channel models. These methods can be summarized as follows.

- **Stored channel modeling approach:** The basic idea of this approach is to measure, digitize, and store channel impulse responses through a channel sounder. This is the most straightforward way to characterize mobile fading behavior. The main advantage of the stored channel modeling approach is that the resulting channel impulse response is realistic. Moreover, the actual physical radio propagation process is reproducible since the stored data can be reused indefinitely. The drawbacks of such a method, however, are obvious as well. Firstly, large efforts are required in acquiring and saving measured data. Secondly, measurements are only valid for a certain propagation environment. When the propagation scenario changes, extensive new measurement data are required, which is time consuming and leads to high cost in carrying out measurement campaigns.

- **Measurement-based channel modeling approach:** The measurement-based channel modeling approach extracts channel parameters or statistical properties of fading channels from channel measurements conducted under a specific environment. Such a modeling approach is very accurate, despite its mathematical simplicity. However, this method has several limitations: (1) It usually takes considerable time and efforts to find a statistically significant amount of data among all collected ones. Moreover, if an error occurs, redoing the measurement is equivalently time consuming. (2) The expense and complexity of the measured system increases rapidly as the measurement goals become more sophisticated. Thus, the size, weight, and power consumption of measurement equipments can be problematic. (3) If the width of the angle of arrival (AOA) distribution exceeds the beamwidth of the antenna, it is difficult to distinguish the distortions introduced by a channel with distortions introduced by the antenna. (4) The results obtained by this method are only valid for the environments which have similar layout as those where the measurements were carried out.

- **Deterministic approach:** Deterministic approaches characterize physical propagation parameters in a completely deterministic manner. A typical deterministic approach is known as the ray-tracing method. This algorithm models the wave propagations by generating all possible paths (rays) from the BS to the MS according to geographical layouts and the rules of geometrical optics. The advantage of the ray-tracing approach is that the computer simulations involved in this method are easier to perform than measurement campaigns. The disadvantage comes from its high computational cost, which depends greatly on the complexity of the geographic database as well as on the interaction order in a ray search. In addition, ray-tracing techniques need to describe site-specific propagation environments in detail, which is time-consuming and consequently cannot be easily generalized to a wide class of scenarios.

- **Geometry-based stochastic approach:** The geometry-based stochastic approach models scattering environments around the BS or the MS or both by considering that local scatterers are placed in specific geometric patterns, e.g., as the one shown in Fig. 1.1. Then, the waves scattered by scatterers are determined by a simplified ray-tracing. Finally, the plane waves reaching at the MS are calculated as the superposition of waves coming from all directions. The geometry-based stochastic approach is especially useful for non-stationary scenarios since it can easily model motion of the BS and the MS.
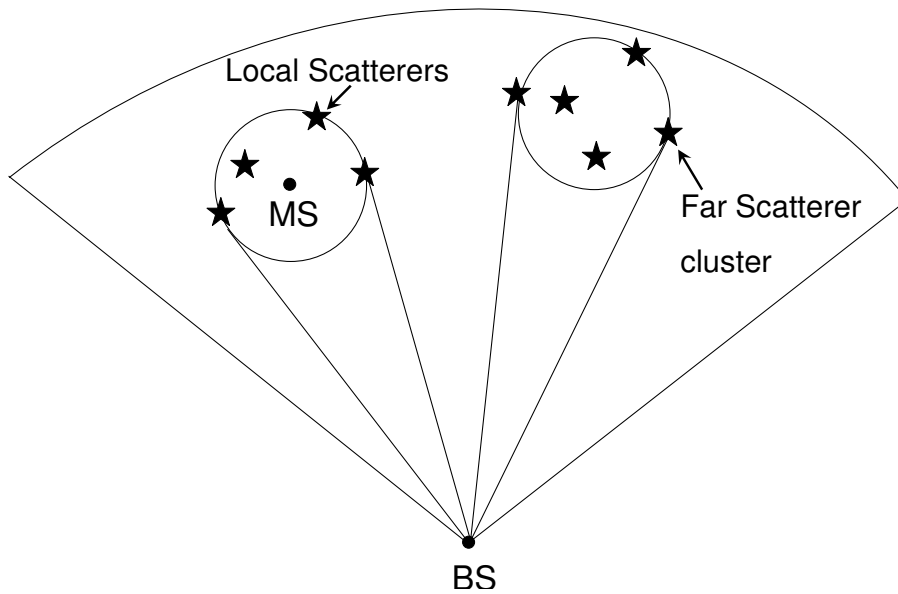
Figure 1.1: Geometry-based channel model

The channel models developed by this method are capable of predicting fading behavior for various propagation environments by only modifying certain predefined channel parameters or scatterer distributions. This is the most attractive feature of geometrical channel modeling. When combined with the concept of deterministic channel modeling, this method can be used to develop geometry-based channel simulators. These resulting channel simulators allow to simulate mobile fading channels with a very low realization expenditure. This can be considered as the other advantage of the geometry-based stochastic approach.

Based on the above comparisons among different modeling approaches, this dissertation makes the decision to adopt the geometry-based stochastic approach to model mobile radio fading channels.

1.3 Performance Analysis of Broadband Wireless Communications

With the advent of 4G wireless communications, current and future broadband communication systems are expected to provide fast and reliable communications over limited bandwidth. In practice, however, signals transmitted over broadband channels often experience severe attenuations and impairments caused by multipath fading. Recently, OFDM, MIMO, and space-time (ST) coding have been widely uti-

lized as efficient solutions to meet the huge demands for high-speed, spectrally efficient, and reliable wireless communications. Especially, OFDM and MIMO have been adopted as the key techniques in the beyond 4G LTE standard proposal. In the following, the main principles of these techniques are briefly described.

OFDM is known not only as a frequency multiplexing technique that mandates orthogonality among subchannel signals but also as a multicarrier modulation scheme [13, 109, 174]. The basic idea of the OFDM technology is to divide the transmitted data stream into several substreams and send them in parallel over multiple subchannels. These subchannels are mutually orthogonal in the frequency domain so that the corresponding signal spectra can overlap in frequency without causing inter-symbol interference (ISI). Moreover, the bandwidth of each subchannel is much smaller than the channel coherence bandwidth so that the fading each subchannel experiences is relatively flat. In a word, OFDM achieves robustness against severe channel conditions by converting a wideband channel into a set of parallel narrowband ISI-free subchannels. By now, OFDM has become a mature technology and been extensively used in several pre-4G cellular networks as well as mobile broadband standards due to its potential advantages.

MIMO is defined as the use of multiple antennas at both the BS and the MS. MIMO is a breakthrough in wireless communication system design. In addition to the time and frequency domains that are used in traditional SISO communication systems, MIMO incorporates the spatial domain by applying multiple antennas. As proved in [37, 155], the application of multiple antennas at both sides can greatly increase the channel capacity. It also offers a large gain in terms of data throughput and coverage range without any additional expense of bandwidth or transmit power. Therefore, MIMO can be regarded as a promising solution to weaken the conflict posed by the increasing demand for high data rates and the scarcity of the radio spectrum. MIMO is an important part of modern wireless communication standards such as 4G, WiMAX[12], and HSPA+[13]. MIMO can also be used in conjunction with OFDM, which has been the concept of the IEEE 802.16e WiMAX broadband mobile standard and IEEE 802.11n (WiFi) high-throughput standard.

ST coding is a new family of code design which simultaneously considers channel coding, modulation, and antenna diversity. In ST coded communication systems, replicated information is sent at different time from multiple transmit antennas. Since the fading on each communication link between a pair of transmit and receive antennas is usually independent, with the increasing number of independent copies, the probability that at least one of the replicas is not experiencing a deep fade

---

[12]WiMAX standards for worldwide interoperability for microwave access

[13]HSPA+ shorts for high-speed packet access plus

increases. Therefore, by properly combing various replicas at the receiver through signal combing techniques (e.g., maximum ratio combining, selective combing, and equal gain combining), the quality and reliability of the reception over multipath fading channels can be improved.

Besides the contribution to wideband channel modeling, this dissertation is also devoted to assess the performance of broadband wireless communication systems based on these advanced technologies. In particular, this dissertation provides a performance analysis for both SISO OFDM systems and ST coded MIMO OFDM systems. The BEP or SER is applied as the prime criterion to measure the system performance. As the name implies, a BEP (or SER) is defined as the percentage of error bits (or symbols) relative to the total number of bits (or symbols) transmitted in a digital communication system. In the dissertation, the BEP or SER performance is studied not only by software simulations but also by theoretical analysis. Here, software simulations indicate that a SISO or MIMO broadband communication system is simulated by a software, e.g., Matlab. The simulation procedure can be summarized as follows. First, a sufficient number of bits are modulated or coded at the transmitter. Then, these bits are sent to a wideband channel simulator, which simulates the fading behavior of mobile radio channels. Severe signal attenuations may occur after passing such a simulated channel component due to the generated multiplicative and additive noises. At the receiver, the transmission errors are measured by comparing the demodulated or decoded information bits with the original transmitted ones. On the contrary, the theoretical performance analysis means that the BEP or SER is directly calculated by some analytical formulas.

1.4   Organization of the Dissertation

The exposition included in this dissertation concentrates on the comprehensive investigations of SISO and MIMO broadband wireless communication systems. The covered topics range from modeling wideband mobile fading channels for different propagation environments up to the performance analysis of a broadband wireless communication system.

This dissertation summarizes the work of the PhD candidate presented in ten technical papers. These papers are included at the end of this dissertation as appendices (Appendices A–J). All the papers dealing with similar topics are collected together to form a chapter. Therein, the major contributions of each paper as well as its connection to other papers are elaborated. The rest of the dissertation is structured as follows:

- **Chapter 2** provides a comprehensive overview of Papers I and II (Appendices A and B), which are dedicated to model, simulate, and analyze wideband MIMO mobile radio channels for various outdoor propagation environments. Two wideband MIMO channel models based on the geometrical one-ring and two-ring scattering models are introduced in this chapter. Furthermore, the statistical properties of the derived wideband geometry-based MIMO channel models in terms of the temporal ACF, the 2D space CCF, and the FCF are discussed.

- **Chapter 3** puts its focus on the modeling, simulation, and statistical characterization of wideband SISO mobile fading channels for indoor scenarios. This chapter provides an insightful review of Papers III and IV (Appendices C and D), where a new geometrical rectangle scattering model is exploited to characterize indoor propagation environments. In these papers, the probability density function (PDF) of the AOA, the PDF of the envelope, the Doppler power spectral density (PSD), the temporal ACF, and the FCF are analyzed and visualized. In addition, the validity of the obtained wideband rectangle channel model is demonstrated by comparing its channel statistics with empirical ones measured from real-world indoor channels.

- **Chapter 4** is devoted to analyze the performance of a SISO broadband wireless communication system composed of a transmitter, a channel simulator, and a receiver. The so-called OFDM technology is applied to combat the effect of multipath fading. The performance analyses are presented in detail in Papers V and VI (Appendices E and F), where analytical expressions for the BEP of an OFDM system are derived under both assumptions that the receiver perfectly and imperfectly knows the CSI.

- **Chapter 5** summarizes the work of Papers VII–X (Appendices G–J), which concentrate on the performance study of a MIMO broadband wireless communication system by means of computer simulations as well as theoretical analyses. In these papers, the space-time coding techniques are applied to improve the reliability of the overall communication link. The performance of the space-time coded MIMO system is evaluated and analyzed under various propagation environments emulated by different wideband geometry-based channel models.

- **Chapter 6** recapitulates the main contributions of this dissertation. In addition, it highlights some open problems that need to be envisaged in future study.

Each chapter comprises several sections with the obligation of discussing the sub-topics addressed in the chapter. The chapter proceeds in the following manner.

- **Introduction** presents a brief background and state of the art of the main topic of the chapter.

- **Section** *N* gives a joint review for papers addressing a similar subject under the umbrella of the main topic of the chapter. Each section elucidates the papers falling into the same sub-topic in the way organized as follows.

  – Each section begins with a short introduction of the subject along with the motivation to address such a subject.

  – It then elaborates the main work of the paper(s) collected in this section. If several papers with a similar subject are included in this section, the connection between these papers is also explained.

  – Thereafter, the main results illustrated in the paper(s) are reviewed.

  – At the end, the significance of the achieved outcome(s) is emphasized. Additionally, the limitation regarding the achievement(s) as well as the disadvantage(s) of the methodology followed by the papers(s) is also revealed if any.

- **Chapter Summary and Conclusion** highlights the major findings of the chapter.

Chapter 2

Modeling and Statistical Characterization of Outdoor MIMO Radio Propagation Channels

2.1   Introduction

The limited frequency spectrum in radio communications as well as the increasing demand for high data-rate wireless communication services encourage investigations of MIMO wireless communications [17, 24, 78]. In order to design, evaluate, and optimize a MIMO wireless communication system, it is necessary to know the most important channel characteristics of MIMO mobile fading channels. Moreover, a profound knowledge of MIMO radio channels can assist in the design of space-time codes [68, 152, 154] and spatial multiplexing techniques [135, 160] so that a robust system performance and a high channel capacity can be achieved. Motivated by the above mentioned benefits from precisely describing the fading behavior of mobile radio channels, Chapter 2 focuses on the modeling of MIMO mobile radio channels for various outdoor propagation environments, while the modeling of indoor propagation channels is addressed in Chapter 3.

As mentioned in Chapter 1, there already exist several approaches to model MIMO channels [172]. One of the most efficient methods is geometry-based channel modeling. The basic idea of this method is to model scattering environments around a BS or a MS or both by specific geometric patterns. Then, the waves scattered by scatterers are determined by a simplified ray-tracing. Finally, the plane waves reaching at the MS are calculated as the superposition of waves coming from all directions. The channel models developed by a geometry-based channel modeling approach are capable to predict accurate channel characteristics for var-

ious propagation scenarios by means of simply modifying scatterer distributions or certain predefined channel parameters such as the maximum Doppler frequency and the position of BS or MS. This can be regarded as the main advantage of the approach. Another advantage is that geometry-based channel modeling combined with the concept of deterministic channel modeling enables to design efficient outdoor channel simulators. With the help of this strategy, different types of outdoor MIMO fading channels can be simulated with low realization expenditure.

Due to the advantages mentioned above, the method of geometry-based channel modeling has been widely applied to characterize narrowband and wideband MIMO fading channels. The scattering environments are commonly modeled by some well known geometric patterns including the one-ring scattering model [63, 117], the two-ring scattering model [14], and the elliptical scattering model [32, 80]. So far, narrowband MIMO geometry-based channel models, which have been derived from the aforementioned geometrical scattering models, can be found in [52, 63, 114, 117, 118, 124]. The extensions of the narrowband MIMO geometry-based channel models with respect to frequency selectivity have been reported in [53, 120, 121, 142].

All these publications [52, 53, 63, 114, 117, 118, 120, 121, 124, 142] have assumed isotropic scattering conditions when modeling MIMO radio propagation channels. Here, isotropic scattering implies that the AOA follows a uniform distribution. However, it has been experimentally demonstrated in [33, 42] that scattering encountered in many environments is more likely to be non-isotropic, resulting in a non-uniform distribution of the AOA at the MS. Under the non-realistic assumption of uniformly distributed AOAs, the level crossing rate of a received envelope and the resulting theoretical correlation functions strongly deviate from the experimental ones obtained from measured data [77]. In addition, the inaccurate AOA characteristics have obvious impacts on a multiuser multichannel array detection and a single user diversity reception [4]. Thus, in order to obtain spatial channel models with more realistic correlation properties as well as to facilitate a user detection/reception, modeling MIMO mobile fading channels has to be taken under non-isotropic scattering conditions. Regarding this work, however, only a few results have been presented in the literature for the narrowband case [5, 15]. Appropriate wideband MIMO geometry-based channel models are still rare for outdoor non-isotropic scattering environments. Therefore, Paper I, summarized in Section 2.2, uses a one-ring scattering model to characterize wideband MIMO mobile radio channels for non-isotropic scattering environments.

Besides non-isotropic scattering, another aspect, known as M2M fading, should

be also taken into account in modeling outdoor MIMO radio propagation channels. The consideration of M2M fading is basically motivated and required by the wide applications of M2M communication systems, e.g., in ad hoc wireless networks [161, 169], intelligent highways [59], and relay-based cellular networks [74]. In contrast to traditional fixed-to-mobile (F2M) cellular radio communication systems, it is considered that both the BS and the MS are in motion in M2M communication systems. The literature study reveals that the statistical properties of M2M channels are quite different from classical F2M channels [114]. Therefore, many currently developed F2M channel models cannot be directly used to model M2M propagation channels. By now, the geometry-based MIMO M2M channel models are only available for narrowband fading channels [119, 54]. Wideband geometry-based MIMO M2M channel models are still rare. This gap will be filled in Paper II summarized in Section 2.3.

2.2   A Wideband One-Ring MIMO Channel Model Under Non-Isotropic Scattering Conditions

Section 2.1 highlights the scarcity of proper wideband MIMO geometry-based channel models for outdoor non-isotropic scattering environments. Motivated by this fact, Paper I in Appendix A [90] of this dissertation, focuses on developing wideband MIMO one-ring channel models for non-isotropic scattering conditions.

The one-ring model was initially utilized to characterize propagation environments in rural and suburban areas. Figure 2.1 illustrates the original one-ring scat-
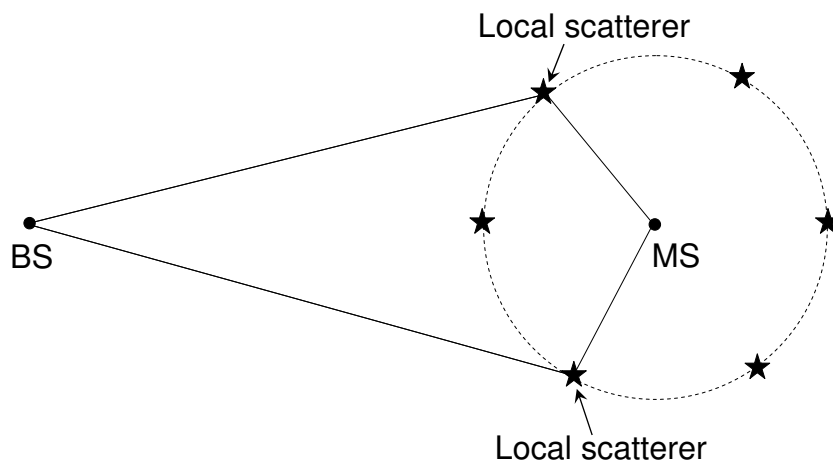
Figure 2.1: Geometrical model (one-ring model) with local scatterers uniformly located on a ring around the MS.

tering model, where the BS is assumed to be elevated and therefore not obstructed by local scatterers, while the MS is surrounded by local scatterers uniformly located on a ring formation. Different with traditional one-ring channel models developed under isotropic scattering environments, Paper I is devoted to propose wideband MIMO one-ring channel model for non-isotropic scattering environments. As can be seen from Fig. 2.2, in such scenarios, local scatterers are non-uniformly placed on the ring around the MS. In this paper, the non-isotropic scattering around the MS is characterized by the von Mises distribution. It has been explained in [3] that the key feature of such a distribution is that it closely approximates several important distributions for modeling the nonuniform distribution of the AOA, e.g., the cardioid distribution [97] and the Gaussian distribution. In addition, the von Mises distribution can model isotropic scattering conditions since it includes the uniform distribution as a special case.

A wideband MIMO one-ring reference channel model is first proposed in Paper I for non-isotropic scattering environments. The basic idea is to derive a wideband MIMO one-ring channel model in such a way so that the delay PSD of the resulting reference channel model is identical to a given delay PSD. This can be implemented by partitioning the ring of scatterers into $\mathscr{L}$ pairs of clusters as described in Fig. 2.3 and assigning a single discrete propagation delay τ'_ℓ to a pair of clusters I_ℓ according to a fixed rule ($\ell = 1, 2, \cdots, \mathscr{L}$) [121]. The obtained reference channel model is regarded as an ideal model since it is assumed that the number of local scatterers around the MS is infinite. Such a channel model, therefore, cannot be exactly realized because of their infinite computational complexity. However, the reference model can be exploited as a starting point to derive an efficient deterministic simu-
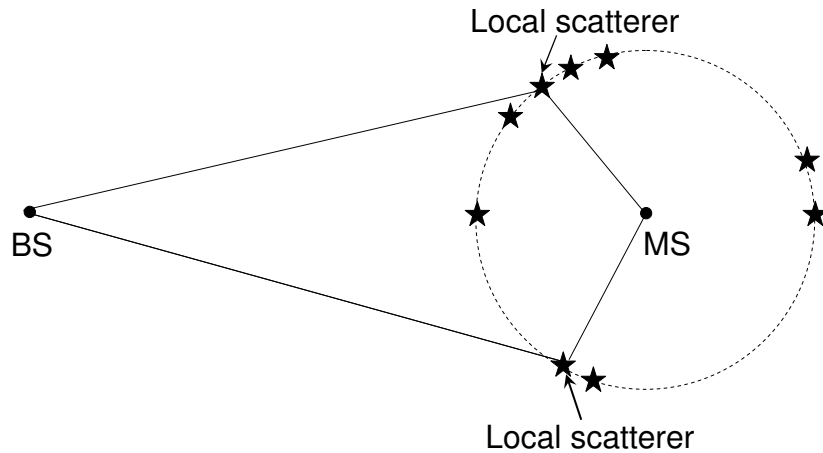
Figure 2.2: Geometrical model (one-ring model) with local scatterers non-uniformly located on a ring around the MS.

$$\text{If } n \subset I_\ell, \quad \text{then} \quad \tau'_n \to \tau'_\ell.$$
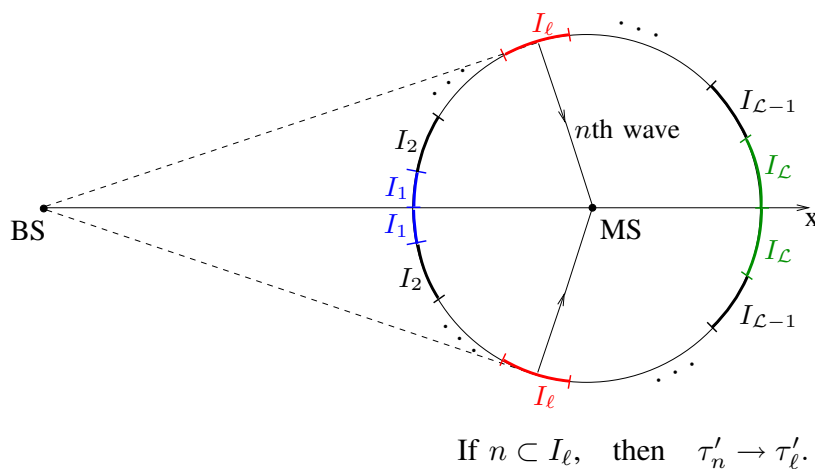
Figure 2.3: Scatterer diagram for the geometrical one-ring model under non-isotropic scattering conditions.

lation channel model. Such a work is completed in Paper I by applying the principle of deterministic channel modeling [115]. The design procedure can be summarized by the following three steps: (a) replacing the infinite number of scatterers by a finite value, (b) determining constant values for the discrete AOAs by means of a proper parameter computation method, (c) setting the phases to random constants following a uniform distribution over $[0, 2\pi)$. Compared with the reference channel model, the underlying deterministic simulation model can be implemented with a low realization expenditure caused by a limited number of scatterers. After the development of the reference model as well as the deterministic simulation model, analytical expressions in terms of the temporal ACF, the 2D space CCF, and the FCF are derived in Paper I for both models. The correctness of all these theoretical results are also validated by simulations in this paper. With the intention to demonstrate the usefulness of the wideband one-ring channel model in the design, testing, and analysis of a communication system, a space-time block coded MIMO OFDM system is simulated in Paper I. In computer simulations, the derived deterministic simulation channel model is integrated as the channel part of the system. By simulating space-time block coded MIMO OFDM system, the influence of different channel parameters, such as the antenna spacing and the number of local scatterers, on the performance of a space-time coded MIMO OFDM system is discussed.

It is shown in Paper I that the statistical properties of the deterministic simulation model can be brought into astonishingly good agreement with those of the reference model. The modified method of equal areas (MMEA) [43] is used to determine the discrete AOAs of the deterministic simulation model. Such a method

is well suited for determining the AOA following non-uniform distributions. The simulation results reveal that the symbol transmission error rate of a space-time coded MIMO OFDM system improves by increasing the antenna spacings at the BS or MS or both sides. This means that the 2D space CCF has an influence on the symbol error rate performance of a space-time coded MIMO OFDM system. When evaluating the performance of MIMO OFDM systems in rich cluster environments, the wideband one-ring channel simulators designed by using a single scatterer in each cluster are equivalent to the channel simulators having multiple scatterers in each cluster.

The significance of the presented work comes from the following four aspects. Firstly, Paper I introduces a general procedure for developing wideband geometry-based MIMO channel models for various non-isotropic scattering environments. The achievement of such a procedure lies in the fact that it guarantees that the delay PSDs of resulting wideband geometry-based MIMO channel models can be identical to any given delay PSD. Secondly, the obtained deterministic simulation channel model considerably reduces the complexity of implementing channel simulators in simulations. Thirdly, the resulting deterministic simulation channel model facilitates the study of the impact of the channel parameters on the performance of outdoor wideband wireless communication systems under non-isotropic scattering conditions. The last but not the end, the wideband extension used in Paper I for the one-ring channel model can be easily extended to the geometrical two-ring channel model due to the fact that the two-ring scattering model can be considered as the combination of two one-ring scattering models.

2.3   Wideband Two-Ring MIMO Channel Models for Mobile-to-Mobile Communications

Paper I presents a wideband MIMO one-ring channel model with the purpose of characterizing fading behavior for outdoor non-isotropic scattering propagation environments. The designed one-ring channel model only considers the MS in motion, while the BS is fixed. Such a channel model only enables to characterize traditional fixed-to-mobile mobile fading channels. For this reason, Paper II targets at modeling wideband MIMO M2M fading channels by making use of a geometrical two-ring scattering model. A short overview of Paper II is given in this section, whereas the full paper is presented in Appendix B [89].

The geometrical two-ring scattering model was originally proposed in [14] for urban and sub-urban areas. This model is shown in Fig. 2.4, where the scattering
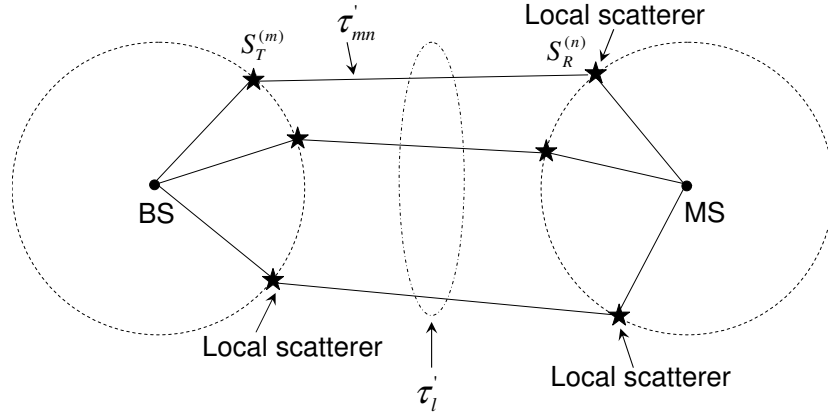
Figure 2.4: Geometrical model (double bounce scattering two-ring model) with local scatterers located on two rings around the BS and the MS.

around the BS and the MS is modeled by two individual rings — one ring of scatterers surrounding the BS and the other ring of scatterers around the MS. Furthermore, the proposed two-ring channel model considers double-bounce scattering, which implies that homogeneous plane waves emitted from the transmit antennas are first captured by scatterers around the BS and then by the scatterers around the MS before reaching the MS (see Fig. 2.4).

The geometrical double-bounce two-ring scattering model has been extensively applied to characterize narrowband MIMO M2M fading channels, where both the BS and the MS are moving. Examples of narrowband two-ring MIMO M2M channel models can be found in [54, 119]. As an extended work, Paper II first extends the traditional narrowband double-bounce two-ring MIMO M2M channel model with respect to frequency-selectivity. The idea of the wideband extension is that if the propagation delay τ'_{mn} from the BS to the MS via the scatterer $S_T^{(m)}$ around the BS and the scatterer $S_R^{(n)}$ around the MS is assigned to the same delay τ'_ℓ if τ'_{mn} is within the range $(\tau'_{\ell-1}, \tau'_\ell]$ $(\ell = 1, 2, \cdots, \mathscr{L})$. Furthermore, this paper proposes a new narrowband two-ring MIMO M2M reference channel model under the assumption of single-bounce scattering. Figure 2.5 shows that in the single-bounce scattering model, plane waves radiated by the transmit antennas are captured by scatterers only around the BS or around the MS before arriving the MS (see Fig. 2.5). In this sense, the single-bounce two-ring scattering model can be considered as the combination of two one-ring models, which is illustrated in Fig. 2.6. Therefore, the work of extending the proposed narrowband single-bounce scattering two-ring MIMO M2M channel model to a wideband channel model can be completed by separately making wideband extension of two one-ring channel models. The way of extending narrowband one-ring channel model with respect to frequency selectivity can
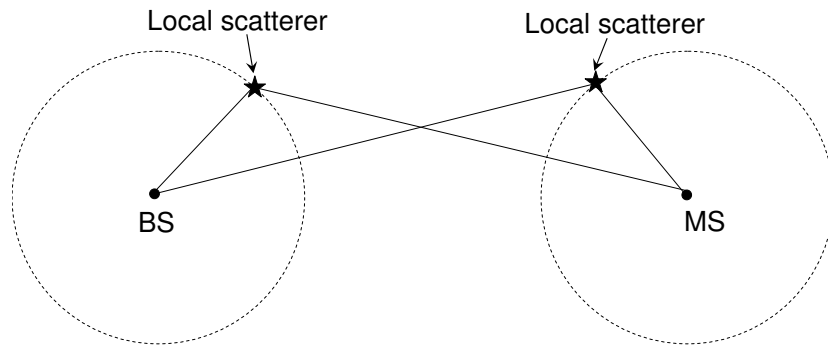
Figure 2.5: Geometrical model (single bounce scattering two-ring model) with local scatterers located on two rings around the BS and the MS.

be referred to Section 2.2. Moreover, Paper II studies the temporal, spatial, and frequency correlation properties for both the wideband double-bounce scattering and single-bounce scattering MIMO channel models. This is also one of the main objectives of the paper. Closed-form solutions are derived for the temporal ACF, the 2D space CCF, and the FCF. To validate the correctness of the theoretical results, these statistical properties are analyzed and visualized under the assumption of isotropic scattering conditions.

It is shown that the temporal ACF of the single-bounce scattering two-ring MIMO M2M channel model is a Bessel function. The 2D space CCF decreases as the antenna spacing at the BS or the MS increases. The FCF of the single-bounce scattering two-ring model is identical to the FCF of double-bounce scattering two-ring models if plotted under the same conditions.

The proposed wideband reference channel models can be used as a basis for the derivation of wideband MIMO M2M channel simulators. Besides, the proposed channel models are of crucial importance for studying the channel capacity of wideband M2M fading channels under various propagation scenarios specified by different PSDs.

2.4   Chapter Summary and Conclusion

MIMO systems appear to be very promising since they can provide high data-rate services. Moreover, they can greatly increase the channel capacity in a sufficiently scattering-rich environment by utilizing spatial diversity. With the intention of designing a real MIMO wireless communication system and predicting its performance, it is necessary to develop accurate and realistic MIMO channel models for different propagation scenarios. Therefore, this chapter pays special attention on the
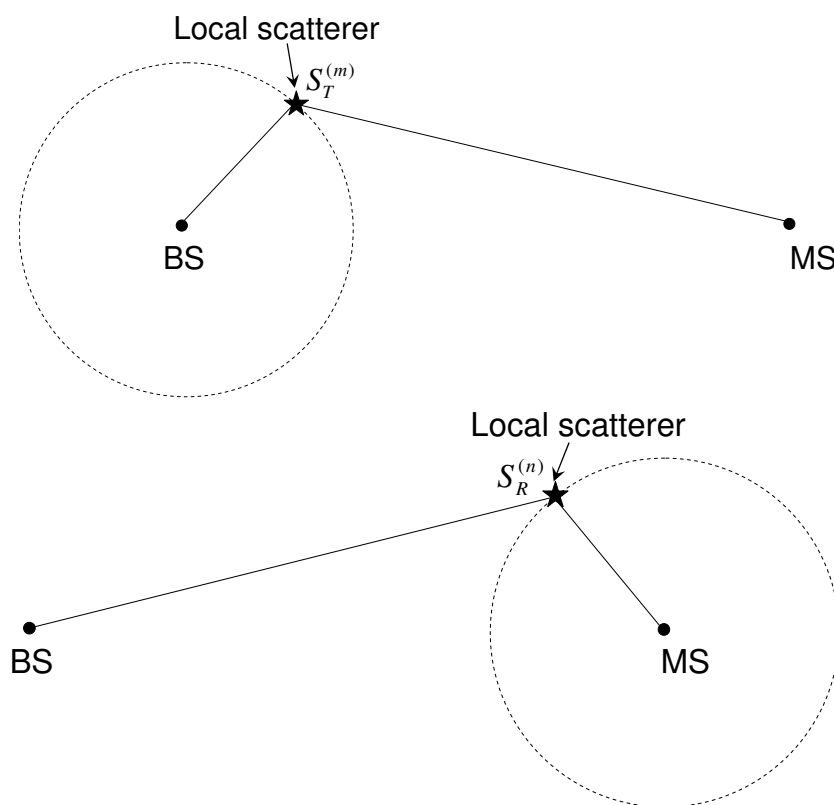
Figure 2.6: Waves impinging on the receiver bounced separately by local scatterers $S_T^{(m)}$ around the transmitter or local scatterers $S_R^{(n)}$ around the receiver.

modeling of MIMO mobile fading channels for outdoor propagation environments.

The chapter began by highlighting the advantages of the geometry-based channel modeling approach. Thereafter, different types of geometry-based channel models were briefly reviewed. The literature study revealed that both non-isotropic scattering as well as M2M fading have been taken into account when developing narrowband outdoor geometry-based MIMO channel models. However, for the wideband case, geometry-based channel models have been proposed only for isotropic scattering environments under the assumption that only the MS is moving. Motivated by these facts, Chapter 2 aimed at proposing new wideband geometry-based MIMO channel models for non-isotropic scattering environments as well as for M2M channels.

The chapter then summarized the work presented in Paper I (Appendix A), which deals with the topic of developing wideband geometry-based channel models for non-isotropic scattering propagation scenarios. In Paper I, a wideband one-ring MIMO reference channel model has been developed for non-isotropic scattering environments. A deterministic simulation channel model, which is required for

computer simulations, has directly been obtained from the reference model by using the principle of deterministic channel modeling. Analytical expressions have been presented for the temporal ACFs, the 2D space CCFs, and the FCFs of both the reference model and the deterministic simulation model. It has been shown by theory, confirmed by simulations, that the statistical properties of the deterministic simulation model match those of the reference model very well. In addition, to demonstrate the usefulness of the derived deterministic simulation channel model, a space-time block coded MIMO OFDM system has been further simulated, where channel fading behavior is described by the developed wideband one-ring deterministic simulation channel model. The simulation results have confirmed the fact that the symbol transmission error rate performance improves with increasing the antenna spacing. The wideband one-ring channel simulators designed with a single scatterer in each cluster is obviously sufficient to guarantee an accurate evaluation of the MIMO-OFDM system performance in non-isotropic scattering environments if the number of discrete paths is sufficiently large. It should be mentioned that the procedure of deriving the wideband one-ring model is quite general and applicable to any given delay PSD. Such a procedure guarantees that the delay PSD of the obtained wideband channel models is identical to a given delay PSD. The resulting wideband deterministic channel model can be used to study the impact of the channel parameters on the performance of wideband wireless communication systems under non-isotropic scattering conditions.

Afterwards, Chapter 2 summarized the work of developing wideband geometry-based channel models for MIMO M2M fading channels. Details regarding this work are reported in Paper II (Appendix B). In Paper II, the narrowband two-ring MIMO channel model based on double-bounce scattering has been extended with respect to frequency selectivity. A new geometrical two-ring reference model under the assumption of single-bounce scattering has been derived for narrowband MIMO M2M fading channels. Thereafter, a further extension of the proposed single-bounce scattering two-ring channel model to frequency selectivity has been made. Closed-form solutions have been presented for the temporal ACF, the 2D space CCF, and the FCF. The proposed wideband reference models can be used as a starting point for the design of stochastic and deterministic MIMO channel simulators. The obtained channel models are useful for the design, test, and optimization of future wideband M2M communication systems. Moreover, these models are important for studying the channel capacity of wideband M2M channels under various propagation conditions specified by different PSDs.

Chapter 3

Modeling and Statistical Characterization of Indoor Radio Propagation Channels

3.1 Introduction

An appropriate channel model, which precisely describes the underlying propagation characteristics, is a prerequisite for designing an efficient wireless communication system and accurately predicting the system performance [102]. Due to this fact, several outdoor geometry-based channel models were developed in Chapter 2 for various types of outdoor wireless communication environments. As a continuation work in the field of channel modeling, Chapter 3 is concerned with the design and simulation of indoor propagation channels.

In order to assist the indoor channel characterization and modeling, numerous measurement tests have been conducted under a variety of indoor scenarios. Offices, corridors, building, and factories are examples of indoor scenarios from where experimental data are measured. Measurement results have been reported in the literature for various frequency bands, such as 900 MHz [7, 12, 138], 1.5 GHz [132, 163], 4–5.5 GHz [48, 133], 17–18 GHz [29, 133], and 60 GHz [29, 103, 182]. Based on these measurement results, many empirical indoor statistical channel models [46, 47, 138, 171, 182] have been developed. The advantage of empirical statistical models is that they are capable of characterizing the realistic fading behavior since these models are developed on the basis of real-world measurements. By changing the values of their channel parameters, these empirical statistical models can simulate other indoor propagation environments. In order to determine the proper parameter values, however, extensive new measurement campaigns are needed to be carried

out. Such actions are expensive and time consuming. Alternatively, ray-tracing techniques [21, 75, 136, 139] can be exploited to simulate indoor propagation channels. Ray-tracing techniques approximate the electromagnetic-wave propagation by generating all possible paths (rays) from the BS to the MS according to the rules of geometrical optics. Ray-tracing channel models [66, 69, 83, 157] can efficiently capture the fading behavior of specified indoor environments. Many ray-tracing channel models developed so far have shown good agreement with measured channel characteristics [10, 79, 128]. Ray-tracing models, nonetheless, greatly depend on the physical layouts and materials through which signals propagate, e.g., walls, floors, and ceilings. On top of it, the main drawback of ray-tracing models is their computational cost, which relies on the size and complexity of the geographic database as well as the interaction order in a ray search. Therefore, the tradeoff between the prediction accuracy and the simulation efficiency has to be considered when modeling indoor propagation channels by means of ray-tracing techniques.

Both the empirical statistical channel models and ray-tracing channel models, have their own strengths and limitations when they are exploited to characterize indoor mobile radio propagation channels. To cope with the drawbacks mentioned above, a geometrical channel model has been proposed in [67] for indoor environments, where it is assumed that scatterers are randomly distributed within a circle centered on the BS. However, the model developed in [67] is only applicable to the indoor environments where the distance between the BS and the scatterers follows the exponential distribution. Moreover, it is not realistic to characterize an indoor scatterer region, like offices and walkpaths, by a circle. In contrast, a rectangle is more appropriate to describe indoor propagation situations. Motivated by the scarcity of proper geometry-based indoor channel models, this chapter is dedicated to develop new geometry-based channel models for indoor radio propagation conditions. As a starting point, a novel geometrical rectangular scattering model is proposed in Section 3.2, from which a narrowband indoor channel model is derived. Section 3.3 will discuss the extension of the narrowband rectangle channel model obtained in Section 3.2 with respect to frequency selectivity.

3.2   Design and Simulation of Narrowband Indoor Radio Propagation Channels

It has been pointed out in Section 3.1 that geometry-based indoor channel models are still rare. For this reason, the aim of Papers III and IV is to design new geometry-based indoor channel models, where the scattering environments around the BS

and the MS are modeled by a geometrical rectangular scattering model. Paper III targets at developing a geometry-based channel model for narrowband indoor radio channels, while Paper IV deals with geometrical channel modeling for wideband indoor propagation scenarios. Section 3.2 briefly summarizes the work presented in Paper III. More details regarding Paper III can be found in Appendix C [93].

As a basis, Paper III first proposes a geometrical rectangular scattering model. See Fig. 3.1 for a better understanding of the considered propagation scenario. The rectangle in this figure represents a room. The BS and the MS are arbitrarily placed in the 2D horizontal plane of the room. It is assumed that the BS is fixed, while the MS is in motion. Moreover, the model only considers single bounce scattering, which means that plane waves emitted from the BS are only bounced once by scatterers before reaching the MS. In Fig. 3.1, the black stars denote local scatterers. In reality, the number of scatterers and their locations differ from one propagation scenario to another. To avoid studying fading characteristics for a specific indoor propagation scenario characterized by a finite number of scatterers, a general statistical model that results from averaging over all possible propagation scenarios is considered. Therefore, it is assumed in Paper III that an infinite number of scatterers is uniformly distributed over the 2D horizontal plane of the room.

Based on the geometrical rectangular scattering model, a narrowband indoor reference channel model is proposed in Paper III. The line-of-sight (LOS) component between the BS and the MS is taken into consideration, which includes the non-LOS (NLOS) scattering scenarios as a special case. The underlying indoor ref-
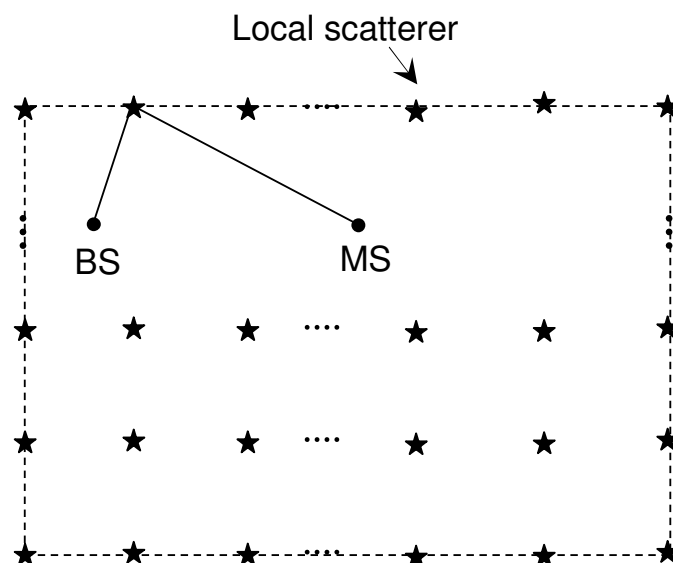
Figure 3.1: Geometrical model (rectangle model) with local scatterers uniformly distributed within the 2D horizontal plane of the room.

erence channel model is nonrealizable due to its tremendously high channel realization complexity. It cannot directly be utilized in simulations. To solve this problem, an efficient SOC channel simulator is derived by applying the sum-of-cisoids (SOC) principle. The idea of the SOC principle is to model the random Gaussian process by the sum of an finite number of cisoids. Analytical expressions in form of the PDF of the AOA, the Doppler PSD, and the temporal ACF are derived in Paper III.

In Paper III, the main theoretical results are illustrated by evaluating the Doppler PSD, the PDF of the envelope, and the temporal ACF of the reference model and the SOC channel simulator. The generalized method of equal areas (GMEA) [43] and the basic Riemann sum method (BRSM) [44] are utilized to compute the main parameters of the SOC channel simulator. The statistical properties are visualized under NLOS and LOS propagation conditions. Here, Paper III only presents the Doppler PSD curves for a channel's diffuse component since the Doppler PSD of a channel under LOS conditions can be obtained from the Doppler PSD of a channel's diffuse component by adding a discrete Doppler spectral line contributed by the LOS component. In the rest of Section 3.2, the Doppler PSD of a channel's diffuse component is referred to as the Doppler PSD for short. The curve of the Doppler PSD resembles a U-shape if the room length increases. It is shown by numerical results that the PDF of the envelope and the temporal ACF of the SOC channel simulator match very closely with the ones of the reference model. As expected, under LOS conditions, the envelope PDF of the derived indoor channel model follows the Rice distribution, while the PDF of the envelope reduces to the Rayleigh distribution for the NLOS case. It can be observed that the BRSM outperforms the GMEA regarding the approximation of the temporal ACF.

Paper III presents a procedure to study the statistical properties of the resulting reference channel model. Different with the traditional procedure, the introduced procedure requires no knowledge of the complex channel gain. The proposal of geometrical rectangle scattering model removes the scarcity of proper geometrical scattering models in the field of indoor channel modeling. In addition, the geometrical rectangle scattering model proposed for narrowband indoor radio propagation channels can be considered as a starting point for the derivation and analysis of new channel models for wideband indoor mobile fading channels. The obtained analytical results in Paper III are important not only for the theoretical study of the performance of indoor communication systems, but also indispensable for deriving efficient channel simulators. The designed SOC channel simulators also facilitate the performance evaluation of narrowband indoor wireless communication systems.

3.3 Statistical Modeling and Experimental Verification of Wideband Indoor Ratio Propagation Channels

As discussed in Section 3.2, Paper III deals with the design and simulation of indoor radio propagation channels for the narrowband case. As a follow-up work, Paper IV is concerned with the statistical modeling, simulation, and experimental verification of mobile fading channels for wideband indoor propagation environments. A short overview of Paper IV is given in this section, while the full paper is available in Appendix D [87].

Paper IV develops a wideband indoor reference channel model by employing the geometrical rectangle scattering model proposed in Paper III. For the same reason as explained in Section 3.2, Paper IV again assumes that there are an infinite number of scatterers located over the 2D horizontal plane of a rectangular room. Analytical expressions are derived for the PDF of the AOA, the power delay profile (PDP), and the FCF. An efficient SOC simulator is obtained from the non-realizable reference channel model by employing the SOC principle. Paper IV demonstrates the usefulness of the proposed geometry-based indoor channel model by comparing its analytical channel statistics with the empirical ones measured from real-world channels. The good agreement between these two types of channel statistics is achieved by optimizing the relevant channel parameters of the indoor channel model [104]. The parameter optimization is carried out by numerically minimizing the error function defined in [87] by means of the quasi-Newton procedure [34]. The channel statistics considered in the optimization procedure include the mean access delay and the root mean square (RMS) delay spread [47, 165], which are known as appropriate measures of multipath spread.

It is shown that the shape of the PDF of the AOA is independent of the position of the BS. Both the room length and width have influence on the FCF. The FCF decreases with increasing the frequency separation. If the room length or width increases, the FCF decays faster. The coherence bandwidth decreases with increasing the room size. It is also illustrated that the SOC channel simulator matches perfectly the wideband reference model with respect to the FCF. The close agreement between the analytical and empirical channel statistics confirms that the proposed indoor channel model enables to characterize various real-world wideband indoor mobile fading channels.

The fundamental procedure introduced in Paper IV for the purpose of confirming the validity of the channel models is general and can be applied to other

geometry-based channel models. The extension is fairly simple. In addition, the wideband indoor SOC channel simulators are quite important for the design and performance evaluation of the wideband indoor mobile radio communication systems. With these SOC channel simulators, present and future wideband indoor communication systems can be studied and optimized on a software platform. This considerably reduces the production costs and shortens the system developing time for new mobile techniques.

3.4   Chapter Summary and Conclusion

An accurate channel model is always indispensable for designing efficient outdoor or indoor wireless communication systems. With the help of precise radio channel models, high performance wireless communication systems can be implemented and the system performance can be accurately predicted. In Chapter 2, several outdoor geometry-based channel models have been developed for various types of outdoor wireless communication environments. As a follow-up work in the area of channel modeling, Chapter 3 mainly focuses on developing channel models for indoor propagation scenarios.

Before proposing a suitable channel model for indoor scenarios, the characteristics of indoor environments have to be studied through measurements. Therefore, Chapter 3 began by introducing measurement results conducted at different frequencies under a variety of indoor situations. Thereafter, Chapter 3 compared the main categories of indoor channel models, known as empirical statistical channel models and ray-tracing channel models, in the aspects of the accuracy and the efficiency. Both types of indoor channel models have their advantages and obvious drawbacks. Inspired by the idea of modeling outdoor mobile fading channels by geometrical scattering models presented in Chapter 2, Chapter 3 attempted to model indoor radio propagation channels based on a geometrical rectangle scattering model. Paper III (Appendix C) summarized the work of deriving a geometry-based channel model for narrowband indoor propagation scenarios. The extension of the resulting narrowband geometry-based channel model with respect to frequency selectivity was described in Paper IV (Appendix D).

Narrowband and wideband geometry-based channel models have been proposed in Chapter 3 for SISO indoor radio propagation channels. Since moving from SISO communication systems to MIMO systems is a major trend in current and future wireless communications, developing MIMO geometry-based indoor channel models will be examined in future work.

Chapter 4

Performance Analysis of SISO Broadband Wireless Communication Systems

4.1 Introduction

In broadband wireless communication systems, an unacceptable system performance degradation always occurs due to severe fading of the signal amplitudes and ISI caused by the multipath phenomenon. To cope with this problem, an innovative so-called OFDM technique is often employed to eliminate multipath fading and ISI. The basic idea of such a technique is to split a high data rate stream into multiple substreams of a lower data rate and transmit these substreams in parallel on adjacent orthogonal subchannels. If the number of subchannels is large, OFDM guarantees that each subchannel operates on a much smaller bandwidth than the coherence bandwidth of a broadband channel. Consequently, all subchannels experience relatively flat fading, which are almost free of ISI. OFDM-based systems have been found widespread applications in almost all domains of radio communications, e.g., for broadcast services (digital audio/video broadcasting) [2, 82, 134, 162, 177], mobile communications (WiMAX, 3GPP-LTE) [64, 131, 144, 26, 70], and wireless local area networks (IEEE 802.11a/g/n) [1, 50, 84]. The performance of OFDM-based systems over frequency-selective Rayleigh fading channels have been theoretically studied in [18, 27, 130, 148, 167, 168]. The BEP of OFDM-based systems in multipath Rice fading channels has been documented in [40, 85]. Moreover, the authors in [30] extended the performance analysis work by presenting an asymptotic BEP of OFDM systems over frequency-selective Nakagami-*m* fading channels. Thereafter, accurate error performance of OFDM systems over Nakagami-*m* fading environ-

ments was provided in [31].

So far, the performance of OFDM systems over different types of fading channels have been well explored. However, the performance of wideband channel simulators with respect to the BEP of a broadband OFDM system is still unknown. To fill this gap, Chapter 4 is dedicated to assess the performance of a SISO broadband wireless communication system by making use of a wideband sum-of-sinusoids (SOS) or SOC channel simulator. A BEP is applied in this chapter as the prime criterion to study the system performance. As the name implies, a BEP is defined as the percentage of bit errors relative to the total number of bits transmitted in a digital communication system.

The motivation of this work can be explained as follows. As revealed in [123], if the number of the sinusoids (or cisoids) used for designing a channel simulator tends to infinity, the envelope distribution of the Rayleigh fading channel simulator converges to the Rayleigh distribution. From this point of view, the BEP over the Rayleigh fading channel is supposed to be equal to the one evaluated by the channel simulator. However, it is also shown in [123] that if the number of harmonic functions is not sufficiently large, the obtained PDF of the envelope does not closely follow the Rayleigh distribution. Similar conclusion can be drawn for other types of channel simulators, whose envelope distributions are supposed to follow, e.g., Rice, Nakagami-*m* distribution [107], only to name a few. The statistics deviation of a channel simulator from a underlying considered mobile fading channel leads to a degradation when evaluating the system peroformance by a channel simulator. Such a finding is also confirmed in [122] by studying the performance of a transmission chain composed of a modulator, a narrowband Rayleigh fading SOS channel simulator, and a demodulator. The theoretical and simulation results in [122] demonstrate that the limited number of harmonic functions as well as the model error [115] introduced by parameter computation methods have an obvious influence on the system performance evaluation.

Inspired by the work in [122], Chapter 4 exemplarily shows how to analyze the BEP of an OFDM system composed of a wideband channel simulator. In particular, the topic of analyzing the performance of wideband SOS-based channel simulators within the framework of an OFDM system is addressed in Paper V. The performance analysis of a wideband SOC-based channel simulator with respect to the BEP of an OFDM system is presented in Paper VI.

4.2   Performance Analysis of Wideband Sum-of-Sinusoids-Based Channel Simulators with Respect to the Bit Error Probability of BPSK OFDM Systems with Perfect and Imperfect CSI

Channel simulators based on Rice's SOS principle are very important for modeling mobile fading channels. By applying the SOS principle combined with the concept of deterministic channel modeling [115], accurate and efficient SOS channel simulators can be easily designed for all kinds of channel models that can be derived from Gaussian random processes, e.g., Rayleigh [63, 115], Rice [129], lognormal [111], Suzuki [147], and Nakagami-*m* [164] fading channels. Moreover, SOS channel simulators can also be used to characterize wideband mobile fading channels [115]. In present days, SOS channel simulators have been commonly used in system simulations due to their low realization expenditure. The statistical properties of narrowband and wideband SOS channel simulators have been studied in [115]. So far, the performance of SOS channel simulators with respect to the BEP of a transmission system has been investigated only for narrowband fading channels [122]. However, the performance of wideband SOS channel simulators with respect to the BEP is not studied. Therefore, Paper V analyzes the performance of wideband SOS-based channel simulators with respect to the BEP of OFDM systems. More details related to this work can be found in Appendix E [91].

In this paper, the performance of a wideband deterministic SOS channel simulator with respect to the BEP of a binary phase-shift keying (BPSK) OFDM system is analyzed in the presence of perfect and imperfect CSI. Analytical expressions are derived for the BEP of the OFDM system composed of a wideband deterministic SOS channel simulator, which is introduced as the actual BEP in this dissertation. Since the SOS channel simulator is derived from a nonrealizable reference channel model, for comparison, Paper V also presents the BEP of a BPSK OFDM system in the presence of a reference model, which is introduced as the reference BEP. From the derived BEP expressions, the deviation of the actual BEP from the reference BEP, which is caused by the finite number of sinusoids used in the channel simulator, is discussed. With this study, it allows to reduce the channel simulator's realization expenditure to a minimum, where the performance degradation is negligible. The correctness of the presented theoretical results is also confirmed by simulations. In simulations, two parameter computation methods, i.e., the generalized method of exact Doppler spread (GMEDS$_1$) and the Monte Carlo method (MCM),

are employed to design the SOS channel simulators. The efficiency of the GMEDS$_1$ (a deterministic parameter computation method) and the MCM (a stochastic procedure) is evaluated on the basis of the obtained theoretical and simulation results.

For the case when the CSI is perfectly known at the receiver, it is proved by theory that the actual BEP evaluated in the presence of a SOS channel simulator converges to the reference BEP if the number of sinusoids tends to infinity. Such a finding is also confirmed by simulations. The results illustrated in Paper V show that the actual BEP is extremely close to the reference BEP even if the actual BEP is evaluated by a wideband SOS channel simulator designed by a few number of sinusoids. Furthermore, it can be observed from the presented results that the plotting of the actual BEP evaluated by the wideband SOS channel simulator designed with the GMEDS$_1$ overlaps with the one obtained from the MCM. The observation indicates that the channel simulators designed with the GMEDS$_1$ and the MCM are equivalent with respect to the impact on the BEP. This can be explained by the fact that the actual BEP is dependent on the Doppler coefficients, which are the same if calculated by the GMEDS$_1$ and the MCM. In addition, Paper V measures the deviation of the actual BEP from the reference BEP by the so-called relative error of the BEP, which is defined as the difference between the two types of the BEPs over the reference BEP. The evaluation of the relative error of the BEP shows that the absolute value of the relative error is below 4.1% if the real and imaginary parts of each propagation path in the wideband SOS channel simulator are designed with no less than 3 sinusoids. In most practical applications, such a deviation is tolerable.

When the CSI is not available at the receiver, the least-square estimation algorithm [125] is applied to estimate the CSI at the pilot position. It is illustrated that the BEP performance degrades if the maximum Doppler frequency or the pilot-inserted period increases. Moreover, the relative error of the BEP is zero if the GMEDS$_1$ is applied to design the channel simulator. However, if the MCM is used, the actual BEP deviates in a random manner from the reference BEP. The deviation of the BEP becomes larger with increasing the maximum Doppler frequency or the pilot-inserted period. It is demonstrated that the relative error of the BEP is approximately Gaussian distributed as the average SNR tends to infinity. Thus, it can be concluded that, under the assumption of imperfect CSI, the GMEDS$_1$ outperforms the MCM with respect to the BEP deviation. All theoretical results in this paper have been confirmed by simulations.

The derived analytical expressions of the BEP can be used to study the degradation of the BEP introduced by an imperfect wideband SOS channel simulator. It allows users to reduce the channel realization expenditure to a minimum without

introducing significant performance degradations. The presented analytical results for the BEP facilitate comparing the efficiency of different parameter computation methods. With this study, Paper V finds a maximum time lag over which the ACF has a strong influence on the BEP. Such a maximum time lag provides important information for some parameter design methods, e.g., the L_p-Norm method [115].

4.3   Performance Analysis of Wideband Sum-of-Cisoids-Based Simulators with Respect to the Bit Error Probability of DPSK OFDM Systems

SOS channel simulators mentioned in Section 4.2 are usually designed under the assumption that the inphase and the quadrature components of the complex channel gain are uncorrelated, which results in symmetrical Doppler PSDs for SOS channel simulators. Therefore, SOS-based channel simulators are advantageous for modeling mobile radio channels under isotropic scattering environments. In real-world, mobile fading channels usually have unsymmetrical Doppler PSDs, implying non-isotropic scattering environments [123]. Such channels can be efficiently modeled and simulated by a sum of a finite number of cisoids. The resulting channel simulator is known as a SOC channel simulator [116]. Paper V (Appendix E), summarized in Section 4.2, has analyzed the performance of wideband SOS-based channel simulators with respect to the BEP of BPSK OFDM systems. As a follow up work, Paper VI places its focus on studying the performance of wideband SOC channel simulators with respect to the BEP of differential phase-shift keying (DPSK) OFDM systems. A short overview regarding this work is presented in Section 4.3, while full details can be referred to Appendix F [92].

Paper VI analyzes the performance of a DPSK OFDM system in the presence of a stochastic wideband SOC channel simulator with respect to the BEP of the simulation system. For comparison, this paper presents the BEP of a DPSK OFDM system using a reference channel model, which is known as the reference BEP. Analytical BEP expressions are derived for coherent and noncoherent DPSK OFDM simulation systems in the presence of a wideband SOC channel simulator. Paper VI also discusses the degradations of the BEP introduced by an imperfect channel simulator. Using the relative error of the BEP as an appropriate measure, the performance of three parameter computation methods are evaluated, known as the method of exact Doppler spread (MEDS) [116], the randomized MEDS (R-MEDS) [180], and the MCM [55]. The R-MEDS and the MCM are typical stochastic parameter design

methods. In contrast to the MEDS, the discrete Doppler frequencies generated by these two methods are random values.

For coherent DPSK OFDM systems, it is shown by theory and confirmed by simulations that the SOC channel simulators designed by the MEDS, the R-MEDS, and the MCM are equivalent with respect to the BEP performance. When the number of cisoids tends to infinity, it is proved that the actual BEP evaluated by a wideband SOC channel simulator converges to the reference BEP. The relative error of the BEP can be neglected if the channel simulator is designed using no less than 5 cisoids for each propagation path. For noncoherent DPSK OFDM systems, a closed-form expression has been derived for the relative error, which provides a powerful tool when discussing the performance of different parameter computation methods. From the results illustrated in Paper VI, it can be concluded that the performance of the MEDS and the R-MEDS is almost the same with respect to the relative error of the BEP. However, both methods outperform the MCM.

The work presented in Paper VI fills the gap in the performance analysis of channel simulators. By now, the performance of OFDM systems in the presence of both the wideband SOS-based channel simulators and the wideband SOC-based channel simulators have been analyzed. The formula for the relative error of the BEP allows to reduce the channel realization expenditure to a lower bound without causing any obvious BEP distortion. Furthermore, the relative error of the BEP can be used as an appropriate criterion to evaluate the efficiency of different parameter computation methods. For example, in this paper, the performance of the best deterministic parameter design method (MEDS), the best stochastic one (R-MEDS), and the MCM are compared.

4.4   Chapter Summary and Conclusion

Wideband mobile fading channel simulators are quite important for the design and performance evaluation of broadband wireless communication systems. Due to their low realization expenditure, wideband channel simulators have been widely used in practical system simulations, e.g., in OFDM systems. So far, the statistical properties of wideband channel simulators have been well studied. However, the performance of a wideband channel simulator with respect to the BEP is unknown. This gap was filled in Chapter 4 by investigating the performance of a broadband OFDM system composed of a transmitter, a receiver, and a channel simulator.

Chapter 4 summarized the work presented in Papers V and VI (Appendices E and F). Paper V (Appendix E) analyzed the performance of wideband SOS-based

channel simulators within the framework of an OFDM system, while Paper VI (Appendix F) was devoted to study the performance of a wideband SOC-based channel simulator with respect to the BEP of an OFDM system. The main difference between these two types of channel simulators is that inphase and quadrature components are uncorrelated for SOS-based channel simulators, but correlated for SOC-based channel simulators. That means the SOS-based channel simulators are advantageous for modeling mobile radio channels under isotropic scattering environments, while SOC-based channel simulators are more efficient for modeling non-isotropic scattering environments.

Chapter 5

Performance Analysis of MIMO Broadband Wireless Communication Systems

5.1   Introduction

In broadband wireless communication systems, severe signal attenuations caused by multipath fading always exist, which make the decoding at the receiver extremely difficult. For a communication link equipped with multiple transmit and receive antennas, ST coding has been commonly utilized to improve the reliability of digital transmission over wireless radio channels [60, 105, 106, 154, 173]. ST coding can achieve diversity gain without increasing the transmitted power or sacrificing the bandwidth [127, 143]. In addition, ST coding is also considered as an effective and practical way to approach the capacity [86, 140, 141] of MIMO wireless channels [49, 96, 175]. Chapter 5 is devoted to assess the performance of ST coded MIMO broadband wireless communication systems.

ST coding is a new family of code design which takes into account channel coding, modulation, and transmit antenna diversity. In ST coded communication systems, multiple redundant copies of signals are sent through various transmit antennas over different time slots, In such a way, ST coding introduces spatial and temporal correlations among transmitted signals. These signal samples fade in a variety of manners over fading channels. For instance, some samples may experience severely faded, while others are less attenuated. The probability that all the samples are simultaneously below a particular threshold is much lower than the possibility of any individual sample below the same level. Then, by properly combining various samples at the receiver [8, 9, 156, 158], the effect of severe fading can be greatly

reduced, and consequently, the transmission reliability is considerably improved.

There are two main types of ST coding known as ST block coding (STBC) and ST trellis coding (STTC). STBC was original proposed by Alamouti as a two transmit antenna diversity scheme [6]. STBC is attractive since it can achieve a full spatial diversity gain and can be decoded by a simple linear processing. As illustrated in [6, 137, 152], STBC techniques are efficient for flat fading environments or indoor scenarios having small delay spreads. When a channel changes rapidly, the combination of STBC with OFDM can be utilized as a promising solution to eliminate the effect of multipath fading [20, 71, 76, 176]. With the help of OFDM techniques, a frequency-selective fading channel can be transformed into multiple flat fading subchannels, on which STBC can be applied. All the existing literature [6, 20, 71, 76, 137, 152] elucidates that STBC schemes work well if the channel is time-invariant over two consecutive symbol durations. However, it is not realistic to assume that the channel remains constant during the period of the STBC codeword transmission, especially not under fast fading conditions. Moreover, since the symbol duration of a multi-carrier system is much longer than that of a single-carrier system, a channel which is quasi-static for a single-carrier system may not be quasi-static for a multi-carrier system, e.g., for an OFDM system. Therefore, when studying the performance of a STBC OFDM system, the channel variations over two consecutive transmission time slots have to be taken into consideration. This issue is addressed in Section 5.2 by investigating the performance of STBC OFDM systems over time-varying multipath fading channels through simulations.

Simulating a STBC OFDM system is an essential step for the system performance evaluation. It provides an insight into the system performance. Moreover, the results obtained by means of computer simulations can be used to confirm the correctness of analytical results derived from the theoretical performance analysis. It has to be mentioned, however, that computer simulations are extremely time-consuming compared with theoretical analyses. To cope with the problem faced by computer simulations, the impact of a time-varying fading channel on the performance of a STBC scheme has been studied analytically in [159] for a single-carrier system and in [81] for a multi-carrier, in particular, an OFDM system. In both papers, the spatial correlation between the time-varying multipath Rayleigh fading subchannels has not been considered. However, it has been shown analytically in [73] that the performance of a STBC OFDM system depends also on the spatial correlation. Then, it is necessary to analyze the performance of a STBC OFDM system over a physically more realistic channel, which can be arbitrarily correlated either in time or in space or in both domains. This work is briefly reviewed in Section 5.3.

STBC schemes, however, have their own drawbacks. The major one is that the decoding of space-time block codes at the receiver requires the channel knowledge. For slow fading channels, the receiver can accurately estimate the CSI with the help of training sequences sent by the transmitter. For high-mobility broadband scenarios, it becomes very costly and difficult to predict the channel precisely. The inaccurate channel estimation leads to severe decoding errors for space-time block codes, which finally results in a significant performance degradation. For rapidly changing fading environments, it is useful to develop ST coding techniques which obviate the need of the CSI for decoding. Motivated by this fact, a differential detection scheme based on orthogonal designs have been proposed in [151] and [62] for two and multiple transmit antennas, respectively. In addition, various differential ST schemes have been also constructed for noncoherent communication systems so that the codes can be demodulated and decoded without employing the CSI at the receiver. For example, the authors of [51, 58] developed differential unitary ST codes, where information bits are encoded by a set of unitary constellations. Differential space-time block codes with a very low linear decoding complexity were presented in [19, 38, 149]. Such codes can provide diversity gain, but no coding gain. To obtain coding gains, a trellis-coded differential unitary ST modulation scheme was implemented in [150, 178], which combines trellis coding with differential unitary ST modulation. Since these trellis codes use unitary group codes as the inner block codes, their decoding complexity becomes extremely high when the transmission rate increases. Motivated by a need for trellis codes having low decoding complexity, a differential SOSTTC was introduced in [181]. Such a code is constructed by using a differential encoding scheme [151] as the inner code and a SOSTTC proposed in [61] as the outer code. In [181], two rather simple and fully-connected trellises were bulit for BPSK and quadrature phase-shift keying (QPSK) constellations. The case of eight phase-shift keying (8PSK) is not included in [181]. Therefore, the work summarized in Section 5.4 will fill this gap by designing differential SOSTTCs for BPSK, QPSK and 8PSK signal constellations.

The remainder of this chapter is organized as follows. Section 5.2 studies the performance of a STBC OFDM system over time-varying fading channels by means of computer simulations. Thereafter, the performance of such a system is theoretically analyzed in Section 5.3. The design of a differential SOSTTC for noncoherent communication systems is presented in Section 5.4. Finally, the chapter summary is given in Section 5.5.

5.2 Performance Comparison of ST Block Coded OFDM System Using One-Ring and Elliptical Wideband MIMO Channel Models

In Paper VII, the performance of STBC OFDM systems is investigated by means of simulations under realistic propagation conditions emulated by different wideband MIMO geometrical-based channel simulators. A SER is utilized to measure the error rate of the considered system. The spatial correlation effects due to the limited antenna spacings and the Doppler effect caused by the movement of the receiver are studied separately. Paper VII summarized in this section can be found in details in Appendix G [88].

In Paper VII, 2×2 and 4×4 STBC OFDM systems are simulated by Matlab. Herein, a 2×2 system means that both the BS and the MS are equipped with two antennas. Similarly, a 4×4 system indicates that four antennas are employed at the BS and the MS. The block diagram of the STBC OFDM system is illustrated in Fig. 5.1 by taking a 2×2 system as an example. The serial data bits are first passed through a serial-to-parallel converter. The resulting parallel data bits are modulated by a 16 quadrature amplitude modulation [41, 146], which produces a sequence of complex data symbols. Then, two consecutive data symbols are coded together by using the Alamouti scheme [6, 153]. After computing the inverse fast Fourier transform, the cyclic prefix is added to each sequence. The OFDM symbol sequences are then transmitted over the MIMO channel. Paper VII considers that the time-variant transfer function changes during the transmission of two consecutive OFDM symbols due to fading. The MIMO channel is modeled by a geometrical one-ring scattering model and an elliptical scattering model. More details regarding the geometry-based channel models will be introduced later in this section. At the receiver side, the demodulated symbol sequences are passed through a combiner.
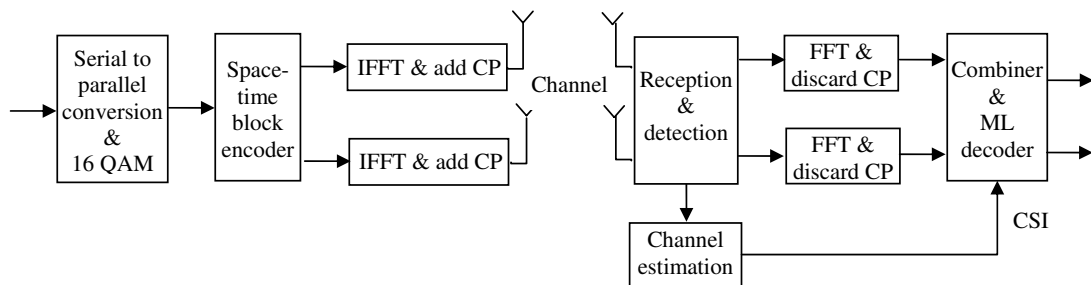
Figure 5.1: Space-time block coded MIMO-OFDM system with two transmit and two receive antennas.

Finally, by using the CSI obtained from the channel estimator, all the symbols can be decoded as described in [6, 153].

As already mentioned, a wideband one-ring channel model and a wideband elliptical channel model are employed to simulate a MIMO fading channel, over which the performance is evaluated. The scattering environments characterized by a one-ring model has already been introduced in Chapter 2 and illustrated in Fig. 2.1, where all scatterers are located on a ring around the MS [117]. The one-ring model is usually exploited to model mobile radio channels in macrocell environments, such as rural and suburban areas. On the contrary, the elliptical model considered in Paper VII was originally proposed for micro- and picocell environments. Figure 5.2 shows that in the wideband elliptical channel model, the BS and the MS are located at the focal points of the ellipse. Local scatterers are placed on several ellipses. All scatterers positioned on the same ellipse are associated with the same propagation delay.

In Paper VII, the performance of space-time block coded MIMO-OFDM systems is compared by employing the above two types of channel models. The comparison of the system performance is made for transmission scenarios proposed in [99] for the high performance radio local area network (HiperLAN/2) standard. The impact of the antenna spacings on the system performance is first discussed under the assumption of isotropic scattering conditions. Thereafter, the effect of the maximum Doppler frequency is studied for both the perfect and imperfect CSI cases. Perfect CSI indicates that channel information is perfectly known at the re-
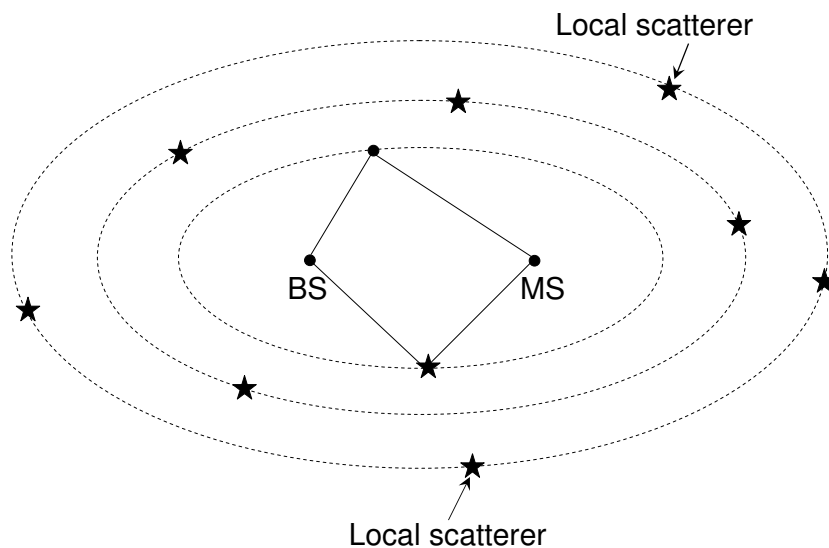
Figure 5.2: Geometrical model (elliptical model) with local scatterers located on several ellipses around the BS and the MS.

ceiver, while imperfect CSI implies that the knowledge of the channel is unavailable at the receiver. For the imperfect CSI case, the improved least square channel estimator described in [110] is used for the channel estimation.

The results presented in Paper VII reveal that the system performance improves if the antenna spacings at the BS or MS or both sides increase. The reason is that the spatial correlation between subchannels becomes smaller with increasing antenna spacings. Moreover, it can be observed that a certain antenna spacing increment at the transmitter leads to a larger performance improvement than that of the same amount at the receiver. However, for the one-ring channel model, if the antenna spacing at the BS, denoted by δ_T, is more than 10 times of the wavelength λ and the antenna spacing at the MS, denoted by δ_R, is larger than λ, then no performance gain can be observed when increasing the antenna spacing at one or both side. For the elliptical channel model, no significant performance improvement can be observed by further increasing the antenna spacings if $\delta_T > 0.5\lambda$ and $\delta_R > 0.3\lambda$. The comparison of the SER performance using the two types of channel models also demonstrates that the MIMO-OFDM system employing the elliptical channel model outperforms the one-ring model under the same conditions regarding the number of antennas and antenna spacings. The system using the elliptical 4×4 channel model with the antenna spacings $\delta_T = 10\lambda$ and $\delta_R = 0.3\lambda$ gains about 3.7 dB against the system using the one-ring channel model at the SER of 10^{-5}. The reason for this observation is that the spatial correlation function of the elliptical model decays faster with increasing antenna spacings than that of the one-ring model. The SER performance for various maximum Doppler frequencies illustrates that the system performance degrades slightly under the assumption of perfect CSI if the maximum Doppler frequency changes from 50 Hz to 500 Hz. However, for the case of imperfect CSI, severe performance degradations occur when the maximum Doppler frequency increases. It should be mentioned that the maximum Doppler frequency has an obvious influence on the SER performance since the fading during two consecutive transmission time slots has been taken into account.

Paper VII determines the antenna spacing ranges, over which the changes of the antenna spacing have strong influence on the system performance. Such a finding is very helpful for the design of antenna arrays. If the antenna spacings exceed the determined values, then the diversity gain does not increase significantly with increasing antenna spacings. The simulation results show that the SER performance degrades with increasing maximum Doppler frequency, especially in case of imperfect CSI. Hence, accurate fast-tracking channel estimators are indispensable for mobile communication systems with high moving speed.

5.3 Performance Analysis of Space-Time Block Coded OFDM System over Rayleigh Fading Channels Correlated in Space and Time

Paper VII revealed by simulations that the performance of a space-time block coded OFDM system depends not only on the temporal correlation but also on the spatial correlation between subchannels. Compared with system simulations, analyzing the system theoretically is more useful since the obtained analytical results make the performance evaluation more straightforward and less time-consuming compared with simulations. Papers VIII and IX therefore deal with the theoretical performance analysis of a space-time block coded OFDM system over time-varying multipath Rayleigh fading channels. Both papers consider an OFDM system equipped with two transmit antennas and a single receive antenna. In the performance analysis, the channel envelope variation during two consecutive transmission time slots will be taken into account. A short overview of Papers VIII and IX is given in this section, while these papers are available in full in Appendices H [95] and I [94], respectively.

Paper VIII studies the system performance over Rayleigh fading channels which are temporally or spatially correlated. It is assumed that the considered channels cannot be correlated simultaneously in time and space. That means, for instance, no spatial correlation exists when analyzing the system performance over channels correlated in time and vice versa. Thus, the theoretical results derived in Paper VIII are not generally valid and they cannot be used for the realistic case where the channels are correlated in both time and space. The drawback of Paper VIII is removed in Paper IX by restricting the attention to the physically more realistic case where the channel can be arbitrarily correlated either in time or in space or even in both domains.

Papers VIII and IX aim at deriving the analytical expressions for the BEP of a space-time block coded OFDM system over three different types of correlated channels, including (i) channels correlated in time, (ii) channels correlated in space, and (iii) channels correlated in both domains. The BEP can be calculated by integrating a conditional BEP (the BEP over an additive white Gaussian noise channel) over the PDF of an instantaneous output signal-to-noise ratio (SNR) [41, 125]. The conditional BEP for a given modulation scheme has been well studied and documented in numerous digital communication books, e.g., in [41, 125, 146, 143]. The major difficulty for computing the average BEP in Papers VIII and IX is to find an analytical expression for the PDF of the instantaneous output SNR. As shown in both papers,

the instantaneous output SNR depends not only on four channel envelopes, but also on four random phases of channels. Even if the joint PDF of the envelopes and phases is known, it is still difficult to derive the theoretical expression for the PDF of the instantaneous output SNR. To solve this problem, Papers VIII and IX introduce an approximation for the instantaneous output SNR by neglecting the overall phase contribution. Based on this simplification, an analytical expression for the PDF of the approximate instantaneous output SNR is derived. The accuracy of the obtained theoretical PDF of the approximate instantaneous output SNR is confirmed by simulations. In simulations, not only the PDF of the approximate instantaneous output SNR but also the PDF of the exact instantaneous output SNR (the one without neglecting the difference between the phase changes) are measured over the preceding three types of correlated fading channels. The correctness of the theoretical BEPs is verified by plotting the theoretical BEPs and those obtained from simulations together. Such a comparison clearly demonstrates that both approaches yield almost the same results.

The results presented for the PDF of the instantaneous output SNR demonstrate that the difference between the PDF of the approximate instantaneous output SNR and the PDF of the exact instantaneous output SNR is indistinguishable. This means that both PDFs are almost equivalent. It also implies that the instantaneous output SNR strongly depends on the statistics of the envelopes of the space-time-variant transfer functions, while the impact of the overall random phase contribution is negligible. The influence of the maximum Doppler frequency as well as the antenna spacing on the system performance is discussed with the help of the theoretical BEPs. It has been shown that the system performance deteriorates if the maximum Doppler frequency increases due to a lower temporal ACF. In contrast, the performance improves if reducing the 2D space CCF, which can be implemented by increasing the antenna spacing. It turns out that the temporal ACF and the space CCF have an inverse effect on the system performance though they have the same shape under isotropic scattering conditions. All the theoretical BEPs in both papers are validated by simulations. Although the overall random phase contribution is neglected when deriving the theoretical BEPs, it has been illustrated that the resulting analytical BEPs match the BEPs evaluated by simulations when the overall phase contribution is taken into account. It is shown by theory and confirmed by simulations that the BEP obtained in Paper IX over channels correlated in space and time includes the BEPs presented in Paper VIII for channels correlated only in time or space as special cases.

The performance of space-time coded OFDM systems over different types of

correlated channels can be numerically evaluated with the help of the derived BEP expressions. The knowledge of the obtained theoretical results makes the determination of the BEP less time-consuming compared with simulations. In addition, the work presented in Papers VIII and IX provides a deep insight into the impact of the Doppler effect and the antenna spacing on the system performance.

5.4   New Super-Orthogonal Space-Time Trellis Codes Using Differential M-PSK for Noncoherent Mobile Communication Systems with Two Transmit Antennas

Papers VII – IX (Appendices G – I) investigated the performance of space-time block coded communication systems. The key feature of STBC is that they can achieve full diversity with remarkably simple maximum likelihood decoding algorithms [152]. However, the drawback of STBC codes is that their decoding requires the knowledge of the channel at the receiver. When no knowledge of the channel is available, pilot sequences have to be sent at the transmitter to assist the receiver to estimate the channel. The performance of STBC codes under such an imperfect CSI condition has been evaluated in Paper VII. Simulation results show that a severe performance degradation exists due to an imprecise channel estimation at the receiver. To avoid the performance degradation caused by the imperfect CSI, it is necessary to develop ST coding techniques which can be decoded without exploiting the CSI. Paper X, included in Appendix J [145] of this dissertation, will address this problem by designing differential SOSTTCs, where neither the transmitter nor the receiver needs the CSI. As the name implies, SOSTTCs can be considered as a type of STTCs constructed based on a super-orthogonal set. Different from traditional STTCs, SOSTTCs label the state transitions of encoder trellis diagram with constituent orthogonal matrices defined in the super-orthogonal set.

Paper X employs a known differential encoding scheme [151] as the inner code and a SOSTTC proposed in [61] as the outer code to design the SOSTTCs for noncoherent communication systems. The differential SOSTTCs are constructed based on three types of signal constellations, i.e., BPSK, QPSK, and 8PSK. Motivated by the need for low-complexity transceivers, Paper X proposes a new decoding algorithm. The BEP performance of differential SOSTTCs decoded by the traditional decoding algorithm and the new strategy is evaluated by computer simulations based on a wideband MIMO two-ring channel model [89]. Furthermore, Pa-

per X studies the impacts of different channel parameters and transmission scenarios on the BEP performance of the differential SOSTTCs. In addition, for comparison, Paper X also simulates SOSTTCs using the coherent encoding scheme [61]. The coherent encoding scheme differs from the differential one by the fact that the signal set to be transmitted over the current signal period is independent on the signal information sent in the previous signal period.

Simulation results of differential SOSTTCs reveal that the proposed algorithm has the same decoding performance as the conventional algorithm. However, for differential SOSTTCs based on BPSK, QPSK and 8PSK signal constellations, the simulation time using the new decoding algorithm is approximately 70%, 68%, and 58%, respectively, of that using the traditional one, from which it can be concluded that the proposed decoding algorithm has a lower complexity. The evaluation of the simulation time also points out that the new decoding algorithm works more efficiently for differential SOSTTCs having a larger size of the signal constellation. The study of the impact of the antenna spacing on the BEP performance shows that the BEP performance improves with increasing antenna spacings, while the performance deteriorates if the antennas are placed very close to each other. The reason for this behavior is that the spatial correlation between the channel gains decreases as the antenna spacing becomes larger. The transmitter and the receiver have almost equivalent influence on the BEP performance. This can be explained by the symmetry of the geometrical two-ring scattering model and meanwhile the utilization of the same values for the main parameters of the transmitter and the receiver leads to this observation. The effect of the angular spread of the incoming waves on the BEP performance is also investigated in Paper X. It can be observed that the performance degrades if the angular spread decreases, which indicates a more scatterer centralized scenario. However, when the scatterers are highly centralized, no significant performance difference can be observed by further decreasing the angular spread of the incoming waves. In addition, a loss of 3 dB occurs when comparing the BEP performance of the differential SOSTTC with that of the coherent SOSTTC, which fully agrees with [151].

Paper X contributes towards the design of differential SOSTTCs for noncoherent mobile communication systems, where the knowledge of the channel is not necessary for decoding. The proposed decoding strategy reduces significantly the overall computing complexity. Additionally, simulation results presented in Paper X confirm the engineering intuition that the system performance greatly depends on the antenna spacing as well as on the angular spread of the incoming waves.

5.5 Chapter Summary and Conclusion

ST coded MIMO systems can achieve a full diversity gain and coding gain by means of simultaneously processing signals across space and time. Here, the spatial dimension is inherent in the use of multiple spatially distributed antennas, while the time dimension exists due to fact of transmitting digital data over consecutive time periods. By exploiting ST codes, such as ST block codes or trellis codes, the reliability of a MIMO communication systems can be significantly improved even in the presence of adverse propagation conditions such as multipath, interference, and severe fading. To evaluate the capability of existing and new proposed ST coding technologies, the performance evaluation of a ST coded MIMO communication system is imperative. Therefore, Chapter 5 is devoted to study the performance of a ST coded MIMO system over frequency selective fading channels.

The chapter began with an overview of the performance analysis of a ST block coded system. It was elucidated that when evaluating the performance under high mobility environments or for a multi-carrier system, the channel variations over two consecutive transmission time slots have to be taken into account. To address this problem, a ST blocked MIMO system is simulated through a software platform, where an OFDM technique is also applied for the purpose of combating multipath fading. More details in constructing such a system can be found in Paper VII (Appendix G). Therein, simulation results illustrate that not only the temporal correlation function but also the spatial correlation function between time-vary subchannels have impacts on the performance of a ST block coded OFDM system.

The chapter then summarized the work presented in Papers VIII and IX (Appendices H and I), which theoretically analyzes the performance of a ST block coded OFDM system over multipath Rayleigh fading channels correlated in space and time. Analytical expressions for the BEP of a ST block coded OFDM system have been derived. With the help of the obtained BEP expressions, the BEP performance of the above considered system over different types of correlated channels is numerically evaluated. The impacts of the maximum Doppler frequency and the antenna spacing on the system performance have been discussed.

Afterwards, the chapter highlighted the motivation and advantages behind extending the coherent ST codes to the noncoherent cases, where the CSI is not necessarily needed at the receiver for decoding. Motivated by this discussion, a differential SOSTTC is designed and presented in Paper X (Appendix J). Paper X demonstrates that the noncoherent scheme is approximately $3\,$dB worse than the coherent one for SOSTTC. The simulation results included in Paper X show that the system performance depends greatly on the antenna spacing and on the angular

spread of the incoming waves. The proposed new decoding strategy in Paper X has exactly the same decoding performance as the traditional one, but it is superior from the standpoint of the overall computing complexity.

Chapter 6

Summary of Contributions and Outlook

6.1 Major Contributions

This dissertation explored various physical layer aspects of broadband mobile radio communication systems. The topics covered the range from modeling wideband mobile fading channels to analyzing the overall performance of a broadband communication system. The main contributions of this doctoral dissertation are summarized as follows.

- Channel models which can accurately predict the fading behavior of real-world mobile radio channels are indispensable. Motivated by this fact, the dissertation was devoted to develop geometry-based channel models for various propagation outdoor and indoor environments.

- It has been experimentally demonstrated that scattering encountered in many environments is more likely to be non-isotropic. The usually made assumption of isotropic scattering in current channel models leads to strong deviations between the theoretical channel statistics and the experimental ones obtained from measured data. To fill this gap, this dissertation was dedicated to characterize outdoor non-isotropic scattering propagation scenarios by making use of a geometrical one-ring scattering model. A wideband one-ring MIMO reference channel model as well as its corresponding deterministic simulation channel model were derived. The most important statistical properties of the developed channel models including their temporal ACF, the 2D space CCF, and the FCF were analyzed.

49

- The single- and double-bounce scattering wideband two-ring MIMO channel models were proposed for M2M communications. Unlike traditional F2M channel models, this study assumed that both the BS and the MS are in motion. Closed-form solutions were presented in terms of the temporal, spatial, and frequency properties.

- This dissertation proposed a geometrical rectangle scattering model to describe indoor propagation scenarios. The importance of the proposed model lies in the fact that it overcomes the scarcity of an appropriate geometrical scattering model in the field of indoor channel modeling.

- Starting from the rectangle scattering model, a narrowband geometry-based SISO reference channel model was proposed for indoor propagation conditions. Thereafter, an indoor SOC channel simulator was derived from the reference channel model by applying the SOC principle. The indoor SOC channel simulator facilities the performance evaluation of mobile communication systems in indoor environments. A general procedure was applied in this dissertation to study the statistical properties of the resulting reference model. In contrast to the traditional procedure, the introduced procedure requires no knowledge of the complex channel gain. Analytical expressions were presented for the PDF of the AOA, the Doppler PSD, and the temporal ACF.

- This dissertation extended the previously proposed narrowband rectangle SISO channel model with respect to frequency selectivity. The usefulness of the proposed wideband rectangle SISO indoor channel model was demonstrated by showing that the statistical properties of the wideband rectangle SISO channel model can be fitted to the empirical ones measured from real-world indoor channels.

- The performance of a wideband deterministic SOS channel simulator with respect to the BEP of a BPSK OFDM system was analyzed in the presence of both the perfect and imperfect CSI. The objective of this study is to derive analytical expressions for the BEP of a BPSK OFDM system which is composed of a transmitter, a receiver, and a SOS deterministic channel simulator. With the help of the derived analytical results, the efficiency of deterministic and stochastic parameter computation methods was also evaluated. To confirm the correctness of the theoretical results, a simple BPSK OFDM system was simulated by Matlab.

- The topic of analyzing the performance of wideband SOC channel simulators within the framework of an OFDM system was also addressed in this dissertation. Analytical BEP expressions were derived for coherent and noncoherent DPSK OFDM systems.

- The dissertation simulated a space-time block coded OFDM system, where the wideband one-ring and elliptical channel simulators were exploited to emulate different propagation environments. This work provides a deep insight into the performance of a MIMO broadband mobile radio communication system over realistic fading channels. By simulating such a communication system, the spatial correlation effects due to the limited antenna spacings as well as the Doppler frequency caused by the movement of receiver were investigated separately.

- To make the performance evaluation of a MIMO broadband communication system less time-consuming, the performance of the space-time blocked OFDM system was theoretically analyzed. In the analysis, the usually made assumption of quasi-static channel conditions was abandoned. Instead of this, the more general and realistic case where the channel envelope changes during two consecutive transmission time slots was considered. An analytical expression was derived for the BEP of a space-time block coded OFDM system over fading channels correlated both in time and space.

- In this dissertation, the presented work dealing with the performance study of space-time block coded MIMO communication systems primarily assumed that the channel knowledge was perfectly known at the receiver. When the CSI is not fully available at the receiver, training sequences have to be sent from the transmitter to assist the receiver in estimating the CSI. Sending training sequences too frequently results in a heavy overhead. Additionally, inaccurate channel estimations often lead to a severe performance degradation. Motivated by these facts, a differential SOSTTC was designed for noncoherent communications, where neither the transmitter nor the receiver needs the CSI for decoding. In addition, a new decoding algorithm was proposed. The new algorithm has exactly the same decoding performance as the traditional one. However, it is superior from the standpoint of overall computing complexity.

6.2   Outlook

In this dissertation, the developed geometry-based channel models have provided a deep insight into the fading behavior of outdoor as well as indoor propagation scenarios. The performance analysis of broadband wireless communication systems has also been completed for both SISO and MIMO cases. However, there are still several open problems that remain unaddressed. The following issues deserve further investigations.

- In the dissertation, a rectangle scattering model was utilized to characterize narrowband and wideband SISO indoor mobile fading channels. However, the extension of such a SISO channel model to the MIMO case was still out of the scope of this doctoral thesis.

- All the geometry-based channel models developed in this dissertation considered 2D propagation environments, which means only electromagnetic waves traveling in the 2D horizontal plane have been considered. Such an assumption is acceptable only for certain environments, e.g., rural areas. In reality, electromagnetic waves may propagate by diffraction from the rooftops of buildings, ground, or other vertically disposed obstacles. Therefore, the vertical traveling plane waves are supposed to be taken into account. That means instead of 2D channel modeling, future channel modeling will more focus on 3D channel modeling.

- Several topics are worth to be investigated in the field of 3D channel modeling in the future, e.g., the development of appropriate 3D geometry-based or measurement-based channel models for both indoor and outdoor propagation environments, confirming the validity of the derived 3D channel models by measurements, the design of 3D channel simulators based on the SOC principle, and proposing new parameter computation methods applicable for determining the main channel parameters of the 3D channel simulators.

- When analyzing the performance of the space-time blocked OFDM system in this dissertation, the considered system was equipped with two antennas at the BS and a single antenna at the MS. To study how the spatial correlation at the MS influences the overall system performance, the performance analysis has to be extended to a system having multiple receive antennas, e.g., at least a 2×2 communication system.

- Although the dissertation managed to provide analytical expressions for the

BEP of the space-time block coded OFDM system, however, these expressions are just approximations. Therefore, exact and closed-form solutions are expected from further study of this topic. In addition, it also makes sense to explore how the model error caused by different parameter computation methods influences the BEP performance evaluation.

- In the literature, numerous techniques have been proposed to exploit the spatial diversity of MIMO fading channels. These techniques can be categorized into two groups, i.e., the space-time coding and spatial multiplexing. So far, the thesis has covered the topic of analyzing the performance of space-time codes over various wideband MIMO channel models. The design and performance evaluation of spatial multiplexing techniques over realistic MIMO fading channels were not studied in the dissertation, and therefore, need further investigations.

REFERENCES

[1] Part 11: Wireless LAN Medium Access Control (MAC) and Physical Layer (PHY) Specifications: High-Speed Physical Layer in the 5 GHz Band, IEEE Standard 802.11a, 1999.

[2] European telecommunications standards institute, Radio broadcasting systems; digital audio broadcasting (DAB) to mobile, portable and fixed receivers, ETS 300 401, May 1997.

[3] A. Abdi, J. A. Barger, and M. Kaveh. A parametric model for the distribution of the angle and the associated correlation function and power spectrum at the mobile station. *IEEE Trans. Veh. Technol.*, 51(3):425–434, May 2002.

[4] A. Abdi and M. Kaveh. A versatile spatio-temporal correlation function for mobile fading channels with nonisotropic scattering. In *Proc. 10th IEEE Workshop on Statistical Signal Array Processing*, pages 58–62. Pocono Manor, PA, USA, Aug. 2000.

[5] A. Abdi and M. Kaveh. A space-time correlation model for multielement antenna systems in mobile fading channel. *IEEE J. Select. Areas Commun.*, 20(3):550–560, Apr. 2002.

[6] S. M. Alamouti. A simple transmit diversity technique for wireless communications. *IEEE Journal on Select Areas in Communications*, 16(8):1451–1458, Oct. 1998.

[7] S. E. Alexander. Characterizing buildings for propagation at 900 MHz. *IEEE Electronics Letters*, 19(20):860, Sept. 1983.

[8] M.-S. Alouini and M. K. Simon. Error rate analysis of M-PSK with equal gain combing over Nakagami fading channels. In *Proc. 49th IEEE Semiannual Vehicular Technology Conference, VTC 1999*, volume 3, pages 2378–2382. Houston, TX, USA, May 1999.

[9] A. Annamalai, C. Tellambura, and V. K. Bhargava. Exact evaluation of maximal-ratio and equal-gain diversity receivers for M-ary QAM on Nakagami fading channels. *IEEE Trans. Commun.*, 47(9):1335–1344, Sept. 1999.

[10] G. E. Athanasiadou, A. R. Nix, and J. P. McGeehan. A microcellular ray-tracing propagation model and evaluation of its narrow-band and wide-band predictions. *IEEE J. Select. Areas Commun.*, 18(3):322–335, Mar. 2000.

[11] P. Bender, P. J. Black, M. S. Grob, R. Padovani, N. T. Sindushayana, and A. J. Viterbi. CDMA/HDR: a bandwidth efficient high speed wireless data service of nomadic users. *IEEE Communications Magazine*, 38(7):70–77, July 2000.

[12] E. Benner and A. B. Sesay. Effects of antenna height, antenna gain, and pattern downtilting for cellular mobile radio. *IEEE Trans. Veh. Technol.*, 45(2):217–224, May 1996.

[13] H. Bolcskei. MIMO-OFDM wireless systems: basics, perspectives, and challenges. 13(4):31–37, Aug. 2006.

[14] G. J. Byers and F. Takawira. The influence of spatial and temporal correlation on the capacity of MIMO channels. In *Proc. IEEE Wireless Communications and Networking, WCNC 2003*, pages 359–364. New Orleans, LA, USA, Mar. 2003.

[15] G. J. Byers and F. Takawira. Spatially and temporally correlated MIMO channels: modeling and capacity analysis. *IEEE Trans. on Veh. Technol.*, 53(3):634–643, May 2004.

[16] J. Cai and D. J. Goodman. General packet radio service in GSM. *IEEE Communications Magazine*, 35(10):122–131, Oct. 1997.

[17] C.-B. Chae, A. Forenza, R. W. Heath, M. McKay, and I. Collings. Adaptive MIMO transmission techniques for broadband wireless communication systems. *IEEE Communications Magazine*, 48(5):112–118, May 2010.

[18] M.-X. Chang and Y. T. Su. Performance analysis of equalized OFDM systems in Rayleigh fading. *IEEE Trans. Wireless Commun.*, 1(4):721–732, Oct. 2002.

[19] Z. Chen, G. Zhu, J. Shen, and Y. Liu. Differential space-time block codes from amicable orthogonal designs. In *Proc. IEEE Wireless Communications and Networking, WCNC 2003*, volume 2, pages 768–772. New Orleans, LA, USA, Mar. 2003.

[20] J. Cheng, H. Wang, and S. Cheng. Space-time block coded transmit diversity for OFDM system in mobile channels. In *Proc. 13th IEEE International Symposium on Personal, Indoor and Mobile RadioCommunications, IEEE PIMRC 2005*, volume 1, pages 208–211. Lisbon, Portugal, Sept. 2002.

[21] S.-H Cheu and S.-K. Jeng. An SBR/image approach to indoor radio propagation modeling. In *Proc. IEEE Antennas and Propagation Society, AP-S international symposium (Digest)*, volume 4, pages 1952–1955. Newport Beach, CA, USA, June 1995.

[22] Y. H. Chung, J. D. Parsons, and A. M. D. Turkmani. The prediction of BER performance in the GSM radio system. *IEEE Trans. Commun.*, 44(9):1064–1069, Sept. 1996.

[23] D. Collins and C. Smith. *3G Wireless Networks*. McGraw-Hill Professional, 2001.

[24] L. M. Correia and R. Prased. An overview of wireless broadband communications. *IEEE Communications Magazine*, 35(1):28–33, Jan. 1997.

[25] E. Dahlman, B. Gudmundson, M. Nilsson, and A. Skold. UMTS/IMT-2000 based on wideband CDMA. *IEEE Communications Magazine*, 36(9):70–80, Sept. 1998.

[26] E. Dahlman, S. Parkvall, J. Skold, and P. Beming. *3G Evolution HSPA and LTE for Mobile Broadband*. Academic Press, 2007.

[27] P. Dharmawansa, N. Rajatheva, and H. Minn. An exact error probability analysis of OFDM systems with frequency offset. *IEEE Trans. Commun.*, 57(1):26–31, Jan. 2009.

[28] G. L. Do and K. Feher. Efficient filter design for IS-95 CDMA systems. *IEEE Trans. Consumer Electronics*, 42(4):1011–1020, Nov. 1996.

[29] H. Droste and G. Kadel. Measurements and analysis of wideband indoor propagation characteristics at 17 GHz and 60 GHz. In *Proc. 9th International Conference on Antennas and Propagation*, volume 2, pages 288–291. Eindhoven, Netherlands, Apr. 1995.

[30] Z. Du, J. Cheng, and N. C. Beaulieu. Asymptotic BER performance of OFDM in frequency selective Nakagami-m channels. In *Proc. 60th IEEE Vehicular Technology Conference, VTC 2004-Fall*, volume 1, pages 612–615. Los Angeles, California, USA, Sept. 2004.

[31] Z. Du, J. Cheng, and N. C. Beaulieu. Accurate error-rate performance analysis of OFDM on frequency-selective Nakagami-m fading channels. *IEEE Trans. Commun.*, 54(2):319–328, Feb. 2006.

[32] R. B. Ertel and J. H. Reed. Angle and time of arrival statistics for circular and elliptical scattering models. *IEEE J. Select. Areas Commun.*, 17(11):1829–1840, Nov. 1999.

[33] P. C. Fannin and A. Molina. Analysis of mobile radio channel sounding measurements in inner city Dublin at 1.808 GHz. In *Proc. IEE Commun.*, volume 143, pages 311–316, Oct. 1996.

[34] R. Fletcher and M. J. D. Powell. A rapidly convergent descent method for minimization. *Computer Journal*, 6(2):163–168, 1963.

[35] Z. C. Fluhr and P. T. Porter. AMPS: Control architecture. *Bell Syst. Tech. J.*, 58(1):1–14, Jan. 1979.

[36] G. J. Foschini. Reliability of the repelling carrier method of implementing optical FDMA. *IEEE Trans. Commun.*, 37(12):1275–1281, Dec. 1989.

[37] G. J. Foschini and M. J. Gans. On limits of wireless communications in a fading environment when using multiple antennas. *Wireless Personal Communications (WPC)*, 6(3):311–335, Mar. 1998.

[38] G. Ganesan and P. Stoica. Differential modulation using space-time block codes. *IEEE Signal Processing Lett.*, 9(2):57–60, Feb. 2002.

[39] A. Ghosh, R. Ratasuk, B. Mondal, N. Mangalvedhe, and T. Thomas. LTE-advanced: next-generation wireless broadband technology. *IEEE Trans. Wireless Commun.*, 17(3):10–22, June 2010.

[40] A. Glavieux, P. Y. Cochet, and A. Picart. Orthogonal frequency division multiplexing with BFSK modulation in frequency selective Rayleigh and Rician fading channels. *IEEE Trans. Commun.*, 42(2/3/4):1919–1928, Feb./Mar./Apr. 1994.

[41] A. Goldsmith. *Wireless Communications*. Cambridge University Press, 2005.

[42] S. Guerin. Indoor wideband and narrowband propagation measurements around 60.5 GHz in an empty and furnished room. In *Proc. 46th Vehicular Technology Conference, VTC-1996*, pages 160–164. Atlanta, USA, Apr./May 1996.

[43] C. A. Gutiérrez and M. Pätzold. Sum-of-sinusoids-based simulation of flat fading wireless propagation channels under non-isotropic scattering conditions. In *Proc. 50th Global Communication Conference, GLOBECOM 2007*, pages 3842–3846. Washington, D.C., USA, Nov. 2007.

[44] C. A. Gutiérrez and M. Pätzold. The Riemann sum method for the design of sum-of-cisoids simulators for Rayleigh fading channels in non-isotropic scattering environments. In *Proc. 1st Workshop on Mobile Computing and Networking Technologies, WMCNT 2009*. St. Petersburg, Russia, Oct. 2009.

[45] S. Hara and R. Prasad. Overview of multicarrier CDMA. *IEEE Communications Magazine*, 35(12):126–133, Dec. 1997.

[46] H. Hashemi. Impulse response modelling of indoor radio propagation channels. *IEEE J. Select. Areas Commun.*, SAC-11(7):967–978, Sept. 1993.

[47] H. Hashemi and D. Tholl. Statistical modeling and simulation of the RMS delay spread of indoor radio propagation channels. *IEEE Trans. Veh. Technol.*, 43(1):110–120, Feb. 1994.

[48] D. A. Hawbaker and T. S. Rappaport. Indoor wideband radiowave propagation measurements at 1.3 GHz and 4 GHz. *IEEE Electronics Letters*, 26(21):1800–1802, Oct. 1990.

[49] A. S. Hiwale, A. A. Ghatol, and P. M. P. M. Gulhane. Capacity and performance analysis of space-time block coded MIMO systems with receive antenna selection in Rayleigh fading channels. In *Proc. IET-UK International Conference on Information and Communication Technology in Electrical Sciences, ICTES 2007*, pages 986–990. Chennai, Tamilnadu, India, Dec. 2007.

[50] M.-J. Ho, J. Wang, K. Shelby, and H. Haisch. IEEE 802.11g OFDM WLAN throughput performance. In *Proc. 58th IEEE Vehicular Technology Conference, VTC 2003-Fall*, volume 4, pages 2252–2256. Orlando, Florida, USA, Oct. 2003.

[51] B. M. Hochwald and W. Sweldens. Differential unitary space-time modulation. *IEEE Trans. Commun.*, 48(12):2041–2052, Dec. 2000.

[52] B. O. Hogstad, M. Pätzold, and A. Chopra. A study on the capacity of narrow- and wideband MIMO channel models. In *Proc. 15th IST Mobile & Communications Summit, IST 2006*. Myconos, Greece, June 2006.

[53] B. O. Hogstad, M. Pätzold, A. Chopra, D. Kim, and K. B. Yeom. A wide-band MIMO channel simulation model based on the geometrical elliptical scattering model. In *Proc. 15th Wireless World Research Forum Meeting, WWRF15, 2005*. Paris, France, Dec. 2005.

[54] B. O. Hogstad, M. Pätzoldand N. Youssef, and D. Kim. A MIMO mobile-to-mobile channel model: part II—the simulation model. In *Proc. IEEE 16th International Symposium on Personal, Indoor and Mobile Radio Communications, PIMRC 2005*, pages 562–567. Berlin, Germany, Sept. 2005.

[55] P. Höher. A statistical discrete-time model for the WSSUS multipath channel. *IEEE Trans. Veh. Technol.*, VT–41(4):461–468, Nov. 1992.

[56] L. M. C. Hoo, B. Halder, J. Tellado, and J. M. Cioffi. Multiuser transmit optimization for multicarrier broadcast channels: asymptotic FDMA capacity region and algorithms. *IEEE Trans. Commun.*, 52(6):922–930, June 2004.

[57] W. Hou and H. M. Kwon. Complementary filter design for testing of IS-95 code division multiple access wireless communication systems. *IEEE Trans. Instrum. Meas.*, 48(1):34–39, Feb. 1999.

[58] B. L. Hughes. Differential space-time modulation. *IEEE Trans. Inform. Theory*, 46:2567–2578, November 2000.

[59] H. Inoue, S. Osawa, A. Yashiki, and H. Makino. Dedicated short-range communications (DSRC) for ahs services. In *IEEE Intelligent Vehicles Symposium, 2004*, pages 369–374. Parma, Italy, Jun. 2004.

[60] H. Jafarkhani. *Space-Time Coding: Theory and Practice*. Cambridge University Press, 2005.

[61] H. Jafarkhani and N. Seshadri. Super-orthogonal space-time trellis codes. *IEEE Trans. Inform. Theory*, 49:937–950, April 2003.

[62] H. Jafarkhani and V. Tarokh. Multiple transmit antenna differential detection from generalized orthogonal designs. *IEEE Trans. Inform. Theory*, 47(6):2626–2631, September 2001.

[63] W. C. Jakes. *Microwave Mobile Communications*. New Jersey: IEEE Press, 1994.

[64] L. M. A. Jalloul and S. P. Alex. Coverage analysis for IEEE 802.16e/WiMAX systems. *IEEE Trans. Wireless Commun.*, 7(11):4627–4634, Nov. 2008.

[65] D. G. Jeong and W. S. Jeon. A data transmission scheme for CDMA wireless networks based on IS-95. *IEEE Trans. Veh. Technol.*, 49(1):11–20, Jan. 2000.

[66] Z. Ji, B.-H. Li, H.-X. Wang, H.-Y Chen, and T. K. Sarkar. Efficient ray-tracing methods for propagation prediction for indoor wireless communications. *IEEE Antennas and Propagation Magazine*, 43(2):41–49, Apr. 2001.

[67] L. Jiang and S. Y. Tan. Geometrically based statistical channel models for ourdoor and indoor propagation. *IEEE Trans. on Veh. Technol.*, 56(6):3587–3593, Nov. 2007.

[68] G. Jöngren, M. Skoglund, and B. Ottersten. Combing beamforming and orthogonal space-time block coding. *IEEE Trans. Inform. Theory*, 48(3):611–627, Mar. 2002.

[69] A. O. Kaya, L. J. Greenstein, and W. Trappe. Characterizing indoor wireless channels via ray tracing combined with stochastic modeling. *IEEE Trans. Wireless Commun.*, 8(8):4165–4175, Aug. 2009.

[70] J. Ketonen, M. Juntti, and J. R. Cavallaro. Performance-complexity comparison of receivers for a LTE MIMO-OFDM system. *IEEE Trans. Signal Processing*, 58(6):3360–3372, June 2010.

[71] J. Kim, R. W. Heath Jr., and E. J. Powers. Receiver designs for Alamouti coded OFDM systems in fast fading channels. *IEEE Trans. Wireless Commun.*, 4(2):550–559, Mar. 2005.

[72] D. N. Knisely, S. Kumar, S. Laha, and S. Nanda. Evolution of wireless data services: IS-95 to cdma2000. *IEEE Communications Magazine*, 36(10):140–149, Oct. 1998.

[73] E. Ko and D. Hong. A robust transmit diversity for OFDM systems in spatially correlated Rayleigh fading channels. In *Proc. 59th Vehicular Technology Conference, VTC 2004-Spring*, volume 4, pages 1840–1843. Milan, Italy, May 2004.

[74] S. Lakkavalli, A. Negi, and S. Singh. Stretchable architectures for next generation cellular networks. In *5th Annual International Symposium on Advanced Radio Technology*, pages 59–65. Colorado, U.S.A, Aug. 2003.

[75] M. C. Lawton and J. P. McGeehan. The application of a deterministic ray launching algorithm for the prediction of radio channel characteristics in

small-cell environments. *IEEE Trans. Veh. Technol.*, 43(4):955–969, Nov. 1994.

[76] K. F. Lee and D. B. Williams. A space-time coded transmitter diversity technique for frequency selective fading channels. In *Proc. IEEE Sensor Array and Multichannel Signal Processing Workshop, SAM 2000*, pages 149–152. Cambridage, USA, Mar. 2000.

[77] W. C. Y. Lee. Finding the approximate angular probability density function of wave arrival by using a directional antenna. *IEEE Trans. Antennas Propagat.*, 21(3):328–334, May 1973.

[78] Q. Li, G. Li, W. Lee, M.-I. Lee, D. Mazzarese, B. Clerckx, and Z. Li. MIMO techniques in WiMAX and LTE: a feature overview. *IEEE Communications Magazine*, 48(5):86–92, May 2010.

[79] G. Liang and H. L. Bertoni. A new approach to 3-D ray tracing for propagation prediction in cities. *IEEE Trans. Antennas Propagat.*, 46(6):853–863, June 1998.

[80] J. C. Liberti and T. S. Rappaport. A geomerically based model for line-of-sight multipath radio channels. In *Proc. 46th IEEE Semiannual Vehicular Technology Conference, VTC 1996*. Atlanta, GA, USA, May 1996.

[81] D. B. Lin, P. H. Chiang, and H. J. Li. Performance analysis of two–branch transmit diversity block–coded OFDM systems in time–varying multipath Rayleigh–fading channels. *IEEE Trans. on Veh. Technol.*, 54(1):136–148, Jan. 2005.

[82] C. Liu, Z. Wang, G. Chen, Y. Li, E. Wu, D. Li, B. Li, W. Dou, and Z. Dong. A DAB transmitter prototype with high flexibility and low cost. *IEEE Trans. Broadcast.*, 48(3):173–178, Sept. 2002.

[83] S. Loredo, A. Rodríguez-Alonso, and R. P. Torres. Indoor MIMO channel modeling by rigorous GO/UTD-based ray tracing. *IEEE Trans. Veh. Technol.*, 57(2):680–692, Mar. 2008.

[84] I.-T. Lu and K.-J. Tsai. Channel estimation in a proposed IEEE 802.11n OFDM MIMO WLAN system. In *Proc. IEEE Sarnoff Symposium, 2007*, pages 1–5. Princeton, NJ, USA, Apr./May 2007.

[85] J. Lu, T. T. Tjhung, F. Adachi, and C. L. Huang. BER performance of OFDM-MDPSK system in frequency-selective Rician fading with diversity reception. *IEEE Trans. Veh. Technol.*, 49(4):1216–1225, July 2000.

[86] M. Luccini, S. Primak, and A. Shami. On the capacity of MIMO channels and its effect on network performance. In *Proc. 3rd International Conference on Information and Communication Technologies: From Theory to Applications, ICTTA 2008*, pages 1–6. Damascus, Syria, Apr. 2008.

[87] Y. Ma and M. Pätzold. Statistical modeling and experimental verification of wideband indoor radio propagation channels. *Wireless Personal Communications (WPC)*, submitted for publication.

[88] Y. Ma and M. Pätzold. Performance comparison of space-time coded MIMO–OFDM systems using different wideband MIMO channel models. In *Proc. 4th IEEE International Symposium on Wireless Communication Systems, ISWCS 2007*, pages 762–766. Trondheim, Norway, Oct. 2007.

[89] Y. Ma and M. Pätzold. Wideband two-ring MIMO channel models for mobile-to-mobile communications. In *Proc. 10th International Symposium on Wireless Personal Multimedia Communications, WPMC 2007*, pages 380–384. Jaipur, India, Dec. 2007.

[90] Y. Ma and M. Pätzold. A wideband one-ring MIMO channel model under non-isotropic scattering conditions. In *Proc. 67th Vehicular Technology Conference, VTC 2008-Spring*, pages 424–429. Singapore, May 2008.

[91] Y. Ma and M. Pätzold. Performance analysis of wideband SOS-based channel simulators with respect to the bit error probability of BPSK OFDM systems with perfect and imperfect CSI. In *Proc. 12nd International Symposium on Wireless Personal Multimedia Communications, WPMC 2009*. Sendai, Japan, Sept. 2009.

[92] Y. Ma and M. Pätzold. Performance analysis of wideband sum-of-cisoids-based channel simulators with respece to the bit error probability of DPSK OFDM systems. In *Proc. 69th IEEE Vehicular Technology Conference, VTC-Spring 2009*, pages 1–6. Barcelona, Spain, Apr. 2009.

[93] Y. Ma and M. Pätzold. Design and simulation of narrowband indoor radio propagation channels under LOS and NLOS propagation conditions. In *Proc. 71st Vehicular Technology Conference, VTC 2010-Spring*, pages 1–7. Taipei, Taiwan, May 2010.

[94] Y. Ma and M. Pätzold. Performance analysis of Alamouti coded OFDM system over Rayleigh fading channels correlated in space and time. In *Proc. 71st IEEE Vehicular Technology Conference, VTC 2010-Spring*, pages 1–6. Taipei, Taiwan, May 2010.

[95] Y. Ma and M. Pätzold. Performance analysis of STBC-OFDM systems in temporally or spatially correlated fading channels. In *Proc. IEEE Wireless Communication and Network Conference, WCNC 2010*. Australia, Apr. 2010.

[96] A. Maaref and S. Aissa. On the capacity of space-time block codes in MIMO Rayleigh fading channels. In *Proc. 47th Global Communication Conference, GLOBECOM 2004*, volume 5, pages 2936–2940. Dallas, Texas, USA, Nov./Dec. 2004.

[97] K. V. Mardia. *Statistics of Directional Data*. London, U.K.: Academic, 1972.

[98] R. Mauger and C. Rosenberg. QoS guarantees for multimedia services on a TDMA-based satellite network. *IEEE Communications Magazine*, 35(7):56–65, Jul. 1997.

[99] J. Medbo and P. Schramm. Channel models for HIPERLAN/2 in different indoor scenarios. Tech. Rep. 3ERI085B, ETSI EP, BRAN Meeting #3, Mar. 1998.

[100] J. Medbo and P. Schramm. Channel models for HIPERLAN/2 in different indoor scenarios. Tech. Rep. 3ERI085B, ETSI EP, BRAN Meeting #3, Mar. 1998.

[101] N. Mehravari. TDMA in a random-access environment: An overview. *IEEE Communications Magazine*, 22(11):54–59, Nov. 1984.

[102] A. F. Molisch. *Wireless Communications*. Chichester: John Wiley & Sons, West Sussex, UK, 2005.

[103] N. Moraitis and P. Constantinou. Indoor channel measurements and characterization at 60 GHz for wireless local area network applications. *IEEE Trans. Antennas Propagat.*, 52(12):3180–3189, Dec. 2004.

[104] N. Moraitis and P. Constantinou. Measurements and characterization of wideband indoor radio channel at 60 GHz. *IEEE Trans. Wireless Commun.*, 5(4):880–889, Apr. 2006.

[105] A. Naguib, V. Tarokh, N. Seshadri, and A. Calderbank. A space-time coding modem for high-data-rate wireless communications. *IEEE J. Select. Areas Commun.*, 16(10):1459–1478, Oct. 1998.

[106] A. Naguib, V. Tarokh, N. Seshadri, and A. Calderbank. Space-time codes for high data rate wireless communication: performance criteria in the presence of channel estimation errors, mobility, and multiple paths. *IEEE Trans. Commun.*, 47(2):199–207, Feb. 1999.

[107] M. Nakagami. The *m*-distribution: A general formula of intensity distribution of rapid fading. In W. G. Hoffman, editor, *Statistical Methods in Radio Wave Propagation*, pages 3–36. Oxford, UK: Pergamon Press, 1960.

[108] N. Narang and S. Kasera. *2G Mobile Networks: GSM and HSCSD*. Tata: McGraw-Hill, 2007.

[109] M. Natkaniec. Wireless ofdm systems: How to make them work? *IEEE Communications Magazine*, 41(2):16–18, Feb. 2003.

[110] V. D. Nguyen and M. Pätzold. Least square channel estimation using special training sequences for MIMO-OFDM systems in the presence of intersymbol interference,. In *Proc. Nordic Radio Symposium (NRS) 2004, including the Finnish Wireless Communications Workshop (FWCW) 2004*. Oulu, Finland, Aug. 2004.

[111] A. Papoulis and S. U. Pillai. *Probability, Random Variables and Stochastic Processes*. New York: McGraw-Hill, 4th edition, 2002.

[112] C. S. Park, Y.-P.E. Wang, G. Jöngren, and D. Hammarwall. Evolution of uplink MIMO for LTE-advanced. *IEEE Communications Magazine*, 49(2):112–121, Feb. 2011.

[113] Y. Park and F. Adachi. *Enhanced Radio Access Technologies for Next Generation Mobile Communication*. Springer, 1st edition, 2007.

[114] C. S. Patel, G. L. Stüber, and T. G. Pratt. Simulation of Rayleigh-faded mobile-to-mobile communication channels. *IEEE Trans. on Commun.*, 53(11):1876–1884, Nov. 2005.

[115] M. Pätzold. *Mobile Fading Channels*. Chichester: John Wiley & Sons, 2002.

[116] M. Pätzold and C. A. Gutiérrez. Level-crossing rate and average duration of fades of the envelope of a sum-of-cisoids. In *Proc. 67th IEEE Vehicular Technology Conference, VTC 2008-Spring*, pages 488–494. Singapore, May 2008.

[117] M. Pätzold and B. O. Hogstad. A space-time channel simulator for MIMO channels based on the geometrical one-ring scattering model. *Wireless Communications and Mobile Computing, Special Issue on Multiple-input Multiple-output (MIMO) Communications*, 4(7):727–737, Nov. 2004.

[118] M. Pätzold and B. O. Hogstad. Design and performance of MIMO channel simulators derived from the two-ring scattering model. In *Proc. 14th IST Mobile & Communications Summit, IST 2005*. Dresden, Germany, June 2005.

[119] M. Pätzold and B. O. Hogstad. A MIMO mobile-to-mobile channel model: Part I–the reference model. In *Proc. 16th IEEE International Symposium on Personal, Indoor and Mobile RadioCommunications, IEEE PIMRC 2005*, volume 1, pages 573–578. Berlin, Germany, Sept. 2005.

[120] M. Pätzold and B. O. Hogstad. A wideband MIMO channel model derived from the geometric elliptical scattering model. In *Proc. 3rd International Symposium on Wireless Communication System, ISWCS 2006*, pages 138–144. Valencia, Spain, Sept. 2006.

[121] M. Pätzold and B. O. Hogstad. A wideband space-time MIMO channel simulator based on the geometrical one-ring model. In *Proc. 64th Vehicular Technology Conference, VTC 2006-Fall*. Montreal, Canada, Sept. 2006.

[122] M. Pätzold and F. Laue. The performance of deterministic Rayleigh fading channel simulators with respect to the bit error probability. In *Proc. 51st Vehicular Technology Conference, VTC 2000-Spring*. Tokyo, Japan, May 2000.

[123] M. Pätzold and B. Talha. On the statistical properties of sum-of-cisoids-based mobile radio channel models. In *Proc. 10th International Symposium on Wireless Personal Multimedia Communications, WPMC 2007*, pages 394–400. Jaipur, India, Dec. 2007.

[124] M. Pätzold and N. Youssef. Modeling and simulation of direction-selective and frequency-selective mobile radio channels. *International Journal of Electronics and Communications*, AEÜ-55(6):433–442, Nov. 2001.

[125] J. Proakis and S. Massoud. *Digital Communications*. New York: McGraw-Hill, 5th edition, 2007.

[126] M.-O. Pun, M. Morelli, and C. C. J. Kuo. *Multi-Carrier Techniques For Broadband Wireless Communications: A Signal Processing Perspectives*. Imperial College Press, 2007.

[127] T. S. Rappaport. *Wireless Communications: Principles and Practice*. Prentice Hall, 2nd edition, 2002.

[128] T. Rautiainen, G. Wolfle, and R. Hoppe. Verifying path loss and delay spread predictions of a 3D ray tracing propagation model in urban environments. In *Proc. 56th IEEE Vehicular technology conference, VTC 2002*, volume 2, pages 2470–2474. Vancouver, Canada, Sept. 2002.

[129] S. O. Rice. Statistical properties of a sine wave plus random noise. *Bell Syst. Tech. J.*, 27:109–157, Jan. 1948.

[130] L. Rugini and P. Banelli. BER of OFDM systems impaired by carrier frequency offset in multipath fading channels. *IEEE Trans. Wireless Commun.*, 4(5):2279–2288, Sept. 2005.

[131] M. E. Sahin and H. Arslan. MIMO-OFDMA measurements; reception, testing, and evaluation of WiMAX MIMO signals with a single channel receiver. *IEEE Trans. Instrum. Meas.*, 58(3):713–721, Mar. 2009.

[132] A. A. M. Saleh and R. A. Valenzuela. A statistical model for indoor multipath propagation. *IEEE J. Select. Areas Commun.*, SAC-5(2):128–137, Feb. 1987.

[133] G. Santella and E. Restuccia. Analysis of frequency domain wide-band measurements of the indoor radio channel at 1, 5.5, 10 and 18 GHz. In *Proc. Global Communication Conference, GLOBECOM 1996*, volume 2, pages 1162–1166. London, UK, Nov. 1996.

[134] F. Sanzi and J. Speidel. An adaptive two-dimensional channel estimator for wireless OFDM with application to mobile DVB-T. *IEEE Trans. Broadcast.*, 46(2):128–133, June 2000.

[135] S. Savazzi, M. Nicoli, and M. Sternad. A comparative analysis of spatial multiplexing techniques for outdoor MIMO-OFDM systems with a limited feedback constraint. *IEEE Trans. Veh. Technol.*, 58(1):218–230, Jan. 2009.

[136] K. R. Schaubach, N. J. Davis, and T. S. Rappaport. A ray tracing method for predicting path loss and delay spread in microcellular environments. In *Proc. 42nd IEEE Vehicular technology conference, VTC 1992*, volume 2, pages 932–935. Denver, CO, USA, May 1992.

[137] H. Schulze and C. Lüders. *Theory and application of OFDM and CDMA: Wideband Wireless Communications*. Wiley, 2005.

[138] S. Y. Seidel and T. S. Rappaport. 914 MHz path loss prediction models for indoor wireless communications in multifloored buildings. *IEEE Trans. Antennas Propagat.*, 40(2):207–217, Feb. 1992.

[139] S. Y. Seidel and T. S. Rappaport. A ray tracing technique to predict path loss and delay spread inside buildings. In *Proc. IEEE Global Communication Conference, GLOBECOM 1992*, volume 2, pages 649–653. Orlando, FL, USA, Dec. 1992.

[140] C. E. Shannon. A mathematical theory of communication. *Bell Syst. Tech. J.*, 27:379–423, July 1948.

[141] C. E. Shannon. A mathematical theory of communication. *Bell Syst. Tech. J.*, 27:623–656, Oct. 1948.

[142] D. S. Shiu, G. J. Foschini, M. J. Gans, and J. M. Kahn. Fading correlation and its effect on the capacity of multielement antenna systems. *IEEE Trans. Commun.*, 48(3):502–513, Mar. 2000.

[143] M. K. Simon and M.-S. Alouini. *Digital Communication Over Fading Channels*. New Jersey: Wiley & Sons, 2005.

[144] C. Snow, L. Lampe, and R. Schober. Impact of WiMAX interference on MB-OFDM UWB systems: analysis and mitigation. *IEEE Trans. Commun.*, 57(9):2818–2827, Sept. 2009.

[145] C. E. D. Sterian, Y. Ma, M. Pätzold, I. Bănică, and H. He. New super-orthogonal space-time trellis codes using differential M-PSK for noncoherent mobile communication systems with two transmit antennas. *Annals of Telecommunications*, July 2010.

[146] G. L. Stüber. *Principles of Mobile Communication*. Academic Press, 2nd edition, 2000.

[147] H. Suzuki. A statistical model for urban radio propagation. *IEEE Trans. Commun.*, 25(7):673–680, July 1977.

[148] P. Tan and N. C. Beaulieu. Precise BER analysis of $\pi/4$-DQPSK OFDM with carrier frequency offset over frequency selective fast fading channels. *IEEE Trans. Wireless Commun.*, 6(10):3770–3780, Oct. 2007.

[149] M. Tao and R. S. Cheng. Differential space-time block codes. In *Proc. Global Communication Conference, GLOBECOM 2001*, volume 2, pages 1098–1102. San Antonio, Texas, USA, Nov. 2001.

[150] M. Tao and R. S. Cheng. Trellis-coded differential unitary space-time modulation over flat fading channels. *IEEE Trans. Commun.*, 51(4):587–596, April 2003.

[151] V. Tarokh and H. Jafarkhani. A differential detection scheme for transmit diversity. *IEEE J. Select. Areas Commun.*, 18(7):1169–1174, July 2000.

[152] V. Tarokh, H. Jafarkhani, and A. R. Calderbank. Space-time block codes from orthogonal designs. *IEEE Trans. Inform. Theory*, 45(5):1456–1467, July 1999.

[153] V. Tarokh, H. Jafarkhani, and A. R. Calderbank. Space-time block coding for wireless communications: performance results. *IEEE J. Select. Areas Commun.*, 17(3):451–460, Mar. 1999.

[154] V. Tarokh, N. Seshadri, and A. R. Calderbank. Space-time codes for high data rate wireless communication: performance criterion and code construction. *IEEE Trans. Inform. Theory*, 44(2):744–765, Mar. 1998.

[155] I. E. Telatar. Capacity of multiantenna Gaussian channels. *Eur. Trans. Telecommun.*, 10(6):585–595, Nov./Dec. 1999.

[156] C. Tellambura, A. J. Mueller, and V. K. Bhargava. Analysis of M-ary phase-shift keying with diversity reception for land-mobile satellite channels. *IEEE Trans. Veh. Technol.*, 46(4):910–922, Nov. 1997.

[157] G. Tiberi, S. Bertini, W. Q. Malik, A. Monorchio, D. J. Edwards, and G. Manara. Analysis of realistic ultrawideband indoor communication channels by using an efficient ray-tracing based method. *IEEE Trans. Antennas Propagat.*, 57(3):777–785, Mar. 2009.

[158] O. C. Ugweje and V. A. Aalo. Performance of selection diversity system in correlated Nakagami fading. In *Proc. 47th IEEE Semiannual Vehicular Technology Conference, VTC 1997*, volume 3, pages 1488–1492. Phoenix, AZ, USA, May 1997.

[159] A. Vielmon, Y. Li, and J. R. Barry. Performance of Alamouti transmit diversity over time–varying Rayleigh–fading channels. *IEEE Trans. on Wire. Commun.*, 3(5):1369–1373, Sept. 2004.

[160] C. Wan and J. G. Andrews. Spatial multiplexing in cellular MIMO-CDMA systems with linear receivers: outage probability and capacity. *IEEE Trans. Wireless Commun.*, 6(7):2612–2621, July 2007.

[161] R. Wang and D. Cox. Channel modeling for ad hoc mobile wireless networks. In *Proc. 57th IEEE Semiannual Vehicular Technology Conference, IEEE VTC 2002–Spring*, volume 1, pages 21–25. Birmingham, AL, May 2002.

[162] T.-C. Wei, W.-C. Liu, C.-Y. Tseng, and S.-J. Jou. Low complexity synchronization design of an OFDM receiver for DVB-T/H. *IEEE Trans. Consumer Electronics*, 55(2):408–413, May 2009.

[163] J. A. Wepman, J. R. Hoffman, and L. H. Loew. Analysis of impulse response measurements for PCS channel modeling application. *IEEE Trans. Veh. Technol.*, 44(3):613–620, Aug. 1995.

[164] T.-M. Wu and S.-Y. Tzeng. Sum-of-sinusoids-based simulator for Nakagami-*m* fading channels. In *Proc. 58th IEEE Vehicular Technology Conference, VTC 2003-Fall*, volume 1, pages 158–162. Orlando, Florida, USA, Oct. 2003.

[165] H. Xu, V. Kukshya, and T. S. Rappaport. Spatial and temporal characteristics of 60-GHz indoor channels. *IEEE J. Select. Areas Commun.*, 20(3):620–630, Apr. 2002.

[166] L.-L Yang and L. Hanzo. Multicarrier DS-CDMA: a multiple access scheme for ubiquitous broadband wireless communications. *IEEE Communications Magazine*, 41(10):116–124, Oct. 2003.

[167] C.-H. Yih. Effects of channel estimation error on the BER performance of OFDM systems in multipath Rayleigh fading channels. In *Proc. IEEE 66th*

Vehicular Technology Conference, VTC 2007-Fall, pages 1097–1101. Baltimore, MD, USA, Sept./Oct. 2007.

[168] C.-H. Yih. BER analysis of OFDM systems impaired by phase noise in frequency-selective Rayleigh fading channels. In *Proc. 51st Global Communication Conference, GLOBECOM 2008*, pages 1–5. New Orleans, LO, USA, Nov./Dec. 2008.

[169] S. Yin and X. Lin. Traffic self-similarity in mobile ad hoc networks. In *Second IFIP International Conference on Wireless and Optical Communications Networks, WOCN 2005*, pages 285–289, Mar. 2005.

[170] W. R. Young. Advanced mobile phone service: introduction, background, and objectives. *Bell Syst. Tech. J.*, 58(1):1–14, Jan. 1979.

[171] K. Yu, M. Bengtsson, B. Ottersten, D. McNamara, P. Karlsson, and M. Beach. Modeling of wide-band MIMO radio channels based on NLoS indoor measurements. *IEEE Trans. Veh. Technol.*, 53(3):655–665, May 2004.

[172] K. Yu and B. Ottersten. Models for MIMO propagation channels: a review. *Wireless Communications and Mobile Computing*, 2(7):653–666, 2002.

[173] J. Yuan, Z. Chen, B. Vucetic, and W. Firmanto. Performance and design of spacectime coding in fading channels. *IEEE Trans. Commun.*, 51(12):1991–1996, Dec. 2003.

[174] A. V. Zelst and T. C. W. Schenk. Implementation of a MIMO OFDM-based wireless lan system. *IEEE Trans. Signal Processing*, 52(2):483–494, Feb. 2004.

[175] H. Zhang and T. A. Gulliver. Capacity and error probability analysis for orthogonal space-time block codes over fading channels. *IEEE Trans. Wireless Commun.*, 4(2):808–819, Mar. 2005.

[176] W. Zhang, X.-G. Xia, and K. B. Letaief. Space-time/frequency coding for MIMO-OFDM in next generation broadband wireless systems. *IEEE Trans. Wireless Commun.*, 14(3):32–43, June 2007.

[177] Y. Zhang, J. Cosmas, M. Bard, and Y.-H. Song. Diversity gain for DVB-H by using transmitter/receiver cyclic delay diversity. *IEEE Trans. Broadcast.*, 52(4):464–474, Dec. 2006.

[178] W. Zhao, G. Leus, and G. B. Giannakis. Orthogonal design of unitary constellations for uncoded and trellis-coded noncoherent space-time systems. *IEEE Trans. Inform. Theory*, 50(6):1319–1327, June 2004.

[179] K. Zheng, B. Fan, J. Liu, Y. Lin, and W. Wang. Interference coordination for OFDM-based multihop LTE-advanced networks. *IEEE Trans. Wireless Commun.*, 18(1):54–63, Feb. 2011.

[180] Y. R. Zheng and C. Xiao. Simulation models with correct statistical properties for Rayleigh fading channels. *IEEE Trans. Commun.*, 51(6):920–928, Jun. 2003.

[181] Y. Zhu and H. Jafarkhani. Differential super-orthogonal space-time trellis codes. *IEEE Trans. Wireless Commun.*, 5(12):3634–3643, December 2006.

[182] T. Zwick, T. J. Beukema, and H. Nam. Wideband channel sounder with measurements and model for the 60 GHz indoor radio channel. *IEEE Trans. Veh. Technol.*, 54(4):1266–1277, July 2005.

List of Publications

This preface records all articles published by the author of this dissertation. The first section details the articles which are briefly described in Chapters 2–5 of this dissertation and are replicated in Appendices A – J. The articles included in those Appendices consist of one submitted paper and nine already published papers. The second section tabulates those papers which are published within the framework of this doctoral thesis, however, they are not included in this dissertation.

Articles Included in this Dissertation

The articles which are included in Appendices A – J of this dissertation are listed as follows:

Paper I   Y. Ma and M. Pätzold, A wideband one-ring MIMO channel model under non-isotropic scattering conditions, *Proc. 67th IEEE Vehicular Technology Conference, VTC2008-Spring*, Singapore, May 2008, pp. 424 – 429, DOI: 10.1109/VETECS.2008.100.

Paper II   Y. Ma and M. Pätzold, Wideband two-ring MIMO channel models for mobile-to-mobile communications, *Proc. 10th International Symposium on Wireless Personal Multimedia Communications, WPMC 2007*, Jaipur, India, Dec. 2007 pp. 380 – 384.

Paper III   Y. Ma and M. Pätzold, Design and simulation of narrowband indoor radio propagation channels under LOS and NLOS propagation conditions, *71st IEEE Vehicular Technology Conference, VTC2010-Spring*, Taipei, Taiwan, May 2010, pp. 1 – 7, DOI: 10.1109/VETECS.2010.5494116.

Paper IV   Y. Ma and M. Pätzold, Statistical modeling and experimental verification of wideband indoor radio propagation channels, *as is*, 2011

Paper V   Y. Ma and M. Pätzold, Performance analysis of wideband SOS-based channel simulators with respect to the bit error probability of BPSK OFDM systems with perfect and imperfect CSI, *Proc. 12th International Symposium on Wireless Personal Multimedia Communications, WPMC 2009*, Sendai, Japan, Sept. 2009.

Paper VI   Y. Ma and M. Pätzold, Performance analysis of wideband sum-of-cisoids-based channel simulators with respect to the bit error probability of DPSK OFDM systems, *Proc. IEEE 69th Vehicular Technology Conference, VTC2009-Spring*, Barcelona, Spain, Apr. 2009, pp. 1 – 6, DOI: 10.1109/VETECS.2009.5073781.

Paper VII   Y. Ma and M. Pätzold, Performance comparison of space-time coded MIMO-OFDM systems using different wideband MIMO channel models, *Proc. 4th IEEE International Symposium on Wireless Communication Systems, ISWCS 2007*, Trondheim, Norway, Oct. 2007, pp. 762 – 766, DOI: 10.1109/ISWCS.2007.4392443.

Paper VIII   Y. Ma and M. Pätzold, Performance analysis of STBC-OFDM systems in temporally or spatially correlated fading channels, *Proc. IEEE Wireless Communications and Networking Conference, WCNC 2010*, Sydney, Australia, Apr. 2010, pp. 1 – 5, DOI: 10.1109/WCNC.2010.5506743.

Paper IX   Y. Ma and M. Pätzold, Performance analysis of Alamouti coded OFDM systems over Rayleigh fading channels correlated in space and time, *Proc. 71st IEEE Vehicular Technology Conference, VTC 2010-Spring*, Taipei, Taiwan, May 2010, pp. 1 – 6, DOI: 10.1109/VETECS.2010.5493855.

Paper X   C. E. D. Sterian, Y. Ma, M. Pätzold, I. Bănică, and H. He, New super-orthogonal space-time trellis codes using differential *M*-PSK for non-coherent mobile communication systems with two transmit antennas, *Annals of Telecommunications*, vol. 66, no. 3 – 4, pp. 257 – 273, July 2010, DOI: 10.1007/s12243-010-0191-1.

The next section lists all the papers which have not been replicated in this paper collection.

Articles Not Included in this Dissertation

The following articles are also published during the PhD study and are equally important as the ones mentioned in previous section. However, to reduce the overlap between the articles included in the final manuscript, they are not presented in this dissertation.

Paper XI Y. Ma and M. Pätzold, Modelling and statistical characterization of wideband indoor radio propagation channels, *Proc. 2nd IEEE International Workshop on Mobile Computing and Networking Technologies, WMCNT 2010*, Moscow, Russia, Oct. 2010.

Paper XII C. E. D. Sterian, Y. Ma, H. He, M. Pätzold, and I. Bănică, Super-orthogonal space-time trellis codes with differential phase modulation for noncoherent mobile communication systems, *Proc. 3rd International Conference on Communications and Electronics, ICCE 2010*, Nha Trang, Vietnam, Aug. 2010.

Appendix A

Paper I

A Wideband One-Ring MIMO Channel Model Under Non-Isotropic Scattering Conditions

Yuanyuan Ma and Matthias Pätzold

Department of Information and Communication Technology

Faculty of Engineering and Science, University of Agder

Servicebox 509, NO-4898 Grimstad, Norway

E-mails: {yuanyuan.ma, matthias.paetzold}@uia.no

Abstract — **In this paper, we present a wideband one-ring multiple-input multiple-output (MIMO) channel model for non-isotropic scattering environments. The model is designed in such a way that the delay power spectral density (PSD) of the resulting reference channel model is identical to a given delay PSD. Furthermore, we present an efficient deterministic channel simulation model obtained by using the principle of deterministic channel modeling. The statistical properties of both the reference model and the simulation model are also studied. Analytical expressions will be presented for the temporal autocorrelation function (ACF), the two-dimensional (2-D) space cross-correlation function (CCF), and the frequency correlation function (FCF). We show that the statistical properties of the deterministic simulation model can be brought into astonishingly good agreement with those of the reference model. The resulting deterministic simulation model enables the performance evaluation of wideband MIMO communication systems by simulation, which is shown exemplarily by studying the system performance of a space-time coded MIMO orthogonal frequency division multiplexing (OFDM) system.**

I. INTRODUCTION

The increasing demand for high data-rate wireless communication services and the limited bandwidth motivate investigations of wideband MIMO wireless communications. In order to simulate, design, and evaluate wideband MIMO wireless communication systems, it is important to develop realistic wideband MIMO channels for different environments.

In the literature, geometrically based channel models, such as the one-ring channel model, the two-ring channel model, and the elliptical channel model, have widely been used for modeling wideband MIMO channels. So far, nearly all publications have assumed isotropic scattering conditions when modeling wideband channels [13, 7, 12]. However, it has been experimentally demonstrated in [3] and

[2] that scattering encountered in many environments is more likely to be non-isotropic, resulting in a nonuniform distribution of the angle of arrival (AOA) at the mobile station (receiver). When assuming that the AOA follows a uniform distribution, the resulting theoretical correlation functions and level crossing rate of a received envelope strongly deviate from the experimental ones obtained from measured data [5]. To obtain spatial channel models with more realistic correlation properties, we aim at modeling wideband MIMO channels for non-isotropic scattering environments.

In this paper, we derive a wideband one-ring MIMO reference channel model for non-isotropic scattering environments. We employ the von Mises density [1] to characterize the nonuniform distribution of the AOA for distinct scatterer clusters. Furthermore, we derive a deterministic simulation model from the reference model. The modified method of equal areas (MMEA) [4] is used to determine the discrete AOAs of the simulation model. Moreover, we present analytical expressions for the temporal ACF, the 2-D space CCF, and the FCF of both the reference model and the simulation model. The resulting deterministic simulation model is used to evaluate the performance of a space-time coded MIMO-OFDM system.

The remainder of the paper is organized as follows. In Section II, we first derive the wideband one-ring MIMO reference channel model. Then, we discuss its statistical properties like the temporal ACF, the 2-D space CCF, and the FCF. The derivation as well as the statistical properties of the corresponding deterministic MIMO channel simulation model are presented in Section III. Several numerical examples are included in Section IV to show the excellent fitting between the statistical properties of the simulation model and those of the reference model. We also study the symbol error rate (SER) performance of a space-time coded MIMO-OFDM system. Finally, we draw the conclusions in Section V.

II. A WIDEBAND ONE-RING REFERENCE CHANNEL MODEL

The geometrical one-ring MIMO channel model is shown in Fig. A.1, in which the transmitter is equipped with M_T transmit antennas and the receiver with M_R receive antennas [11]. It is assumed that there are N local scatterers $S_R^{(n)}$ ($n = 1, 2, \ldots, N$) located on a ring around the receiver. We assume furthermore that the ring radius R is small compared with the distance D between the transmitter and the receiver. The antenna spacings at the transmitter and the receiver are denoted by δ_T and δ_R, respectively, and the multielement antenna tilt angles are described by α_T and α_R. The angle of motion is denoted by α_V and $\phi_T^{\max}$ describes the maximum angle of departure seen at the transmitter. Notice that the AOA $\phi_R^{(n)}$ is determined by the location of the scatterer $S_R^{(n)}$ ($n = 1, 2, \ldots, N$).

Figure A.1: Geometrical one-ring scattering model for an $M_T \times M_R$ MIMO channel with local scatterer $S_R^{(n)}$ around the receiver.

A. Derivation of a Wideband Reference Channel Model

Our aim is to derive a wideband one-ring MIMO channel model in such a way that the delay PSD of the reference channel model is equal to a specified delay PSD. The given delay PSD describes the average power of $\mathscr{L}$ discrete propagation paths according to

$$S_{\tau'}^*(\tau') = \sum_{\ell=1}^{\mathscr{L}} a_\ell^2 \, \delta(\tau' - \tau_\ell') \tag{1}$$

where a_ℓ represents the delay coefficient of the ℓth propagation path and τ_ℓ' denotes the corresponding propagation delay.

Keeping this goal in mind, we will partition all scatterers located on the ring around the receiver into $\mathscr{L}$ cluster pairs.

According to the results in [13], the mean angles μ_ℓ of the ℓth cluster pair can be determined via the relation

$$\mu_\ell = \pm \arccos\left(2\frac{\tau_\ell'}{\tau_{\mathscr{L}}'} - 1\right), \qquad\qquad \ell = 1, 2, \ldots, \mathscr{L} \tag{2}$$

where τ_ℓ' is known from the given delay PSD [see (1)]. The scatterer $S_R^{(n)}$ is assigned to the ℓth cluster pair if

$$\frac{\mu_\ell + \mu_{\ell+1}}{2} < \phi_R^{(n)} \le \frac{\mu_{\ell-1} + \mu_\ell}{2} \qquad \text{or} \qquad -\frac{\mu_{\ell-1} + \mu_\ell}{2} < \phi_R^{(n)} \le -\frac{\mu_\ell + \mu_{\ell+1}}{2} \tag{3a,b}$$

where we assume that $\mu_0 = \pi$ and $\mu_{\mathscr{L}+1} = 0$. The number of scatterers within the ℓth cluster pair, denoted by N_ℓ, must fulfil the boundary condition $\sum_{\ell=1}^{\mathscr{L}} N_\ell = N$. Moreover, we use a set $\mathscr{I}_\ell$ to denote the scatterer locations of the ℓth cluster pair. The nth scatterer $S_R^{(n)}$ is located in the ℓth cluster pair if $n \in \mathscr{I}_\ell$. The condition $\bigcup_{\ell=1}^{\mathscr{L}} \mathscr{I}_\ell = \mathscr{I}$ must hold, where $\mathscr{I} = \{1, 2, \ldots, N\}$ represents the universal set.

The real propagation delay from the transmitter to the receiver via the scatterer $S_R^{(n)}$ is assigned to the delay τ'_ℓ if the scatterer $S_R^{(n)}$ is located in the ℓth cluster pair. As a result, we obtain a wideband one-ring MIMO channel model with $\mathscr{L}$ discrete propagation paths. The time-variant impulse response of the link from $A_T^{(l)}$ to $A_R^{(k)}$ can be expressed as

$$h_{kl}(\tau', t) = \sum_{\ell=1}^{\mathscr{L}} a_\ell \, g_{kl,\ell}(t) \delta(\tau' - \tau'_\ell) \tag{4}$$

for $l = 1, 2, \ldots, M_T$ and $k = 1, 2, \ldots, M_R$. In (4), $g_{kl,\ell}(t)$ denotes the channel gain of the ℓth propagation path, which can be obtained from [11] as

$$g_{kl,\ell}(t) = \lim_{N_\ell \to \infty} \frac{1}{\sqrt{N_\ell}} \sum_{n_\ell \in \mathscr{I}_\ell} a_{n_\ell,l} b_{n_\ell,k} e^{j(2\pi f_{n_\ell} t + \theta_{n_\ell})} \tag{5}$$

where

$$a_{n_\ell,l} = e^{j\pi(M_T - 2l + 1)\frac{\delta_T}{\lambda}[\phi_T^{max} \sin(\alpha_T) \sin(\phi_R^{(n_\ell)}) + \cos(\alpha_R)]} \tag{6}$$

$$b_{n_\ell,k} = e^{j\pi(M_R - 2k + 1)\frac{\delta_R}{\lambda} \cos(\phi_R^{(n_\ell)} - \alpha_R)} \tag{7}$$

$$f_{n_\ell} = f_{max} \cos(\phi_R^{(n_\ell)} - \alpha_V). \tag{8}$$

Here, λ describes the carrier's wavelength and f_{max} denotes the maximum Doppler frequency. In the reference model, the phases θ_{n_ℓ} are independent and identically distributed random variables, which are uniformly distributed over $[0, 2\pi)$.

B. Distribution of the AOA

The number of scatterers in the reference model approaches infinity. Therefore, it is reasonable to assume that the discrete AOA $\phi_R^{(n_\ell)}$ related to the ℓth cluster pair tends to a continuous random variable ϕ_R following a certain distribution. Such an assumption provides mathematical convenience to analyze the statistical properties of the resulting reference model and to compute the parameters of the simulation model.

In this paper, we use the von Mises distribution to characterize the nonuniform distribution of the AOA ϕ_R, which represents the uniform distribution as a special

case and closely approximates some important distributions like the Gaussian distribution and the cardioid distribution. The AOA distribution $p_\ell(\phi_R)$ of the ℓth cluster pair can be expressed as [1]

$$p_\ell(\phi_R) = \frac{1}{2\pi I_0(\kappa_\ell)} e^{\kappa_\ell \cos(\phi_R - \mu_\ell)} \tag{9}$$

where $I_0(\cdot)$ is the zeroth-order modified Bessel function of the first kind. One should note that the parameters of the AOA distribution $p_\ell(\phi_R)$ can be related to the given delay PSD. For example, the mean value μ_ℓ can be calculated using (2). Based on the partition performed in Subsection II-A, we can easily determine the angular spread $\triangle_\ell$ of the ℓth cluster pair according to

$$\triangle_\ell = \min\{\frac{\mu_\ell - \mu_{\ell+1}}{2}, \frac{\mu_{\ell-1} - \mu_\ell}{2}\}. \tag{10}$$

Finally, the parameter κ_ℓ in (9), which controls the angular spread, can be determined by the following relation [1]

$$\kappa_\ell = (\frac{2}{\triangle_\ell})^2. \tag{11}$$

C. Statistical Properties of the Reference Channel Model

The time-variant impulse response provides the basis for analyzing the statistical properties of the wideband reference channel model. In this subsection, we are concerned with the analysis of the statistical properties of the resulting wideband reference channel model.

Similar to the Doppler PSD, direction PSD, and delay PSD that are presented in [10] for spatial deterministic Gaussian uncorrelated scattering processes, analogous relations can be established for the present wideband one-ring reference channel model.

The Doppler PSD $S_f(f)$ of the reference channel model can be represented by the following relation

$$S_f(f) = \sum_{\ell=1}^{\mathscr{L}} a_\ell^2 S_{f,\ell}(f). \tag{12}$$

Here, $S_{f,\ell}(f)$ denotes the Doppler PSD of the ℓth propagation path. The inverse Fourier transform of the Doppler PSD $S_f(f)$ with respect to the Doppler frequency

f results in the temporal ACF of the wideband reference channel model, i.e.,

$$r_{h_{kl}}(\tau) = \sum_{\ell=1}^{\mathscr{L}} a_\ell^2 \, r_{g_{kl,\ell}}(\tau). \tag{13}$$

In the preceding equation,

$$
\begin{aligned}
r_{g_{kl,\ell}}(\tau) &= E\{g_{kl,\ell}(t)g_{kl,\ell}^*(t+\tau)\} \\
&= \int_{-\pi}^{\pi} e^{-j2\pi f_{\max}\cos(\phi_R - \alpha_V)\tau} p_\ell(\phi_R)d\phi_R
\end{aligned} \tag{14}
$$

represents the temporal ACF of the ℓth propagation path.

The direction PSD $S_\Omega(\Omega_T,\Omega_R)$ of the reference channel model can be described formally by

$$S_\Omega(\Omega_T,\Omega_R) = \sum_{\ell=1}^{\mathscr{L}} a_\ell^2 \, S_{\Omega,\ell}(\Omega_T,\Omega_R) \tag{15}$$

where Ω_T and Ω_R represent the incidence directions at the transmitter and the receiver, respectively. The quantity $S_{\Omega,\ell}(\Omega_T,\Omega_R)$ denotes the direction PSD of the ℓth path. The inverse Fourier transform of (15) leads to the expression

$$\rho_{kl,k'l'}(\delta_T,\delta_R) = \sum_{\ell=1}^{\mathscr{L}} a_\ell^2 \, \rho_{kl,k'l',\ell}(\delta_T,\delta_R) \tag{16}$$

which describes the spatial correlation function between the diffuse components $h_{kl}(t)$ and $h_{k'l'}(t)$. In the equation above, $\rho_{kl,k'l',\ell}$ denotes the 2-D space CCF of the ℓth propagation path, which is defined as

$$
\begin{aligned}
\rho_{kl,k'l',\ell}(\delta_T,\delta_R) &= E\{g_{kl,\ell}(t)g_{k'l',\ell}^*(t)\} \\
&= \int_{-\pi}^{\pi} e^{-j2\pi(l-l')\frac{\delta_T}{\lambda}[\phi_T^{\max}\sin(\alpha_T)\sin(\phi_R)+\cos(\alpha_R)]} \\
&\quad \times e^{-j2\pi(k-k')\frac{\delta_R}{\lambda}\cos(\phi_R-\alpha_R)} p_\ell(\phi_R)d\phi_R.
\end{aligned} \tag{17}
$$

We employ the delay PSD of the reference channel model

$$S_{\tau'}(\tau') = \sum_{\ell=1}^{\mathscr{L}} a_\ell^2 \, \delta(\tau'-\tau'_\ell) \tag{18}$$

to calculate an analytical expression for the FCF. The inverse Fourier transform of the delay PSD $S_{\tau'}(\tau')$ with respect to the propagation delay τ' results in the FCF of

the wideband reference channel model, which is given by

$$r_{\tau'}(v') = \sum_{\ell=1}^{\mathscr{L}} a_\ell^2 e^{j2\pi v' \tau'_\ell}. \tag{19}$$

III. WIDEBAND ONE-RING CHANNEL SIMULATION MODEL

In this section, we will deal with the derivation and the statistical analysis of a wideband one-ring deterministic channel simulation model.

A. Derivation of the Wideband Channel Simulation Model

For the purpose of designing the wideband deterministic channel simulation model, we can apply the concept of deterministic channel modeling described in [9]. We proceed by first replacing the infinite number of scatterers by a finite value N. Then, we determine constant values for the discrete AOAs $\phi_R^{(n_\ell)}$ as well as for the phases θ_{n_ℓ}. The AOAs $\phi_R^{(n_\ell)}$ can be determined by the parameter computation method described in Subsection III-B. The sets $\{\theta_{n_\ell}\}$ can be obtained by generating N_ℓ outcomes from a random generator with a uniform distribution over $[0, 2\pi)$. As a result, the wideband deterministic channel simulation model is completely determined and the corresponding impulse response can be described as

$$\tilde{h}_{kl}(\tau', t) = \sum_{\ell=1}^{\mathscr{L}} a_\ell \tilde{g}_{kl,\ell}(t) \delta(\tau' - \tau'_\ell). \tag{20}$$

In (20), the complex channel gain $\tilde{g}_{kl,\ell}(t)$ of the ℓth discrete propagation path is given by

$$\tilde{g}_{kl,\ell}(t) = \frac{1}{\sqrt{N_\ell}} \sum_{n_\ell \in \mathscr{I}_\ell} a_{n_\ell,l} b_{n_\ell,k} e^{j(2\pi f_{n_\ell} t + \theta_{n_\ell})}. \tag{21}$$

When assuming that the constant AOAs $\phi_R^{(n_\ell)}$ are known, the quantities $a_{n_\ell,l}$, $b_{n_\ell,k}$, and f_{n_ℓ} in the above equation can easily be computed using (6), (7), and (8), respectively.

B. The Parameter Computation Method

The MMEA [4] is recommended in this paper for calculating the AOAs $\phi_R^{(n_\ell)}$. This method is quite useful and advantageous for determining the AOA especially for nonuniform distributions of the AOA. Using the MMEA, the parameters of the sets $\{\phi_R^{(n_\ell)}\}$ can be obtained by solving numerically the following equation

$$\int_{-\pi}^{\phi_R^{(n_\ell)}} p_\ell(\phi_R) d\phi_R - \frac{1}{N_\ell}\left(n_\ell - \frac{1}{4}\right) = 0 \tag{22}$$

for all $n_\ell = 1, 2, \ldots, N_\ell$. As an example, the resulting scatter diagram determined by the delay PSD of the 18-path HiperLAN/2 model C [8] is shown in Fig. A.2. The number of scatterers N_ℓ in each cluster is equal to 5.

In the limit $\kappa_\ell \to \infty$, the von Mises distribution in (9) converges to a delta function, i.e., $p_\ell(\phi_R) = \delta(\phi_R - \mu_\ell)$ [1]. A scatter diagram is depicted in Fig. A.3 for such an extremely non-isotropic scattering scenario, where the delay PSD is again chosen according to the 18-path HiperLAN/2 model C. In this case, each cluster consists of only one scatterer seen from the receiver under the mean angle μ_ℓ. As a consequence, the reference channel model consists of only $N = 2\mathscr{L}$ scatterers. For such a special scenario, the resulting simulation model equals the reference model.

C. Statistical Properties of the Channel Simulation Model

It can be shown in a similar way that the temporal ACF of the wideband one-ring deterministic channel simulation model can be represented in the form [10]

$$\tilde{r}_{h_{kl}}(\tau) = \sum_{\ell=1}^{\mathscr{L}} a_\ell^2 \, \tilde{r}_{g_{kl,\ell}}(\tau) \tag{23}$$

where

$$\tilde{r}_{g_{kl,\ell}}(\tau) = <\tilde{g}_{kl,\ell}(t)\tilde{g}_{kl,\ell}^*(t+\tau)>$$
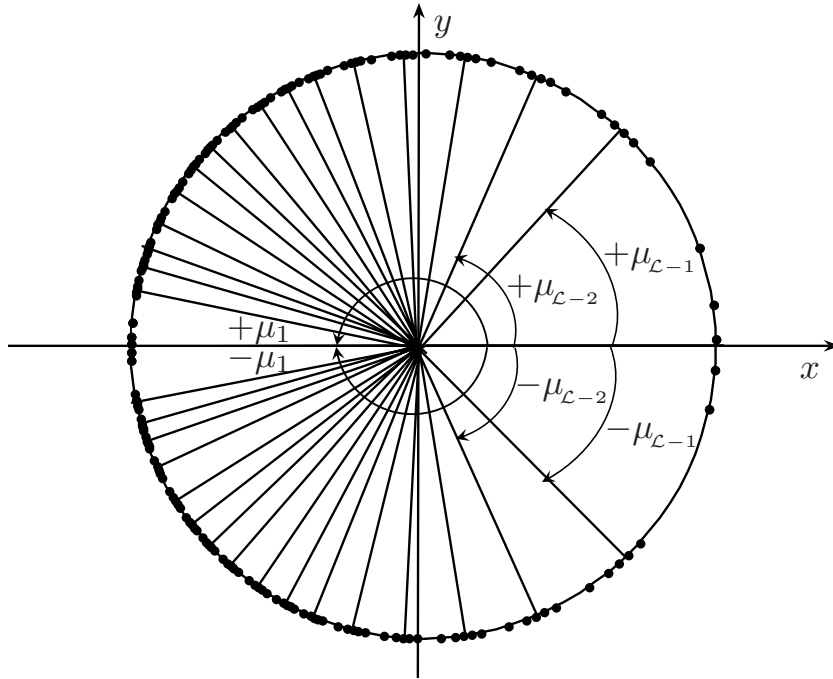
Figure A.2: Scatter diagram for the geometrical one-ring model under non-isotropic scattering conditions.
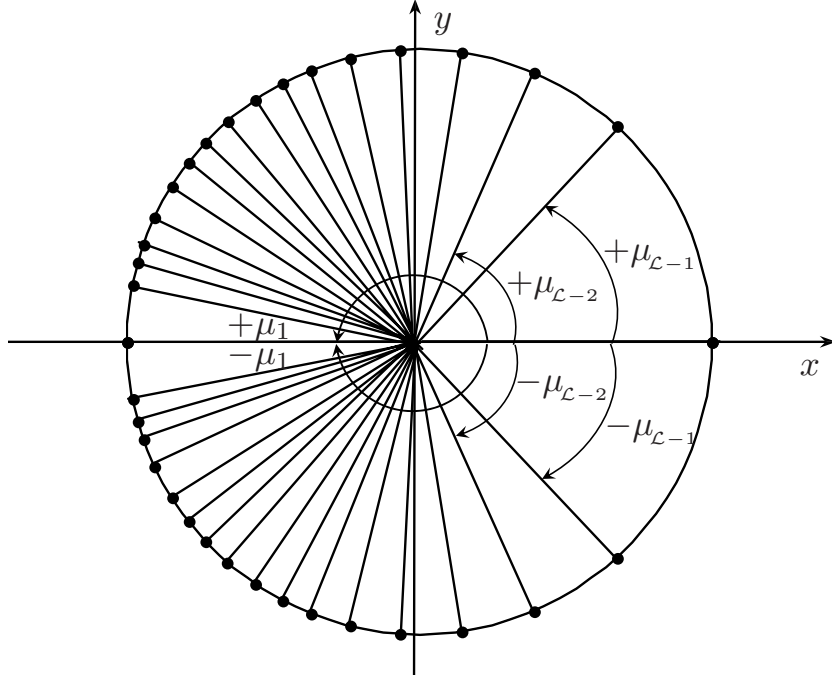
Figure A.3: Scatter diagram for the geometrical one-ring model under extremely non-isotropic scattering conditions ($\kappa_\ell \to \infty$).

$$= \frac{1}{N_\ell} \sum_{n_\ell \in \mathscr{I}_\ell} e^{-j2\pi f_{\max} \cos(\phi_R^{(n_\ell)} - \alpha_V)\tau} \tag{24}$$

represents the corresponding temporal ACF of the ℓth propagation path and $< \cdot >$ denotes the time average operator.

Using the result in [10], we obtain the following expression for the 2-D space CCF of the deterministic simulation model

$$\tilde{\rho}_{kl,k'l'}(\delta_T, \delta_R) = \sum_{n_\ell \in \mathscr{I}_\ell} a_\ell^2 \tilde{\rho}_{kl,k'l',\ell}(\delta_T, \delta_R) \tag{25}$$

where

$$
\begin{aligned}
\tilde{\rho}_{kl,k'l',\ell}(\delta_T, \delta_R) &= < \tilde{g}_{kl,\ell}(t)\tilde{g}^*_{k'l',\ell}(t) > \\
&= \frac{1}{N_\ell} \sum_{n_\ell \in \mathscr{I}_\ell} e^{-j2\pi(l-l')\frac{\delta_T}{\lambda}[\phi_T^{\max}\sin(\alpha_T)\sin(\phi_R^{(n_\ell)}) + \cos(\alpha_R)]} \\
&\quad \times e^{-j2\pi(k-k')\frac{\delta_R}{\lambda}\cos(\phi_R^{(n_\ell)} - \alpha_R)}
\end{aligned}
\tag{26}
$$

denotes the corresponding 2-D space CCF of the ℓth path.

Finally, we also compute the FCF of the deterministic simulation model, which is defined as

$$\tilde{r}_{\tau'}(v') = < \tilde{H}_{kl}(f',t)\tilde{H}_{kl}^*(f'+v',t) > \tag{27}$$

where $\tilde{H}_{kl}(f',t)$ is the Fourier transform of the impulse response $\tilde{h}_{kl}(\tau',t)$ with respect to the propagation delay τ'. Substituting the Fourier transform of (20) into (27), we obtain

$$\tilde{r}_{\tau'}(v') = \sum_{\ell=1}^{\mathscr{L}} a_{\ell}^2 e^{j2\pi v' \tau'_{\ell}}. \tag{28}$$

From the comparison between the equation above and (19), it becomes clear that the FCF $\tilde{r}_{\tau'}(v')$ of the simulation model is in fact equal to the FCF $r_{\tau'}(v')$ of the reference model. The equality will be confirmed in the next section by simulations.

IV. NUMERICAL RESULTS

In this section, we present some analytical results as well as simulation results for the statistical properties of the wideband reference channel model and the corresponding deterministic simulation model. The temporal ACF, the 2-D space CCF, and the FCF are the focus of our investigations.

The obtained results are valid for the following parameters: $f_{\max} = 91\,\text{Hz}$, $\alpha_{\text{T}} = \alpha_{\text{R}} = 90°$, $\alpha_V = 180°$, and $\phi_{\text{T}}^{\max} = 2°$. As a given delay PSD, we choose exemplarily the delay PSD of the 18-path HiperLAN/2 model C [8]. For the reference model, we assume that the AOA PDF $p_{\ell}(\phi_R)$ of the ℓth cluster follows the von Mises distribution, where the parameters μ_{ℓ} and κ_{ℓ} are determined as described in Section II. Moreover, it is assumed that there are $N_{\ell} = 5$ scatterers in each cluster when designing the deterministic simulation model using the MMEA method. In the extremely non-isotropic scattering case ($\kappa_{\ell} \to \infty$), we assume that there is only 1 scatterer in each cluster, i.e., $N_{\ell} = 1$.

Figure A.4 shows the analytical results for the absolute value of the temporal ACFs $|r_{h_{kl}}(\tau)|$ and $|\tilde{r}_{h_{kl}}(\tau)|$. This figure also shows the corresponding simulation results, which match the analytical results for $|r_{h_{kl}}(\tau)|$ and $|\tilde{r}_{h_{kl}}(\tau)|$ very well.

On the assumption that $\kappa_{\ell} \to \infty$ holds, the absolute value of the temporal ACF of the reference model is also depicted in Fig. A.4. As Fig. A.3 reveals, there is only a fixed singular scatterer in each cluster. Therefore, the absolute value of the temporal ACF of the simulation model is identical to that of the reference model in such a special scenario. Fig. A.4 shows the excellent fitting between the temporal ACF of
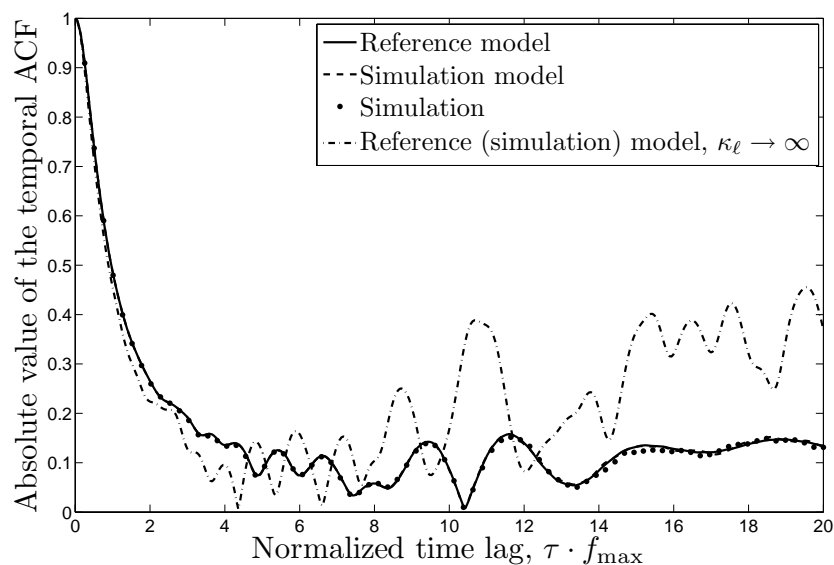
Figure A.4: Absolute value of the temporal ACFs $|r_{h_{kl}}(\tau)|$ (reference model) and $|\tilde{r}_{h_{kl}}(\tau)|$ (simulation model) for non-isotropic scattering environments.

the simulation model and that of the reference model, which can be obtained easily without using any parameter computation method.

The absolute value of the 2-D space CCF $\rho_{kl,k'l'}(\delta_T, \delta_R)$ of the reference model is computed according to (16) and presented in Fig. A.5. For reasons of comparison, the absolute value of the 2-D space CCF $\tilde{\rho}_{kl,k'l'}(\delta_T, \delta_R)$ of the deterministic simulation model is calculated according to (25) and depicted in Fig. A.6.
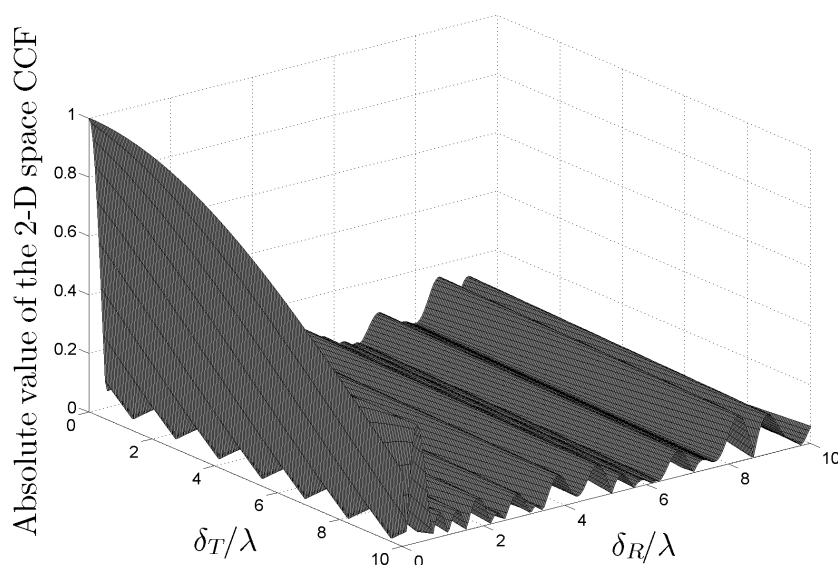
Figure A.5: Absolute value of the 2-D space CCF $|\rho_{kl,k'l'}(\delta_T, \delta_R)|$ of the reference model for non-isotropic scattering environments.
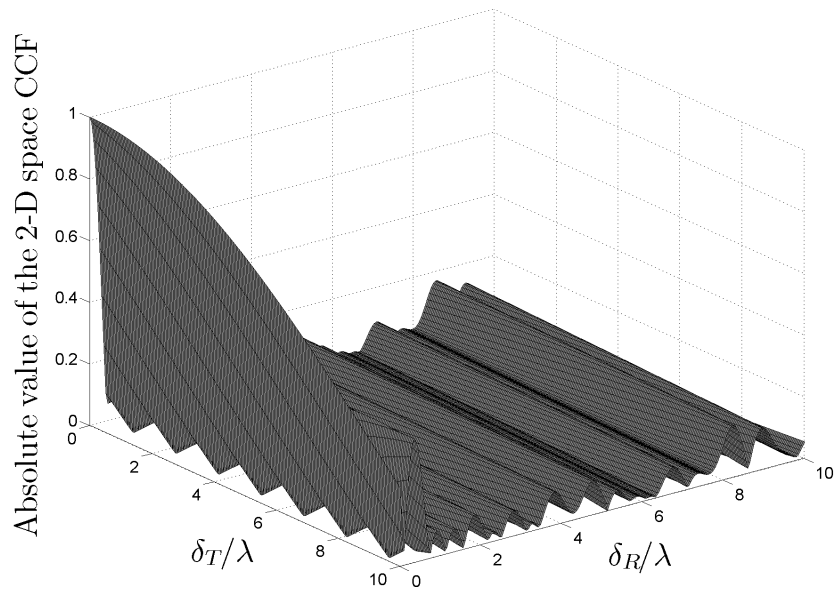
Figure A.6: Absolute value of the 2-D space CCF $|\tilde{\rho}_{kl,k'l'}(\delta_T, \delta_R)|$ of the simulation model for non-isotropic scattering environments.

The absolute value of the 2-D space CCF of the reference channel model is plotted in Fig. A.7 for the extremely non-isotropic scattering case ($\kappa_\ell \to \infty$). As mentioned before, this result also describes the absolute value of the 2-D space CCF of the deterministic simulation model.
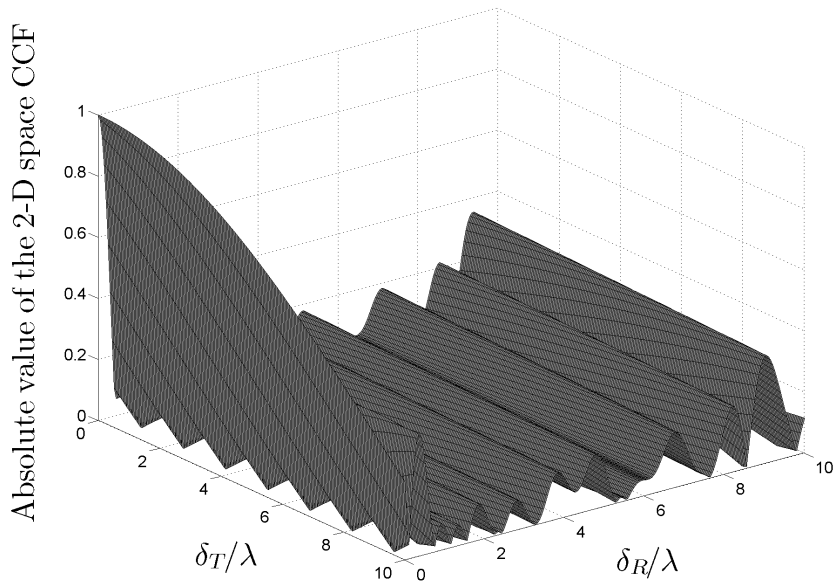
Figure A.7: Absolute value of the 2-D space CCF of the reference (simulation) model for extremely non-isotropic scattering environments ($\kappa_\ell \to \infty$).

Figure A.8 shows the absolute value of the FCFs, calculated according to (19) and (28) for the reference model and the deterministic simulation model, respectively. The fact that the FCF of the deterministic simulation model is identical to that of the reference model is also confirmed by simulation in Fig. A.8.

We also investigated the SER performance of the space-time coded MIMO-OFDM system described in [6] using the resulting one-ring 2×2 MIMO channel model. Assuming perfect channel state information at the receiver, we present the SER performance for various antenna spacings in Fig. A.9. As a comparison, we also present the system performance using the one-ring 2×2 MIMO channel model developed for isotropic scattering environments [13]. As expected, the SER performance improves with increasing the antenna spacings. However, different with what we have expected, no obvious SER performance difference can be observed in Fig. A.9 when evaluating the MIMO-OFDM system performance under isotropic and non-isotropic scattering conditions. The assumption that the scatterers are located in clusters or distributed uniformly on a ring has in the present case obviously no strong influence on the MIMO-OFDM system performance.

Figure A.10 shows the results of the MIMO-OFDM system performance under the extremely non-isotropic scattering condition, where only $N_\ell = 1$ scatterer exists in each cluster (the total number of scatterers equals $N = 2\mathscr{L} = 36$). It can be observed from Fig. A.10 that the MIMO-OFDM system performance evaluated using the channel simulator with $N = 36$ scatterers approaches the system performance
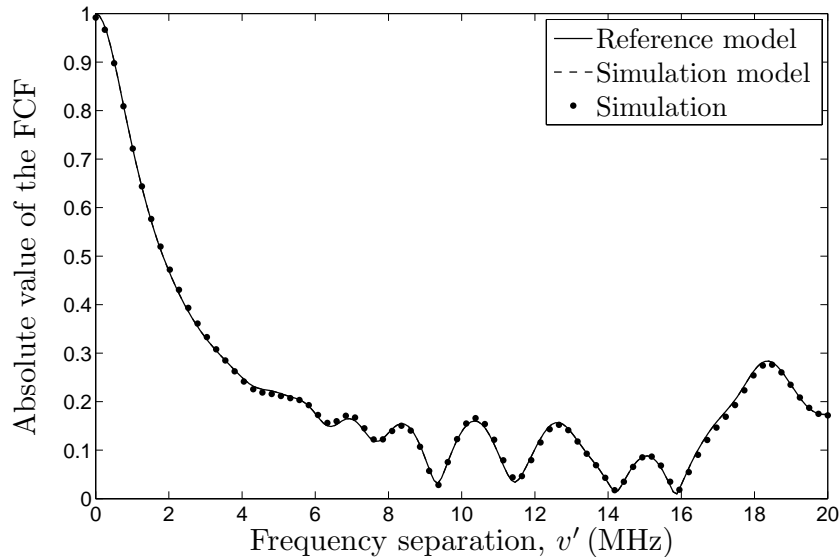
Figure A.8: Absolute value of the FCFs $|r_{\tau'}(v')|$ (reference model) and $|\tilde{r}_{\tau'}(v')|$ (simulation model) for non-isotropic scattering environments using the 18-path HiperLAN/2 model C [8].
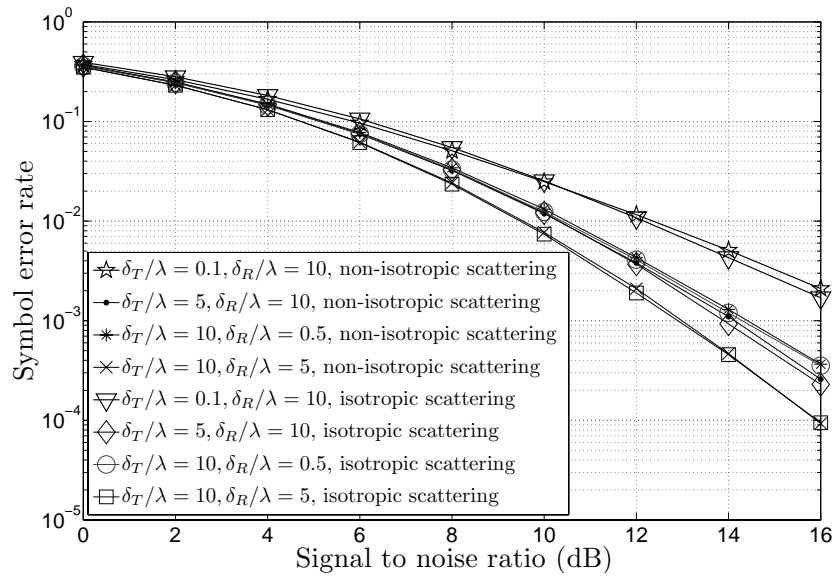
Figure A.9: SER performance of a space-time coded MIMO-OFDM system with different antenna spacings using the one-ring 2×2 channel model under isotropic and non-isotropic scattering conditions.
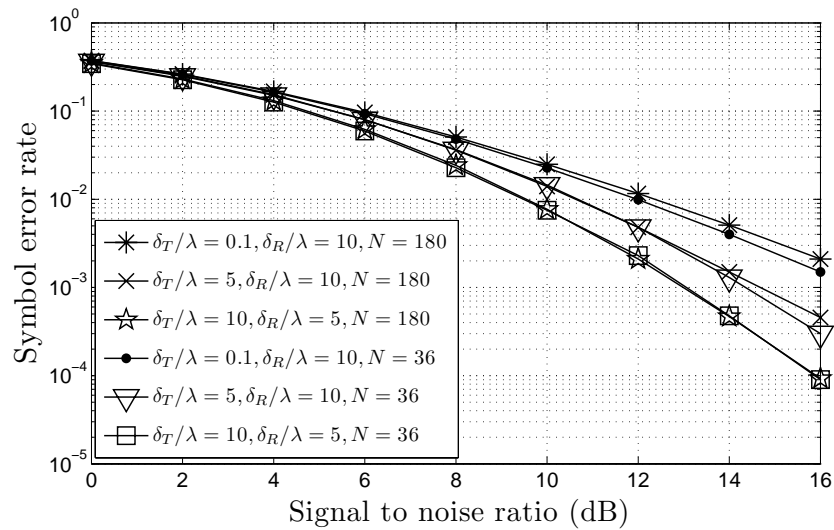
Figure A.10: SER performance of a space-time coded MIMO-OFDM system with different antenna spacings using the one-ring 2×2 channel model under isotropic and non-isotropic scattering conditions.

evaluated using the channel simulator with $N = 180$ scatterers under the same conditions regarding the number of antennas and antenna spacings. The reason for this observation is that the spatial correlation function difference between the two channel simulators is small and can be neglected (compare Fig. A.6 and Fig. A.7).

V. Conclusion

In this paper, we have developed a wideband one-ring MIMO reference channel model for non-isotropic scattering environments. A deterministic simulation channel model, which is required for computer simulations, has directly been obtained from the reference model by using the principle of deterministic channel modeling. Analytical expressions have been presented for the temporal ACFs, the 2-D space CCFs, and the FCFs of both the reference model and the deterministic simulation model. It has been shown by theory, confirmed by simulations, that the statistical properties of the deterministic simulation model match those of the reference model very well. We have furthermore investigated the performance of a space-time coded MIMO-OFDM system using the developed wideband one-ring MIMO deterministic channel simulation model. Our simulations have confirmed that the SER performance improves with increasing antenna spacings. Whether the scatterers located in clusters or distributed uniformly on a ring has no strong influence on the MIMO-OFDM system performance. The wideband one-ring channel simulators designed with a single scatterer in each cluster is obviously sufficient to guarantee an accurate evaluation of the MIMO-OFDM system performance in non-isotropic scattering environments if the number of discrete paths is sufficiently large.

It should be mentioned that the procedure of deriving the wideband one-ring model is quite general and applicable to any given delay PSD. The delay PSD of the obtained wideband channel models is identical to the given delay PSD. The resulting wideband deterministic channel model can be used to study the impact of the channel parameters on the performance of wideband wireless communication systems under non-isotropic scattering conditions.

References

[1] A. Abdi, J. A. Barger, and M. Kaveh. A parametric model for the distribution of the angle and the associated correlation function and power spectrum at the mobile station. *IEEE Trans. Veh. Technol.*, 51(3):425–434, May 2002.

[2] P. C. Fannin and A. Molina. Analysis of mobile radio channel sounding measurements in inner city Dublin at 1.808 GHz. In *Proc. IEE Commun.*, volume 143, pages 311–316, Oct. 1996.

[3] S. Guerin. Indoor wideband and narrowband propagation measurements around 60.5 GHz in an empty and furnished room. In *Proc. 46th Vehicular*

Technology Conference, VTC-1996, pages 160–164. Atlanta, USA, Apr./May 1996.

[4] C. A. Gutiérrez and M. Pätzold. Sum-of-sinusoids-based simulation of flat fading wireless propagation channels under non-isotropic scattering conditions. In *Proc. 50th Global Communication Conference, GLOBECOM 2007*, pages 3842–3846. Washington, D.C., USA, Nov. 2007.

[5] W. C. Y. Lee. Finding the approximate angular probability density function of wave arrival by using a directional antenna. *IEEE Trans. Antennas Propagat.*, 21(3):328–334, May 1973.

[6] Y. Ma and M. Pätzold. Performance comparison of space-time coded MIMO–OFDM systems using different wideband MIMO channel models. In *Proc. 4th IEEE International Symposium on Wireless Communication Systems, ISWCS 2007*, pages 762–766. Trondheim, Norway, Oct. 2007.

[7] Y. Ma and M. Pätzold. Wideband two-ring MIMO channel models for mobile-to-mobile communications. In *Proc. 10th International Symposium on Wireless Personal Multimedia Communications, WPMC 2007*, pages 380–384. Jaipur, India, Dec. 2007.

[8] J. Medbo and P. Schramm. Channel models for HIPERLAN/2 in different indoor scenarios. Tech. Rep. 3ERI085B, ETSI EP, BRAN Meeting #3, Mar. 1998.

[9] M. Pätzold. *Mobile Fading Channels*. Chichester: John Wiley & Sons, 2002.

[10] M. Pätzold. System function and characteristic quantities of spatial deterministic Gaussian uncorrelated scattering processes. In *Proc. 57th Vehicular Technology Conference, VTC 2003-Spring*, pages 256–261. Jeju, Korea, Apr. 2003.

[11] M. Pätzold and B. O. Hogstad. A space-time channel simulator for MIMO channels based on the geometrical one-ring scattering model. *Wireless Communications and Mobile Computing, Special Issue on Multiple-input Multiple-output (MIMO) Communications*, 4(7):727–737, Nov. 2004.

[12] M. Pätzold and B. O. Hogstad. A wideband MIMO channel model derived from the geometric elliptical scattering model. In *Proc. 3rd International Symposium on Wireless Communication System, ISWCS 2006*, pages 138–144. Valencia, Spain, Sept. 2006.

[13] M. Pätzold and B. O. Hogstad. A wideband space-time MIMO channel simulator based on the geometrical one-ring model. In *Proc. 64th Vehicular Technology Conference, VTC 2006-Fall*. Montreal, Canada, Sept. 2006.

Appendix B

Paper II

Wideband Two-Ring MIMO Channel Models for Mobile-to-Mobile Communications

Yuanyuan Ma and Matthias Pätzold

Department of Information and Communication Technology

Faculty of Engineering and Science, University of Agder

Servicebox 509, NO-4898 Grimstad, Norway

E-mails: {yuanyuan.ma, matthias.paetzold}@uia.no

Abstract — **This paper deals with the design of wideband multiple-input multiple-output (MIMO) reference channel models for mobile-to-mobile (M2M) communications. We present a wideband extension of the traditional geometrical two-ring MIMO channel model assuming double-bounce scattering. Furthermore, we propose a new narrowband two-ring MIMO reference channel model under the assumption of single-bounce scattering and show how the model can be extended with respect to frequency selectivity. The statistical properties of both wideband MIMO channel models are studied. Analytical solutions are presented for the temporal autocorrelation function (ACF), the two-dimensional (2-D) space cross-correlation function (CCF), and the frequency correlation function (FCF). The proposed wideband reference channel models can be used as a starting point for the derivation of wideband space-time MIMO channel simulators. Such a simulator enables the performance evaluation of future wideband MIMO M2M communication systems. Furthermore, the proposed channel models are very useful for studying the MIMO channel capacity.**

Keywords — MIMO channel modeling, wideband MIMO channels, mobile-to-mobile channels, geometrical two-ring scattering model, double-bounce scattering, single-bounce scattering, space-time correlation.

I. INTRODUCTION

Recently, M2M communication systems have found important applications in ad-hoc wireless networks [12, 13], intelligent highways [6], and relay-based cellular networks [7], where extremely reliable communication links are important. In contrast to traditional fixed-to-mobile cellular radio systems, in M2M communication systems the transmitter and the receiver are in motion. Therefore, many currently developed channel models for conventional cellular radio systems cannot directly be used for M2M communication systems.

In the literature, the modeling of M2M propagation channels for single-input single-output (SISO) systems has been investigated in [3, 2, 9]. A reference channel model applicable to urban and suburban areas has been proposed in [3] for SISO M2M Rayleigh fading channels. The corresponding statistical properties have been studied in [2]. The sum-of-sinusoids method and the inverse fast Fourier transform (IFFT) filtering based method have been used in [9] to design simulation models for narrowband M2M channels. Reference models derived from the geometrical two-ring scattering model have been proposed in [4, 10] for narrowband MIMO M2M Rayleigh channels. In these reference models, double-bounce scattering is assumed. Waves radiated by the transmit antennas are first captured by scatterers around the transmitter and then by the scatterers around the receiver before they are re-radiated to the receive antennas. However, due to increasing demands for high-speed communications, future M2M communication systems are required to operate in much larger bandwidths than today's systems. Hence, for the design and performance evaluation, it is of crucial importance to have accurate and realistic wideband MIMO M2M channel models.

In this paper, we extend the narrowband two-ring MIMO reference channel model in [10] to a wideband channel model. Thereafter, we propose a new geo-metrical two-ring reference model based on single-bounce scattering for narrow-band MIMO M2M fading channels. This model assumes that waves radiated by the transmit antennas are captured by scatterers only around the transmitter or around the receiver. We show how the proposed MIMO channel model can be extended with respect to frequency-selectivity. The temporal, spatial, and frequency cor-relation properties will be analyzed and visualized assuming isotropic scattering conditions.

The remainder of this paper is organized as follows. Section II extends the double-bounce two-ring scattering model with respect to frequency selectivity. In Section III, we propose a narrowband two-ring MIMO M2M reference channel model based on single-bounce scattering. Moreover, we extend the proposed reference model with respect to frequency selectivity. The temporal, spatial, and frequency correlation properties will be analyzed and visualized in Section IV assuming isotropic scattering conditions. Finally, some concluding remarks are given in Section V.

II. A DOUBLE-BOUNCE SCATTERING WIDEBAND TWO-RING MIMO M2M REFERENCE CHANNEL MODEL

In this section, we will show how the double-bounce scattering narrowband two-ring reference model can be extended with respect to frequency selectivity.

A. Review of the Narrowband Reference Channel Model

The starting point for the extension to frequency selectivity is the narrowband two-ring channel model as shown in Fig. B.1, where double-bounce scattering is assumed [10]. Both the transmitter and the receiver are in motion and equipped with M_T transmit antennas and M_R receive antennas, respectively. The local scatterers $S_T^{(m)}$ ($m = 1, 2, \ldots, M$) around the transmitter lie on a ring of radius R_T, while the scatterers $S_R^{(n)}$ ($n = 1, 2, \ldots, N$) around the receiver are located on a second ring of radius R_R. The reference model is based on the assumption that the number of local scatterers, M and N, are infinite. Homogeneous plane waves emitted from the transmitter are first captured by the scatterers $S_T^{(m)}$ and then by the scatterers $S_R^{(n)}$ before they are re-radiated to the receiver. The distance between the transmitter and the receiver, denoted by D, is very large compared to the radii R_T and R_R, i.e., $D \gg \max\{R_T, R_R\}$. The antenna spacings at the transmitter and the receiver are denoted by δ_T and δ_R, respectively. It is assumed that $(M_T - 1)\delta_T \ll R_T$ and $(M_R - 1)\delta_R \ll R_R$.

The complex channel gain of the link from the transmit antenna element $A_T^{(l)}$ ($l = 1, 2, \ldots, M_T$) to the receive antenna element $A_R^{(k)}$ ($k = 1, 2, \ldots, M_R$) can be expressed as [10]

$$g_{kl}(t) = \lim_{\substack{M \to \infty \\ N \to \infty}} \frac{1}{\sqrt{MN}} \sum_{m,n=1}^{M,N} g_{mn} e^{j[2\pi(f_T^{(m)} + f_R^{(n)})t + \theta_{mn}]} \tag{1}$$

where

$$g_{mn} = a_m b_n c_{mn} \tag{2}$$
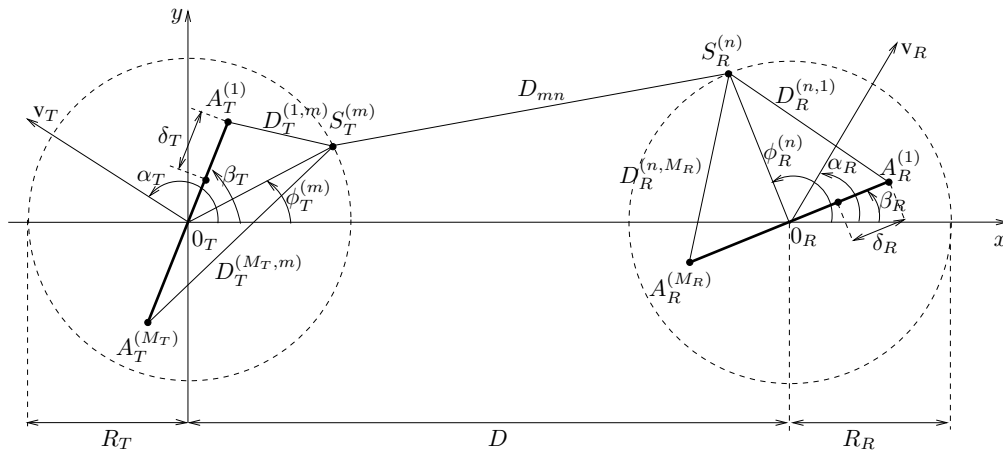
Figure B.1: Geometrical two-ring double-bounce scattering model for an $M_T \times M_R$ MIMO channel.

$$a_m = e^{j(M_T - 2l + 1)\pi(\delta_T/\lambda)\cos(\phi_T^{(m)} - \beta_T)} \tag{3}$$

$$b_n = e^{j(M_R - 2k + 1)\pi(\delta_R/\lambda)\cos(\phi_R^{(n)} - \beta_R)} \tag{4}$$

$$c_{mn} = e^{j\frac{2\pi}{\lambda}(R_T \cos\phi_T^{(m)} - R_R \cos\phi_R^{(n)})} \tag{5}$$

$$f_T^{(m)} = f_{T_{\max}}\cos(\phi_T^{(m)} - \alpha_T) \tag{6}$$

$$f_R^{(n)} = f_{R_{\max}}\cos(\phi_R^{(n)} - \alpha_R). \tag{7}$$

In the equations presented above, the angle β_T describes the tilt angle of the antenna array at the transmitter. Analogously, the angle β_R denotes the tilt angle of the antenna array at the receiver. The transmitter and the receiver move in the direction determined by the angles α_T and α_R. The maximum Doppler frequencies caused by the movements of the transmitter and the receiver are denoted by $f_{T_{\max}}$ and $f_{R_{\max}}$, respectively. The carrier's wavelength is λ. The angle $\phi_T^{(m)}$ represents the angle of departure (AOD) at the transmitter, while the angle of arrival (AOA) is described by $\phi_R^{(n)}$. In the double-bounce scattering two-ring model, both the AOD $\phi_T^{(m)}$ and the AOA $\phi_R^{(n)}$ are independent random variables determined by the distributions of the local scatterers. The joint phases θ_{mn} are independent and identically distributed (i.i.d.) random variables, each having a uniform distribution over $[0, 2\pi)$.

B. Extension with Respect to Frequency Selectivity

From the narrowband MIMO channel model shown in Fig. B.1, we can observe that the minimum propagation delay is given by $\tau'_{\min} = D/c_0$, where c_0 represents the speed of light. The propagation delay τ'_{mn} corresponding to the scatterers $S_T^{(m)}$ to $S_R^{(n)}$ can be expressed as

$$\begin{aligned}
\tau'_{mn} &= \frac{R_T + R_R + D_{mn}}{c_0} \\
&\approx \frac{R_T}{c_0}(1 - \cos\phi_T^{(m)}) + \frac{R_R}{c_0}(1 + \cos\phi_R^{(n)}) + \frac{D}{c_0}
\end{aligned} \tag{8}$$

where we have assumed that the inequality $D \gg \max\{R_T, R_R\}$ holds. In (8), D_{mn} represents the distance between the scatterer $S_T^{(m)}$ and the scatterer $S_R^{(n)}$. Without loss of generality, the minimum delay $\tau'_{\min} = D/c_0$ can be set to 0, since it is common to all paths and can be neglected. Therefore, the (relative) propagation delay can be written as

$$\tau'_{mn} \approx \frac{R_T}{c_0}(1 - \cos\phi_T^{(m)}) + \frac{R_R}{c_0}(1 + \cos\phi_R^{(n)}). \tag{9}$$

In wideband transmission systems, the propagation delay differences must be considered in comparison to the data symbol duration T_s. All propagation delays τ'_{mn},

which are within the range $\tau'_{\ell-1} < \tau'_{mn} \leq \tau'_\ell$, are gathered together and assigned to a single delay τ'_ℓ ($\ell = 1, 2, \ldots, \mathcal{L}$). The propagation delays τ'_ℓ are assumed to be known from a specification or measurements.

For each scatterer $S_T^{(m)}$, a set of scatterers $S_R^{(n)}$ can make the corresponding propagation delay τ'_{mn} within the interval $(\tau'_{\ell-1}, \tau'_\ell]$ and be assigned to the same delay τ'_ℓ. Therefore, an index set $\mathscr{I}_{\ell,m}$ is defined to denote the locations of these scatterers $S_R^{(n)}$, which is a subset of $\mathscr{I} = \{1, 2, \cdots, N\}$. We assume that the propagation delay corresponding to the scatterer $S_T^{(m)}$ to any scatterer $S_R^{(n)}$ is assigned to the same delay τ'_ℓ if $n \in \mathscr{I}_{\ell,m}$. The number of the propagation delays which have been assigned to the same propagation delay τ'_ℓ is denoted by K_ℓ. Moreover, the condition $\sum_{\ell=1}^{\mathscr{L}} K_\ell = M \times N$ must hold. Hence, the complex channel gain $g_{kl,\ell}(t)$ associated with the ℓth discrete propagation path can be expressed as

$$g_{kl,\ell}(t) = \lim_{K_\ell \to \infty} \frac{1}{\sqrt{K_\ell}} \sum_{m=1}^{M} \sum_{n \in \mathscr{I}_{\ell,m}} g_{mn} e^{j[2\pi(f_T^{(m)} + f_R^{(n)})t + \theta_{mn}]}. \tag{10}$$

Then, the complex channel gain in (1) can be extended to the impulse response of a wideband MIMO channel model as follows

$$h_{kl}(\tau', t) = \sum_{\ell=1}^{\mathscr{L}} a_\ell g_{kl,\ell}(t) \delta(\tau' - \tau'_\ell). \tag{11}$$

In (11), a_ℓ denotes the path gain of the ℓth discrete propagation path and $\delta(\cdot)$ is the delta function.

III. A SINGLE-BOUNCE SCATTERING WIDEBAND TWO-RING MIMO M2M REFERENCE CHANNEL MODEL

We propose a single-bounce two-ring scattering model for narrowband MIMO M2M channels in this section. Then, its extension to frequency selectivity will be described.

A. Derivation of the Narrowband Reference Channel Model

In the single-bounce two-ring scattering model as shown in Fig. B.2, the diffuse component at the receiver are composed of waves scattered only by the scatterers $S_T^{(m)}$ and only by the scatterers $S_R^{(n)}$. For ease of comprehension, we draw the two propagation scenarios separately in Figs. B.3(a) and B.3(b). In the first scenario illustrated in Fig. B.3(a), it is assumed that plane waves travel from $A_T^{(l)}$ to $A_R^{(k)}$ via the scatterers $S_T^{(m)}$, while the second scenario, as shown in Fig. B.3(b), takes into account that the waves traveling from $A_T^{(l)}$ to $A_R^{(k)}$ via the scatterers $S_R^{(n)}$. Hence,
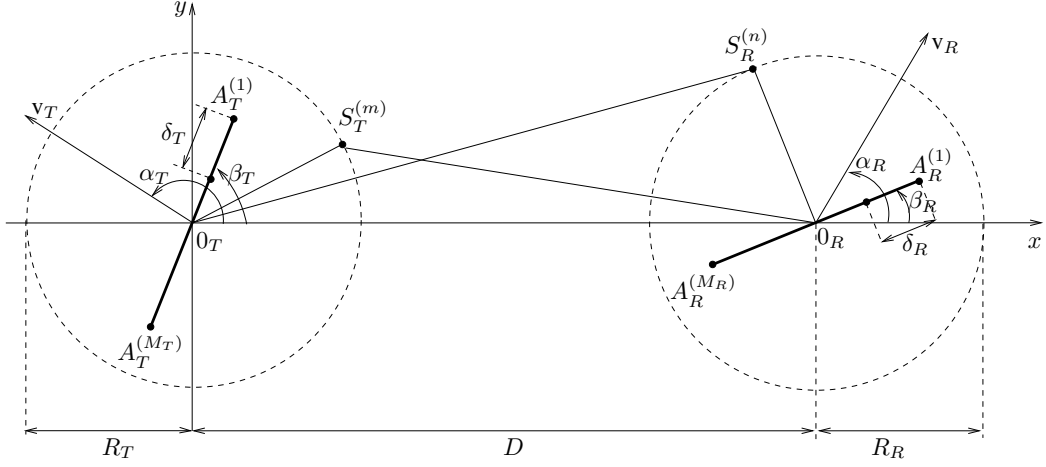
Figure B.2: Geometrical single-bounce scattering two-ring model for an $M_T \times M_R$ MIMO channel.

the channel gain can be expressed as a sum of components derived from the two scenarios [4, 5], i.e.,

$$
\begin{aligned}
g_{kl}(\vec{r}_R) = &\lim_{M \to \infty} \sum_{m=1}^{M} E_{1,m} e^{j[\theta_{1,m} + \vec{k}_{T_1}^{(m)} \cdot \vec{r}_{T_1} - \vec{k}_{R_1}^{(m)} \cdot \vec{r}_{R_1} - k_0 D_{1,m}]} \\
&+ \lim_{N \to \infty} \sum_{n=1}^{N} E_{2,n} e^{j[\theta_{2,n} + \vec{k}_{T_2}^{(n)} \cdot \vec{r}_{T_2} - \vec{k}_{R_2}^{(n)} \cdot \vec{r}_{R_2} - k_0 D_{2,n}]}
\end{aligned}
\tag{12}
$$

where $E_{1,m}$ and $\theta_{1,m}$ represent the gains and the phase shifts caused by the interaction of the local scatterers $S_T^{(m)}$ in the first scenario, respectively. Moreover, $\vec{k}_{T_1}^{(m)}$ is the wave vector pointing in the propagation direction of the mth transmitted plane wave and $\vec{r}_{T_1}$ denotes the spatial translation vector of the transmitter. By analogy, $\vec{k}_{R_1}^{(m)}$ describes the wave vector pointing in the propagation direction of the mth received plane wave and $\vec{r}_{R_1}$ represents the spatial translation vector of the receiver. In the first scenario, the total propagation distance from the transmit antenna $A_T^{(l)}$ to the receive antenna $A_R^{(k)}$ is denoted by $D_{1,m}$. Furthermore, $k_0 = 2\pi/\lambda$ represents the free-space wave number and λ is the wavelength. Similarly, $E_{2,n}$ and $\theta_{2,n}$ denote the gains and the phase shifts related to the second scenario. The wave vectors pointing in the propagation direction of the nth transmitted and received plane are described by $\vec{k}_{T_2}^{(n)}$ and $\vec{k}_{R_2}^{(n)}$, respectively, $\vec{r}_{T_2}$ and $\vec{r}_{R_2}$ denote the spatial translation vector of the transmitter and the receiver. The total wave propagation distance from the transmit antenna $A_T^{(l)}$ to the receive antenna $A_R^{(k)}$ in the second scenario is denoted by $D_{2,n}$.

In the proposed model, it is assumed that the inequalities $D \gg \max\{R_T, R_R\}$, $(M_T - 1)\delta_T \ll R_T$, and $(M_R - 1)\delta_R \ll R_R$ hold. Thus, for a particular scatterer $S_T^{(m)}$

(a)

(b)
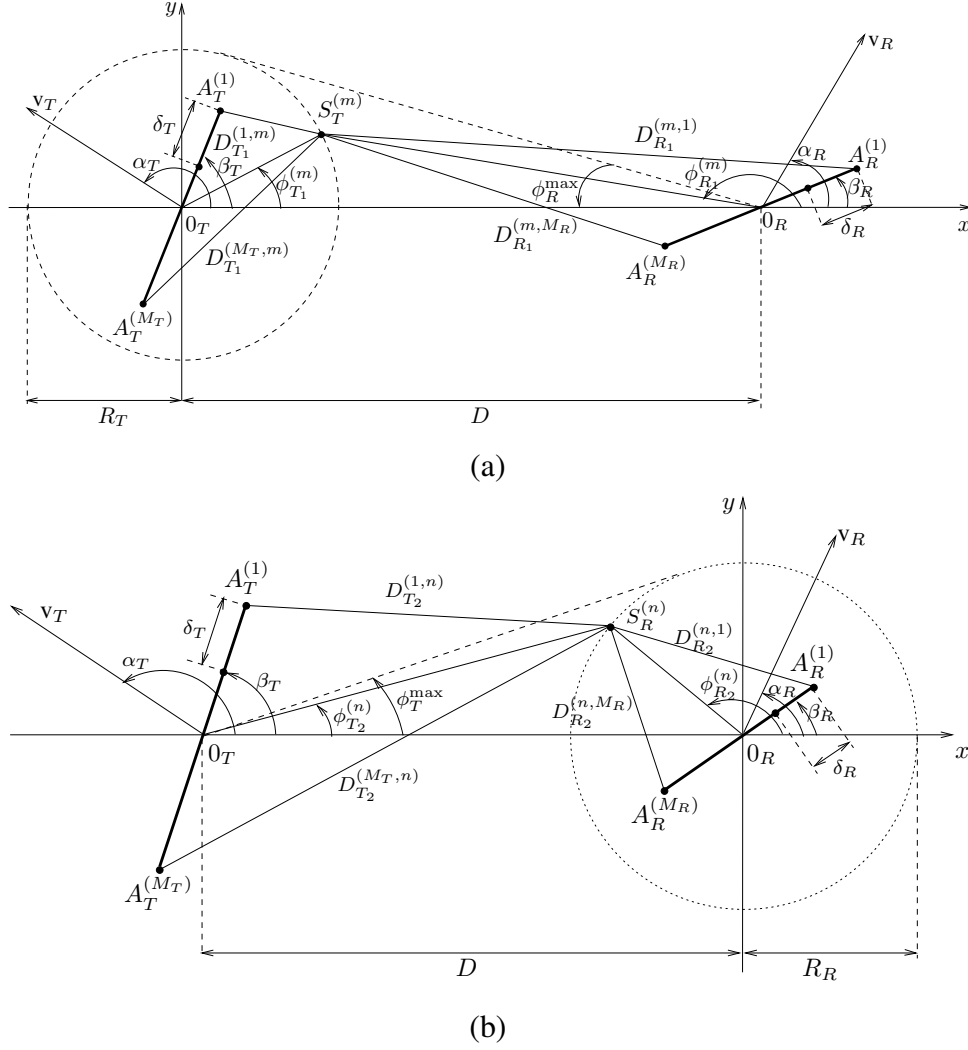
Figure B.3: Waves impinging on the receiver bounced by local scatterers $S_T^{(m)}$ around the transmitter and local scatterers $S_R^{(n)}$ around the receiver.

(or $S_R^{(n)}$), the gain and the phase shift are the same for waves arriving from (or traveling to) different antenna elements [4]. The gains $E_{1,m}$ and $E_{2,n}$ are assumed to be constant and given by $E_{1,m} = 1/\sqrt{2M}$ and $E_{2,n} = 1/\sqrt{2N}$. The phase shifts $\theta_{1,m}$ and $\theta_{2,n}$ are i.i.d. random variables uniformly distributed over the interval $[0, 2\pi)$.

In the first scenario illustrated in Fig. B.3(a), the AOA $\phi_{R_1}^{(m)}$ can be related to the AOD $\phi_{T_1}^{(m)}$ according to the following equation, derived by using the law of sines in the triangle $O_T S_T^{(m)} O_R$:

$$\frac{R_T}{\sin(\pi - \phi_{R_1}^{(m)})} = \frac{D}{\sin(\phi_{R_1}^{(m)} - \phi_{T_1}^{(m)})}. \tag{13}$$

By using the approximation $\sin x \approx x$ for small x, $\sin(\pi - \phi_{R_1}^{(m)})$ can be approximated as $\pi - \phi_{R_1}^{(m)}$ since the angle $\pi - \phi_{R_1}^{(m)}$ is small. Moreover, the approximation $\sin(\phi_{R_1}^{(m)} - \phi_{T_1}^{(m)}) = \sin[(\pi - \phi_{R_1}^{(m)}) + \phi_{T_1}^{(m)}] \approx \sin \phi_{T_1}^{(m)}$ holds. Then, we can approximate the AOA $\phi_{R_1}^{(m)}$ as follows

$$\phi_{R_1}^{(m)} \approx \pi - \phi_R^{\max} \sin \phi_{T_1}^{(m)} \tag{14}$$

where $\phi_R^{\max} \approx R_T/D$. The phase changes $\vec{k}_{T_1}^{(m)} \cdot \vec{r}_{T_1}$ and $\vec{k}_{R_1}^{(m)} \cdot \vec{r}_{R_1}$ are given by

$$\vec{k}_{T_1}^{(m)} \cdot \vec{r}_{T_1} = 2\pi f_{T_{\max}} \cos(\phi_{T_1}^{(m)} - \alpha_T)t \tag{15}$$

$$\vec{k}_{R_1}^{(m)} \cdot \vec{r}_{R_1} = -2\pi f_{R_{\max}} \cos(\phi_{R_1}^{(m)} - \alpha_R)t \tag{16}$$

respectively. Furthermore, the phase change $k_0 D_{1,m}$ due to the total propagation distance can be written as

$$k_0 D_{1,m} = \frac{2\pi}{\lambda}(D_{T_1}^{(1,m)} + D_{R_1}^{(m,1)}) \tag{17}$$

where $D_{T_1}^{(1,m)}$ and $D_{R_1}^{(m,1)}$ are the distances as illustrated in Fig. B.3(a). Since $(M_T - 1)\delta_T \ll R_T$ and $(M_R - 1)\delta_R \ll R_R$, the distances $D_{T_1}^{(1,m)}$ and $D_{R_1}^{(m,1)}$ can be approximated by using the approximation $\sqrt{1+x} \approx 1 + x/2$ $(x \ll 1)$, i.e.,

$$D_{T_1}^{(1,m)} \approx R_T - \frac{(M_T - 2l + 1)\delta_T}{2} \cos(\phi_{T_1}^{(m)} - \beta_T) \tag{18}$$

$$D_{R_1}^{(m,1)} \approx D - R_T \cos \phi_{T_1}^{(m)} - \frac{(M_R - 2k + 1)\delta_R}{2} \cos(\phi_{R_1}^{(m)} - \beta_R). \tag{19}$$

Analogously, we can express the corresponding terms for the second scenario represented in Fig. B.3(b) [1]. The relationship between the AOD $\phi_{T_2}^{(n)}$ and AOA $\phi_{R_2}^{(n)}$ can be established as

$$\phi_{T_2}^{(n)} \approx \phi_{T_2}^{\max} \sin \phi_{R_2}^{(n)} \tag{20}$$

where the quantity $\phi_T^{\max} \approx R_R/D$ designates one half of the maximum AOD $\phi_{T_2}^{(n)}$. The phase changes $\vec{k}_{T_2}^{(n)} \cdot \vec{r}_{T_2}$ and $\vec{k}_{R_2}^{(n)} \cdot \vec{r}_{R_2}$ can be expressed as

$$\vec{k}_{T_2}^{(n)} \cdot \vec{r}_{T_2} = 2\pi f_{T_{\max}} \cos(\phi_{T_2}^{(n)} - \alpha_T)t \tag{21}$$

$$\vec{k}_{R_2}^{(n)} \cdot \vec{r}_{R_2} = -2\pi f_{R_{\max}} \cos(\phi_{R_2}^{(n)} - \alpha_R)t \tag{22}$$

respectively. Moreover, the phase change $k_0 D_{2,n}$ can be written as

$$k_0 D_{2,n} = \frac{2\pi}{\lambda}(D_{T_2}^{(1,n)} + D_{R_2}^{(n,1)}). \tag{23}$$

The distances $D_{T_2}^{(1,n)}$ and $D_{R_2}^{(n,1)}$ can be approximated as

$$D_{T_2}^{(1,n)} \approx D + R_R \cos\phi_{T_2}^{(n)} - \frac{(M_T - 2l + 1)\delta_T}{2}\cos(\phi_{T_2}^{(n)} - \beta_T) \tag{24}$$

$$D_{R_2}^{(n,1)} \approx R_R - \frac{(M_R - 2k + 1)\delta_R}{2}\cos(\phi_{R_2}^{(n)} - \beta_R) \tag{25}$$

respectively. Finally, by substituting (14)–(25) in (12), the complex channel gain $g_{kl}(t)$ describing the transmission link from the transmit antenna element $A_T^{(l)}$ to the receive antenna element $A_R^{(k)}$ can be represented as follows

$$g_{kl}(t) = \lim_{M \to \infty} \frac{1}{\sqrt{2M}} \sum_{m=1}^{M} a_{l,m} b_{k,m} e^{j(2\pi f_{1,m}t + \theta_{1,m})} + \lim_{N \to \infty} \frac{1}{\sqrt{2N}} \sum_{n=1}^{N} c_{l,n} d_{k,n} e^{j(2\pi f_{2,n}t + \theta_{2,n})} \tag{26}$$

where

$$a_{l,m} = e^{j\pi(M_T - 2l + 1)\frac{\delta_T}{\lambda}\cos(\phi_{T_1}^{(m)} - \beta_T)} \tag{27}$$

$$b_{k,m} = e^{j\pi(M_R - 2k + 1)\frac{\delta_R}{\lambda}[\phi_R^{\max}\sin\phi_{T_1}^{(m)}\sin\beta_R - \cos\beta_R]} \tag{28}$$

$$c_{l,n} = e^{j\pi(M_T - 2l + 1)\frac{\delta_T}{\lambda}[\phi_T^{\max}\sin\phi_{R_2}^{(n)}\sin\beta_T + \cos\beta_T]} \tag{29}$$

$$d_{k,n} = e^{j\pi(M_R - 2k + 1)\frac{\delta_R}{\lambda}\cos(\phi_{R_2}^{(n)} - \beta_R)} \tag{30}$$

$$f_{1,m} = f_{T_{\max}}\cos(\phi_{T_1}^{(m)} - \alpha_T) - f_{R_{\max}}\cos(\phi_R^{\max}\sin\phi_{T_1}^{(m)} + \alpha_R) \tag{31}$$

$$f_{2,n} = f_{T_{\max}}\cos(\phi_T^{\max}\sin\phi_{R_2}^{(n)} - \alpha_T) + f_{R_{\max}}\cos(\phi_{R_2}^{(n)} - \alpha_R). \tag{32}$$

B. Extension with Respect to Frequency Selectivity

It can be observed from Fig. B.3(a) that the minimum and maximum propagation delays related to the first scenario are given by $\tau'_{\min} = D/c_0$ and $\tau'_{T_{\max}} = \tau'_{\min} + 2R_T/c_0$, respectively. We can express the propagation delays from $A_T^{(l)}$ via the scatterers $S_T^{(m)}$ to $A_R^{(k)}$ as

$$\tau'_m = \frac{R_T + \sqrt{D^2 + R_T^2 - 2DR_T\cos\phi_{T_1}^{(m)}}}{c_0}$$

$$\approx \frac{R_T}{c_0}(1 - \cos\phi_{T_1}^{(m)}) + \frac{D}{c_0}. \tag{33}$$

Without loss of generality, we can set $\tau'_{\min}$ to 0. Then, the (relative) maximum propagation delay is given by $\tau'_{T_{\max}} = 2R_T/c_0 = \tau'_{\mathscr{L}}$. Furthermore, the (relative) propagation delay can be expressed as

$$\tau'_m = \tau'_{T_{\max}} \cdot \frac{1 - \cos \phi_{T_1}^{(m)}}{2}. \tag{34}$$

By analogy with (34), the propagation delay the from $A_T^{(l)}$ to $A_R^{(k)}$ via the scatterers $S_R^{(n)}$ is

$$\tau'_m \approx \tau'_{R_{\max}} \cdot \frac{1 + \cos \phi_{R_2}^{(n)}}{2} \tag{35}$$

where $\tau'_{R_{\max}} = 2R_R/c_0 = \tau'_{\mathscr{L}}$ holds [11]. Hence, we may write

$$\phi_{T_1}^{(m)} = \arccos(1 - 2\frac{\tau'_m}{\tau'_{T_{\max}}}) \tag{36}$$

$$\phi_{R_2}^{(n)} = \arccos(2\frac{\tau'_n}{\tau'_{R_{\max}}} - 1). \tag{37}$$

In order to extend the proposed channel model to the general case of a wideband channel model, we partition each ring of scatterers into $\mathscr{L}$ pairs of segments. Each segment consists of M_ℓ scatterers around the transmitter and N_ℓ scatterers around the receiver. Moreover, the condition $\sum_{\ell=1}^{\mathscr{L}} M_\ell = M$ and $\sum_{\ell=1}^{\mathscr{L}} N_\ell = N$ must hold. The angles limiting the segments are denoted by $\varphi_{T,\ell}$ and $\varphi_{R,\ell}$. According to (36) and (37), we can establish the relationship between the given delays τ'_ℓ and the angles $\varphi_{T,\ell}$ and $\varphi_{R,\ell}$ as follows

$$\varphi_{T,\ell} = \arccos(1 - 2\frac{\tau'_\ell}{\tau'_{\mathscr{L}}}) \tag{38}$$

$$\varphi_{R,\ell} = \arccos(2\frac{\tau'_\ell}{\tau'_{\mathscr{L}}} - 1). \tag{39}$$

The angles $\phi_{T_1}^{(m)}$ and $\phi_{R_2}^{(n)}$ are within the ℓth interval if

$$\frac{\varphi_{T,\ell-1} + \varphi_{T,\ell}}{2} < \phi_{T_1}^{(m)} \leq \frac{\varphi_{T,\ell} + \varphi_{T,\ell+1}}{2}$$

$$\text{or} \qquad 2\pi - \frac{\varphi_{T,\ell} + \varphi_{T,\ell+1}}{2} < \phi_{T_1}^{(m)} \leq 2\pi - \frac{\varphi_{T,\ell-1} + \varphi_{T,\ell}}{2} \tag{40}$$

$$\frac{\varphi_{R,\ell} + \varphi_{R,\ell+1}}{2} < \phi_{R_2}^{(m)} \leq \frac{\varphi_{R,\ell-1} + \varphi_{R,\ell}}{2}$$

$$\text{or} \qquad 2\pi - \frac{\varphi_{R,\ell-1} + \varphi_{R,\ell}}{2} < \phi_{R_2}^{(m)} \leq 2\pi - \frac{\varphi_{R,\ell} + \varphi_{R,\ell+1}}{2} \qquad (41)$$

for $\ell = 2, 3, \ldots, \mathscr{L}$. We assume that the indexes of the scatterers $S_T^{(m)}$ and $S_R^{(n)}$ can be described by $\mathscr{I}_T = \{1, 2, \cdots, M\}$ and $\mathscr{I}_R = \{1, 2, \cdots, N\}$, respectively. Then, the locations of the scatterers $S_T^{(m)}$ and $S_R^{(n)}$ in the ℓth segment can be denoted by the index sets $\mathscr{I}_{T,\ell}$ and $\mathscr{I}_{R,\ell}$, which belong to the sets $\mathscr{I}_T$ and $\mathscr{I}_R$, respectively. The channel gain $g_{kl,\ell}(t)$ can be expressed according to (26) as

$$g_{kl,\ell}(t) = \lim_{M_\ell \to \infty} \frac{1}{\sqrt{2M_\ell}} \sum_{m \in \mathscr{I}_{T,\ell}} a_{l,m} b_{k,m} e^{j(2\pi f_{1,m}t + \theta_{1,m})}$$

$$+ \lim_{N_\ell \to \infty} \frac{1}{\sqrt{2N_\ell}} \sum_{n \in \mathscr{I}_{R_\ell}} c_{l,n} d_{k,n} e^{j(2\pi f_{2,n}t + \theta_{2,n})}. \qquad (42)$$

Finally, the impulse response of the new wideband model can be presented in the same form as (11).

IV. CORRELATION PROPERTIES

In this section, we study the statistical properties of the proposed single-bounce two-ring scattering model. The temporal ACF, the 2-D space CCF, and the FCF are of special interest. Since the extension with respect to frequency selectivity is the main topic of this paper, the FCF of the double-bounce two-ring scattering model will also be discussed in this section. For simplicity, we consider a 2×2 channel in the following.

The three-dimensional (3-D) space-time CCF between the diffuse components $g_{11}(t)$ and $g_{22}(t)$ is defined as

$$\rho_{11,22}(\delta_T, \delta_R, \tau) = E\{g_{11}(t)g_{22}^*(t+\tau)\} \qquad (43)$$

where $(\cdot)^*$ denotes the complex conjugation and $E\{\cdot\}$ is the expectation operator. Submitting (26) in (43) gives

$$\rho_{11,22}(\delta_T, \delta_R, \tau) = \lim_{M \to \infty} \frac{1}{2M} \sum_{m=1}^{M} a_{1,m}^2 b_{1,m}^2 e^{-j2\pi f_{1,m}\tau} + \lim_{N \to \infty} \frac{1}{2N} \sum_{n=1}^{N} c_{1,n}^2 d_{1,n}^2 e^{-j2\pi f_{2,n}\tau}.$$

$$(44)$$

As the number of local scatterers M and N is infinite, the 3-D CCF in (44) can be expressed in the integral form as

$$\rho_{11,22}(\delta_T, \delta_R, \tau) = \frac{1}{2} \int_0^{2\pi} a_{1,m}^2(\delta_T, \phi_{T_1}) b_{1,m}^2(\delta_R, \phi_{T_1}) e^{-j2\pi f_{1,m}\tau} p(\phi_{T_1}) d\phi_{T_1}$$
$$+ \frac{1}{2} \int_0^{2\pi} c_{1,n}^2(\delta_T, \phi_{R_2}) d_{1,n}^2(\delta_R, \phi_{R_2}) e^{-j2\pi f_{2,n}\tau} p(\phi_{R_2}) d\phi_{R_2}. \quad (45)$$

The temporal ACF $r_{g_{kl}}(\tau)$ is defined as $r_{g_{kl}}(\tau) = E\{g_{kl}(t) g_{kl}^*(t+\tau)\}$, which can be obtained from $\rho_{11,22}(\delta_T, \delta_R, \tau)$ by setting the antenna spacings δ_T and δ_R to zero, i.e., $r_{g_{kl}}(\tau) = \rho_{11,22}(0, 0, \tau)$. Thus,

$$r_{g_{kl}}(\tau) = \frac{1}{2} \int_0^{2\pi} e^{-j2\pi f_{1,m}\tau} p(\phi_{T_1}) d\phi_{T_1} + \frac{1}{2} \int_0^{2\pi} e^{-j2\pi f_{2,n}\tau} p(\phi_{R_2}) d\phi_{R_2}. \quad (46)$$

The 2-D space CCF $\rho_{11,22}(\delta_T, \delta_R)$, defined as $\rho_{11,22}(\delta_T, \delta_R) = E\{g_{11}(t) g_{22}^*(t)\}$, equals to the 3-D CCF $\rho_{11,22}(\delta_T, \delta_R, \tau)$ at $\tau = 0$. In both cases, we obtain

$$\rho_{11,22}(\delta_T, \delta_R) = \frac{1}{2} \int_0^{2\pi} a_{1,m}^2(\delta_T, \phi_{T_1}) b_{1,m}^2(\delta_R, \phi_{T_1}) p(\phi_{T_1}) d\phi_{T_1}$$
$$+ \frac{1}{2} \int_0^{2\pi} c_{1,n}^2(\delta_T, \phi_{R_2}) d_{1,n}^2(\delta_R, \phi_{R_2}) p(\phi_{R_2}) d\phi_{R_2}. \quad (47)$$

The FCF of the wideband MIMO reference channel model is defined as

$$r_{\tau'}(v') = E\{H_{kl}(f', t) H_{kl}^*(f' + v', t)\}. \quad (48)$$

Here, $H_{kl}(f', t)$ is the time-variant transfer function, which is the Fourier transform of the impulse response $h_{kl}(\tau', t)$. Submitting $H_{kl}(f', t)$ obtained from the single-bounce scattering model or from the double-bounce scattering model in (48), we can express the FCF of the models as

$$r_{\tau'}(v') = \sum_{\ell=1}^{\mathscr{L}} a_\ell^2 e^{-j2\pi v' \tau_\ell'}. \quad (49)$$

Some results for the temporal ACF and the 2-D CCF of the single-bounce two-ring scattering channel model are presented in Figs. B.4 and B.5, respectively. The absolute value of the FCF of the two kinds of wideband two-ring channel models using the HiperLAN/2 model C is shown in Fig. B.6 [8]. These results are valid for a 2×2 MIMO channel under the assumption of isotropic scattering, where the maximum Doppler frequencies $f_{T_{\max}}$ and $f_{R_{\max}}$ were set to 91 Hz. The wavelength
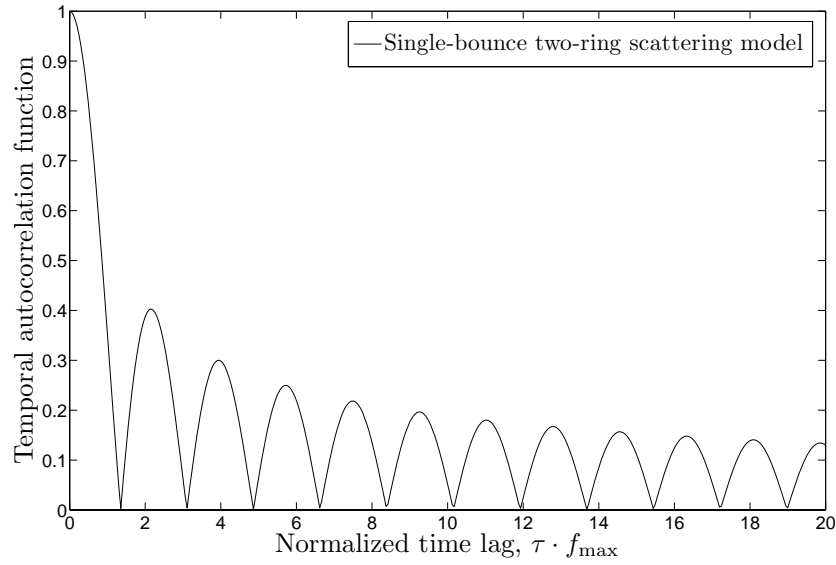
Figure B.4: Absolute value of the temporal ACF $\mid r_{g_{kl}}(\tau) \mid$ of the single-bounce two-ring scattering model for isotropic scattering environments.
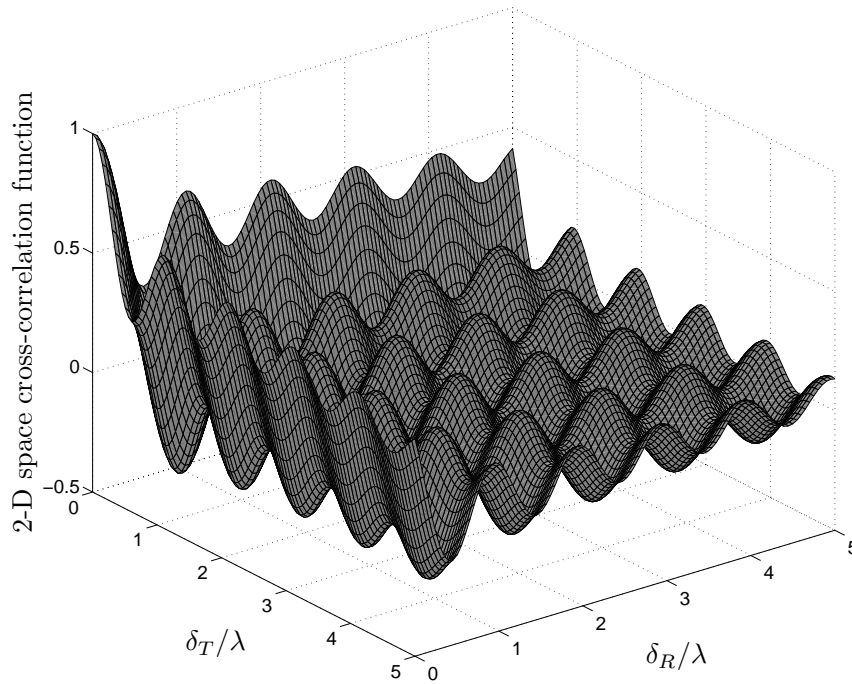
Figure B.5: The 2-D space CCF $\rho_{kl,k'l'}(\delta_T, \delta_R)$ of the single-bounce two-ring scattering model for isotropic scattering environments.

$\lambda = 0.15\,\mathrm{m}$. The angles of motion α_T and α_R at the transmitter and the receiver were set to $\pi/3$, respectively. The tilt angles β_T and β_R were equal to $\pi/2$ and $\phi_T^{\max} = \phi_R^{\max} = 2°$.
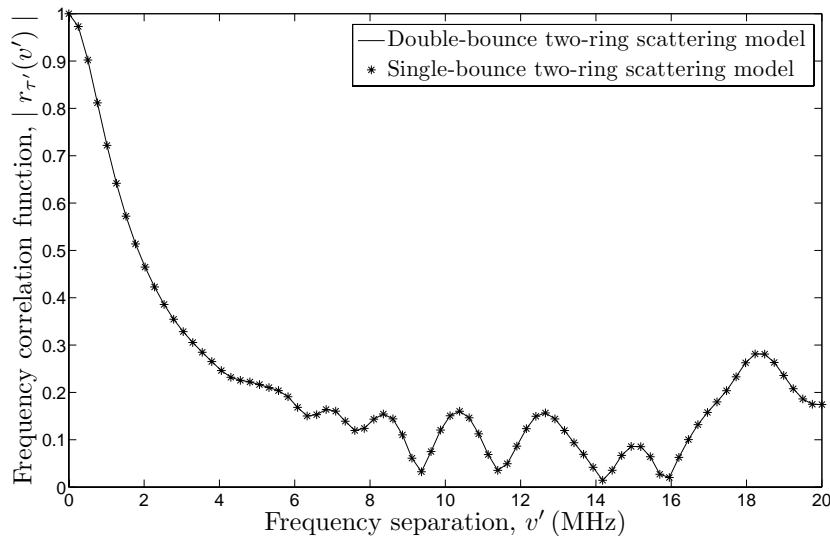
Figure B.6: Absolute value of the FCFs $\mid r_{\tau'}(v') \mid$ of the double-bounce two-ring scattering model and the single-bounce two-ring scattering model using the 18-path HiperLAN/2 model C [8].

V. CONCLUSION

In this paper, the narrowband two-ring MIMO channel model based on double-bounce scattering has been extended with respect to frequency selectivity. A new geometrical two-ring reference model under the assumption of single-bounce scattering has been derived for narrowband MIMO M2M communication channels. Thereafter, a further extension of the proposed channel model to frequency selectivity has been made. Closed-form solutions have been presented for the temporal ACF, the 2-D space CCF, and the FCF. Our proposed reference models can be used as a starting point for the design of stochastic and deterministic MIMO channel simulators. The proposed channel models are useful for the design, test, and optimization of future wideband M2M communication systems. Moreover, these models are of crucial importance for studying the channel capacity of wideband channels under specific propagation conditions.

REFERENCES

[1] A. Abdi and M. Kaveh. A space-time correlation model for multielement antenna systems in mobile fading channel. *IEEE J. Select. Areas Commun.*, 20(3):550–560, Apr. 2002.

[2] A. S. Akki. Statistical properties of mobile-to-mobile land communication channels. *IEEE Trans. on Veh. Tech.*, 43(4):826–831, Nov. 1994.

[3] A. S. Akki and F. Haber. A statistical model for mobile-to-mobile land communication channel. *IEEE Trans. on Veh. Tech.*, 35(1):2–7, Feb. 1986.

[4] G. J. Byers and F. Takawira. Spatially and temporally correlated MIMO channels: modeling and capacity analysis. *IEEE Trans. on Veh. Technol.*, 53(3):634–643, May 2004.

[5] J. Fuhl, A. F. Molisch, and E. Bonek. Unified channel model for mobile radio systems with smart antennas. In *IEE proc. Radar, Sonar and Navigation*, volume 145, pages 32–41, Feb. 1998.

[6] H. Inoue, S. Osawa, A. Yashiki, and H. Makino. Dedicated short-range communications (DSRC) for ahs services. In *IEEE Intelligent Vehicles Symposium, 2004*, pages 369–374. Parma, Italy, Jun. 2004.

[7] S. Lakkavalli, A. Negi, and S. Singh. Stretchable architectures for next generation cellular networks. In *5th Annual International Symposium on Advanced Radio Technology*, pages 59–65. Colorado, U.S.A, Aug. 2003.

[8] J. Medbo and P. Schramm. Channel models for HIPERLAN/2 in different indoor scenarios. Tech. Rep. 3ERI085B, ETSI EP, BRAN Meeting #3, Mar. 1998.

[9] C. S. Patel, G. L. Stüber, and T. G. Pratt. Simulation of Rayleigh-faded mobile-to-mobile communication channels. *IEEE Trans. on Commun.*, 53(11):1876–1884, Nov. 2005.

[10] M. Pätzold and B. O. Hogstad. A MIMO mobile-to-mobile channel model: Part I–the reference model. In *Proc. 16th IEEE International Symposium on Personal, Indoor and Mobile RadioCommunications, IEEE PIMRC 2005*, volume 1, pages 573–578. Berlin, Germany, Sept. 2005.

[11] M. Pätzold and B. O. Hogstad. A wideband space-time MIMO channel simulator based on the geometrical one-ring model. In *Proc. 64th Vehicular Technology Conference, VTC 2006-Fall*. Montreal, Canada, Sept. 2006.

[12] R. Wang and D. Cox. Channel modeling for ad hoc mobile wireless networks. In *Proc. 57th IEEE Semiannual Vehicular Technology Conference, IEEE VTC 2002–Spring*, volume 1, pages 21–25. Birmingham, AL, May 2002.

[13] S. Yin and X. Lin. Traffic self-similarity in mobile ad hoc networks. In *Second IFIP International Conference on Wireless and Optical Communications Networks, WOCN 2005*, pages 285–289, Mar. 2005.

Appendix C

Paper III

Design and Simulation of Narrowband Indoor Radio Propagation Channels Under LOS and NLOS Propagation Conditions

Yuanyuan Ma and Matthias Pätzold

Department of Information and Communication Technology

Faculty of Engineering and Science, University of Agder

Servicebox 509, NO-4898 Grimstad, Norway

E-mails: {yuanyuan.ma, matthias.paetzold}@uia.no

Abstract — **This paper deals with the design and simulation of narrowband indoor propagation channels under line-of-sight (LOS) and non-LOS (NLOS) propagation conditions. We propose a reference channel model assuming that the scatterers are uniformly distributed in the two-dimensional (2D) horizontal space of a room. We derive analytical expressions for the probability density function (PDF) of the angle-of-arrival (AOA), the Doppler power spectral density (PSD), and the temporal autocorrelation function (ACF). We derive a sum-of-cisoids (SOC) channel simulator from the reference model. It is shown by numerical results that the statistical properties of the SOC channel simulator match very closely with the ones of the reference model. It turns out that our indoor reference model can be approximated by an SOC channel simulator with reduced realization expenditure. The resulting SOC channel simulator allows us to evaluate the performance of mobile communication systems in indoor environments by simulations. It is demonstrated that the generalized method of equal areas (GMEA) and the basic Riemann sum method (BRSM) are efficient parameter computation methods for the design of SOC indoor channel simulators.**

I. INTRODUCTION

The growing interest in wireless indoor communication systems and applications of local area networks has resulted in many investigations on the characteristics of indoor radio propagation channels. In the last few years, several empirical channel models [4, 16, 17, 2] have been developed based on indoor channel measurements. The obtained experimental results, such as the PDF of the AOA and the angular spread, are important statistical quantities describing the characteristics of fading channels. However, the empirical models are only useful and accurate for

environments having the same specific characteristics as those where the measurements were made. They cannot be applied to other indoor environments without further modifications.

To cope with the problems faced by empirical models, several geometrical scattering models have been proposed in the literature, e.g., the one-ring scattering model [10, 13], the two-ring scattering model [1, 9], and the elliptical scattering model [3]. The application of geometrical scattering models has even been extended to characterize mobile fading channels for three-dimensional scattering environments [15]. Most of the aforementioned geometrical models have been widely used to characterize fading channels for outdoor environments. But few applications are found for the indoor channel modeling. A geometrically based statistical channel model has been proposed in [8] for indoor and outdoor propagation environments assuming scatterers are randomly distributed around the BS within a circle. However, the model proposed in [8] is only applicable to indoor environments when considering the distance between the BS and the scatterers follows the exponential distribution. Such an assumption limits applications of such a model in the indoor channel modeling.

In this paper, we propose a new geometrical-based channel model for indoor propagation environments. Our starting point is a geometrical indoor scattering model, where we assume that an infinite number of scatterers are uniformly distributed in the 2D horizontal space of a room. In our channel model, we will consider the general case, where the base station (BS) and the mobile station (MS) are arbitrarily located in the room. Moreover, the LOS component between the BS and the MS will be taken into consideration, which allows us to include the NLOS scattering scenarios as a special case. Analytical expressions are derived for the PDF of the AOA, the Doppler PSD, and the temporal ACF. Moreover, we will describe how to derive an SOC channel simulator from the reference model. To compute the main parameters of the SOC channel simulator, we apply the GMEA [6] and the BRSM [7]. The PDF of the envelope and the temporal ACF will be visualized assuming NLOS and LOS propagation conditions. It will be shown that the most important statistical properties of the SOC channel simulator match very closely the ones of the reference channel model. The excellent fitting demonstrates that the reference channel model can be approximated by an SOC channel simulator using a finite number of cisoids. It also indicates that the GMEA and the BRSM are efficient parameter computation methods for designing indoor SOC channel simulators. When comparing the two methods, we find that the BRSM is better regarding the approximation of the temporal ACF.

The rest of the paper is organized as follows. Section II describes the geometrical scattering model for indoor propagation environments. Section III presents a new indoor reference channel model and its statistical characterization in form of the PDF of the AOA, the Doppler PSD, and the temporal ACF. Section IV shows how to derive an SOC channel simulator from the reference model. Numerical results are presented in Section V under the assumption of LOS and NLOS propagation conditions. Finally, our conclusions are given in Section VI.

II. THE GEOMETRICAL INDOOR SCATTERING MODEL

We consider the geometrical indoor scattering model as illustrated in Fig. C.1. The rectangle in Fig. C.1 represents a room with length *A* and width *B*. The BS and the MS are arbitrarily placed in the horizontal plane of the room. We assume that the transmitter is the BS and the receiver is the MS. The MS moves along the *x* direction.

To guarantee that the derived indoor channel model can be applied to various indoor propagation scenarios, we first concentrate on a general geometrical indoor scattering model by comprehensively considering different possible scenarios.
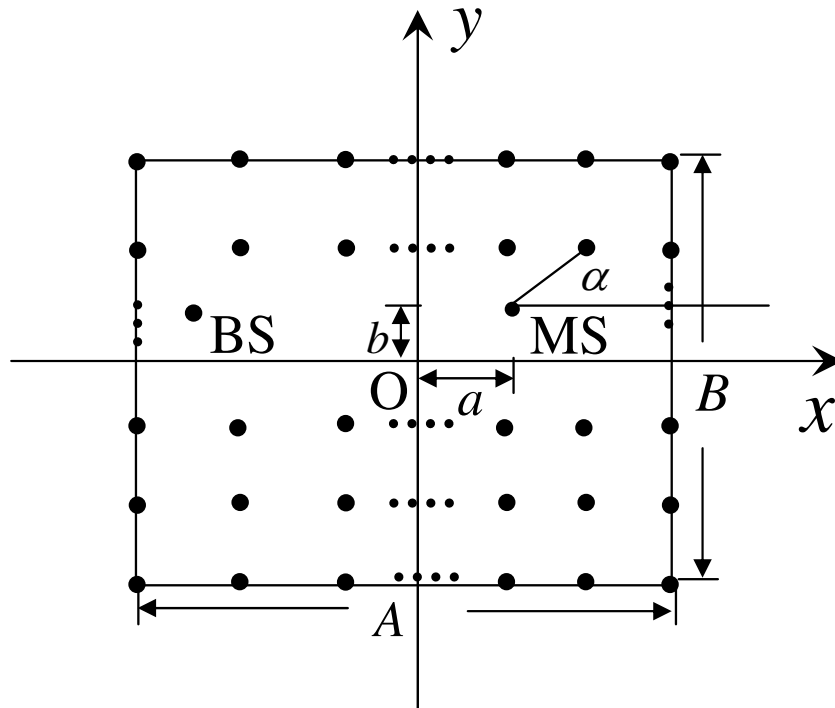
Figure C.1: Geometrical model for an indoor channel with local scatterers uniformly distributed within the 2D horizontal plane of the room. (The origin of the coordinate system is located at the center of the room.)

Therefore, we assume that there are an infinite number of local scatterers, which are uniformly distributed across the 2D horizontal plane of the room. It should be mentioned that such an indoor model acts only as a nonrealizable reference model, from which we can obtain different channel simulators with scatterers located in different positions.

III. THE INDOOR REFERENCE CHANNEL MODEL AND ITS STATISTICAL CHARACTERIZATION

In this section, we first give an introductory description of the reference channel model. Then, we analyze the PDF of the AOA and the Doppler PSD for the proposed indoor reference channel model.

A. Description of the Reference Channel Model

Taking the LOS component between the transmitter and the receiver into account, we can model the frequency-nonselective fading channel by a complex process

$$\mu_\rho(t) = \mu(t) + m_\rho(t), \tag{1}$$

where the process $\mu(t)$ represents the sum of the diffuse part and $m_\rho(t)$ denotes the LOS component. Here, the LOS component can be described by a time-variant deterministic process in the following form [12]

$$m_\rho(t) = \rho\, e^{j(2\pi f_\rho t + \theta_\rho)}. \tag{2}$$

The quantities ρ, f_ρ, and θ_ρ in (2) are constant, which denote the gain, the Doppler frequency, and the phase of the LOS component, respectively.

The diffuse part $\mu(t)$ representing the sum of an infinite number of scattered plane waves is modeled by a complex Gaussian random process. Usually, we assume that the real part and the imaginary part of $\mu(t)$ are zero-mean Gaussian processes, each having the variance $\sigma_\mu^2/2$. It turns out that the absolute value of $\mu_\rho(t)$, denoted by $\xi(t) = |\mu_\rho(t)|$, follows the Rice distribution [12]. Under NLOS conditions ($\rho = 0$), the PDF $p_\xi(z)$ of the envelope reduces to the Rayleigh distribution. According to the results in [5], the average power of $\mu_\rho(t)$ is time invariant and equal to $\sigma_{\mu_\rho}^2 = \sigma_\mu^2 + \rho^2$.

B. Derivation of the PDF of the AOA

Suppose that the location of all scatterers is described by $(\boldsymbol{x}, \boldsymbol{y})$. The position of

the MS is denoted by (a, b). As shown in Fig. C.1, the AOA α can be expressed as

$$
\alpha = \begin{cases}
\text{acrtan}\dfrac{y-b}{x-a}, & \text{if} \quad x \geq a, \\[2mm]
\pi + \text{acrtan}\dfrac{y-b}{x-a}, & \text{if} \quad x < a \text{ and } y \geq b, \\[2mm]
-\pi + \text{acrtan}\dfrac{y-b}{x-a}, & \text{if} \quad x < a \text{ and } y < b.
\end{cases}
\tag{3}
$$

For convenience of analysis, we shift the origin of the coordinate system in Fig. C.1 to the position where the MS is placed. The geometrical model in the new coordinate system is shown in Fig. C.2, where we have $x' = x - a$ and $y' = y - b$. In this figure, the location of the BS has been neglected since it has no influence on the statistical properties of the reference channel model. Thus, the AOA α in (3) can be rewritten as

$$
\alpha = \begin{cases}
\text{acrtan}\dfrac{y'}{x'}, & \text{if} \quad x' \geq 0, \\[2mm]
\pi + \text{acrtan}\dfrac{y'}{x'}, & \text{if} \quad x' < 0 \text{ and } y' \geq 0, \\[2mm]
-\pi + \text{acrtan}\dfrac{y'}{x'}, & \text{if} \quad x' < 0 \text{ and } y' < 0.
\end{cases}
\tag{4}
$$

As already mentioned in Section II, the scatterers are uniformly distributed within the 2D horizontal plane of the room. Therefore, the random variable $x' =$
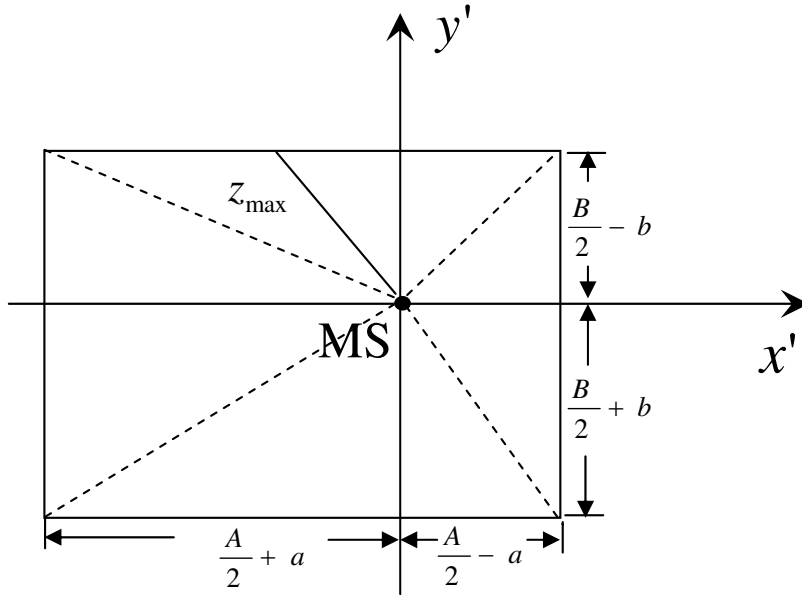
Figure C.2: Geometrical model for an indoor channel in the shifted coordinate system ($a \geq 0$ and $b \geq 0$).

$x - a$ is also uniformly distributed over $[-A/2 - a, A/2 - a]$, while $y' = y - b$ follows the uniform distribution over $[-B/2 - b, B/2 - b]$. Thus, the PDF $p_{x'}(x')$ of x' and the PDF $p_{y'}(y')$ of y' are given by

$$p_{x'}(x') = \frac{1}{A}, \qquad p_{y'}(y') = \frac{1}{B}. \tag{5a,b}$$

Assuming that the random variables x' and y' are independent, the joint PDF $p_{x'y'}(x', y')$ of x' and y' can be expressed as

$$p_{x'y'}(x', y') = p_{x'}(x') \cdot p_{y'}(y')$$
$$= \frac{1}{AB}. \tag{6}$$

The transformation of the Cartesian coordinates (x', y') into polar coordinates (z, α) gives the joint PDF $p_{z\alpha}(z, \alpha)$ of $z = \sqrt{x'^2 + y'^2}$ and the AOA $\alpha = \arg\{y'/x'\}$

$$p_{z\alpha}(z, \alpha) = \frac{z}{AB}. \tag{7}$$

After integrating the joint PDF $p_{z\alpha}(z, \alpha)$ over z, we obtain the PDF of the AOA α

$$p_\alpha(\alpha) = \frac{z_{\max}^2}{2AB}. \tag{8}$$

Here, $z_{\max}$ describes the distance from the origin to the boundary of the room, which is a function of A, B, and the AOA α. Using the geometrical relationships, we derive an expression for $z_{\max}$ in form of a piecewise function depending on the AOA ranges separated by the dashed lines in Fig. C.2. For brevity, we only present here the final expression for the PDF of the AOA, which can be found at the bottom of this page [see (9)].

$$p_\alpha(\alpha) = \begin{cases} \dfrac{(A-2a)^2}{8AB\cos^2(\alpha)}, & \text{if} \quad -\operatorname{acrtan}\dfrac{B+2b}{A-2a} < \alpha \leq \operatorname{acrtan}\dfrac{B-2b}{A-2a}, \\[3mm] \dfrac{(B-2b)^2}{8AB\sin^2(\alpha)}, & \text{if} \quad \operatorname{acrtan}\dfrac{B-2b}{A-2a} < \alpha \leq \pi - \operatorname{acrtan}\dfrac{B-2b}{A+2a}, \\[3mm] \dfrac{(A+2a)^2}{8AB\cos^2(\alpha)}, & \text{if} \quad \pi - \operatorname{acrtan}\dfrac{B-2b}{A+2a} < \alpha \leq \pi \\[3mm] & \text{or} \quad -\pi < \alpha \leq -\pi + \operatorname{acrtan}\dfrac{B+2b}{A+2a}, \\[3mm] \dfrac{(B+2b)^2}{8AB\sin^2(\alpha)}, & \text{if} \quad -\pi + \operatorname{acrtan}\dfrac{B+2b}{A+2a} < \alpha \leq -\operatorname{acrtan}\dfrac{B+2b}{A-2a}. \end{cases} \tag{9}$$

C. Derivation of the Doppler PSD

According to [5], the Doppler PSD $S_{\mu_\rho \mu_\rho}(f)$ of the process $\mu_\rho(t)$ can be presented as

$$S_{\mu_\rho \mu_\rho}(f) = S_{\mu\mu}(f) + \rho^2 \delta(f - f_\rho), \tag{10}$$

which is composed of the Doppler PSD $S_{\mu\mu}(f)$ of $\mu(t)$ and a weighted delta function at $f = f_\rho$ contributed by the LOS component. In the following, we will concentrate on deriving an analytical expression for the Doppler PSD $S_{\mu\mu}(f)$, so that the solution for the PSD $S_{\mu_\rho \mu_\rho}(f)$ is straightforward by making use of (10).

Since the AOA α is a random variable, it turns out that the corresponding Doppler frequency, defined by

$$f = f(\alpha) := f_{\max} \cdot \cos(\alpha), \tag{11}$$

is also a random variable. Here, $f_{\max}$ denotes the maximum Doppler frequency. According to the fundamental theorem of transformation of random variables [11, Eq. (5.16)], the PDF of the Doppler frequencies f, denoted by $p_f(f)$, can be calculated by means of the relation

$$p_f(f) = \sum_{v=1}^{m} \frac{p_\alpha(\alpha_v)}{|\frac{d}{d\alpha} f(\alpha)|_{\alpha=\alpha_v}}. \tag{12}$$

In (12), m is the number of solutions of the function in (11) within the interval $[-\pi, \pi)$. If $f \le |f_{\max}|$, we find two real-valued solutions within the interval, which are known as

$$\alpha_1 = -\alpha_2 = \text{arcos}(f/f_{\max}). \tag{13}$$

Therefore, we have $m = 2$ and the PDF in (12) can be expressed as

$$p_f(f) = \frac{p_\alpha(\alpha_1) + p_\alpha(\alpha_2)}{\sqrt{f_{\max}^2 - f^2}} \Bigg|_{\alpha_1=-\alpha_2=\text{arcos}(f/f_{\max})}. \tag{14}$$

In the reference channel model, we assume that the number of scatterers is infinite. Therefore, the Doppler PSD $S_{\mu\mu}(f)$ of the diffuse part $\mu(t)$ is continuous. The average power within an infinitesimal frequency interval df can be represented by $S_{\mu\mu}(f)df$. On the other hand, the incoming power between f and $f + df$ is

proportional to $p_f(f)df$. Thus, the following relation holds

$$S_{\mu\mu}(f)df \sim p_f(f)df. \tag{15}$$

We remind that the total power of the diffuse part $\mu(t)$ is equal to σ_μ^2. Thus, we have $\int_{-\infty}^{\infty} S_{\mu\mu}(f)df = \sigma_\mu^2$. After employing the property $\int_{-\infty}^{\infty} p_f(f)df = 1$, it follows

$$S_{\mu\mu}(f) = \sigma_\mu^2 \cdot p_f(f). \tag{16}$$

By taking (16) into account and using (9) and (14), we obtain the final result for the Doppler PSD $S_{\mu\mu}(f)$ of $\mu(t)$, which can be found in (17)

$$S_{\mu\mu}(f) = \begin{cases} \frac{(B^2+4b^2)\sigma_\mu^2 f_{\max}^2}{4AB(f_{\max}^2-f^2)^{3/2}}, & \text{if } -\frac{(A+2a)f_{\max}}{\sqrt{(A+2a)^2+(B+2b)^2}} < f \leq \frac{(A-2a)f_{\max}}{\sqrt{(A-2a)^2+(B+2b)^2}}, \\[3ex] \frac{[(B-2b)^2 f^2+(\pm A-2a)^2(f_{\max}^2-f^2)]\sigma_\mu^2 f_{\max}^2}{8ABf^2(f_{\max}^2-f^2)^{3/2}}, \\[2ex] \qquad\qquad \text{if } \frac{(\pm A-2a)f_{\max}}{\sqrt{(\pm A-2a)^2+(B\pm 2b)^2}} < f \leq \frac{(\pm A-2a)f_{\max}}{\sqrt{(\pm A-2a)^2+(B\mp 2b)^2}}, \\[3ex] \frac{[A-2(-1)^k a]^2\sigma_\mu^2 f_{\max}^2}{4ABf^2\sqrt{f_{\max}^2-f^2}}, & \text{if } \frac{[A-2(-1)^k a]f_{\max}}{\sqrt{[A-2(-1)^k a]^2+(B-2b)^2}} < (-1)^k f \leq f_{\max}, \quad k=0,1. \end{cases} \tag{17}$$

We can observe from (17) that the Doppler PSD $S_{\mu\mu}(f)$ tends to infinity at $f = \pm f_{\max}$. However, to avoid discussing the detail of $S_{\mu\mu}(f)$ at $f = \pm f_{\max}$, we follow the traditional notation using $|f| \leq f_{\max}$ instead of $|f| < f_{\max}$, which has been done by other publications, e.g. [12].

Thus, the Doppler PSD $S_{\mu_\rho\mu_\rho}(f)$ of $\mu_\rho(t)$ can easily be derived by substituting (17) into (10). From the $S_{\mu_\rho\mu_\rho}(f)$, we can directly obtain the ACF $r_{\mu_\rho\mu_\rho}(\tau) = E\{\mu_\rho^*(t)\mu_\rho(t+\tau)\}$ by computing the inverse Fourier transform of the Doppler PSD $S_{\mu_\rho\mu_\rho}(f)$, i.e.,

$$r_{\mu_\rho\mu_\rho}(\tau) = \int_{-\infty}^{\infty} S_{\mu_\rho\mu_\rho}(f) e^{j2\pi f\tau} df. \tag{18}$$

By taking (10) into consideration, we can express the temporal ACF $r_{\mu_\rho\mu_\rho}(\tau)$ [see (18)] in terms of the temporal ACF $r_{\mu\mu}(\tau)$ of $\mu(t)$ as follows

$$r_{\mu_\rho\mu_\rho}(\tau) = r_{\mu\mu}(\tau) + \rho^2 e^{j2\pi f_\rho \tau}. \tag{19}$$

Since no closed-form solution exists for the temporal ACF $r_{\mu\mu}(\tau) = \int_{-\infty}^{\infty} S_{\mu\mu}(f) e^{j2\pi f \tau} df$, this integral has to be solved numerically.

IV. THE INDOOR SOC CHANNEL SIMULATOR

Due to the infinite realization complexity of the reference model, this model cannot be used directly in system simulations. For the design and performance evaluation of indoor radio communication systems, fading channel simulators with low realization expenditure are desirable, by which the overall production cost and the simulation time can be reduced considerably.

In this section, we present a stochastic SOC channel simulator, which can be obtained from the reference model by applying the SOC principle [14]. The idea is to model the diffuse component $\mu(t)$ of a flat fading channel by a sum of N cisoids, i.e.,

$$\hat{\mu}(t) = \sum_{n=1}^{N} c_n e^{j(2\pi f_n t + \theta_n)}. \tag{20}$$

Here, c_n, f_n, and θ_n are called the gain, the Doppler frequency, and the phase of the nth propagation path, respectively. For a stochastic channel simulator, it is often assumed that the gains c_n and the Doppler frequencies f_n are constant, which can be determined by a parameter computation method in such a way that the statistical properties of the stochastic channel simulator are as close as possible to those of the reference channel model. The phases θ_n are independent, identically distributed random variables, which are uniformly distributed over $(0, 2\pi]$. Thus, we can model the stochastic SOC channel simulator by a random process of the form

$$\hat{\mu}_\rho(t) = \hat{\mu}(t) + m_\rho(t), \tag{21}$$

where the time-variant deterministic process $m_\rho(t)$ equals the LOS component in (2). The stochastic process $\hat{\mu}_\rho(t)$ can be interpreted as a family of sample functions depending on the phases θ_n. If we fix θ_n, e.g., by considering them as the outcomes of a random generator with a uniform distribution over $(0, 2\pi]$, then the stochastic channel simulator becomes a deterministic one, which can be used for system simulations.

A. Parameter Computation Methods
In the following, we apply two parameter computation methods, namely the GMEA [6] and the BRSM [7], to compute the SOC parameters c_n and f_n.

1) *The GMEA:* According to the GMEA, the gains c_n are defined as

$$c_n = \frac{\sigma_\mu}{\sqrt{N}}. \tag{22}$$

Due to the relation $f_n = f_{\max} \cdot \cos \alpha_n$, we can determine the Doppler frequencies f_n by finding the AOAs α_n that satisfy the following equation

$$\int_0^{\alpha_n} g_\alpha(\alpha)\, d\alpha = \frac{1}{2N}\left(n - \frac{1}{2}\right), \tag{23}$$

where $g_\alpha(\alpha) = [p_\alpha(\alpha) + p_\alpha(-\alpha)]/2$ is the even part of the PDF $p_\alpha(\alpha)$ of the AOA. Performing algebraic manipulations on (9) allows us to present the even part of the PDF $p_\alpha(\alpha)$ in the form shown in (24)

$$g_\alpha(\alpha) = \begin{cases} \dfrac{(A-2a)^2}{8AB\cos^2(\alpha)}, & \text{if } |\alpha| \leq \operatorname{acrtan}\frac{B-2b}{A-2a}, \\[2ex] \dfrac{1}{16AB}\cdot\left[\dfrac{(A-2a)^2}{\cos^2(\alpha)} + \dfrac{(B-2b)^2}{\sin^2(\alpha)}\right], & \text{if } |\alpha| > \operatorname{acrtan}\frac{B-2b}{A-2a} \text{ and } |\alpha| \leq \operatorname{acrtan}\frac{B+2b}{A-2a}, \\[2ex] \dfrac{B^2+4b^2}{8AB\sin^2(\alpha)}, & \text{if } |\alpha| > \operatorname{acrtan}\frac{B+2b}{A-2a} \text{ and } |\alpha| \leq \pi - \operatorname{acrtan}\frac{B+2b}{A+2a}, \\[2ex] \dfrac{1}{16AB}\cdot\left[\dfrac{(A+2a)^2}{\cos^2(\alpha)} + \dfrac{(B-2b)^2}{\sin^2(\alpha)}\right], & \text{if } |\alpha| > \pi - \operatorname{acrtan}\frac{B+2b}{A+2a} \text{ and } |\alpha| \leq \pi - \operatorname{acrtan}\frac{B-2b}{A+2a}, \\[2ex] \dfrac{(A+2a)^2}{8AB\cos^2(\alpha)}, & \text{if } |\alpha| > \pi - \operatorname{acrtan}\frac{B-2b}{A+2a} \quad \text{and} \quad |\alpha| \leq \pi. \end{cases} \tag{24}$$

2) *The BRSM:* According to the BRSM, the gains c_n and the Doppler frequencies f_n can be determined by the equations

$$c_n = \sigma_\mu \sqrt{\frac{g_\alpha(\alpha_n)}{\sum_{n=1}^{N} g_\alpha(\alpha_n)}}, \tag{25a}$$

$$f_n = f_{\max} \cdot \cos(\alpha_n), \tag{25b}$$

where $\alpha_n = \pi(n - \frac{1}{2})/N$.

B. Statistical Properties of the SOC Channel Simulator

It is shown in [14] that the PDF $p_{\hat{\xi}}(z)$ of the envelope $\hat{\xi} = |\mu_\rho(t)|$ has the following form

$$p_{\hat{\xi}}(z) = (2\pi)^2 z \int_0^\infty \left[\prod_{n=1}^{N} J_0(2\pi|c_n|x)\right] J_0(2\pi z x) J_0(2\pi \rho x) x\, dx, \tag{26}$$

which is completely determined by the number of cisoids N, the gains c_n, and the amplitude ρ of the LOS component. In (26), $J_0(\cdot)$ denotes the zeroth-order modified Bessel function of the first kind.

The temporal ACF of $\hat{\mu}_\rho(t)$, defined by $r_{\hat{\mu}_\rho \hat{\mu}_\rho}(\tau) = E\{\hat{\mu}_\rho^*(t)\hat{\mu}_\rho(t+\tau)\}$, is given by [5]

$$r_{\hat{\mu}_\rho \hat{\mu}_\rho}(\tau) = \sum_{n=1}^{N} c_n^2 e^{j2\pi f_n \tau} + \rho^2 e^{j2\pi f_\rho \tau}. \qquad (27)$$

V. NUMERICAL RESULTS

In this section, we will illustrate the main theoretical results by evaluating the Doppler PSD, the PDF of the envelope, and the temporal ACF of the reference model and the simulation model.

We consider a rectangular room with the length $A = 8\,\text{m}$ and the width $B = 5\,\text{m}$ as our indoor environment. All theoretical results were evaluated by choosing $\sigma_{\hat{\mu}_\rho}^2 = \sigma_\mu^2 + \rho^2 = 1$, $f_\rho = 65\,\text{Hz}$, $\theta_\rho = 0°$, and $f_{\max} = 91\,\text{Hz}$. The Rice factor $c_R = \rho^2/\sigma_\mu^2$ was chosen from the set $\{0,2,4\}$. The SOC channel simulator was designed with $N = 20$ cisoids. Its main parameters, i.e., the gains c_n and the Doppler frequencies f_n, were determined by applying the GMEA and the BRSM described in Subsection IV-A.

The theoretical results for the Doppler PSD $S_{\mu\mu}(f)$ [see (17)] of the channel's diffuse component $\mu(t)$ are presented in Fig.C.3 and C.4 for different MS loca-
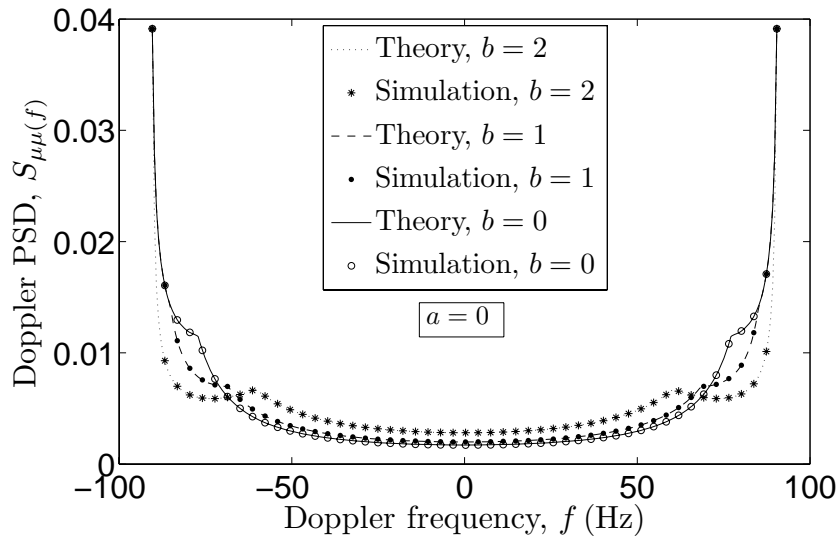
Figure C.3: Doppler PSD $S_{\mu\mu}(f)$ of the channel's diffuse component $\mu(t)$ for the case when the abscissa of the MS location equals zero ($A = 8$ $B = 5$, and $a = 0$).
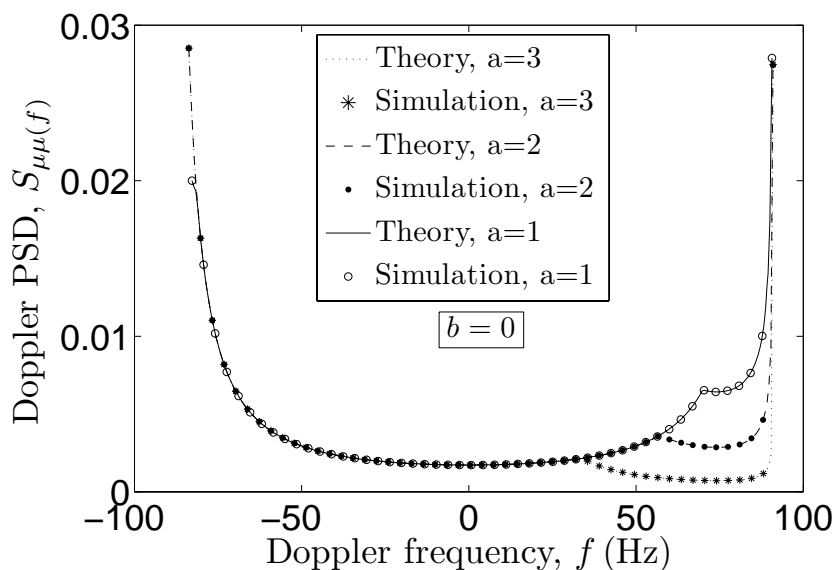
Figure C.4: Doppler PSD $S_{\mu\mu}(f)$ of the channel's diffuse component $\mu(t)$ for the case when the ordinate of the MS location is zero ($A = 8$, $B = 5$, and $b = 0$).

tions. With reference to (10), it becomes obvious that the Doppler PSD $S_{\mu_\rho\mu_\rho}(f)$ of the process $\mu_\rho(t)$ can be obtained from the graph of $S_{\mu\mu}(f)$ by adding a discrete Doppler spectral line located at $f = f_\rho$ with a weighting factor of ρ^2. By comparing the two figures, we may conclude that the Doppler PSD $S_{\mu\mu}(f)$ of the diffuse component is symmetrical if the abscissa of the MS location equals zero, i.e., $a = 0$, while it is not the case if the ordinate of the MS location equals zero. Moreover, it can be seen from Fig. C.3 that if $a = 0$, the Doppler PSD at $|f|$ close to $f_{\max}$ are the same for different values of b. This can be explained by the fact that, at the pole which is close to $\pm f_{\max}$, the Doppler PSD depends on the value of a, while it is independent on the value of b [see (17)].

Figure C.5 shows the Doppler PSD $S_{\mu\mu}(f)$ for different values of the room length A. The curve of the Doppler PSD resembles a U shape when the length A increases. The theoretical results illustrated in Figs. C.3–C.5 are also verified by simulations. In simulations, we generated scatterers located randomly in the 2D horizontal plane of the room. The horizontal (and vertical) locations of all scatterers in the shifted coordinate system have been determined as outcomes of a random generator with a uniform distribution over $[-A/2-a, A/2-a]$ (and $[-B/2-b, B/2-b]$). By making use of the relations (4) and (11), we can measure the distribution of the Doppler frequencies from which we can find the Doppler PSD by means of (16).

In Fig. C.6, we plot the envelope PDF $p_\xi(z)$ of the reference channel model by considering different values for the Rice factor c_R. As shown in this figure, under LOS conditions ($c_R \neq 0$), the PDF of the envelope follows the Rice distribution,
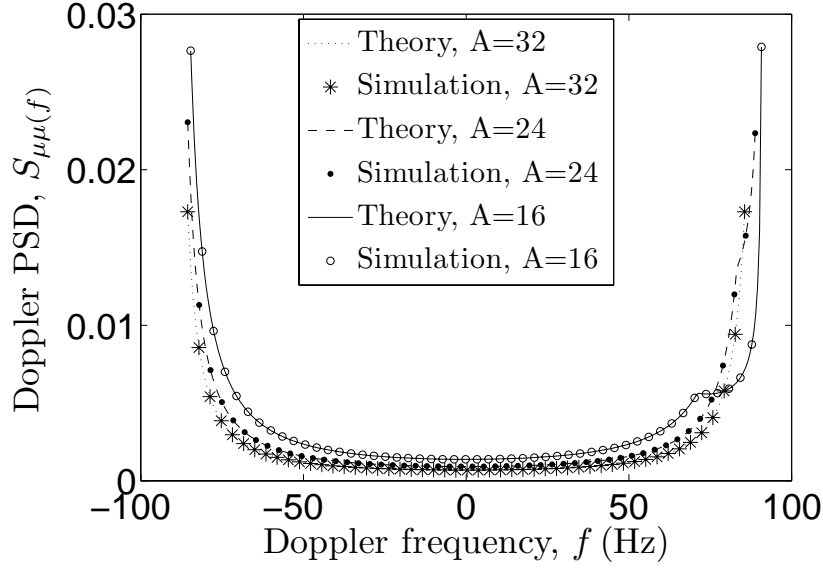
Figure C.5: Doppler PSD $S_{\mu\mu}(f)$ of the channel's diffuse component $\mu(t)$ for different values of room length A ($B = 4$, $a = 3$, and $b = 2$).
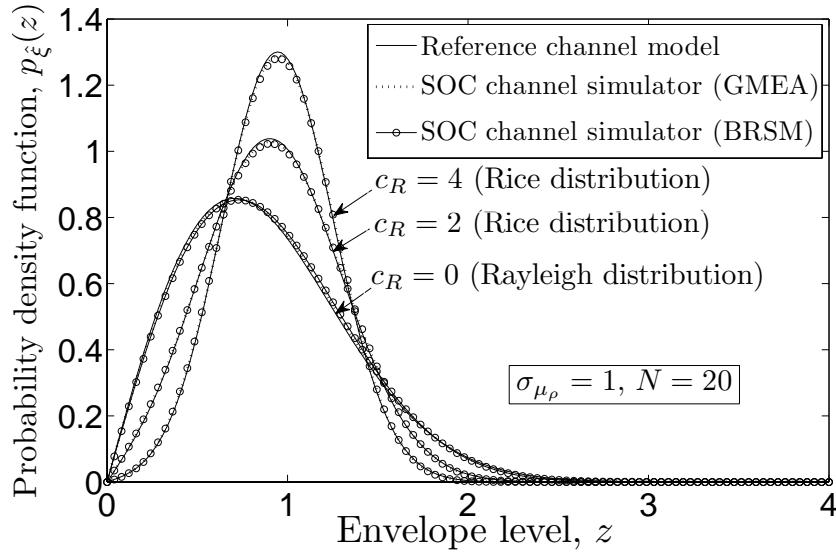
Figure C.6: Comparison between the theoretical envelope PDF $p_\xi(z)$ of the reference channel model and the envelope PDF $p_{\hat{\xi}}(z)$ of the SOC channel simulator designed with the GMEA and the BRSM.

while the envelope PDF reduces to the Rayleigh distribution for the NLOS case ($c_R = 0$). In Fig. C.6, we also present the theoretical envelope PDF $p_{\hat{\xi}}(z)$, introduced in (26), of the SOC channel simulator. Both parameter computation methods, i.e., the GMEA and the BRSM, have been applied to determine the gains c_n of the SOC channel simulator. It can be concluded from Fig. C.6 that the GMEA and the

BRSM are resulting in an excellent approximation $p_\xi(z) \approx p_{\hat\xi}(z)$.

In the case when the Doppler PSD $S_{\mu\mu}(f)$ is symmetrical, we compare the absolute value of the temporal ACF $|r_{\mu_\rho\mu_\rho}(\tau)|$ [see (19)] of the reference channel model with the one of the SOC channel simulator, denoted by $|r_{\hat\mu_\rho\hat\mu_\rho}(\tau)|$ [see (27)]. For the sake of clarity, we present the ACF $|r_{\hat\mu_\rho\hat\mu_\rho}(\tau)|$ in Fig.C.7 by applying the GMEA, while the corresponding ACF results obtained by using the BRSM are shown in Fig.C.8. Assuming the Doppler PSD $S_{\mu\mu}(f)$ is asymmetrical, a comparison between $|r_{\mu_\rho\mu_\rho}(\tau)|$ and $|r_{\hat\mu_\rho\hat\mu_\rho}(\tau)|$ by applying the GMEA is illustrated in Fig.C.9, while we plot the graphs of $|r_{\hat\mu_\rho\hat\mu_\rho}(\tau)|$ in Fig.C.10 for the BRSM. As depicted in Figs.C.7 and C.9, when the GMEA is applied, the graphs of $|r_{\hat\mu_\rho\hat\mu_\rho}(\tau)|$ match perfectly the ones of $|r_{\mu_\rho\mu_\rho}(\tau)|$ within the interval $[0, N/(8f_{\max})]$. It can be seen from Figs.C.8 and C.10 that the BRSM yields a good approximation $|r_{\hat\mu_\rho\hat\mu_\rho}(\tau)| \approx |r_{\mu_\rho\mu_\rho}(\tau)|$ for $\tau \in [0, N/(4f_{\max})]$. Thus, we can conclude that the BRSM outperforms the GMEA in terms of the evaluation of the ACF. We also confirm the correctness of the theoretical results presented in Figs.C.7–C.10 by simulations.
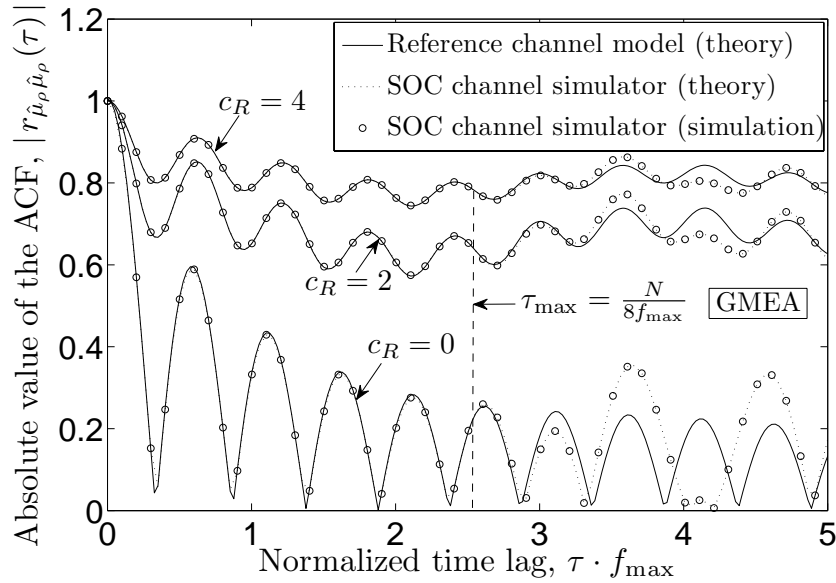
Figure C.7: Comparison between the ACF $r_{\mu_\rho\mu_\rho}(\tau)$ of the reference channel model and the ACF $r_{\hat\mu_\rho\hat\mu_\rho}(\tau)$ of the SOC channel simulator designed with the GMEA for the case when the Doppler PSD $S_{\mu\mu}(f)$ of the channel's diffuse component $\mu(t)$ is symmetrical ($a=0, b=1$).
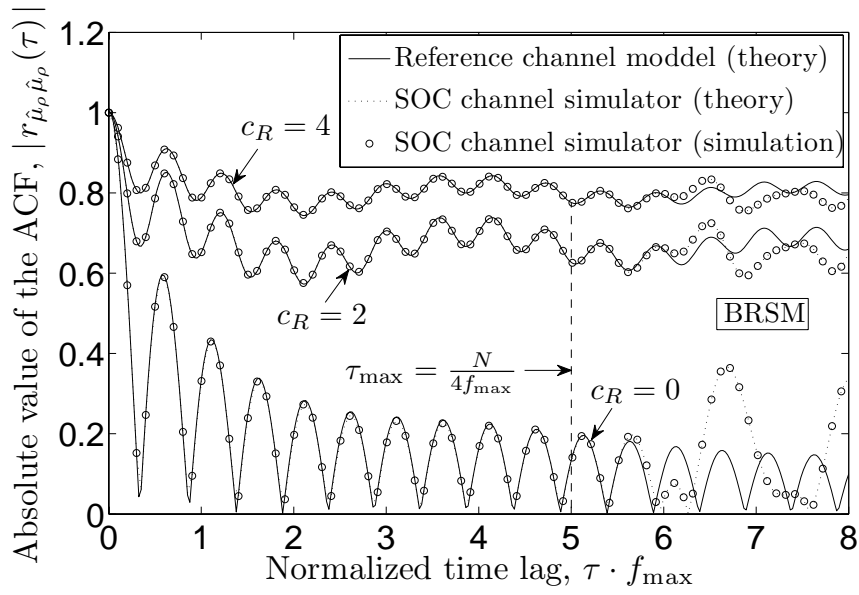
Figure C.8: Comparison between the ACF $r_{\mu_\rho \mu_\rho}(\tau)$ of the reference channel model and the ACF $r_{\hat{\mu}_\rho \hat{\mu}_\rho}(\tau)$ of the SOC channel simulator designed with the BRSM for the case when the Doppler PSD $S_{\mu\mu}(f)$ of the channel's diffuse component $\mu(t)$ is symmetrical ($a = 0, b = 1$).
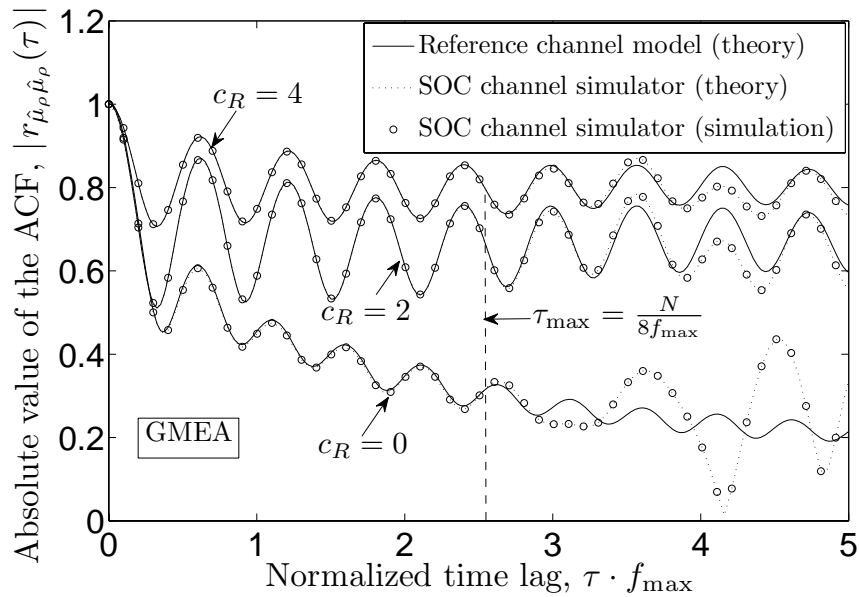
Figure C.9: Comparison between the ACF $r_{\mu_\rho \mu_\rho}(\tau)$ of the reference channel model and the ACF $r_{\hat{\mu}_\rho \hat{\mu}_\rho}(\tau)$ of the SOC channel simulator designed with the GMEA for the case when the Doppler PSD $S_{\mu\mu}(f)$ of the channel's diffuse component $\mu(t)$ is asymmetrical ($a = 2, b = 1$).
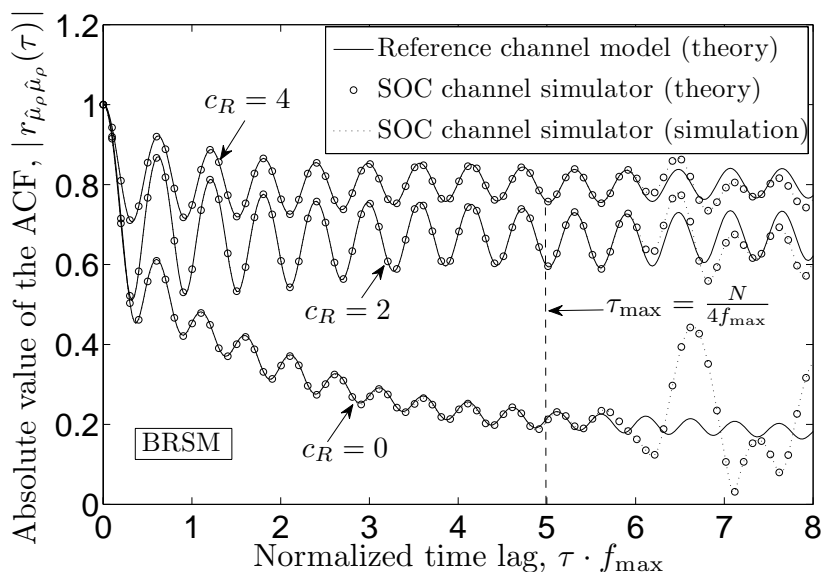
Figure C.10: Comparison between the ACF $r_{\mu_\rho \mu_\rho}(\tau)$ of the reference channel model and the ACF $r_{\hat{\mu}_\rho \hat{\mu}_\rho}(\tau)$ of the SOC channel simulator designed with the BRSM for the case when the Doppler PSD $S_{\mu\mu}(f)$ of the channel's diffuse component $\mu(t)$ is asymmetrical ($a = 2, b = 1$).

VI. CONCLUSION

In this paper, we have proposed a reference channel model for indoor propagation scenarios, where the LOS component has been taken into account. Analytical expressions have been derived for the PDF of the AOA, the even part of the PDF of the AOA, the Doppler PSD, and the temporal ACF. The obtained analytical results are not only important for theoretically studying the performance of indoor communication systems, but also indispensable for deriving efficient channel simulators.

It has been shown that the Doppler PSD of the diffuse component is symmetrical if the abscissa of the MS location equals zero, while it becomes asymmetrical if the ordinate of the MS location is equal to zero.

We have also shown in this paper how to derive an SOC channel simulator from a reference channel model. Two parameter computation methods—the GMEA and the BRSM have been applied to simulate indoor fading channels. It has been shown that the PDF of the envelope and the temporal ACF of the SOC channel simulator match perfectly the ones of the reference channel model.

REFERENCES

[1] G. J. Byers and F. Takawira. Spatially and temporally correlated MIMO channels: modeling and capacity analysis. *IEEE Trans. on Veh. Technol.*,

53(3):634–643, May 2004.

[2] G. D. Durgin, V. Kukshya, and T. S. Rappaport. Wideband measurements of angle and delay dispersion of outdoor and indoor peer–to–peer radio channels at 1920 MHz. *IEEE Trans. on Antennas Propag.*, 51(5):936–944, May 2003.

[3] R. B. Ertel and J. H. Reed. Angle and time of arrival statistics for circular and elliptical scattering models. *IEEE J. Select. Areas Commun.*, 17(11):1829–1840, Nov. 1999.

[4] S. Guerin. Indoor wideband and narrowband propagation measurements around 60.5 GHz in an empty and furnished room. In *Proc. 46th Vehicular Technology Conference, VTC-1996*, pages 160–164. Atlanta, USA, Apr./May 1996.

[5] C. A. Gutiérrez. *Channel Simulation Models for Mobile Broadband Wireless Communication Systems*. Doctoral Dissertations, Kristiansand: University of Agder, 2009.

[6] C. A. Gutiérrez and M. Pätzold. Sum-of-sinusoids-based simulation of flat fading wireless propagation channels under non-isotropic scattering conditions. In *Proc. 50th Global Communication Conference, GLOBECOM 2007*, pages 3842–3846. Washington, D.C., USA, Nov. 2007.

[7] C. A. Gutiérrez and M. Pätzold. The Riemann sum method for the design of sum-of-cisoids simulators for Rayleigh fading channels in non-isotropic scattering environments. In *Proc. 1st Workshop on Mobile Computing and Networking Technologies, WMCNT 2009*. St. Petersburg, Russia, Oct. 2009.

[8] L. Jiang and S. Y. Tan. Geometrically based statistical channel models for ourdoor and indoor propagation. *IEEE Trans. on Veh. Technol.*, 56(6):3587–3593, Nov. 2007.

[9] Y. Ma and M. Pätzold. Wideband two-ring MIMO channel models for mobile-to-mobile communications. In *Proc. 10th International Symposium on Wireless Personal Multimedia Communications, WPMC 2007*, pages 380–384. Jaipur, India, Dec. 2007.

[10] Y. Oda, K. Tsunekawa, and M. Hata. Geometrically based directional channel model for urban mobile communication systems. In *Proc. Antennas and Propagation for Wireless Communications, IEEE-APS 2000*, pages 87–90. Waltham, Massachusetts, Nov. 2000.

[11] A. Papoulis and S. U. Pillai. *Probability, Random Variables and Stochastic Processes*. New York: McGraw-Hill, 4th edition, 2002.

[12] M. Pätzold. *Mobile Fading Channels*. Chichester: John Wiley & Sons, 2002.

[13] M. Pätzold and B. O. Hogstad. A space-time channel simulator for MIMO channels based on the geometrical one-ring scattering model. *Wireless Communications and Mobile Computing, Special Issue on Multiple-input Multiple-output (MIMO) Communications*, 4(7):727–737, Nov. 2004.

[14] M. Pätzold and B. Talha. On the statistical properties of sum-of-cisoids-based mobile radio channel models. In *Proc. 10th International Symposium on Wireless Personal Multimedia Communications, WPMC 2007*, pages 394–400. Jaipur, India, Dec. 2007.

[15] S. Qu. An analysis for probability distribution of Doppler shift in three-dimensional mobile radio environments. *IEEE Trans. on Veh. Technol.*, 58(4):1634–1639, May 2009.

[16] H. Xu, V. Kukshya, and T. S. Rappaport. Spatial and temporal characteristics of 60–GHz indoor channels. *IEEE J. Select. Areas Commun.*, 20(3):620–630, Apr. 2002.

[17] E. D. Zand, K. Pahlavan, and J. Beneat. Measurement of TOA using frequency domain characteristics for indoor geolocation. In *Proc. 14th Personal, Indoor and Mobile Radio Communications, PIMRC 2003*, pages 2213–2217. Beijing, China, Sep. 2003.

Appendix D

Paper IV

Statistical Modeling and Experimental Verification of Wideband Indoor Radio Propagation Channels

Yuanyuan Ma and Matthias Pätzold

Department of Information and Communication Technology

Faculty of Engineering and Science, University of Agder

Servicebox 509, NO-4898 Grimstad, Norway

E-mails: {yuanyuan.ma, matthias.paetzold}@uia.no

Abstract — **This paper focuses on the modeling, simulation, and experimental verification of wideband single-input single-output (SISO) mobile fading channels for indoor propagation environments. The indoor reference channel model is derived from a geometrical rectangle scattering model, which consists of an infinite number of scatterers exponentially distributed over the two-dimensional (2D) horizontal plane of a rectangular room. Analytical expressions are derived for the probability density function (PDF) of the angle of arrival (AOA), the power delay profile (PDP), and the frequency correlation function (FCF). An efficient sum-of-cisoids (SOC) simulator is obtained from the non-realizable reference channel model by employing the SOC principle. It is shown that the SOC channel simulator approximates the reference with respect to the FCF. The SOC channel simulator enables to evaluate the performance of wideband indoor wireless communication systems with reduced realization expenditure. Moreover, the validity of the derived indoor channel model is confirmed by measurements.**

I. INTRODUCTION

Recent years, indoor wireless communications has captured more and more attentions due to the various emerging indoor services deployed by personal communication systems [26, 15], wireless local area networks [23, 6] and wireless private branch exchanger [19]. In order to design an efficient indoor wireless communication system and predict accurately its system performance, a prerequisite is to develop an appropriate indoor channel model describing precisely underlying propagation characteristics.

To assist the indoor channel characterization and modeling, numerous measurement tests have been conducted under a variety of indoor situations such as offices, corridors, buildings, and factories. The obtained measurement results have been reported in literature at various frequency bands, such as 900 MHz [1, 3, 37],

1.5 GHz [34, 40], 4-5.5 GHz [12, 35], 17-18 GHz [5, 35], and 60 GHz [5, 24, 43].
Based on these measurements results, many empirical statistical channel models [9,
10, 37, 42, 43] have been developed for the simulation and performance analysis
of various indoor communication systems. The advantage of statistical models is
that they are capable of characterizing realistic fading behaviors since these model
are based on real-world measurements. By changing their channel parameters, the
developed statistical models can be employed to simulate other indoor propagation
channels. However, to determine appropriate parameters for different propagation
scenarios, extensive new measurement data are required, which is time consum-
ing and leads to a high channel implementation cost. Alternatively, an approach
based on ray-tracing techniques [4, 17, 36, 38] was used to simulate indoor propa-
gation channels. Ray-tracing channel models [13, 16, 20, 39] can efficiently capture
fading behaviors of specified indoor environments. Many developed ray-tracing
channel models have shown good agreement with measured channel characteris-
tics [2, 18, 33]. However, ray-tracing models greatly depends on the physical lay-
outs and materials through which signals propagate, e.g., walls, floors, and ceilings.
In addition, the main drawback of ray-tracing models comes from their computa-
tional cost, which relies on the size and complexity of the geographic database as
well as the interaction order in a ray search. Therefore, the tradeoff between the
prediction accuracy and the simulation efficiency has to be taken into account when
modeling indoor propagation channels by means of ray-tracing techniques.

The two main types of indoor channel models, i.e., empirical statistical channel
models and ray-tracing channel models, have their own strengths and limitations
when they are applied to characterize radio propagation channels for indoor envi-
ronments. To cope with drawbacks mentioned above, a geometrical channel model
has been proposed in [14] for indoor environments, where it is assumed that scat-
terers are randomly distributed around the BS within a circle. However, the model
developed in [14] is only applicable to the indoor environments where the distance
between the BS and the scatterers follows the exponential distribution. Such an
assumption limits applications of the model in the indoor channel modeling. In ad-
dition, it is not reasonable to represent an indoor scatterer region, such as offices
and corridors, by a circle. In contrast, a rectangle is a more appropriate geometry
shape to model various indoor propagation environments. A geometrical rectan-
gle scattering model has been used in [22] to characterize narrowband indoor radio
propagation channels. However, to the author's knowledge, modeling wideband in-
door radio channels by employing an appropriate geometrical scattering model is
still an open problem.

Motivated by the scarcity of proper wideband geometry-based indoor channel models, in this paper, we are concerned with developing a wideband indoor geometry-based channel model by further extending the geometrical rectangle scattering model [22] with respect to frequency selectivity. We concentrate on the statistical characterization of a wideband reference channel model, which is based on the assumption that an infinite number of scatterers is exponentially distributed over the 2D horizontal plane of a rectangular room. In contrast to [31, 30, 21], we apply a different procedure to study the statistical properties of the resulting reference channel model, which requires no knowledge of the complex channel gain. We obtain the analytical expressions for the PDF of the AOA, the PDP, and the FCF. Moreover, we derive an SOC channel simulator from the reference model. It is shown that the designed SOC channel simulator matches the underlying reference model with respect to the FCF. The obtained SOC channel simulator enables to simulate indoor mobile fading channels with reduced realization expenditure. At the end, we demonstrate the validity of the proposed reference channel model by comparing its mean access delay and the root mean square (RMS) delay spread with empirical ones measured form corridors and offices [25].

The rest of the paper is structured as follows. In Section II, we briefly describe the 2D geometrical scattering model. Section III analyzes the statistical characteristics of the wideband reference channel model in the form of the PDF of the AOA, the PDP and the FCF. Section IV introduces the procedure of designing the wideband indoor SOC channel simulator. Numerical and simulation results are presented in Section V to confirm the correctness of the derived theoretical results. Section VI validates the validity of the derived indoor channel model by comparing its channel statistics with the empirical ones measured from real-world channels. Finally, Section 7 draws the conclusion.

II. THE GEOMETRICAL INDOOR SCATTERING MODEL

This section briefly describes the geometrical scattering model, which was first proposed in [22] to characterize indoor propagation scenarios. Although a room has three dimensional, we only consider its 2D horizontal plane where all local scatterers, the base station (BS) and the mobile station (MS) are located. As shown in Fig. D.1, the rectangle represents a 2D horizontal plane of a room. Its length and width are denoted by A and B, respectively. The BS is considered as the transmitter, while the MS is the receiver. It is also assumed that the MS moves along the x direction. Moreover, we consider single bounce scattering, which means that plane waves emitted from the BS are only bounced once by scatterers before reaching the MS. The black nodes in Fig. D.1 represent local scatterers. In real world,
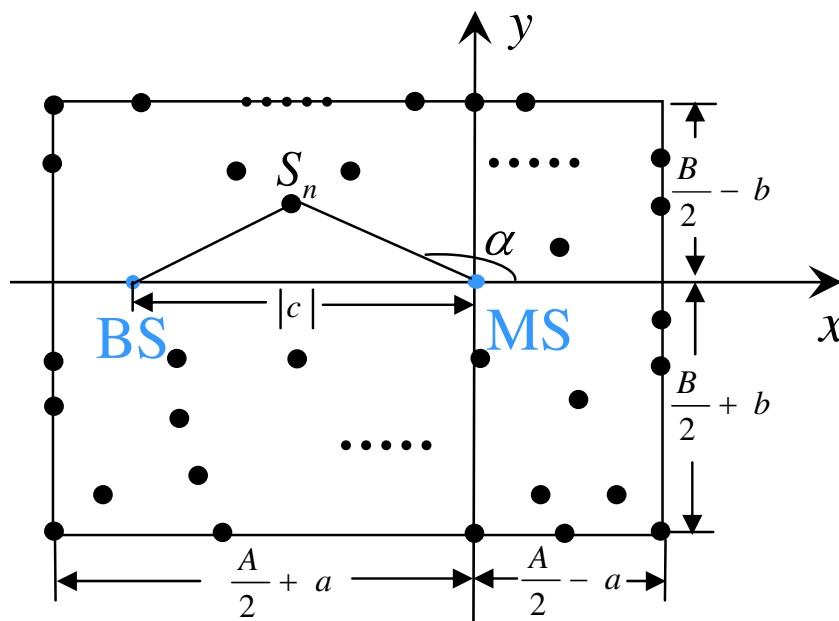
Figure D.1: Geometrical indoor scattering model with local scatterers S_n exponentially distributed over the 2D horizontal plane of the room ($a \geq 0$ and $b \geq 0$).

the number of scatterers and their locations differ from one propagation scenario to another. To avoid studying fading characteristics for a specific indoor propagation scenario characterized by a finite number of scatterers, we focus on a general statistical model that results from averaging over all possible propagation scenarios. Therefore, we assume that an infinite number of scatterers is exponentially distributed over the 2D horizontal plane of the room. Such a model acts here as a non-realizable stochastic reference model. From the reference channel model, efficient channel simulators with low realization expenditure can be easily derived by making use of the SOC principle [32].

III. STATISTICAL CHARACTERIZATION OF THE REFERENCE CHANNEL MODEL

This section deals with studying the statistical properties of the proposed indoor wideband reference channel model. The PDF of the AOA, the PDP, and the FCF are of special interest.

It is shown in Fig. D.1 that the BS is placed at the position $(c, 0)$ $(c \leq 0)$, while the MS is located at the origin of the coordinate system. The AOA is described by α. As already mentioned in Section 2, the scatterers are exponentially distributed within the 2D horizontal plane of the room. Therefore, the random variable x is exponentially distributed over $[-A/2 - a, A/2 - a]$, while y follows the exponential distribution over $[-B/2 - b, B/2 - b]$. Thus, the PDF $p_x(x)$ of x and the PDF $p_y(y)$

of y are given by

$$p_x(x) = P_1 \cdot e^{-w_1 \cdot x}, \qquad p_y(y) = P_2 \cdot e^{-w_2 \cdot y}, \qquad (1a,b)$$

where

$$P_1 = \frac{w_1}{e^{(\frac{A}{2}+a) \cdot w_1} - e^{-(\frac{A}{2}-a) \cdot w_1}}, \qquad (2a)$$

$$P_2 = \frac{w_2}{e^{(\frac{B}{2}+b) \cdot w_2} - e^{-(\frac{B}{2}-b) \cdot w_2}}, \qquad (2b)$$

Under the assumption that the random variables x and y are independent, the joint PDF $p_{xy}(x,y)$ of x and y can be expressed as

$$p_{xy}(x,y) = p_x(x) \cdot p_y(y) = P_1 \cdot P_2 \cdot e^{-(w_1 \cdot x + w_2 \cdot y)}. \qquad (3)$$

The position of scatterers is described using the polar coordinates by (z, α). According to [22], the joint PDF $p_{z\alpha}(z, \alpha)$ of z and α can be expressed as

$$p_{z\alpha}(z, \alpha) = z \cdot P_1 \cdot P_2 \cdot e^{-z[w_1 \cdot \cos(\alpha) + w_2 \cdot \sin(\alpha)]}. \qquad (4)$$

Let D be the overall plane wave traveling distance from the BS to the MS via a single scatterer, then D is given by

$$D = z + \sqrt{z^2 - 2cz\cos\alpha + c^2}. \qquad (5)$$

We now focus on finding the joint PDF of the distance D and the AOA α from (4). For this purpose, we introduce the auxiliary random variable $\theta = \alpha$. Solving the system of equations determined by (5) and $\theta = \alpha$ gives us the following solution

$$\alpha = \theta, \qquad (6a)$$

$$z = \frac{D^2 - c^2}{2(D - c\cos\theta)}. \qquad (6b)$$

By applying the fundamental theorem of transformation of random variables [27, p. 201], the joint PDF $p_{D\theta}(D, \theta)$ of the distance D and the auxiliary random variable θ is given by

$$p_{D\theta}(D, \theta) = |J(D, \theta)| \cdot p_{z\alpha}\left(\frac{D^2 - c^2}{2(D - c\cos\theta)}, \alpha\right), \qquad (7)$$

where

$$J(D,\theta) = \begin{vmatrix} \dfrac{\partial \alpha}{\partial D} & \dfrac{\partial \alpha}{\partial \theta} \\[2ex] \dfrac{\partial z}{\partial D} & \dfrac{\partial z}{\partial \theta} \end{vmatrix} = -\frac{D^2 - 2Dc\cos\theta + c^2}{2(D - c\cos\theta)^2} \tag{8}$$

denotes the Jacobian determinant of the inverse transformation. Substituting (8) into (7) and considering (4), we find the expression for the joint PDF $p_{D\theta}(D,\theta)$. Due to $\boldsymbol{\theta} = \boldsymbol{\alpha}$, the joint PDF $p_{D\alpha}(D,\alpha)$ can be directly expressed using the joint PDF $p_{D\theta}(D,\theta)$ by replacing θ in (7) by α. Finally, we have

$$p_{D\alpha}(D,\alpha) = \frac{P_1 \cdot P_2 \cdot [D^2 - 2cD\cos(\alpha) + c^2] \cdot (D^2 - c^2)}{4[D - c\cos(\alpha)]^3} \cdot e^{-\frac{[w1 \cdot \cos(\alpha) + w2 \cdot \sin(\alpha)] \cdot (D^2 - c^2)}{2 \cdot [D - c \cdot \cos(\alpha)]}}. \tag{9}$$

A. The PDF of the AOA

In this subsection, we are concerned with the derivation of the PDF of the AOA from (9). For this purpose, we divide all propagation delays, defined as,

$$\tau' = \frac{D - |c|}{c_0}, \tag{10}$$

where c_0 denotes the speed of light, into $\mathscr{L}$ subintervals as follows

$$I_\ell = \begin{cases} [0, \frac{\tau_1' + \tau_2'}{2}), & \text{if} \quad \ell = 1, \\[2ex] [\frac{\tau_{\ell-1}' + \tau_\ell'}{2}, \frac{\tau_\ell' + \tau_{\ell+1}'}{2}), & \text{if} \quad \ell = 2, 3, \ldots, \mathscr{L} - 1, \\[2ex] [\frac{\tau_{\mathscr{L}-1}' + \tau_{\mathscr{L}}'}{2}, \tau_{\max}'), & \text{if} \quad \ell = \mathscr{L}. \end{cases} \tag{11}$$

Here, $\tau_{\max}'$ is the maximum propagation delay, and τ_ℓ' denotes the propagation delay of the ℓth path $(\ell = 1, 2, \ldots, \mathscr{L})$. The PDF of the AOA related to the propagation delay $\tau' \in I_\ell$ can be obtained from the joint PDF $p_{D\alpha}(D,\alpha)$ as follows

$$p_{\alpha|\tau' \in I_\ell}(\alpha) = \int\limits_{D \in I_D} p_{D\alpha}(D,\alpha) dD. \tag{12}$$

The value $D \in \boldsymbol{I_D}$ in (12) must satisfy the following two conditions: i) $D \leq D_{\max}(\alpha)$ and ii) $(D - |c|)/c_0 \in I_\ell$. Here, $D_{\max}(\alpha)$ denotes the maximum traveling distance of the plane wave reaching the receiver antenna under the AOA α.

After carrying out some algebraic manipulations, we obtain the PDF $p_{\alpha|\tau' \in I_\ell}(\alpha)$ as follows

$$
p_{\alpha|\tau' \in I_\ell}(\alpha) = P_1 \cdot P_2 \cdot \left\{ \frac{(c^2 - D^2) \cdot [w1 \cdot \cos(\alpha) + w2 \cdot \sin(\alpha)] - 2[D - c \cdot \cos(\alpha)]}{2[w1 \cdot \cos(\alpha) + w2 \cdot \sin(\alpha)]^2 [D - c \cdot \cos(\alpha)]} \right.
$$

$$
\left. \cdot \ e^{-\frac{[w1 \cdot \cos(\alpha) + w2 \cdot \sin(\alpha)] \cdot (D^2 - c^2)}{2 \cdot [D - c \cdot \cos(\alpha)]}} \right\} \Bigg|_{f_1(\alpha)}^{f_2(\alpha)} .
$$

where

$$
f_1(\alpha) = \min\left(D_{\max}(\alpha), \frac{(\tau'_{\ell-1} + \tau'_\ell) \cdot c_0}{2} + |c| \right), \tag{13a}
$$

$$
f_2(\alpha) = \min\left(D_{\max}(\alpha), \frac{(\tau'_\ell + \tau'_{\ell+1}) \cdot c_0}{2} + |c| \right), \tag{13b}
$$

and, as proved in Appendix D.A, $D_{\max}$ is given by

$$
D_{\max}(\alpha) = \begin{cases}
\dfrac{A - 2a}{2\cos(\alpha)} + \sqrt{\left[\dfrac{A - 2a}{2\cos(\alpha)}\right]^2 - c(A - 2a) + c^2}, \\[2em]
\qquad\qquad \text{if} \quad -\operatorname{acrtan}\dfrac{B + 2b}{A - 2a} < \alpha \le \operatorname{acrtan}\dfrac{B - 2b}{A - 2a}, \\[3em]
\dfrac{B - 2b}{2\sin(\alpha)} + \sqrt{\left[\dfrac{B - 2b}{2\sin(\alpha)}\right]^2 - c(B - 2b)\cot(\alpha) + c^2}, \\[2em]
\qquad\qquad \text{if} \quad \operatorname{acrtan}\dfrac{B - 2b}{A - 2a} < \alpha \le \pi - \operatorname{acrtan}\dfrac{B - 2b}{A + 2a}, \\[3em]
\dfrac{A + 2a}{2\cos(\alpha)} + \sqrt{\left[\dfrac{A + 2a}{2\cos(\alpha)}\right]^2 + c(A + 2a) + c^2}, \\[2em]
\qquad\qquad \text{if} \quad \pi - \operatorname{acrtan}\dfrac{B - 2b}{A + 2a} < \alpha \le \pi \text{ or } -\pi < \alpha \le -\pi + \operatorname{acrtan}\dfrac{B + 2b}{A + 2a}, \\[3em]
\dfrac{B + 2b}{2\sin(\alpha)} + \sqrt{\left[\dfrac{B + 2b}{2\sin(\alpha)}\right]^2 + c(B + 2b)\cot(\alpha) + c^2}, \\[2em]
\qquad\qquad \text{if} \quad -\pi + \operatorname{acrtan}\dfrac{B + 2b}{A + 2a} < \alpha \le -\operatorname{acrtan}\dfrac{B + 2b}{A - 2a}.
\end{cases}
\tag{14}
$$

Finally, the overall PDF of the AOA, denoted by $p_\alpha(\alpha)$, is given by

$$p_{\boldsymbol{\alpha}(\alpha)} = \sum_{\ell=1}^{\mathscr{L}} p_{\boldsymbol{\alpha}|\tau' \in I_\ell}(\alpha). \tag{15}$$

B. The PDP

The PDF of the distance D, denoted by $p_D(D)$, can be calculated via the following relation

$$p_D(D) = \int_\alpha p_{D\alpha}(D,\alpha)d\alpha. \tag{16}$$

Solving the integral in (16) over α [see (B.9) in Appendix D. B], we finally find the analytical expression for the PDF of the traveling distance D, which is shown as follows

$$p_D(D) = \begin{cases} g_2(-\pi,\pi), & \text{if} \quad |c| \le D \le D_4, \\[2mm] g_2(-\pi,\alpha_1) + g_2(\alpha_2,\pi), & \text{if} \quad D_4 < D \le D_8, \\[2mm] g_2(-\pi,\alpha_3) + g_2(\alpha_4,\alpha_1) + g_2(\alpha_2,\pi), & \text{if} \quad D_8 < D \le D_1, \\[2mm] g_2(-\pi,\alpha_3) + g_2(\alpha_4,\alpha_5) + g_2(\alpha_6,\alpha_1) + g_2(\alpha_2,\pi), & \text{if} \quad D_1 < D \le D_2, \\[2mm] g_2(-\pi,\alpha_3) + g_2(\alpha_4,\alpha_5) + g_2(\alpha_2,\pi), & \text{if} \quad D_2 < D \le D_3, \\[2mm] g_2(-\pi,\alpha_3) + g_2(\alpha_2,\pi), & \text{if} \quad D_3 < D \le D_6, \\[2mm] g_2(\alpha_8,\alpha_3) + g_2(\alpha_2,\alpha_7), & \text{if} \quad D_6 < D \le D_5, \\[2mm] g_2(\alpha_8,\alpha_3), & \text{if} \quad D_5 < D \le D_7, \end{cases} \tag{17}$$

where

$$g_2(m,n) = \int_m^n p_{D\alpha}(D,\alpha)d\alpha, \tag{18a}$$

$$\alpha_{1,2} = 2\arctan\frac{D^2-c^2 \mp \sqrt{(D^2-c^2)^2-(B-2b)^2(D^2-c^2)}}{(B-2b)(d+c)}, \tag{18b}$$

$$\alpha_{3,4} = -2\arctan\frac{(D^2-c^2) \pm \sqrt{(D^2-c^2)^2-(B+2b)^2(D^2-c^2)}}{(B+2b)(d+c)}, \tag{18c}$$

$$\alpha_{5,6} = \mp \arccos \frac{(A-2a)D}{(A-2a)c+D^2-c^2}, \qquad (18d)$$

$$\alpha_{7,8} = \pm \arccos \frac{(A+2a)D}{(A+2a)c-(D^2-c^2)}. \qquad (18e)$$

Taking the relation between the propagation delay τ' and the traveling distance D in (10) into account and applying the fundamental theorem of transformation of random variables [27, p. 201], we can express the PDF of the delay τ' as

$$p_{\tau'}(\tau') = c_0 \cdot p_D(c_0 \cdot \tau' + |c|). \qquad (19)$$

Here, $p_D(c_0 \cdot \tau' + |c|)$ has a similar form as (17). One only needs to replace D in (17) by the term $c_0 \cdot \tau' + |c|$. For brevity, the expression for $p_D(c_0 \cdot \tau' + |c|)$ is not presented here. Let the total power of the reference model be denoted by σ_0^2, and let $S_{\tau'}(\tau')$ represent the PDP. It follows that $\int_0^\infty S_{\tau'}(\tau')\,d\tau' = \sigma_0^2$. By taking the property $\int_0^\infty p_{\tau'}(\tau')d\tau' = 1$ into account, the following relation holds

$$S_{\tau'}(\tau') = \sigma_0^2 \cdot p_{\tau'}(\tau'). \qquad (20)$$

C. The FCF

According to the Wiener Khinchine theorem, the PDP and the FCF form a Fourier transform pair. The inverse Fourier transform of the PDP gives us the FCF $r_{\tau'}(v')$, i.e.,

$$r_{\tau'}(v') = \int_0^\infty S_{\tau'}(\tau')e^{j2\pi v'\tau'}\,d\tau'. \qquad (21)$$

Substituting (20) in (21) and taking (19) into account result finally in the expression for the FCF, which is given by

$$r_{\tau'}(v') = c_0\sigma_0^2 \int_0^\infty p_D(c_0 \cdot \tau' + |c|)e^{j2\pi v'\tau'}\,d\tau'. \qquad (22)$$

Since no closed-form solution exists, the integral above has to be solved numerically.

IV. DESIGN OF THE SOC CHANNEL SIMULATOR

This section deals with the design of the stochastic SOC channel simulator [32, 29]. Suppose that the time-variant impulse response of the wideband SOC channel simulator, consisting of $\mathscr{L}$ discrete propagation paths, can be formulated as

$$\hat{h}(\tau',t) = \sum_{\ell=0}^{\mathscr{L}-1} a_\ell \, \hat{\mu}_\ell(t) \, \delta(\tau' - \tau'_\ell). \tag{23}$$

Here, the delay coefficients a_ℓ measure the square root of the power delay profile assigned to the ℓth discrete propagation delay. Therefore, we have [28, p. 282]

$$a_\ell = \sqrt{\int_{\tau' \in I_\ell} S_{\tau'}(\tau') \, d\tau'}, \qquad \ell = 1, 2, \ldots, \mathscr{L}. \tag{24}$$

The stochastic complex process $\hat{\mu}_\ell(t)$ in (23) denotes the time-variant impulse response of the ℓth propagation path. According to the SOC principle, such an stochastic process can be represented by a sum of N_ℓ cisoids as follows [32]

$$\hat{\mu}_\ell(t) = \sum_{n=1}^{N_\ell} c_{n,\ell} e^{j(2\pi f_{n,\ell} t + \theta_{n,\ell})}. \tag{25}$$

Here, the quantities $c_{n,\ell}$, $f_{n,\ell}$, and $\theta_{n,\ell}$ represent the Doppler coefficient, the Doppler frequency, and the Doppler phase of the ℓth path, respectively. The Doppler coefficients $c_{n,\ell}$ and the Doppler frequencies $f_{n,\ell}$ are constant, which can be determined by a proper parameter computation method. For example, according to the MMEA [8], the Doppler coefficients $c_{n,\ell}$ are given by

$$c_{n,\ell} = \frac{\sigma_0}{\sqrt{N_\ell}}. \tag{26}$$

Determining the Doppler frequencies $f_{n,\ell}$ are equivalent to determine the AOAs $\hat{\alpha}_{n,\ell}$ due to the following relation

$$f_{n,\ell} = f_{\max} \cdot \cos(\hat{\alpha}_{n,\ell}). \tag{27}$$

Here, $f_{\max}$ is called the maximum Doppler frequency. The AOAs $\hat{\alpha}_{n,\ell}$ are realizations of the random variable α. They can be obtained by the MMEA by solving the following equation

$$\int_{-\pi}^{\alpha_{n,\ell}} p_{\alpha|\tau' \in I_\ell}(\alpha) d\alpha = \frac{1}{N_\ell}(n - \frac{1}{4}), \qquad n = 1, 2, \ldots, N_\ell. \tag{28}$$

The Doppler phases $\theta_{n,\ell}$ of the stochastic SOC channel simulator are independent and identically distributed random variables, each following a uniform distribution over $[0,2\pi)$. Thus, the stochastic SOC channel simulator can be interpreted as a family of sample functions depending on the Doppler phases $\theta_{n,\ell}$. A sample function can be obtained from the stochastic channel simulator by fixing all Doppler phases. Such a sample function, which is also known as a deterministic channel simulator, can be used in simulations.

V. NUMERICAL RESULTS

This section illustrates the theoretical results given by (15) and (22). The correctness of the theoretical results will be verified by simulations. We will also show that the SOC channel simulator matches the reference channel model by evaluating the FCF. The validity of the proposed indoor channel model is also confirmed by measurements by studying the mean delay and the root mean square delay spread. In all simulations, we consider a room with length $A = 10\,\mathrm{m}$ and width $B = 5\,\mathrm{m}$ as our indoor environment. The parameters a and b have been chosen to be 2 and 1, respectively. The SOC channel simulator is designed by the MMEA [8] using $N_\ell = 8$ $(\ell = 1, 2, \ldots, \mathscr{L})$ harmonic functions in each discrete propagation path.

The theoretical result for the PDF of the AOA [see (15)] of the wideband reference channel model is presented in Fig. D.2 for different BS locations ($c = -2$ and $c = -4$). It can be observed from this figure that the shape of the PDF of the AOA is independent of the position of the BS. The theoretical results illustrated
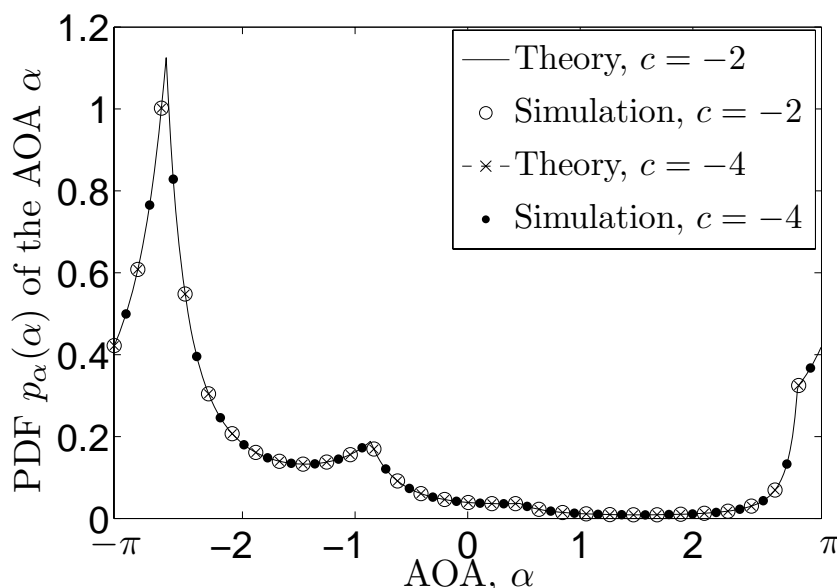
Figure D.2: The PDF $p_\alpha(\alpha)$ of the AOA α for different locations of the BS.

in Fig. D.2 have been verified by simulations. In our simulations, we determined the horizontal (and vertical) locations of all scatterers in the coordinate system as outcomes of a random generator exponentially distributed over $[-A/2-a,A/2-a]$ (and $[-B/2-b,B/2-b]$). Starting from the position of a scatterer, we calculate the AOA and the propagation delay. Then, we measure the conditional PDF of the AOA $p_{\alpha|\tau'\in I_\ell}(\alpha)\,(\ell = 1,2,\ldots,\mathscr{L})$ from the obtained random values of the AOAs. Summing up all the $\mathscr{L}$ conditional PDFs of the AOA gives us the simulation results for the overall PDF of the AOA. Figure D.2 also shows the PDF of the AOA of the narrowband channel model (see [22, Eq. (9)]).

The impact of the parameters a and b on the shape of the PDF of the AOA are illustrated in Fig. D.3 and Fig. D.4, respectively. As shown in Fig. D.1, the parameters a and b control the symmetry of the room with respect to the MS location. It can be observed from Fig. D.3 that when we increase the value of a from 0 to 4, the probability for the small AOAs, which means the angles belong to the range $[-\mathrm{acrtan}\frac{B+2b}{A-2a},\mathrm{acrtan}\frac{B-2b}{A-2a}]$, decreases. In contrast, the PDF of the large values of the AOA, i.e. $\alpha \in [-\mathrm{acrtan}\frac{B+2b}{A+2a},-\pi]$ or $[\mathrm{acrtan}\frac{B-2b}{A+2a},\pi]$, increases.

Figure D.4 points out that an increase of b leads to an inverse impact on the shape of the PDF of the AOA compared with that of increasing a.

Figure D.5 shows the absolute value of the FCF calculated using (22) for different values of the room length A. For comparison purposes, we also plot the theoretical curve for the FCF computed by Eq. (31) in [31]. We consider $\mathscr{L} = 10$ propagation paths for the SOC channel simulator with the corresponding delays
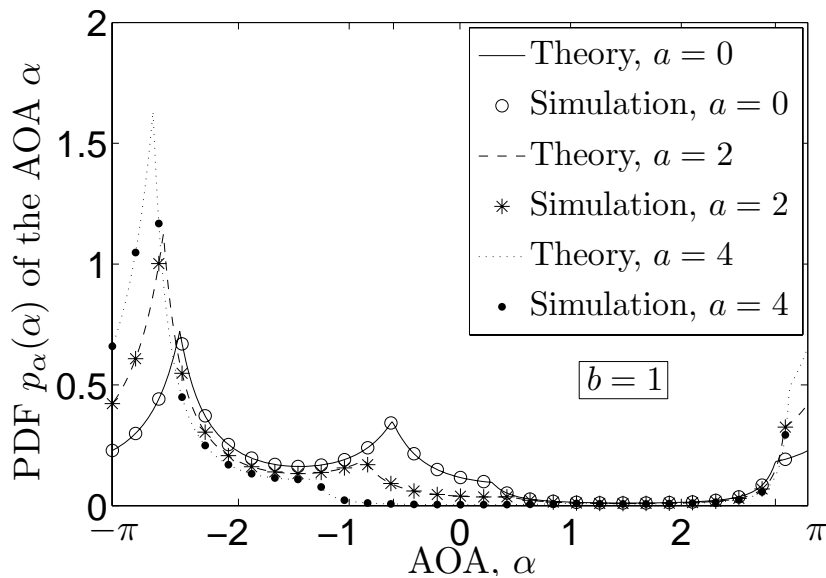
Figure D.3: The PDF $p_\alpha(\alpha)$ of the AOA α for different locations of the MS.
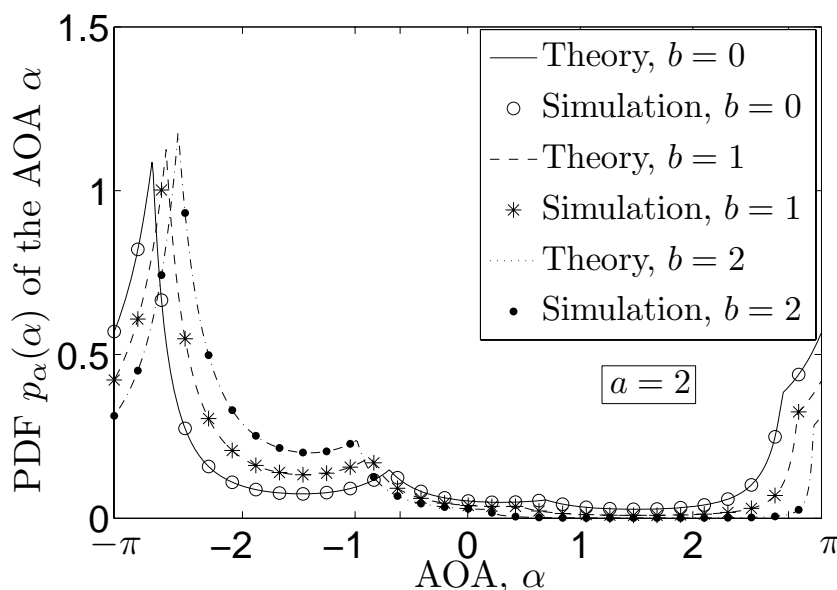
Figure D.4: The PDF $p_\alpha(\alpha)$ of the AOA α for different locations of the MS.
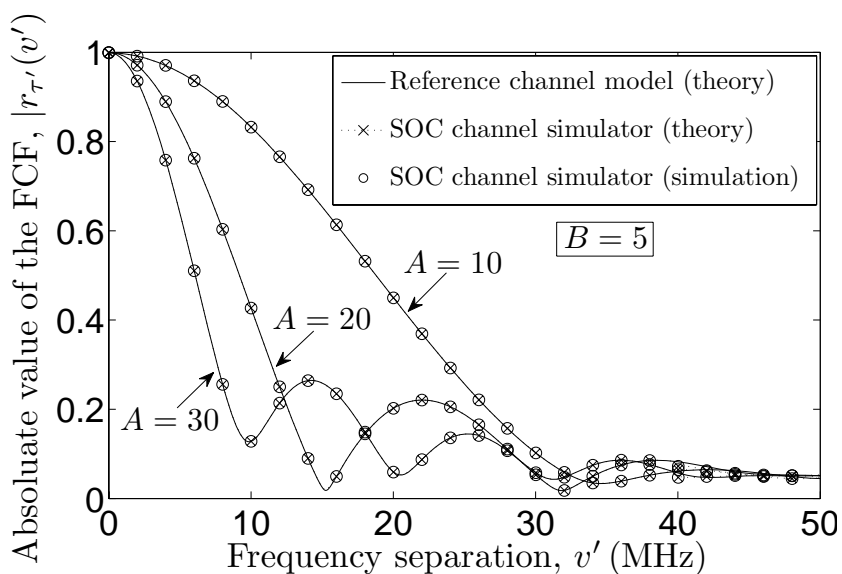
Figure D.5: Absolute values of the FCFs $|r_{\tau'}(v')|$ (reference model) and $|\tilde{r}_{\tau'}(v')|$ (simulation model) for different values of the room length A.

$\tau'_\ell = \{0, 1, 3, 8, 12, 17, 25, 28, 32, 36\}$ ns. The powers assigned to different paths are determined according to the method described in [28, pp. 281–282]. The AOAs of the SOC are computed by employing the modified method of equal areas [8]. We observe from Fig. D.5 that the FCF of the SOC channel simulator can be brought into extremely good agreement with that of the reference model. The FCF decays faster with increasing the frequency separation v' if the room length A increases

(here from 10 m to 30 m). The coherence bandwidth[1] B_c becomes smaller as increasing A.

The influence of the room width on the FCF is presented in Fig. D.6, from which the same conclusions can be drawn.

VI. EXPERIMENTAL VERIFICATION

To demonstrate the usefulness of the proposed geometrical-based indoor reference channel model, we will show how the statistics of the reference channel model can be fitted to the statistics of real-world channels by optimizing the relevant parameters of the reference model. Here, two of the most important wideband channel statistics, i.e., the mean access delay and the RMS delay spread, are considered.

The mean access delay $m_{\tau'}$ is defined as the first moment of the PDP, i.e., [41, 11]

$$m_{\tau'} = \frac{\int\limits_{0}^{\infty} \tau' \cdot S_{\tau'}(\tau') \, d\tau'}{\int\limits_{0}^{\infty} S_{\tau'}(\tau') \, d\tau'}. \qquad (29)$$

---

[1] The coherence bandwidth B_c is the smallest positive value of the frequency separation variable $v' = B_c$ which fulfills the condition $|r_{\tau'}(B_c)| = |r_{\tau'}(0)|/2$.
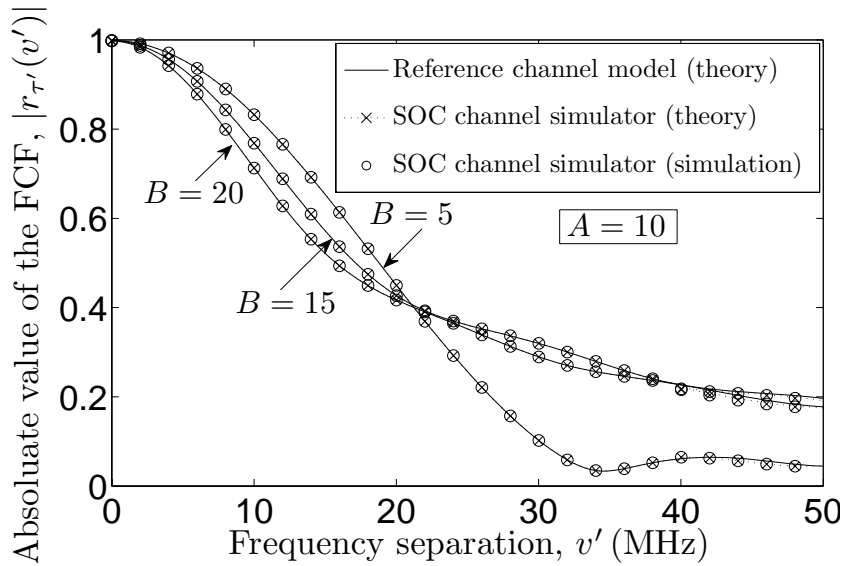
Figure D.6: Absolute values of the FCFs $|r_{\tau'}(v')|$ (reference model) and $|\tilde{r}_{\tau'}(v')|$ (simulation model) for different values of the room width B.

The RMS delay spread can be expressed as follows,

$$
\sigma_{\tau'} = \sqrt{\frac{\int\limits_{0}^{\infty} (\tau' - m_{\tau'})^2 \cdot S_{\tau'}(\tau') \, d\tau'}{\int\limits_{0}^{\infty} S_{\tau'}(\tau') \, d\tau'}}, \tag{30}
$$

which is the square root of the second central moment of the PDP. The mean access delay m_{τ} and the RMS delay spread $\sigma_{\tau'}$ of the reference model can easily be calculated by substituting the PDP [see (20)] into (29) and (30), respectively.

The experimental results of the mean access delay $m_{\tau'}^{\star}$ and the RMS delay spread $\sigma_{\tau'}^{\star}$ considered in this section are taken from [25]. The measurement experiments were carried out at $60\,\mathrm{GHz}$ in two $30\,\mathrm{m} \times 1.75\,\mathrm{m} \times 2.80\,\mathrm{m}$ corridors as well as inside the laboratory with dimensions $19.5\,\mathrm{m} \times 7.5\,\mathrm{m}$.

We combine all the relevant model parameters, which determine the mean access delay $m_{\tau'}$ and the RMS delay spread $\sigma_{\tau'}$ of the reference channel model, into a parameter vector denoted and defined by $\Omega := (A, B, a, b, c, w_1, w_2)$. We also introduce the following error function

$$
E(\Omega) = W_1 \cdot (m_{\tau'}^{\star} - m_{\tau'}) + W_2 \cdot (\sigma_{\tau'}^{\star} - \sigma_{\tau'}), \tag{31}
$$

for measuring the deviations between the mean access delay $m_{\tau'}^{\star}$ and $m_{\tau'}$ as well as between $\sigma_{\tau'}^{\star}$ and $\sigma_{\tau'}$. In (31), W_1 and W_2 represent the weighting factor.

The optimization of the parameter vector Ω is carried out by minimizing numerically the above error function $E(\Omega)$ by means of the quasi-Newton procedure [7]. The optimization results are presented in Table D.1 for corridor and library scenarios. For convenience, the measured mean assess delay $m_{\tau'}^{\star}$ and the measured RMS delay spread $\sigma_{\tau'}^{\star}$, presented in [25], are shown again in Table D.1. The mean assess delay in the range of $3.84\,\mathrm{ns}$ to $8.18\,\mathrm{ns}$ is for hallways and $3.52\,\mathrm{ns}$ to $14.69\,\mathrm{ns}$ is for offices. In addition, the RMS delay spread varies from $12.34\,\mathrm{ns}$ to $15.04\,\mathrm{ns}$ for corridors and from $12.56\,\mathrm{ns}$ to $21.09\,\mathrm{ns}$ for the laboratory. In our optimization procedure, the weighting factors W_1 and W_2 are assigned to 0.35 and 0.65, respectively.

Table D.2 presents the mean access delay m_{τ} and the RMS delay spread $\sigma_{\tau'}$ of the reference channel model, which have been computed according to the channel parameters taken from Table D.1. This table also compares the mean access delay and the RMS delay spread of the reference model with those obtained from the real-world channel. The deviation between $m_{\tau'}^{\star}$ and $m_{\tau'}$ is measured by the relative

Table D.1: The optimized parameters of the reference models for corridor and library scenarios (values for the measured mean access delay $m_{\tau'}^{\star}$ and the RMS delay spread $\sigma_{\tau'}^{\star}$ are in nanoseconds)

	$m_{\tau'}^{\star}$	$\sigma_{\tau'}^{\star}$	A	B	a	b	c	w_1	w_2
Loc. 1	5.17	13.70	24.67	2.92	11.23	0.71	-11.61	-0.13	-5.27
Loc. 2	8.18	15.04	27.48	5.22	6.21	2.02	-12.51	0.036	-34.63
Loc. 3	3.84	12.35	29.12	6.23	13.93	2.27	-13.92	-0.091	-19.92
Loc. 4	5.37	12.34	23.59	3.02	11.74	0.75	-10.88	-0.15	-7.02
Average Corridor	**5.64**	**13.36**	24.11	2.85	10.92	0.68	-11.07	-0.13	-8.62
Loc. 5	8.42	14.72	25.56	2.78	11.12	0.87	-12.39	-0.13	-4.85
Loc. 6	3.52	12.56	28.32	5.98	12.79	2.03	-13.24	-0.085	-20.84
Average Lab (LOS)	**5.97**	**13.64**	23.75	2.96	11.34	0.77	-10.93	-0.14	-7.95
Loc. 7	12.81	19.94	18.68	7.51	9.07	3.14	-8.79	-0.032	-25.17
Loc. 8	14.69	21.09	19.73	6.34	9.82	2.56	-9.52	-0.03	-34.65
Average Lab (NLOS)	**13.75**	**20.52**	17.55	9.21	8.64	4.37	-8.58	-0.029	-28.79
Overall	**7.75**	**15.22**	20.84	5.57	10.11	2.55	-10.25	-0.027	-23.53

Table D.2: Comparisons of channel statistics between the reference model and the real-world channel.

	$m_{\tau'}^{\star}$(ns)	$\sigma_{\tau'}^{\star}$(ns)	$m_{\tau'}$(ns)	$\sigma_{\tau'}$(ns)	$\varepsilon_{m_{\tau'}}(\%)$	$\varepsilon_{\sigma_{\tau'}}(\%)$
Loc. 1	5.17	13.70	5.17	13.70	4.82×10^{-12}	2.16×10^{-13}
Loc. 2	8.18	15.04	8.24	15.04	0.76	1.79×10^{-8}
Loc. 3	3.84	12.35	3.86	12.35	0.56	6.54×10^{-9}
Loc. 4	5.37	12.34	5.37	12.34	3.23×10^{-13}	8.04×10^{-14}
Average Corridor	**5.64**	**13.36**	5.64	13.36	4.40×10^{-14}	2.48×10^{-14}
Loc. 5	8.42	14.72	8.42	14.72	5.91×10^{-12}	2.57×10^{-13}
Loc. 6	3.52	12.56	3.52	12.56	6.41×10^{-13}	6.95×10^{-14}
Average Lab (LOS)	**5.97**	**13.64**	5.97	13.64	8.8×10^{-14}	7.25×10^{-14}
Loc. 7	12.81	19.94	12.81	19.94	5.27×10^{-13}	3.74×10^{-14}
Loc. 8	14.69	21.09	14.69	21.09	6.76×10^{-13}	5.19×10^{-14}
Average Lab (NLOS)	**13.75**	**20.52**	13.75	20.52	1.53×10^{-13}	2.16×10^{-13}
Overall	**7.75**	**15.22**	7.75	15.22	9.89×10^{-14}	9.95×10^{-14}

error of the mean access delay[2] $\varepsilon_{m_{\tau'}}$. We also introduce the relative error of the RMS delay spread[3], denoted by $\varepsilon_{\sigma_{\tau'}}$, to evaluate the deviation between the RMS delay spread $\sigma_{\tau'}^{\star}$ and $\sigma_{\tau'}$. As shown in Talbe D.2, the theoretical mean access delay

---

[2]The relative error of the mean access delay is defined as

$$\varepsilon_{m_{\tau'}} = \frac{m_{\tau'} - m_{\tau'}^{\star}}{m_{\tau'}^{\star}}.$$

[3]The relative error of the RMS delay spread is given by

$$\varepsilon_{\sigma_{\tau'}} = \frac{\sigma_{\tau'} - \sigma_{\tau'}^{\star}}{\sigma_{\tau'}^{\star}}.$$

and the RMS delay spread are extremely close to those empirical ones for different indoor propagation scenarios, which demonstrates that the proposed reference channel model is usefulness for characterizing real-world wideband indoor mobile fading channels.

VII. CONCLUSION

In this paper, we developed a wideband mobile fading channel model for indoor propagation environments. The wideband extension is applied on the geometrical scattering model under the assumption that an infinite number of scatterers is exponentially distributed over the 2D horizontal plane of a rectangular room. Analytical expressions have been derived for the PDF of the AOA, the PDP, and the FCF. We have shown that the shape of the PDF of the AOA is independent of the position of the BS. Both the room length and width have influence on the PDF of the AOA and the FCF. If the room length or width increases, the FCF decays faster with increasing the frequency separation. The coherence bandwidth decreases with increasing the room size. The usefulness of the proposed reference channel model has been demonstrated by the close agreement between the theoretical and empirical channel statistics.

An efficient channel simulator has been derived from the reference channel model by applying the SOC principle. It should be mentioned that the SOC channel simulator matches perfectly the wideband reference model with respect to the FCF. Thus, instead of using the reference channel model, the designed SOC channel simulators enable to evaluate the performance of wideband indoor wireless communication systems more efficiently due to the reduced realization expenditure.

D. A   Derivation of the Maximum plane wave traveling distance for a given value of the AOA

The function $D(z, \alpha)$, defined by

$$D(z, \alpha) = z + \sqrt{z^2 - 2cz\cos\alpha + c^2}, \tag{A.1}$$

describes the traveling distance from the BS to the MS via a single scatterer located at an arbitrary place of the 2D horizontal plane of the room. Due to the fact that the derivative of $D(z, \alpha)$ with respect to z is always positive, i.e.,

$$\frac{d}{dz}D(z, \alpha) = \frac{z - c\cos\alpha}{\sqrt{z^2 - 2cz\cos\alpha + c^2} + 1} > 0, \tag{A.2}$$

$D(z, \alpha)$ is a monotonic increasing function with respect to z. That means for a given AOA, the traveling distance takes a maximum value when the distance z from the MS to a scatterer is maximum. The maximum z, denoted by z_{max}, always occurs when a scatterer is located at the boundary of the rectangle.

According to the geometrical relationship in Fig.D.1, if the AOA $\alpha \in (-\arctan\frac{B+2b}{A-2a}, \arctan\frac{B-2b}{A-2a}]$, we have

$$z_{max} = \frac{A-2a}{2\cos(\alpha)}. \tag{A.3}$$

Substituting (A.3) into (A.1) gives an analytical expression for the maximum traveling distance $D_{max}(\alpha)$

$$D_{max}(\alpha) = \frac{A-2a}{2\cos(\alpha)} + \sqrt{\left[\frac{A-2a}{2\cos(\alpha)}\right]^2 - c(A-2a) + c^2}, \tag{A.4}$$

which depends only on the AOA α. By analogy, we can obtain the maximum traveling distance $D_{max}(\alpha)$ for the rest range of the AOAs. For brevity, we only present the final expression for $D_{max}(\alpha)$ in (14).

D. B Determination of the values D_i and α_i in (17)

In this appendix, we first determine the value D_i, denoting the maximum or minimum value of D_{max}, for the following four cases.

Case I: $-\arctan\frac{B+2b}{A-2a} < \alpha \le \arctan\frac{B-2b}{A-2a}$

It can easily be seen from (A.4) that $D_{max}(\alpha)$ is a monotonic increasing function with respect to α within the range $[0, \arctan\frac{B-2b}{A-2a}]$. We find that $D_{max}(\alpha)$ takes the minimum value D_1 when $\alpha = 0$, while $D_{max}(\alpha)$ is maximum when $\alpha = \arctan\frac{B-2b}{A-2a}$, i.e.,

$$
\begin{aligned}
D_1 &= \min(D_{max}(\alpha)) \\
&= D_{max}(\alpha)\Big|_{\alpha=0} \\
&= A - 2a - c \tag{B.1a} \\
D2 &= \max(D_{max}(\alpha)) \\
&= D_{max}(\alpha)\Big|_{\alpha=\arctan\frac{B-2b}{A-2a}} \\
&= \frac{\sqrt{(A-2a)^2+(B-2b)^2} + \sqrt{(A-2a-2c)^2+(B-2b)^2}}{2}. \tag{B.1b}
\end{aligned}
$$

If $\alpha \in (-\arctan \frac{B+2b}{A-2a}, 0)$, $D_{\max}(\alpha)$ decreases if α increases. Thus, the maximum $D_{\max}(\alpha)$ over this range is given by

$$
\begin{aligned}
D3 &= \max\left(D_{\max}(\alpha)\right) \\
&= D_{\max}(\alpha)\Big|_{\alpha=-\arctan \frac{B+2b}{A-2a}} \\
&= \frac{\sqrt{(A-2a)^2+(B+2b)^2}+\sqrt{(A-2a-2c)^2+(B+2b)^2}}{2}.
\end{aligned} \tag{B.2}
$$

Case II: If the AOA α belongs to the range $(\arctan \frac{B-2b}{A-2a}, \pi - \arctan \frac{B-2b}{A+2a}]$, by setting the first derivative of $D_{\max}(\alpha)$ [see the second part of the piecewise function in (14)] with respect to α to zero, then we obtain the fixed point $\alpha = \pi + \arctan \frac{B-2b}{c}$. Since the second derivative of $D_{\max}(\alpha)$ with respect to α is positive, $D_{\max}(\alpha)$ has a minimum value D_4 at the fixed point $\alpha = \pi + \arctan \frac{B-2b}{c}$, i.e.,

$$
\begin{aligned}
D_4 &= \min\left(D_{\max}(\alpha)\right) \\
&= D_{\max}(\alpha)\Big|_{\alpha=\pi+\arctan \frac{B-2b}{c}} \\
&= \sqrt{(B-2b)^2+c^2}
\end{aligned} \tag{B.3}
$$

If $\alpha \in \left(\pi + \arctan \frac{B-2b}{c}, \pi - \arctan \frac{B-2b}{A+2a}\right]$, $D_{\max}$ is a monotonic increasing function. Therefore, $D_{\max}(\alpha)$ takes a maximum value D_5 at $\alpha = \pi - \arctan \frac{B-2b}{A+2a}$, i.e.,

$$
\begin{aligned}
D_5 &= \max\left(D_{\max}(\alpha)\right) \\
&= D_{\max}(\alpha)\Big|_{\alpha=\pi-\arctan \frac{B-2b}{A+2a}} \\
&= \frac{\sqrt{(A+2a)^2+(B-2b)^2}+\sqrt{(A+2a+2c)^2+(B-2b)^2}}{2}.
\end{aligned} \tag{B.4}
$$

If $\alpha \in (\arctan \frac{B-2b}{A-2a}, \pi + \arctan \frac{B-2b}{c}]$, $D_{\max}(\alpha)$ decreases when increasing α. Thus, we have $D_{\max}(\alpha) < D_2$.

Case III: $\alpha \in (\pi - \arctan \frac{B-2b}{A+2a}, \pi] \cup (-\pi, -\pi + \arctan \frac{B+2b}{A+2a}]$

By studying the first and second derivatives of $D_{\max}(\alpha)$ [see the third part of the piecewise function in (14)], it can be shown that $D_{\max}(\alpha)$ is a monotonic decreasing function within $(\pi - \arctan \frac{B-2b}{A+2a}, \pi]$. Thus, we have $D_6 \leq D_{\max}(\alpha) < D_5$, where

$$
\begin{aligned}
D_6 &= \min\left(D_{\max}(\alpha)\right) \\
&= D_{\max}(\alpha)\Big|_{\alpha=\pi}
\end{aligned}
$$

$$= A + 2a + c. \tag{B.5}$$

If $\alpha \in (-\pi, -\pi + \arctan \frac{B+2b}{A+2a}]$, $D_6 < D_{\max}(\alpha) \leq D_7$, where

$$
\begin{aligned}
D_7 &= \max\left(D_{\max}(\alpha)\right) \\
&= D_{\max}(\alpha)\big|_{\alpha = -\pi + \arctan \frac{B+2b}{A+2a}} \\
&= \frac{\sqrt{(A+2a)^2 + (B+2b)^2} + \sqrt{(A+2a+2c)^2 + (B+2b)^2}}{2}. \tag{B.6}
\end{aligned}
$$

Case IV: Processing the similar procedures as shown in Case II, we obtain the range of $D_{\max}(\alpha)$ for the rest range of the AOAs $\alpha \in (-\pi + \arctan \frac{B+2b}{A+2a}, -\arctan \frac{B+2b}{A-2a}]$. For brevity, we only present the final results here. The function $D_{\max}(\alpha)$ has a minimum value at the fixed point $\alpha = -\pi - \arctan \frac{B+2b}{c}$, i.e.,

$$
\begin{aligned}
D_8 &= \min\left(D_{\max}(\alpha)\right) \\
&= D_{\max}(\alpha)\bigg|_{\alpha = -\pi - \arctan \frac{B+2b}{c}} \\
&= \sqrt{(B+2b)^2 + c^2}. \tag{B.7}
\end{aligned}
$$

The value of $D_{\max}(\alpha)$ decreases if the AOA changes from $-\pi + \arctan \frac{B+2b}{A+2a}$ to the fixed point given above. Within this range, we have $D_8 \leq D_{\max}(\alpha) < D_7$. If $\alpha \in (-\pi - \arctan \frac{B+2b}{c}, -\arctan \frac{B+2b}{A-2a}]$, $D_{\max}(\alpha)$ increases and the maximum value occurs at $\alpha = -\arctan \frac{B+2b}{A-2a}$ and we have $D_8 < D_{\max}(\alpha) \leq D_3$.

An example for the maximum traveling distance $D_{\max}(\alpha)$ is illustrated in Fig. D.7. It should be mentioned that a traveling distance D is always less than or equal to $D_{\max}(\alpha)$. Since D_4 is the minimum value of $D_{\max}(\alpha)$ [see Fig. D.7], for a given value of the traveling distance $D \leq D_4$, all the AOAs $\alpha \in (-\pi, \pi]$ satisfy the inequality $D \leq D_{\max}(\alpha) \leq D_4$. However, if the traveling distance $D_4 < D \leq D_8$, the inequality $D \leq D_{\max}(\alpha)$ can be guaranteed if $\alpha \in (-\pi, \alpha_1]$ or $\alpha \in [\alpha_2, \pi]$. Here, the AOAs α_1 and α_2 can be obtained by solving the equation

$$D_{\max}(\alpha) = D. \tag{B.8}$$

As shown in Fig. D.7, $\alpha_1, \alpha_2 \in (\arctan \frac{B-2b}{A-2a}, \pi - \arctan \frac{B-2b}{A+2a}]$. Thus, we select the second piece of $D_{\max}(\alpha)$ in (14) as the expression for the left-hand side of (B.8). Solving (B.8) results finally in the expressions for α_1 and α_2 as presented in (18b).

For the other given values of D, it is necessary to meet the condition $D \leq$
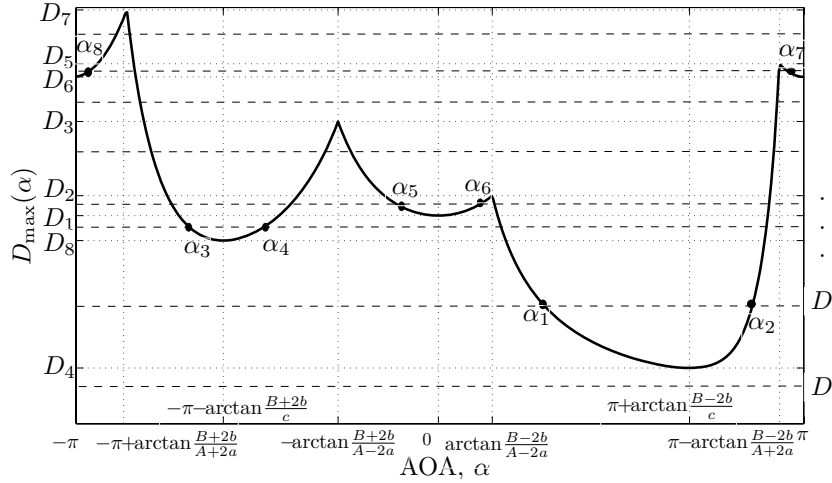
Figure D.7: The maximum traveling distance $D_{\max}(\alpha)$ for different values of the AOA α ($A = 10\,\text{m}$, $B = 5\,\text{m}$, $a = 2\,\text{m}$, $b = 1\,\text{m}$, and $c = -2\,\text{m}$).

$D_{\max}(\alpha)$. According to Fig. D.7, we have

$$
\begin{aligned}
&1) \quad \alpha \in (-\pi, \alpha_3] \cup [\alpha_4, \alpha_1] \cup [\alpha_2, \pi], && \text{if}\, D_8 < D \le D_1, \\
&2) \quad \alpha \in (-\pi, \alpha_3] \cup [\alpha_4, \alpha_5] \cup [\alpha_6, \alpha_1] \cup [\alpha_2, \pi], && \text{if}\, D_1 < D \le D_2, \\
&3) \quad \alpha \in (-\pi, \alpha_3] \cup [\alpha_4, \alpha_5] \cup [\alpha_2, \pi], && \text{if}\, D_2 < D \le D_3, \\
&4) \quad \alpha \in (-\pi, \alpha_3] \cup [\alpha_2, \pi], && \text{if}\, D_3 < D \le D_6, \\
&5) \quad \alpha \in [\alpha_8, \alpha_3] \cup [\alpha_2, \alpha_7], && \text{if}\, D_6 < D \le D_5, \\
&6) \quad \alpha \in [\alpha_8, \alpha_3], && \text{if}\, D_5 < D \le D_7.
\end{aligned}
$$

$$\text{(B.9)}$$

The AOA $\alpha_i\,(i = 3, 4, \ldots, 8)$ can be determined similarly by solving (B.8). The expression for $D_{\max}(\alpha)$ on the left-hand side of (B.8) is chosen in accordance to the range of α_i. For example, since $\alpha_3 \in (-\pi + \arctan\frac{B+2b}{A+2a}, -\arctan\frac{B+2b}{A-2a}]$, the fourth part of $D_{\max}(\alpha)$ [see (14)] obtained for Case IV is selected.

REFERENCES

[1] S. E. Alexander. Characterizing buildings for propagation at 900 MHz. *IEEE Electronics Letters*, 19(20):860, Sept. 1983.

[2] G. E. Athanasiadou, A. R. Nix, and J. P. McGeehan. A microcellular ray-tracing propagation model and evaluation of its narrow-band and wide-band predictions. *IEEE J. Select. Areas Commun.*, 18(3):322–335, Mar. 2000.

[3] E. Benner and A. B. Sesay. Effects of antenna height, antenna gain, and pattern downtilting for cellular mobile radio. *IEEE Trans. Veh. Technol.*, 45(2):217–224, May 1996.

[4] S.-H Cheu and S.-K. Jeng. An SBR/image approach to indoor radio propagation modeling. In *Proc. IEEE Antennas and Propagation Society, AP-S international symposium (Digest)*, volume 4, pages 1952–1955. Newport Beach, CA, USA, June 1995.

[5] H. Droste and G. Kadel. Measurements and analysis of wideband indoor propagation characteristics at 17 GHz and 60 GHz. In *Proc. 9th International Conference on Antennas and Propagation*, volume 2, pages 288–291. Eindhoven, Netherlands, Apr. 1995.

[6] P. Ferre, A. Doufexi, J. Chung-How, A. R. Nix, and D. R. Bull. Robust video transmission over wireless LANs. *IEEE Trans. Veh. Technol.*, 57(4):2596–2602, July 2008.

[7] R. Fletcher and M. J. D. Powell. A rapidly convergent descent method for minimization. *Computer Journal*, 6(2):163–168, 1963.

[8] C. A. Gutiérrez and M. Pätzold. Sum-of-sinusoids-based simulation of flat fading wireless propagation channels under non-isotropic scattering conditions. In *Proc. 50th Global Communication Conference, GLOBECOM 2007*, pages 3842–3846. Washington, D.C., USA, Nov. 2007.

[9] H. Hashemi. Impulse response modelling of indoor radio propagation channels. *IEEE J. Select. Areas Commun.*, SAC-11(7):967–978, Sept. 1993.

[10] H. Hashemi and D. Tholl. Statistical modeling and simulation of the RMS delay spread of indoor radio propagation channels. *IEEE Trans. Veh. Technol.*, 43(1):110–120, Feb. 1994.

[11] H. Hashemi and D. Tholl. Statistical modeling and simulation of the RMS delay spread of indoor radio propagation channels. *IEEE Trans. Veh. Technol.*, 43(1):110–120, Feb. 1994.

[12] D. A. Hawbaker and T. S. Rappaport. Indoor wideband radiowave propagation measurements at 1.3 GHz and 4 GHz. *IEEE Electronics Letters*, 26(21):1800–1802, Oct. 1990.

[13] Z. Ji, B.-H. Li, H.-X. Wang, H.-Y Chen, and T. K. Sarkar. Efficient ray-tracing methods for propagation prediction for indoor wireless communications. *IEEE Antennas and Propagation Magazine*, 43(2):41–49, Apr. 2001.

[14] L. Jiang and S. Y. Tan. Geometrically based statistical channel models for ourdoor and indoor propagation. *IEEE Trans. on Veh. Technol.*, 56(6):3587–3593, Nov. 2007.

[15] J. Karaoguz. High-rate wireless personal area networks. *IEEE Communications Magazine*, 39(12):96–102, Dec. 2001.

[16] A. O. Kaya, L. J. Greenstein, and W. Trappe. Characterizing indoor wireless channels via ray tracing combined with stochastic modeling. *IEEE Trans. Wireless Commun.*, 8(8):4165–4175, Aug. 2009.

[17] M. C. Lawton and J. P. McGeehan. The application of a deterministic ray launching algorithm for the prediction of radio channel characteristics in small-cell environments. *IEEE Trans. Veh. Technol.*, 43(4):955–969, Nov. 1994.

[18] G. Liang and H. L. Bertoni. A new approach to 3-D ray tracing for propagation prediction in cities. *IEEE Trans. Antennas Propagat.*, 46(6):853–863, June 1998.

[19] P. Lin and Y.-B. Lin. Implementation and performance evaluation for mobility management of a wireless PBX network. *IEEE J. Select. Areas Commun.*, 19(6):1138–1146, June 2001.

[20] S. Loredo, A. Rodríguez-Alonso, and R. P. Torres. Indoor MIMO channel modeling by rigorous GO/UTD-based ray tracing. *IEEE Trans. Veh. Technol.*, 57(2):680–692, Mar. 2008.

[21] Y. Ma and M. Pätzold. Wideband two-ring MIMO channel models for mobile-to-mobile communications. In *Proc. 10th International Symposium on Wireless Personal Multimedia Communications, WPMC 2007*, pages 380–384. Jaipur, India, Dec. 2007.

[22] Y. Ma and M. Pätzold. Design and simulation of narrowband indoor radio propagation channels under LOS and NLOS propagation conditions. In *Proc. 71st Vehicular Technology Conference, VTC 2010-Spring*, pages 1–7. Taipei, Taiwan, May 2010.

[23] A. F. Molisch. *Wireless Communications*. Chichester: John Wiley & Sons, West Sussex, UK, 2005.

[24] N. Moraitis and P. Constantinou. Indoor channel measurements and characterization at 60 GHz for wireless local area network applications. *IEEE Trans. Antennas Propagat.*, 52(12):3180–3189, Dec. 2004.

[25] N. Moraitis and P. Constantinou. Measurements and characterization of wideband indoor radio channel at 60 GHz. *IEEE Trans. on Wire. Commun.*, 5(4):880–889, Apr. 2006.

[26] J. E. Padgett, C. G. Gunther, and T. Hattori. Overview of wireless personal communications. *IEEE Communications Magazine*, 33(1):28–41, Jan. 1995.

[27] A. Papoulis and S. U. Pillai. *Probability, Random Variables and Stochastic Processes*. New York: McGraw-Hill, 4th edition, 2002.

[28] M. Pätzold. *Mobile Fading Channels*. Chichester: John Wiley & Sons, 2002.

[29] M. Pätzold and C. A. Gutiérrez. Level-crossing rate and average duration of fades of the envelope of a sum-of-cisoids. In *Proc. 67th IEEE Vehicular Technology Conference, VTC 2008-Spring*, pages 488–494. Singapore, May 2008.

[30] M. Pätzold and B. O. Hogstad. A wideband MIMO channel model derived from the geometric elliptical scattering model. In *Proc. 3rd International Symposium on Wireless Communication System, ISWCS 2006*, pages 138–144. Valencia, Spain, Sept. 2006.

[31] M. Pätzold and B. O. Hogstad. A wideband space-time MIMO channel simulator based on the geometrical one-ring model. In *Proc. 64th Vehicular Technology Conference, VTC 2006-Fall*. Montreal, Canada, Sept. 2006.

[32] M. Pätzold and B. Talha. On the statistical properties of sum-of-cisoids-based mobile radio channel models. In *Proc. 10th International Symposium on Wireless Personal Multimedia Communications, WPMC 2007*, pages 394–400. Jaipur, India, Dec. 2007.

[33] T. Rautiainen, G. Wolfle, and R. Hoppe. Verifying path loss and delay spread predictions of a 3D ray tracing propagation model in urban environments. In *Proc. 56th IEEE Vehicular technology conference, VTC 2002*, volume 2, pages 2470–2474. Vancouver, Canada, Sept. 2002.

[34] A. A. M. Saleh and R. A. Valenzuela. A statistical model for indoor multipath propagation. *IEEE J. Select. Areas Commun.*, SAC-5(2):128–137, Feb. 1987.

[35] G. Santella and E. Restuccia. Analysis of frequency domain wide-band measurements of the indoor radio channel at 1, 5.5, 10 and 18 GHz. In *Proc. Global Communication Conference, GLOBECOM 1996*, volume 2, pages 1162–1166. London, UK, Nov. 1996.

[36] K. R. Schaubach, N. J. Davis, and T. S. Rappaport. A ray tracing method for predicting path loss and delay spread in microcellular environments. In *Proc. 42nd IEEE Vehicular technology conference, VTC 1992*, volume 2, pages 932–935. Denver, CO, USA, May 1992.

[37] S. Y. Seidel and T. S. Rappaport. 914 MHz path loss prediction models for indoor wireless communications in multifloored buildings. *IEEE Trans. Antennas Propagat.*, 40(2):207–217, Feb. 1992.

[38] S. Y. Seidel and T. S. Rappaport. A ray tracing technique to predict path loss and delay spread inside buildings. In *Proc. IEEE Global Communication Conference, GLOBECOM 1992*, volume 2, pages 649–653. Orlando, FL, USA, Dec. 1992.

[39] G. Tiberi, S. Bertini, W. Q. Malik, A. Monorchio, D. J. Edwards, and G. Manara. Analysis of realistic ultrawideband indoor communication channels by using an efficient ray-tracing based method. *IEEE Trans. Antennas Propagat.*, 57(3):777–785, Mar. 2009.

[40] J. A. Wepman, J. R. Hoffman, and L. H. Loew. Analysis of impulse response measurements for PCS channel modeling application. *IEEE Trans. Veh. Technol.*, 44(3):613–620, Aug. 1995.

[41] H. Xu, V. Kukshya, and T. S. Rappaport. Spatial and temporal characteristics of 60-GHz indoor channels. *IEEE Journal on Select Areas in Communications*, 20(3):620–630, Apr. 2002.

[42] K. Yu, M. Bengtsson, B. Ottersten, D. McNamara, P. Karlsson, and M. Beach. Modeling of wide-band MIMO radio channels based on NLoS indoor measurements. *IEEE Trans. Veh. Technol.*, 53(3):655–665, May 2004.

[43] T. Zwick, T. J. Beukema, and H. Nam. Wideband channel sounder with measurements and model for the 60 GHz indoor radio channel. *IEEE Trans. Veh. Technol.*, 54(4):1266–1277, July 2005.

Appendix E

Paper V

Performance Analysis of Wideband SOS-based Channel Simulators with Respect to the Bit Error Probability of BPSK OFDM Systems with Perfect and Imperfect CSI

Yuanyuan Ma and Matthias Pätzold

Department of Information and Communication Technology

Faculty of Engineering and Science, University of Agder

Servicebox 509, NO-4898 Grimstad, Norway

E-mails: {yuanyuan.ma, matthias.paetzold}@uia.no

Abstract — **This paper analyzes the performance of wideband sum-of-sinusoid (SOS) channel simulators w.r.t. the bit error probability (BEP) of orthogonal frequency division multiplexing (OFDM) systems. Analytical expressions for the BEP are derived for a binary phase-shift keying (BPSK) OFDM system in the presence of perfect and imperfect channel state information (CSI). The derived analytical expressions are used to study the degradation of the BEP introduced by an imperfect channel simulator. It allows us to reduce the channel realization expenditure to a minimum without introducing significant performance degradations. Analytical and simulation results for the BEP enable a fair evaluation of the efficiency of different parameter computation methods, such as the generalized method of exact Doppler spread (GMEDS$_1$) and the Monte Carlo method (MCM). The performance of both methods w.r.t. the BEP of OFDM systems is also investigated in this paper.**

I. INTRODUCTION

In the last two decades, Rice's sum-of-sinusoids (SOS) method [12] has emerged as one of the key approaches for designing channel simulators for mobile fading channels, such as narrowband fading channels [5], wideband fading channels [8], and multiple-input multiple-output channels [6]. Due to their low realization expenditure, SOS channel simulators have been widely used in practical system simulations, e.g., in OFDM systems [7]. The statistical properties of narrowband and wideband SOS channel simulators have been studied in [8]. So far, the performance of SOS channel simulators w.r.t. the BEP of a transmission system has been studied only for narrowband fading channels [10]. However, the performance of wideband SOS channel simulators w.r.t. the BEP is unknown.

In this paper, we analyze the performance of a wideband deterministic SOS channel simulator w.r.t. the BEP of a BPSK OFDM system assuming both perfect and imperfect CSI. Analytical expressions are derived for the BEP of the system composed of a wideband deterministic SOS channel simulator, which is introduced as the actual BEP. Since the SOS channel simulator is derived from a nonrealizable reference channel model, for comparison, we also present the BEP of a BPSK OFDM system in the presence of a reference model, which is introduced as the reference BEP. From our derived BEP expressions, we study the deviation of the actual BEP from the reference BEP, which is caused by the finite number of sinusoids used in the channel simulator. The deviation of the BEP enables us to reduce the channel simulator realization expenditure to a minimum, where the performance degradation is negligible. It is proved that the actual BEP approaches to the reference BEP as the number of sinusoids tends to infinity. Moreover, we determine the maximum time lag over which the temporal autocorrelation function (ACF) has a strong influence on the BEP. Such a maximum time lag provides important information for some parameter design methods, e.g., the L_p-Norm method [8]. Finally, we compare the performance of the stochastic parameter computation method (MCM) with the deterministic one (GMEDS$_1$).

The rest of the paper is structured as follows. In Section II, we briefly review the wideband reference channel model and the corresponding SOS channel simulator. Under the assumption of perfect CSI, Section III analyzes the performance of a BPSK OFDM system by using a wideband SOS channel simulator. Section IV concentrates on the performance analysis of a pilot-based BPSK OFDM system in the presence of imperfect CSI. Finally, the conclusions are drawn in Section V.

II. WIDEBAND CHANNEL MODELS

Section II mainly studies the statistical properties of the wideband reference channel and the corresponding SOS channel simulator, which are relevant to the subject of this paper.

A. *The Wideband Reference Channel Model*

Under the assumption of wide-sense stationary uncorrelated scattering (WSSUS) [1], the time-variant transfer function of the reference channel model can be expressed as

$$H(f',t) = \sum_{\ell=1}^{\mathscr{L}} a_\ell \mu_\ell(t) e^{-j2\pi f' \tau'_\ell}. \tag{1}$$

Here, $\mathscr{L}$ is the number of discrete propagation paths. The path gain and the propagation delay of the ℓth path are denoted by the quantities a_ℓ and τ'_ℓ, respectively.

We assume that the power constraint $\sum_{\ell=1}^{\mathscr{L}} a_\ell^2 = 1$ is fulfilled to ensure that the average power of the channel model is normalized to unity [8]. In (1), the processes $\mu_\ell(t)$ represent uncorrelated zero-mean complex Gaussian random processes, each having the variance $2\sigma_0^2 = 1$.

For isotropic scattering environments, the temporal ACF $r_{HH}(\tau) = E\{H^*(f',t) H(f',t+\tau)\}$ of $H(f',t)$ is given by

$$r_{HH}(\tau) = 2\sigma_0^2 J_0(2\pi f_{\max}\tau), \tag{2}$$

where $J(\cdot)$ denotes the zeroth-order Bessel function of the first kind and $f_{\max}$ is the maximum Doppler frequency [8].

Let us denote the envelope of the time-variant transfer function $H(f',t)$ at a specific frequency $f' = f_0'$ as $\zeta(t) = |H(f_0',t)|$. According to (1), $H(f_0',t)$ is a superposition of $\mathscr{L}$ weighted statistically uncorrelated Gaussian processes $\mu_\ell(t)$. It follows that $H(f_0',t)$ is a zero-mean complex Gaussian random process with the variance $\sigma_H^2 = 2\sigma_0^2$. Thus, the probability density function (PDF) $p_\zeta(r)$ of the envelope $\zeta(t)$ follows the Rayleigh distribution [13].

B. The Wideband SOS Channel Simulator

Reference models are nonrealizable due to their tremendously high realization complexity. By applying Rice's SOS principle combined with the concept of deterministic channel modeling [8], we can easily derive an efficient SOS channel simulator from the reference model, which can be used for the purpose of system simulations.

The time-variant transfer function $\tilde{H}(f',t)$ of the wideband SOS channel simulator can be expressed as

$$\tilde{H}(f',t) = \sum_{\ell=1}^{\mathscr{L}} a_\ell \tilde{\mu}_\ell(t) e^{-j2\pi f' \tau_\ell'}, \tag{3}$$

where $\tilde{\mu}_\ell(t) = \tilde{\mu}_{1,\ell}(t) + j\tilde{\mu}_{2,\ell}(t)$ represents a deterministic Gaussian process. According to Rice's SOS method, $\tilde{\mu}_{i,\ell}(t)$ can be described mathematically as

$$\tilde{\mu}_{i,\ell}(t) = \sum_{n=1}^{N_{i,\ell}} c_{i,n,\ell} \cos(2\pi f_{i,n,\ell} + \theta_{i,n,\ell}), \quad i = 1,2, \tag{4}$$

where $N_{i,\ell}$ denotes the number of sinusoids belonging to the real part ($i = 1$) or the imaginary part ($i = 2$) of $\tilde{\mu}_\ell(t)$. In (4), the parameters $c_{i,n,\ell}$, $f_{i,n,\ell}$, and $\theta_{i,n,\ell}$ represent the Doppler coefficient, the Doppler frequency, and the Doppler phase of the ℓth path, respectively. In this paper, two parameter computation methods are applied to determine these parameters.

1) The GMEDS$_1$ [9]: according to the GMEDS$_1$, the parameters $c_{i,n,\ell}$ and $f_{i,n,\ell}$ are given by

$$c_{i,n,\ell} = \sigma_0 \sqrt{\tfrac{2}{N_{i,\ell}}}, \qquad\qquad f_{i,n,\ell} = f_{\max} \sin\left[\tfrac{\pi}{2N_{i,\ell}}\left(n - \tfrac{1}{2}\right) + \alpha_{i,\ell}\right], \qquad\qquad \text{(5a,b)}$$

where $\alpha_{i,\ell} = (-1)^{i-1}\pi\ell/(4N_{i,\ell}\mathcal{L})$ is the angle of rotation.

2) The MCM [4]: based on the MCM, the primary parameters can be determined by the equations

$$c_{i,n,\ell} = \sigma_0 \sqrt{\tfrac{2}{N_{i,\ell}}}, \qquad\qquad f_{i,n,\ell} = f_{\max} \sin\left(\tfrac{\pi}{2}u_{n,\ell}\right), \qquad\qquad \text{(6a,b)}$$

where $u_{n,\ell}$ is a random variable uniformly distributed over the interval $(0,1]$. For both methods, the phases $\theta_{i,n,\ell}$ are considered as outcomes of a random generator with a uniform distribution over $(0,2\pi]$.

When designing the wideband SOS channel simulator, it has to be taken into account that the processes $\tilde{\mu}_\ell(t)$ are uncorrelated for different propagation paths. Such a condition can easily be guaranteed if the resulting sets $\{f_{i,n,\ell}\}$ are disjoint for different propagation paths. For both methods, we can choose the same number of sinusoids $N_{i,\ell}$ not only for the real and imaginary parts of $\tilde{\mu}_\ell(t)$, but also for all propagation paths, i.e., $N_{1,\ell} = N_{2,\ell} = N$ for $\ell = 1, 2, \ldots, \mathcal{L}$.

The temporal ACF of $\tilde{H}(f',t)$ is given by [8]

$$\tilde{r}_{HH}(\tau) = \sum_{\ell=1}^{\mathcal{L}} a_\ell^2 \tilde{r}_{\mu_\ell\mu_\ell}(\tau), \qquad\qquad \text{(7)}$$

where $\tilde{r}_{\mu_\ell\mu_\ell}(\tau) = \sum_{i=1}^{2}\sum_{n=1}^{N_{i,\ell}}(c_{i,n,\ell}^2/2)\cos(2\pi f_{i,n,\ell}\tau)$ describes the temporal ACF of the deterministic process $\tilde{\mu}_\ell(t)$.

We denote the envelope of the time-variant transfer function $\tilde{H}(f',t)$ at a specific frequency $f' = f_0'$ as $\tilde{\zeta}(t) = |\tilde{H}(f_0',t)|$. By applying the concept of the characteristic function and using similar mathematical techniques as described in [8, pp. 64–68], we obtain the PDF $\tilde{p}_\zeta(r)$ of the envelope $\tilde{\zeta}(t)$ in the form

$$\tilde{p}_\zeta(r) = 4\pi r \int_0^\pi \int_0^\infty \prod_{\ell=1}^{\mathcal{L}} [h_{1,\ell}(y,\theta) \cdot h_{1,\ell}'(y,\theta) \cdot h_{2,\ell}(y,\theta) \cdot h_{2,\ell}'(y,\theta)] \cdot J_0(2\pi r y)\, y\, dy\, d\theta,$$

$$\text{(8)}$$

where

$$h_{1,\ell}(y,\theta) = \prod_{n=1}^{N_{1,\ell}} J_0[2\pi a_\ell y \cos\theta \cos(2\pi f_0' \tau_\ell') c_{1,n,\ell}], \tag{9a}$$

$$h_{1,\ell}'(y,\theta) = \prod_{n=1}^{N_{1,\ell}} J_0[2\pi a_\ell y \sin\theta \sin(2\pi f_0' \tau_\ell') c_{1,n,\ell}], \tag{9b}$$

$$h_{2,\ell}(y,\theta) = \prod_{m=1}^{N_{2,\ell}} J_0[2\pi a_\ell y \cos\theta \sin(2\pi f_0' \tau_\ell') c_{2,m,\ell}], \tag{9c}$$

$$h_{2,\ell}'(y,\theta) = \prod_{m=1}^{N_{2,\ell}} J_0[2\pi a_\ell y \sin\theta \cos(2\pi f_0' \tau_\ell') c_{2,m,\ell}]. \tag{9d}$$

The theoretical results for the PDF $p_\zeta(r)$ and $\tilde{p}_\zeta(r)$ [see (8)] are illustrated in Fig. E.1. The channel simulator is designed by the GMEDS$_1$ with $N = 6$. It can be seen from Fig. E.1 that $\tilde{p}_\zeta(r)$ approximates to $p_\zeta(r)$ very well. This observation is also confirmed by simulations. We show in Appendix E.A that $\tilde{p}_\zeta(r) \to p_\zeta(r)$ if $N_{i,\ell} \to \infty$.

III. SYSTEM PERFORMANCE WITH PERFECT CSI

Under the assumption of perfect CSI, this section will analyze the performance of the wideband SOS channel simulator w.r.t. the BEP of the BPSK OFDM system.

In fading channels, we can derive the BEP by averaging the conditional BEP over the fading channel statistics [11], i.e.,

$$\tilde{P}_b = \int_0^\infty P_{b|\zeta}(r)\tilde{p}_\zeta(r)dr. \tag{10}$$
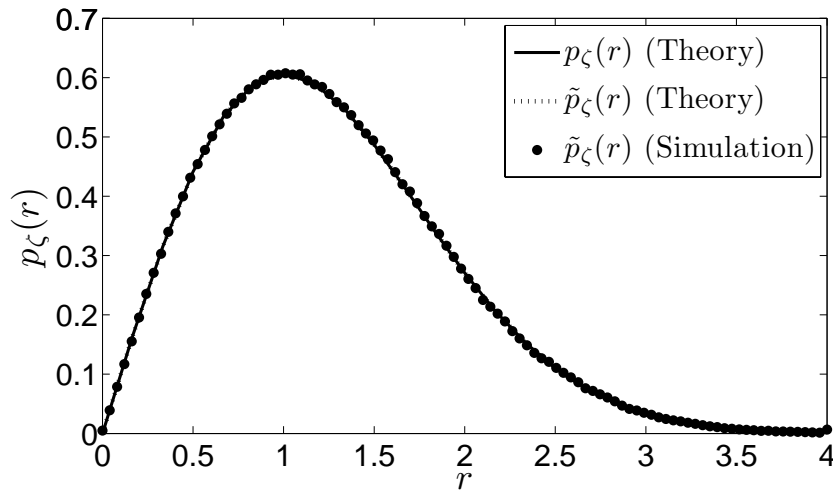
Figure E.1: Probability density function $p_\zeta(r)$ of the absolute value of the time-variant transfer function $\zeta(t) = |H(f_0', t)|$.

The conditional BEP $P_{b|\zeta}(r)$ in (10) is given by [11]

$$P_{b|\zeta}(r) = \frac{1}{2}\text{erfc}\left(r\sqrt{\frac{E_b}{N_0}}\right) \tag{11}$$

for the BPSK scheme. In (11), $\text{erfc}(x) = \int_x^\infty \frac{2}{\sqrt{\pi}}e^{-y^2}dy$ represents the complementary error function and E_b/N_0 denotes the bit-to-noise ratio.

After substituting (8) and (11) into (10), and carrying out some algebraic manipulations (see Appendix E. B), we finally obtain the BEP expression for the BPSK OFDM system using the channel simulator

$$\tilde{P}_b = \frac{1}{2\pi}\int\limits_0^\pi \int\limits_0^\infty \frac{1}{y} \cdot e^{-\frac{\pi^2 y^2}{2\overline{\gamma}_b}} \cdot M_{\frac{1}{2},\frac{1}{2}}\left(\frac{\pi^2 y^2}{\overline{\gamma}_b}\right) \tag{12}$$
$$\prod_{\ell=1}^{\mathscr{L}}[h_{1,\ell}(y,\theta) \cdot h'_{1,\ell}(y,\theta)][h_{2,\ell}(y,\theta) \cdot h'_{2,\ell}(y,\theta)]\,dy\,d\theta,$$

where $\overline{\gamma}_b = 2\sigma_0^2 E_b/N_0$ is the average signal-to-noise ratio (SNR) per bit and $M_{\lambda,\mu}(x)$ is the Whittaker function [3].

As discussed in Section II, the absolute value of the time-variant transfer function $H(f_0',t)$ of the reference model is Rayleigh distributed. Thus, the BEP for the BPSK OFDM system using the reference model can be formulated as [11]

$$P_b = \frac{1}{2}\left(1 - \sqrt{\frac{\overline{\gamma}_b}{1 + \overline{\gamma}_b}}\right). \tag{13}$$

It is shown in Appendix E. C that the BEP $\tilde{P}_b$ in (12) converges to the reference BEP P_b [see (13)] if $N_{i,\ell} \to \infty$.

The analytical result for the reference BEP P_b given by (13) is shown in Fig. E.2. This figure also shows the BEP performance evaluated by employing the wideband SOS simulators designed with the MCM and the GMEDS$_1$. All the presented results are obtained by using the 6-path Rural Area channel model specified by COST 207 [8]. We further assume that each OFDM symbol consists of $K = 128$ subcarriers. A cyclic prefix (CP) sequence with 16 samples is appended to each OFDM symbol. The sampling duration T equals $0.1\mu s$. The theoretical results in Fig. E.2 are also validated by simulations.

It can be seen from Fig. E.2 that the approximation $P_b \approx \tilde{P}_b$ is excellent. The channel simulators designed with the GMEDS$_1$ and the MCM are equivalent w.r.t. the impact on the BEP. The reason for this observation is that the BEP $\tilde{P}_b$ is depen-
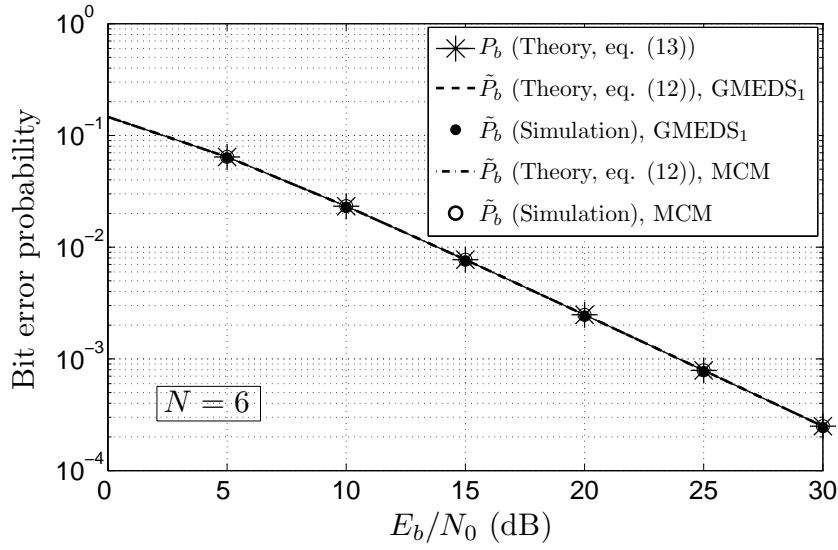
Figure E.2: BPSK OFDM system performance using the reference channel model and the channel simulators designed with the GMEDS$_1$ and the MCM.

dent on the Doppler coefficients $c_{i,n,\ell}$, which are the same for the GMEDS$_1$ and the MCM.

Finally, we measure the deviation of the BEP in (12) from the reference BEP in (13) by the so-called relative error

$$\varepsilon_{BEP} = \frac{\tilde{P}_b - P_b}{P_b}. \tag{14}$$

The relative error of the BEP enables us to reduce the channel realization expenditure to a minimum, such that the deviation from the reference BEP P_b can be neglected. Figure E.3 illustrates the relative error ε_{BEP} for various values of N. It can be seen from this figure that, even for $N = 3$, the absolute value of ε_{BEP} is below 4.1%, which can be tolerated in most practical applications. Therefore, the approximation $\tilde{P}_b \approx P_b$ is astonishingly good if $N \geq 3$.

IV. SYSTEM PERFORMANCE WITH IMPERFECT CSI

In the following, we study the BPSK OFDM system performance assuming imperfect CSI. Suppose that we insert a pilot symbol before every block of P OFDM symbols. By applying the least-square (LS) estimation algorithm [11], we estimate the CSI at the pilot position, which is also used for the symbol decisions for the next P OFDM symbol interval.
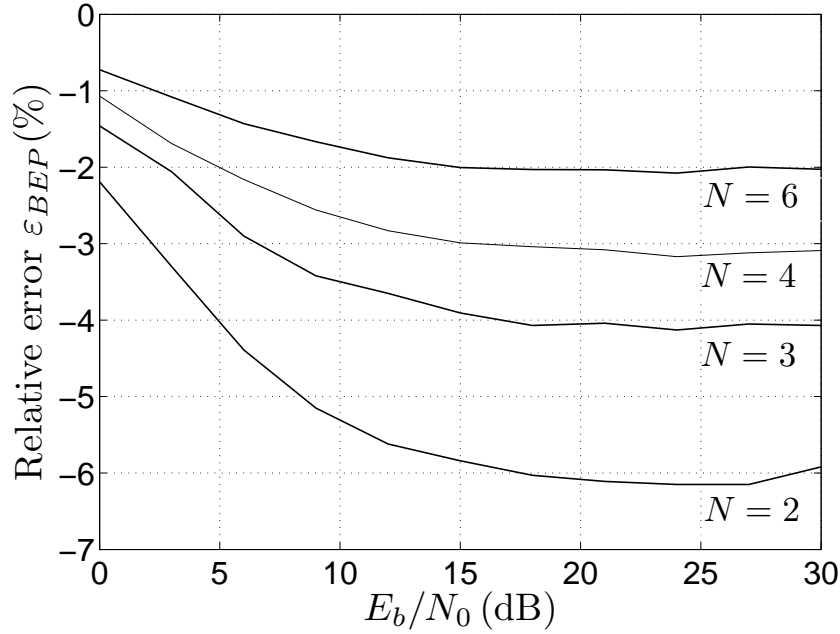
Figure E.3: Evaluation of the relative error of the BEP ε_{BEP} for various values of the number of sinusoids N.

If the mth symbol is a pilot symbol, according to the LS algorithm, the estimated CSI is determined by

$$\hat{H}_{km} = H_{km} + V_{km}, \quad k = 1, 2, \dots, K, \tag{15}$$

where $\hat{H}_{km}$ and H_{km} describe the estimated and the real CSI of the kth subchannel in the mth symbol time slot. In this equation, V_{km} represents the error term due to the presence of additive white Gaussian noise (AWGN). Both the error term V_{km} and the AWGN noise have the same variance denoted by $2\sigma_n^2$ [2]. Since H_{km} and V_{km} are independent complex Gaussian random variables, the resulting estimated CSI $\hat{H}_{km}$ remains a Gaussian random variable with the variance $\hat{\sigma}_H^2 = 2\sigma_0^2 + 2\sigma_n^2$.

According to [2], the BEP of the $(m+p)$th OFDM symbol can be written as

$$P_p = \frac{1}{2} \left[1 - \frac{\rho_1}{\sqrt{1 + \frac{1}{\bar{\gamma}_b} + \rho_2}} \right], \quad p = 1, 2, \dots, P, \tag{16}$$

where ρ_1 and ρ_2 represent the real and imaginary parts of the correlation coefficient of $\hat{H}_{km}$ and H_{km}. For isotropic scattering environments, we have $\rho_1 = \frac{r_{HH}(p \cdot T_s)}{\sigma_H \hat{\sigma}_H}$ and $\rho_2 = 0$, where T_s represents the OFDM symbol duration.

Thus, the average reference BEP on condition that the pilot sequence is inserted before *P* OFDM symbols is given by

$$P_b = \sum_{p=1}^{P} \frac{1}{P} P_p = \frac{1}{2} \left[1 - \frac{\sum\limits_{p=1}^{P} r_{HH}(p \cdot T_s)}{2\sigma_0^2 P(1 + \frac{1}{\bar{\gamma}_b})} \right]. \tag{17}$$

On the assumption that the PDF $\tilde{p}_\zeta(r)$ is close to the PDF $p_\zeta(r)$ of the reference model, the actual BEP is closely related to the expression (17). We only need to replace $r_{HH}(p \cdot T_s)$ in (17) by $\tilde{r}_{HH}(p \cdot T_s)$, which is defined in (7). Thus, we can formally write

$$\tilde{P}_b \approx \frac{1}{2} \left[1 - \frac{\sum\limits_{p=1}^{P} \tilde{r}_{HH}(p \cdot T_s)}{2\sigma_0^2 P(1 + \frac{1}{\bar{\gamma}_b})} \right]. \tag{18}$$

From (17) and (18), we realize that the temporal ACF has a strong influence on the BEP. Furthermore, the deviation of the temporal ACF $\tilde{r}_{HH}(\tau)$ from the ACF $r_{HH}(\tau)$ of the reference model has a significantly influence on the relative error of the BEP. It is worth mentioning that, according to our analysis, we find the interval $[0, P \cdot T_s]$, over which the approximation $\tilde{r}_{HH}(\tau) \approx r_{HH}(\tau)$ is of special interest.

According to (7) and the results in [10], the temporal ACF of a wideband channel simulator can be approximated by

$$\tilde{r}_{HH}(p \cdot T_s) \approx r_{HH}(p \cdot T_s) - \frac{(p \cdot T_s)^2}{2} \sum_{\ell=1}^{\mathscr{L}} a_\ell^2 \triangle \beta_\ell. \tag{19}$$

Here, $\triangle \beta_\ell$ describes the model error introduced by an imperfect channel simulator.

After substituting the preceding approximation into (18) and taking (17) into account, we obtain

$$\tilde{P}_b = P_b + \triangle P_b, \tag{20}$$

where

$$\triangle P_b = \frac{\sum\limits_{p=1}^{P} \left(\frac{p \cdot T_s}{2} \right)^2 \sum\limits_{\ell=1}^{\mathscr{L}} a_\ell^2 \triangle \beta_\ell}{2\sigma_0^2 P(1 + \frac{1}{\bar{\gamma}_b})} \tag{21}$$

denotes the deviation of the BEP.

For the GMEDS$_1$, it has been proved in [8] that the model error $\triangle\beta_\ell$ is zero. Thus, the deviation of the BEP results in $\triangle P_b = 0$, which means that the BEP $\tilde{P}_b$ given by (18) equals the reference BEP P_b in (17). The result for the reference BEP P_b and actual BEP $\tilde{P}_b$ are presented in Fig. E.4, which describes the performance of OFDM system using the reference channel model and the channel simulator. It can be seen that the actual BEP $\tilde{P}_b$ coincides exactly with the reference BEP P_b.

For the MCM, the model error $\triangle\beta_\ell$ is approximately normally distributed with zero-mean and the variance $\text{Var}\{\triangle\beta_\ell\} = \beta_\ell^2/N$, where $\beta_\ell = -\ddot{r}_{\mu_\ell\mu_\ell}(0) = (2\pi f_{\max}\sigma_0)^2$ [8]. We find that in the limit $\bar{\gamma}_b \to \infty$, the relative error ε_{BEP} in (14) is approximately Gaussian distributed with zero-mean and variance

$$\text{Var}\left\{\frac{\triangle P_b}{P_b}\right\} \approx \text{Var}\left\{\sum_{\ell=1}^{\mathscr{L}} a_\ell^2 \triangle\beta_\ell \Big/ \sum_{\ell=1}^{\mathscr{L}} a_\ell^2 \beta_\ell\right\} = \frac{1}{N}. \tag{22}$$

The BEPs P_b and $\tilde{P}_b$ computed according to (17) and (18) are presented in Fig. E.5 for $f_{\max} = 100\,\text{Hz}$ and $f_{\max} = 500\,\text{Hz}$. The channel parameters have been computed by applying the MCM. It is shown that increasing $f_{\max}$ or the value of P leads to BEP performance degradations. We observe that a single realization of the BEP $\tilde{P}_b$ deviates in a random manner from the reference BEP P_b. The deviation from P_b becomes larger if the maximum Doppler frequency $f_{\max}$ or the value of P is increased.
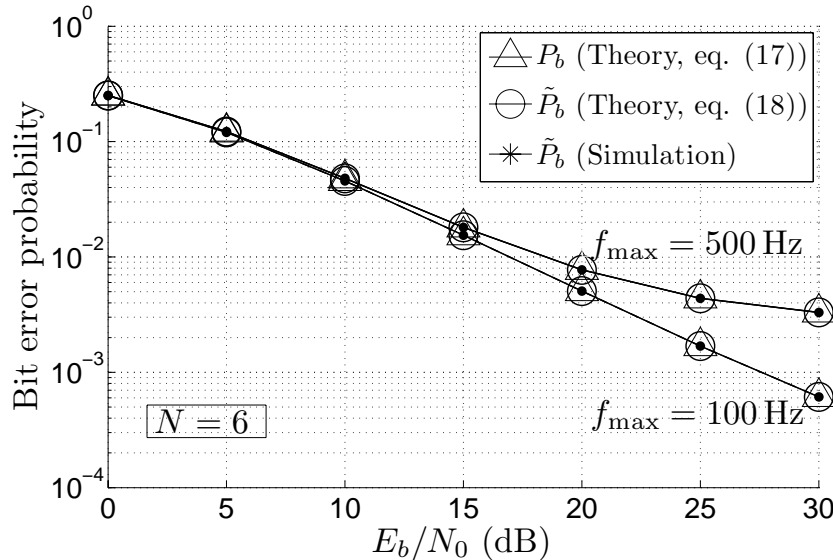
Figure E.4: Pilot-based OFDM system performance using the reference channel model and the channel simulator designed with the GMEDS$_1$ (single realization, $P = 5$, $T_s = 12.8\,\mu s$).
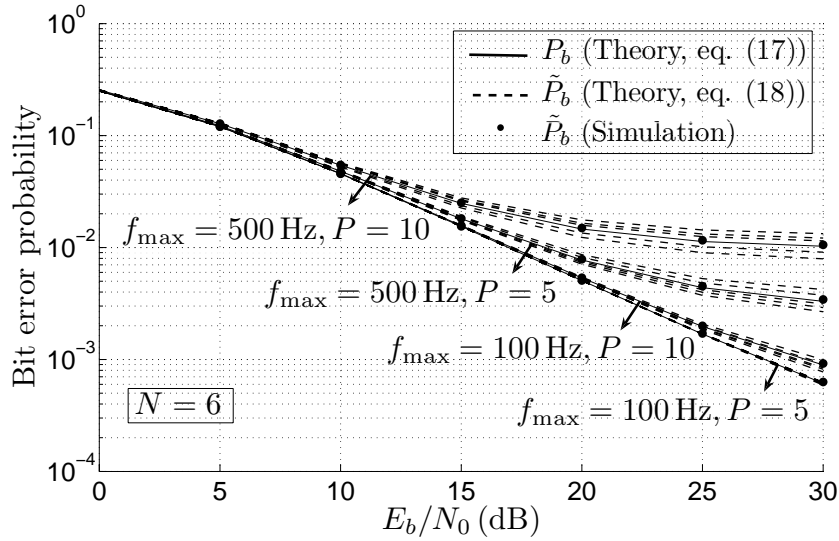
Figure E.5: Pilot-based OFDM system performance using the reference channel model and the channel simulator designed with the MCM (5 realizations, $T_s = 12.8\,\mu s$).

V. CONCLUSION

This paper has analyzed the performance of wideband SOS channel simulators w.r.t. the BEP of BPSK OFDM systems. Analytical expressions for the BEP have been derived for these systems in the presence of perfect and imperfect CSI.

Under the assumption of perfect CSI, it is shown by theory and confirmed by simulations that both parameter computation methods, the GMEDS$_1$ and the MCM, are equivalent w.r.t. the BEP. We have demonstrated that the actual BEP evaluated in the presence of a SOS channel simulator converges to the reference BEP if the number of sinusoids tends to infinity. It turns out that the absolute value of the relative error of the BEP is below 4.1% if $N \geq 3$.

In the presence of imperfect CSI, closed-form expressions have been presented not only for the actual BEP but also for the deviation of the BEP. It is shown that the BEP performance degrades if the maximum Doppler frequency or the pilot-inserted period increases. It has been shown that the relative error of the BEP is zero if the GMEDS$_1$ is applied to design the channel simulator. However, if the MCM is used, the actual BEP deviates in a random manner from the reference BEP. The deviation of the BEP becomes larger with increasing the maximum Doppler frequency or the pilot-inserted period. We proved that the relative error of the BEP is approximately Gaussian distributed as the average SNR tends to infinity. Thus, we can conclude that, assuming imperfect CSI, the GMEDS$_1$ outperforms the MCM w.r.t. the BEP deviation. All theoretical results in this paper have been confirmed by simulations.

E. A   Proof of $\tilde{p}_\zeta(r) \to p_\zeta(r)$

Due to [4, p. 335], the functions $h_{1,\ell}(y,\theta)$ and $h'_{1,\ell}(y,\theta)$ tend to

$$h_{1,\ell}(y,\theta) = e^{-2(\pi a_\ell y \sigma_0)^2 \cos^2(\theta) \cos^2(2\pi f' \tau'_\ell)}, \tag{A.1a}$$

$$h'_{1,\ell}(y,\theta) = e^{-2(\pi a_\ell y \sigma_0)^2 \sin^2(\theta) \sin^2(2\pi f' \tau'_\ell)}, \tag{A.1b}$$

if $N_{1,\ell} \to \infty$. Similarly, if $N_{2,\ell} \to \infty$, then we obtain

$$h_{2,\ell}(y,\theta) = e^{-2(\pi a_\ell y \sigma_0)^2 \cos^2(\theta) \sin^2(2\pi f' \tau'_\ell)}, \tag{A.2a}$$

$$h'_{2,\ell}(y,\theta) = e^{-2(\pi a_\ell y \sigma_0)^2 \sin^2(\theta) \cos^2(2\pi f' \tau'_\ell)}. \tag{A.2b}$$

By submitting the right-hand side of (A.1a)–(A.2b) in (8) and performing the integration over the variable θ give us

$$\lim_{N_{i,\ell} \to \infty} \tilde{p}_\zeta(r) = 4\pi^2 r \int_0^\infty J_0(2\pi r y) \cdot e^{-2(\pi y \sigma_0)^2} y \, dy. \tag{A.3}$$

Then, by making use of the relation [3, Eq. (6.631.4)]

$$\int_0^\infty y e^{-\alpha y^2} J_0(\beta y) dy = \frac{e^{-\frac{\beta^2}{4\alpha}}}{2\alpha}, \quad \text{Re}\{\alpha\} > 0, \beta > 0, \tag{A.4}$$

we obtain

$$\lim_{N_{i,\ell} \to \infty} \tilde{p}_\zeta(r) = \frac{r}{\sigma_0^2} e^{-\frac{r^2}{2\sigma_0^2}}, \quad r \geq 0, \tag{A.5}$$

which is known as the Rayleigh distribution.

E. B   Derivation of the BEP $\tilde{P}_b$

Substituting (8) and (11) into (10), we obtain

$$\tilde{P}_b = \int_0^\pi \int_0^\infty \int_0^\infty \text{erfc}\left(r\sqrt{\frac{E_b}{N_0}}\right) \prod_{\ell=1}^{\mathscr{L}} [h_{1,\ell}(y,\theta) \cdot h'_{1,\ell}(y,\theta)]$$

$$[h_{2,\ell}(y,\theta) \cdot h'_{2,\ell}(y,\theta)] \cdot 2\pi r y \cdot J_0(2\pi r y) \, dr \, dy \, d\theta. \tag{B.1}$$

We can reduce the threefold integral on the right-hand side of (B.1) to a double integral by using [3, Eq. (6.784.1)]

$$\int_0^\infty x^{\nu+1}\mathrm{erfc}(ax)J_\nu(bx)dx = a^{-\nu}\frac{\Gamma(\nu+\frac{3}{2})}{b^2\cdot\Gamma(\nu+2)}e^{-\frac{b^2}{8a^2}}\cdot M_{\frac{1}{2}\nu+\frac{1}{2},\frac{1}{2}\nu+\frac{1}{2}}\left(\frac{b^2}{4a^2}\right), \quad \text{(B.2)}$$

where $|\arg a| < \dfrac{\pi}{4}$, $b > 0$, and $\mathrm{Re}\{\nu\} > -1$. After carrying out some algebraic manipulations, we finally obtain (12).

E. C   Proof of $\tilde{P}_b \to P_b$ hold if $N_{i,\ell} \to \infty$

If we put the right-hand side of (A.1a)–(A.2b) in (12) and solve the integral over the variable θ, (12) simplifies to

$$\tilde{P}_b = \frac{1}{2}\int_0^\infty \frac{1}{y}e^{-\frac{\pi^2 y^2}{2\tilde{\gamma}_b}}M_{\frac{1}{2},\frac{1}{2}}\left(\frac{\pi^2 y^2}{\tilde{\gamma}_b}\right)\cdot e^{-2(\pi y\sigma_0)^2}dy. \quad \text{(C.1)}$$

The remaining integral over y can be solved by making use of Eq. (7.621.8) in [3]. Finally, if $N_{i,\ell} \to \infty$, we find $\tilde{P}_b = P_b$.

REFERENCES

[1] P. A. Bello. Characterization of randomly time-variant linear channels. *IEEE Trans. Commun. Syst.*, 4:360–393, Dec. 1963.

[2] M. Chang and Y. T. Su. Performance analysis of equalized OFDM systems in Rayleigh fading. *IEEE Trans. Commun.*, 1(4):721–732, Oct. 2002.

[3] I. S. Gradshteyn and I. M. Ryzhik. *Tables of Integrals, Series, and Products*. Academic Press, 6th edition, 2000.

[4] P. Hoeher. A statistical discrete-time model for the WSSUS multipath channel. *IEEE Trans. Veh. Technol.*, 41(4):461–468, Nov. 1992.

[5] W. C. Jakes. *Microwave Mobile Communications*. New Jersey: IEEE Press, 1994.

[6] Y. Ma and M. Pätzold. A wideband one-ring MIMO channel model under non-isotropic scattering conditions. In *Proc. 67th Vehicular Technology Conference, VTC 2008-Spring*, pages 424–429. Singapore, May 2008.

[7] V. D. Nguyen and M. Pätzold. Least square channel estimation using special training sequences for MIMO-OFDM systems in the presence of intersymbol interference,. In *Proc. Nordic Radio Symposium (NRS) 2004, including the Finnish Wireless Communications Workshop (FWCW) 2004*. Oulu, Finland, Aug. 2004.

[8] M. Pätzold. *Mobile Fading Channels*. Chichester: John Wiley & Sons, 2002.

[9] M. Pätzold and B. O. Hogstad. Two new methods for the generation of multiple uncorrelated Rayleigh fading waveforms. In *Proc. 63th Vehicular Technology Conference, VTC 2006-Spring*, volume 6, pages 2782–2786. Melbourne, Australia, May 2006.

[10] M. Pätzold and F. Laue. The performance of deterministic Rayleigh fading channel simulators with respect to the bit error probability. In *Proc. 51st Vehicular Technology Conference, VTC 2000-Spring*. Tokyo, Japan, May 2000.

[11] J. Proakis. *Digital Communications*. New York: McGraw-Hill, 3rd edition, 1995.

[12] S. O. Rice. Mathematical analysis of random noise. *Bell Syst. Tech. J.*, 23:282–332, Jul. 1944.

[13] M. K. Simon and M.-S. Alouini. *Digital Communication Over Fading Channels*. New Jersey: Wiley & Sons, 2005.

Appendix F

Paper VI

Performance Analysis of Wideband Sum-of-Cisoids-Based Channel Simulators with Respect to the Bit Error Probability of DPSK OFDM System

Yuanyuan Ma and Matthias Pätzold

Department of Information and Communication Technology

Faculty of Engineering and Science, University of Agder

Servicebox 509, NO-4898 Grimstad, Norway

E-mails: {yuanyuan.ma, matthias.paetzold}@uia.no

Abstract — **In this paper, we analyze the performance of a wideband sum-of-cisoids (SOC) channel simulator w.r.t. the bit error probability (BEP) of differential phase-shift keying (DPSK) orthogonal frequency division multiplexing (OFDM) systems. Analytical BEP expressions are derived for coherent and noncoherent DPSK OFDM simulation systems in the presence of a wideband SOC channel simulator. We also study the degradations of the BEP introduced by an imperfect channel simulator. Using the deviation of the BEP as an appropriate measure, we evaluate the performance of three parameter computation methods, known as the method of exact Doppler spread (MEDS), the randomized MEDS (R-MEDS), and the Monte Carlo method (MCM). For coherent DPSK OFDM systems, it turns out that these three methods are equivalent. For noncoherent DPSK OFDM systems, it is theoretically shown that both the MEDS and the R-MEDS outperform the MCM. The correctness of all theoretical results are validated by simulations.**

I. INTRODUCTION

Rice's sum-of-sinusoids (SOS) principle has been accepted as a proper method for modeling mobile fading channels [13, 14, 7]. By applying the SOS principle combined with the concept of deterministic channel modeling [7], accurate and efficient SOS channel simulators can be easily designed for all kinds of channel models that can be derived from Gaussian random processes. Such channel simulators have been commonly used in system simulations due to their low realization expenditure. In recent years, the performance analysis of SOS channel simulators has been an important research subject. In [10], the performance of narrowband SOS channel simulators w.r.t. the BEP has been investigated.

The SOS method has been extensively employed in modeling flat fading channels [7], frequency-selective channels [7], and even wideband multiple-input multiple-output channels [6]. However, it has been shown in [11] that the SOS principle is of advantage for developing mobile radio channels in isotropic scattering environments, while in case of non-isotropic scattering environments, the SOC method is more efficient. So far, the performance of SOC channel simulators w.r.t. the BEP has not been studied. The purpose of this paper is to fill this gap.

In this paper, we study the performance of a DPSK OFDM system in the presence of a stochastic wideband SOC channel simulator w.r.t. the BEP of the simulation system. For comparison, we present the BEP of a DPSK OFDM system using a reference channel model, which is known as the reference BEP. As a starting point, we study the probability density functions (PDFs) of the absolute value of the time-variant transfer function and the temporal-frequency correlation function (CF) of both channel models. Next, we derive the BEP expressions for the OFDM systems using coherent and noncoherent DPSK schemes. For the coherent DPSK OFDM system, we demonstrate that the BEP of the simulation system approaches to the reference BEP if the number of cisoids in the SOC channel simulator tends to infinity. Based on the analytical BEP results, we discuss the deviation between the reference BEP and the BEP of the simulation system. Then, we compare the performance of three parameter computation methods: the MEDS, the R-MEDS, and the MCM. We assume isotropic scattering conditions here. However, it should be mentioned that the obtained BEP expressions are general and also applicable to non-isotropic scattering conditions.

The rest of this paper is organized as follows. In Section II, we first give a brief review of the frequency-selective reference channel model and the corresponding SOC channel simulator. Then, we study the statistical properties of both channel models. Section III provides an analysis of the BEP performance of coherent DPSK OFDM systems. In Section IV, we concentrate on the noncoherent DPSK OFDM system performance analysis. Finally, the conclusions are given in Section VI.

II. Frequency-Selective Channel Models

In this section, a wide-sense stationary uncorrelated scattering (WSSUS) model [7, 1] is employed as an appropriate frequency-selective reference channel from which the SOC channel simulator is derived.

A. The Frequency-Selective Reference Channel Model

The time-variant transfer function of the wideband reference channel model can be

formulated as [7]

$$H(f',t) = \sum_{\ell=1}^{\mathscr{L}} a_\ell \mu_\ell(t) e^{-j2\pi f' \tau'_\ell}, \tag{1}$$

where $\mathscr{L}$ denotes the number of discrete propagation paths. The quantities a_ℓ and τ'_ℓ describe the path gain and the propagation delay of the ℓth discrete propagation path, respectively. The symbol $\mu_\ell(t)$ in (1) represents a complex random Gaussian process. It is supposed that the constraint $\sum_{\ell=1}^{\mathscr{L}} a_\ell^2 = 1$ holds to ensure that the average power of the channel model is normalized to unity. We assume that the real and imaginary parts of $\mu_\ell(t)$ in (1) are uncorrelated Gaussian processes with zero-mean and the same variance $\sigma_0^2 = 1/2$.

Let $r_{HH}(v',\tau) = E\{H^*(f',t)H(f'+v',t+\tau)\}$ be the temporal-frequency CF of $H(f',t)$. According to [8], $r_{HH}(v',\tau)$ can be expressed in closed-form as

$$r_{HH}(v',\tau) = \sum_{\ell=1}^{\mathscr{L}} a_\ell^2 r_{\mu_\ell \mu_\ell}(\tau) e^{-j2\pi v' \tau'_\ell}, \tag{2}$$

where $r_{\mu_\ell \mu_\ell}(\tau)$ denotes the temporal autocorrelation function (ACF) of the Gaussian process $\mu_\ell(t)$. If we consider isotropic scattering conditions, the temporal ACF can be written as

$$r_{\mu_\ell \mu_\ell}(\tau) = 2\sigma_0^2 J_0(2\pi f_{\max} \tau), \tag{3}$$

where $J(\cdot)$ represents the zeroth-order Bessel function of the first kind and $f_{\max}$ is the maximum Doppler frequency.

According to (1), the real part and the imaginary part of $H(f',t)$ are statistically independent Gaussian processes, each having the variance σ_0^2. Let us denote the envelope of the time-variant transfer function $H(f',t)$ at a specific carrier frequency $f' = f_0'$ as $\zeta(t) = |H(f_0',t)|$. The PDF of the envelope $\zeta(t)$ can be described by the Rayleigh distribution [12]

$$p_\zeta(r) = \begin{cases} \dfrac{r}{\sigma_0^2} e^{-\frac{r^2}{2\sigma_0^2}}, & r \geq 0, \\[2mm] 0, & r < 0. \end{cases} \tag{4}$$

B. Frequency-Selective SOC Channel Simulator

In this subsection, we design a frequency-selective channel simulator by making use of the SOC principle.

In the reference model described by (1), we replace the Gaussian processes $\mu_\ell(t)$ by stochastic complex processes $\hat{\mu}_\ell(t)$ $(\ell = 1, 2, \ldots, \mathscr{L})$, which can be represented by a sum of N_ℓ cisoids as follows [11]

$$\hat{\mu}_\ell(t) = \sum_{n=1}^{N_\ell} c_{n,\ell} e^{j(2\pi f_{n,\ell} t + \theta_{n,\ell})}, \tag{5}$$

where $c_{n,\ell}$, $f_{n,\ell}$, and $\theta_{n,\ell}$ represent the Doppler coefficient, the Doppler frequency, and the Doppler phase of the ℓth path, respectively. According to (5), the real part and the imaginary part of $\hat{\mu}_\ell(t)$ are correlated. However, such a correlation can be neglected under isotropic scattering conditions [11].

The Doppler phases $\theta_{n,\ell}$ are independent and identically distributed (i.i.d.) random variables, each having a uniform distribution over $[0, 2\pi)$. The Doppler coefficients $c_{n,\ell}$ and the Doppler frequencies $f_{n,\ell}$ are constant, which can be determined in such a way that the statistical properties of $\hat{\mu}_\ell(t)$ are as close as possible to those of the Gaussian random processes $\mu_\ell(t)$. In this paper, three parameter computation methods will be applied for computing the primary model parameters. Since most of the parameter design methods proposed for SOS models cannot directly be adopted to the SOC model, they need to be modified [4].
1) MEDS [9]: The parameters $c_{n,\ell}$ and $f_{n,\ell}$ can be determined by the MEDS as follows

$$c_{n,\ell} = \sigma_0 \sqrt{\frac{2}{N_\ell}}, \qquad f_{n,\ell} = f_{\max} \sin\left[\frac{2\pi}{N_\ell}\left(n - \frac{1}{4}\right)\right]. \tag{6a,b}$$

2) R-MEDS: Performing the modification on the R-MEDS [15] results in the following equations

$$c_{n,\ell} = \sigma_0 \sqrt{\frac{2}{N_\ell}}, \qquad f_{n,\ell} = f_{\max} \cos\left[\frac{2\pi}{N_\ell}\left(n - \frac{1}{4}\right) + \alpha_{n,\ell}\right], \tag{7a,b}$$

where the quantities $\alpha_{n,\ell}$ are i.i.d. random variables with a uniform distribution over $\left(-\frac{\pi}{2N_\ell}, \frac{\pi}{2N_\ell}\right]$.
3) MCM [5]: The application of the MCM allows us to compute the parameters $c_{n,\ell}$ and $f_{n,\ell}$ according to

$$c_{n,\ell} = \sigma_0 \sqrt{\frac{2}{N_\ell}}, \qquad f_{n,\ell} = f_{\max} \sin\left(2\pi u_{n,\ell}\right), \tag{8a,b}$$

where $u_{n,\ell}$ are i.i.d. random variables uniformly distributed over the interval $(0, 1]$.

To guarantee the uncorrelated scattering (US) condition, the processes $\hat{\mu}_\ell(t)$ must be uncorrelated for different paths, i.e., for different values of ℓ. For the MEDS, the almost uncorrelatedness of the processes $\hat{\mu}_\ell(t)$ can be ensured by the

convention $N_\ell = N + \ell - 1$, where N denotes the number of cisoids used in the first process $\hat{\mu}_1(t)$. Since the Doppler frequencies generated by the R-MEDS and the MCM are random variables, the uncorrelatedness is guaranteed even by using the same number of cisoids for different paths. In this paper, we assume that the number of cisoids belonging to different processes equals to N if the R-MEDS or the MCM is applied.

Similar to (1), we can express the time-variant transfer function $\hat{H}(f',t)$ of the stochastic SOC channel simulator as

$$\hat{H}(f',t) = \sum_{\ell=1}^{\mathscr{L}} a_\ell \hat{\mu}_\ell(t) e^{-j2\pi f' \tau'_\ell}, \tag{9}$$

which can be interpreted as a family of sample functions depending on the parameters $\theta_{n,\ell}$. If all phases $\theta_{n,\ell}$ are fixed, the stochastic process $\hat{\mu}_\ell(t)$ in (5) becomes a deterministic one. Hence, we obtain a single realization of $\hat{H}(f',t)$, which is also deterministic and can be used in simulations.

The mathematical description of the channel simulator allows us to study the temporal-frequency CF of the channel simulator. Due to the US condition, the temporal-frequency CF $\hat{r}_{HH}(v',\tau) = E\{\hat{H}^*(f',t)\hat{H}(f'+v',t+\tau)\}$ is given by [7]

$$\hat{r}_{HH}(v',\tau) = \sum_{\ell=1}^{\mathscr{L}} a_\ell^2 \hat{r}_{\mu_\ell \mu_\ell}(\tau) e^{-j2\pi v' \tau'_\ell}, \tag{10}$$

where $\hat{r}_{\mu_\ell \mu_\ell}(\tau) = \sum_{n=1}^{N_\ell} c_{n,\ell}^2 e^{j2\pi f_{n,\ell}\tau}$ describes the temporal ACF of the stochastic process $\hat{\mu}_\ell(t)$ [11].

The PDF $\hat{p}_\zeta(r)$ of the envelope $\hat{\zeta}(t) = |\hat{H}(f'_0,t)|$ can be calculated similarly to [11]. According to Appendix F.A, we have

$$\hat{p}_\zeta(r) = (2\pi)^2 r \int_0^\infty \left[\prod_{\ell=1}^{\mathscr{L}} \prod_{n=1}^{N_\ell} J_0(2\pi a_\ell c_{n,\ell} y) \right] J_0(2\pi r y) y \, dy. \tag{11}$$

The envelope PDF $p_\zeta(r)$ of the reference channel model as well as the envelope PDF $\hat{p}_\zeta(r)$ of the SOC channel simulator designed by the MEDS with $\mathscr{L} = 6$ and $N = 6$ is depicted in Fig. F.1. A good correspondence between the envelope PDFs of the reference model and that of the corresponding channel simulator can be observed. This figure shows also the simulation results of the PDF of $\hat{\zeta}(t) = |\hat{H}(f'_0,t)|$ obtained from the simulation of $\hat{H}(f',t)$ given by (9) and averaging over 50 trials. Moreover, we prove in Appendix F.B that $\hat{p}_\zeta(r) \to p_\zeta(r)$ for $N_\ell \to \infty$.
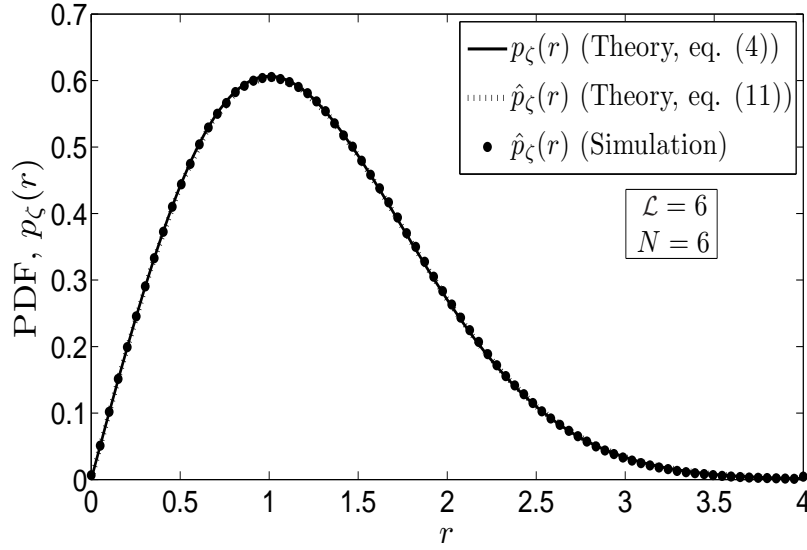
Figure F.1: Probability density function $p_\zeta(r)$ of the absolute value of the time-variant transfer function $\zeta(t) = |H(f_0', t)|$.

III. PERFORMANCE OF THE SOC CHANNEL SIMULATOR IN COHERENT DPSK OFDM SYSTEMS

Section III analyzes the performance of the wideband SOC channel simulator in a coherent DPSK OFDM system.

For the reference channel model, it is shown in Section II that the absolute value of the time-variant transfer function follows the Rayleigh distribution. Therefore, the reference BEP is given by [12]

$$P_b = \frac{1}{2(1 + \overline{\gamma}_b)}, \tag{12}$$

where $\overline{\gamma}_b = 2\sigma_0^2 E_b/N_0$ is the average signal-to-noise ratio.

The BEP of the simulation system $\hat{P}_b$ can be calculated by the relation

$$\hat{P}_b = \int_0^\infty P_{b|r}(r)\hat{p}_\zeta(r)dr, \tag{13}$$

where

$$P_{b|r}(r) = \frac{1}{2}e^{-r^2\frac{E_b}{N_0}}, \tag{14}$$

is the conditional BEP of the coherent DPSK system [12].

If we substitute (11) and (14) in (13), we obtain the following analytical expression for the BEP of the DPSK OFDM system using the SOC channel simulator

$$\hat{P}_b = \frac{\pi^2}{E_b/N_0} \int_0^\infty e^{-\frac{\pi^2 y^2}{E_b/N_0}} \left[\prod_{\ell=1}^{\mathscr{L}} \prod_{n=1}^{N_\ell} J_0(2\pi a_\ell c_{n,\ell} y) \right] y\, dy. \qquad (15)$$

The derivation of the BEP $\hat{P}_b$ can be found in Appendix F.C. Note that the BEP $\hat{P}_b$ is independent of the Doppler frequencies $f_{n,\ell}$. The channel simulators designed with the MEDS, the R-MEDS, and the MCM are equivalent w.r.t. the BEP, since the Doppler coefficients $c_{n,\ell}$ calculated by these three methods are the same.

The BEP P_b computed according to (12) is presented in Fig. F.2. This figure also illustrates the BEP performance of the coherent DPSK OFDM system using different SOC channel simulators designed with the MEDS, the R-MEDS, and the MCM. The theoretical results are validated by simulations. In all simulations, we use the 6-path channel model with the propagation delays $\tau_\ell' \in \{0, 100, 200, 300, 400, 500\}\, \mu s$ ($\ell = 1, 2, \ldots, \mathscr{L}$). The powers assigned to the 6 different paths equal to $\{0, -4, -8, -12, -16, -20\}$ dB. We consider the DPSK OFDM system consisting of $K = 128$ subcarriers with a sampling duration of $T = 100\, \mu s$.

We also prove in Appendix F.C that $\hat{P}_b \to P_b$ holds as $N_\ell \to \infty$. However, the deviation of the BEP between $\hat{P}_b$ and P_b cannot be ignored if the number of cisoids

Figure F.2: Coherent DPSK OFDM system performance using the reference model and the SOC channel simulators designed with the MEDS, the R-MEDS, and the MCM.

is small. Here, we introduce the relative error of the BEP $\hat{P}_b$

$$\varepsilon_{BEP} = \frac{\hat{P}_b - P_b}{P_b} \tag{16}$$

to evaluate the BEP deviation in terms of N.

The influence of the number of cisoids N on the relative error is illustrated in Fig. F.3. From this figure, we can conclude that the absolute value of the relative error $|\varepsilon_{BEP}|$ is less than 4.327% if $N \geq 5$.

IV. Performance of the SOC Channel Simulator in Noncoherent DPSK OFDM Systems

According to [2, pp. 193], the BEP of noncoherent DPSK in Rayleigh fading is given by

$$P_b = \frac{1}{2}\left[1 - \frac{r_{hh}(T)}{1 + \frac{1}{\bar{\gamma}_b}}\right], \tag{17}$$

where $r_{hh}(T)$ denotes the value of the temporal ACF $r_{hh}(\tau) = \sum_{\ell=1}^{\mathscr{L}} a_\ell^2 r_{\mu_\ell \mu_\ell}(\tau)$ of the channel impulse response at $\tau = T$. Different from [2], the channel response in this paper is described by a time-variant transfer function. Thus, we can express the BEP of a noncoherent DPSK OFDM system by replacing $r_{hh}(T)$ in (17) with the
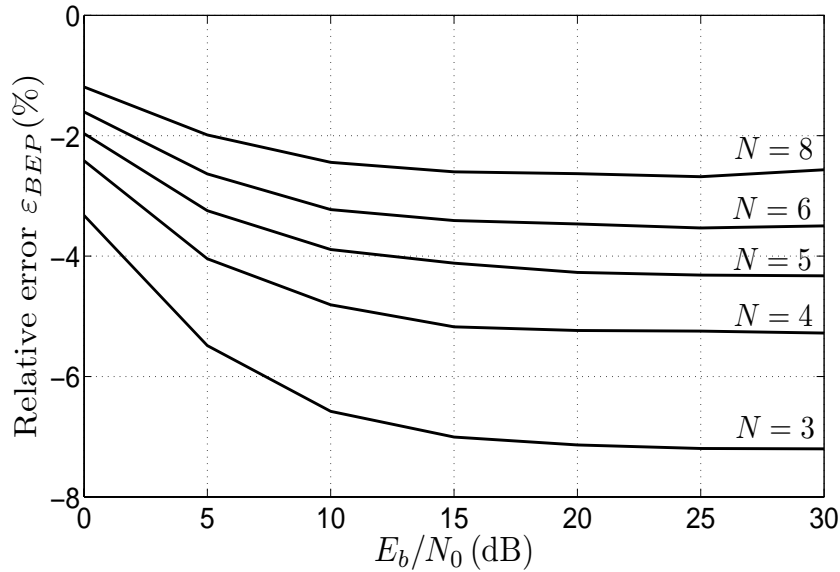
Figure F.3: Evaluation of the relative error of the BEP ε_{BEP} for the coherent DPSK OFDM system for various values of the number of cisoids N.

temporal-frequency CF $r_{HH}(v', \tau)$ at $v' = f_s$ and $\tau = T$, i.e.,

$$P_b = \frac{1}{2}\left[1 - \frac{r_{HH}(f_s, T)}{1 + \frac{1}{\bar{\gamma}_b}}\right]. \tag{18}$$

Here $f_s = 1/(KT)$ is the subcarrier spacing. Substituting $r_{HH}(v', \tau)$ given by (2) in (18), we have

$$P_b = \frac{1}{2}\left[1 - \frac{2\sigma_0^2 J_0(2\pi f_{\max}T)\sum\limits_{\ell=1}^{\mathscr{L}} a_\ell^2 e^{-j2\pi f_s \tau_\ell'}}{1 + \frac{1}{\bar{\gamma}_b}}\right]. \tag{19}$$

Assuming that the PDF $\hat{p}_\zeta(r)$ is close to the PDF $p_\zeta(r)$ of the reference channel model, the BEP of the simulation system $\hat{P}_b$ for the DPSK OFDM system employing the wideband SOC channel simulator is similar to the expression in (18). We only need to replace $r_{HH}(f_s, T)$ in (18) by $\hat{r}_{HH}(v', \tau)$ at $v' = f_s$ and $\tau = T$ [see eq. (10)]. Thus, we finally obtain

$$\hat{P}_b \approx \frac{1}{2}\left[1 - \frac{\sum\limits_{\ell=1}^{\mathscr{L}} a_\ell^2 e^{-j2\pi f_s \tau_\ell'}\sum\limits_{n=1}^{N_\ell} c_{n,\ell}^2 e^{j2\pi f_{n,\ell}T}}{1 + \frac{1}{\bar{\gamma}_b}}\right]. \tag{20}$$

Using the relative error ε_{BEP} in (16) as a criterion, we can now evaluate the performance of the MEDS, the R-MEDS, and the MCM. In this paper, the inequality $f_{n,\ell}T \ll 1$ holds. According to the approximation $e^x \approx 1 + x + x^2/2\,(x \ll 1)$, the temporal ACF $\hat{r}_{\mu_\ell\mu_\ell}(T) = \sum_{n=1}^{N_\ell} c_{n,\ell}^2 e^{j2\pi f_{n,\ell}T}$ can be approximated as follows

$$\hat{r}_{\mu_\ell\mu_\ell}(T) \approx \sum_{n=1}^{N_\ell} c_{n,\ell}^2[1 + j2\pi f_{n,\ell}T - 2(\pi f_{n,\ell}T)^2]$$

$$= \hat{r}_{\mu_\ell\mu_\ell}(0) + T\dot{\hat{r}}_{\mu_\ell\mu_\ell}(0) + \frac{T^2}{2}\ddot{\hat{r}}_{\mu_\ell\mu_\ell}(0). \tag{21}$$

Here, $\dot{\hat{r}}_{\mu_\ell\mu_\ell}(\cdot)$ and $\ddot{\hat{r}}_{\mu_\ell\mu_\ell}(\cdot)$ denote the derivative and the second derivative of $\hat{r}_{\mu_\ell\mu_\ell}(\cdot)$, respectively.

For the special case, where the power spectral density (PSD) is symmetrical, the value for the imaginary part of $\hat{r}_{\mu_\ell\mu_\ell}(T)$ is zero. Since the power constraint $\hat{r}_{\mu_\ell\mu_\ell}(0) = r_{\mu_\ell\mu_\ell}(0)$ holds for all the three methods mentioned above, we make a

further simplification concerning (21) [10]

$$
\begin{aligned}
\hat{r}_{\mu_\ell \mu_\ell}(T) &\approx \hat{r}_{\mu_\ell \mu_\ell}(0) + \frac{T^2}{2}\ddot{\hat{r}}_{\mu_\ell \mu_\ell}(0) \\
&= r_{\mu_\ell \mu_\ell}(0) + \frac{T^2}{2}\ddot{r}_{\mu_\ell \mu_\ell}(0) - \frac{T^2}{2}\triangle\beta_\ell \\
&= r_{\mu_\ell \mu_\ell}(T) - \frac{T^2}{2}\triangle\beta_\ell.
\end{aligned}
\tag{22}
$$

In the preceding equation, $\triangle\beta_\ell = \ddot{r}_{\mu_\ell \mu_\ell}(0) - \ddot{\hat{r}}_{\mu_\ell \mu_\ell}(0)$ represents the model error of the SOC channel simulator. For the Jakes PSD, we have $\beta_\ell = -\ddot{r}_{\mu_\ell \mu_\ell}(0) = (2\pi\sigma_0 f_{\max})^2$ for the reference channel model and for the SOC channel simulator, we obtain $\ddot{\hat{r}}_{\mu_\ell \mu_\ell}(0) = -(2\pi)^2 \sum_{n=1}^{N_\ell}(c_{n,\ell} f_{n,\ell})$.

By making use of (2), (10), and (22), we can rewrite the temporal-frequency CF $\hat{r}_{HH}(f_s, T)$ in (10) as follows

$$
\hat{r}_{HH}(f_s, T) \approx r_{HH}(f_s, T) - \frac{T^2}{2}\sum_{n=1}^{N_\ell} a_\ell^2 \triangle\beta_\ell e^{-j2\pi f_s \tau_\ell'}.
\tag{23}
$$

Putting (23) into (20) and taking the relation (19) into consideration, the BEP $\hat{P}_b$ can be expressed in closed-form as

$$
\hat{P}_b = P_b + \triangle P_b,
\tag{24}
$$

where

$$
\triangle P_b = \frac{\left(\dfrac{T}{2}\right)^2 \sum\limits_{\ell=1}^{\mathscr{L}} a_\ell^2 \triangle\beta_\ell e^{-j2\pi f_s \tau_\ell'}}{1 + \dfrac{1}{\overline{\gamma}_b}}.
\tag{25}
$$

By making use of (25), we can express the relative error of the BEP as follows

$$
\varepsilon_{BEP} = \frac{\dfrac{T^2}{2}\sum\limits_{\ell=1}^{\mathscr{L}} a_\ell^2 \triangle\beta_\ell e^{-j2\pi f_s \tau_\ell'}}{1 + \dfrac{1}{\overline{\gamma}_b} - 2\sigma_0^2 J_0(2\pi f_{\max}T)\sum\limits_{\ell=1}^{\mathscr{L}} a_\ell^2 e^{-j2\pi f_s \tau_\ell'}}.
\tag{26}
$$

Since the model error $\triangle\beta_\ell = 0$ if the MEDS is applied [7], it follows that the relative error $\varepsilon_{BEP} = 0$. Thus, we can say that the SOC channel simulator designed with the MEDS is equivalent to the reference channel model in terms of the BEP. The analytical results for the BEP P_b and $\hat{P}_b$ are depicted in Fig. F.4 for different

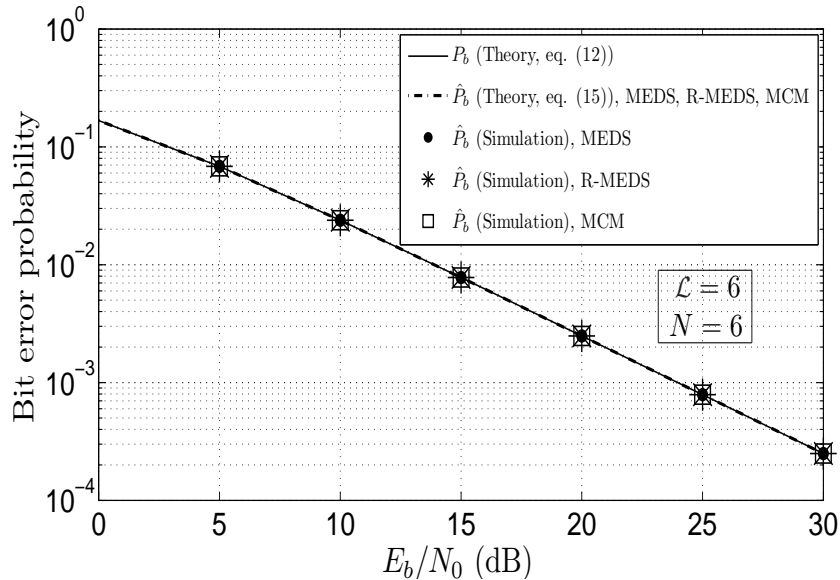Figure F.4: Noncoherent DPSK OFDM system performance using the reference model and the SOC channel simulator designed with the MEDS.

maximum Doppler frequencies. This figure also shows the relevant simulation results, which match the analytical results very well. All parameters are identical to the parameters used in Section III.

When designing the SOC channel simulator by the R-MEDS, we find the expected value $E\{\triangle\beta_\ell\}$ of the model error $\triangle\beta_\ell$ equals to 0 and the variance $\text{Var}\{\triangle\beta_\ell\}$ is $\beta_\ell^2/(4N_\ell^2)$. For the MCM, the model error $\triangle\beta_\ell$ is approximately normally distributed, i.e., $\triangle\beta_\ell \sim N(0, \beta_\ell^2/(2N_\ell))$ [7]. The BEP performances of the noncoherent DPSK OFDM system using the channel simulator designed with the R-MEDS and the MCM are shown in Fig. F.5 and Fig. F.6 (4 realizations of the BEP $\hat{P}_b$ without averaging), respectively. For comparison, we replot in these two figures the BEP P_b computed according to (19). From these figures, it can be seen that the single realization of the BEP, denoted by $\tilde{P}_b$, deviates from P_b in a random manner. The reason is that the R-MEDS and the MCM are typical stochastic parameter design methods. Different from the MEDS, the discrete Doppler frequencies generated by these two methods are random variables. It can be observed that the BEP degrades if the maximum Doppler frequency f_{max} changes from 100 Hz to 500 Hz. The approximation $\tilde{P}_b \approx P_b$ is good when using the R-MEDS. However, comparing Fig. F.5 and Fig. F.6, we find that the deviation between $\tilde{P}_b$ and P_b in Fig. F.6 is large and cannot be neglected. The reason for this observation is that the variance of the model error using the MCM is larger than that of using the R-MEDS. Therefore, averaging over the BEP $\tilde{P}_b$ obtained from different realizations is unavoidable if the MCM is used.
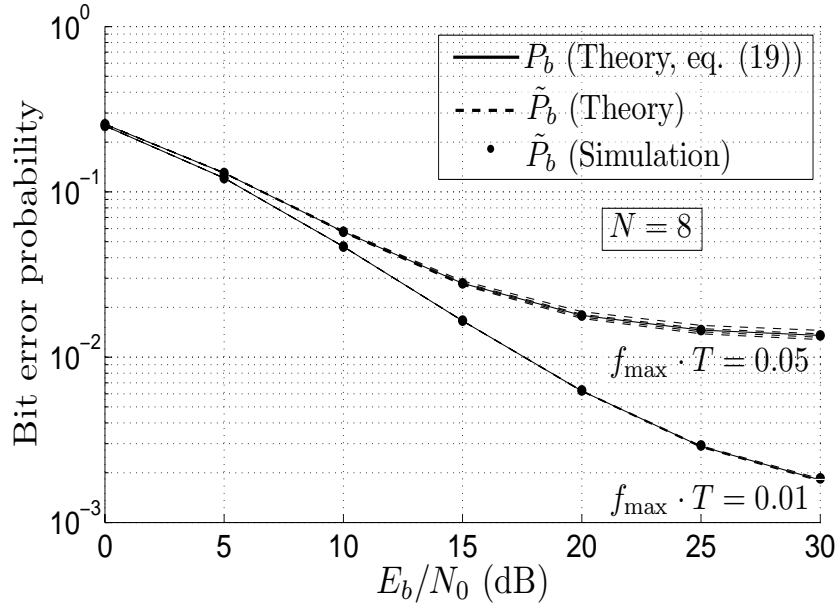
Figure F.5: Noncoherent DPSK OFDM system performance using the reference model and the SOC channel simulator designed with the R-MEDS ($\tilde{P}_b$: realizations of $\hat{P}_b$ in (20)).
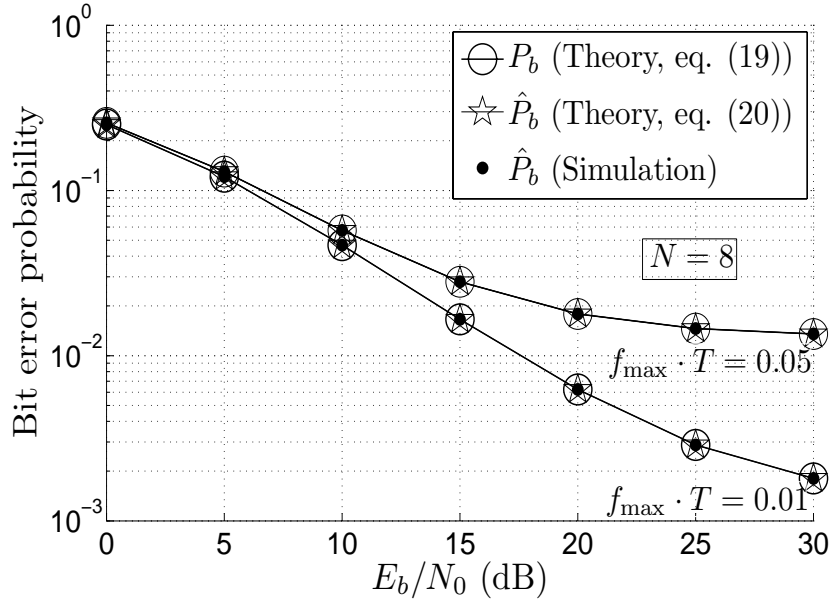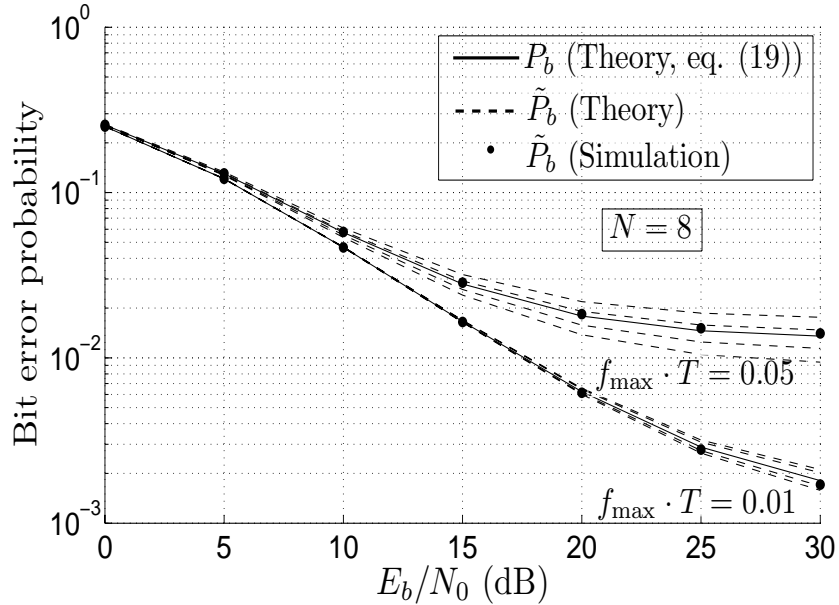

Figure F.6: Noncoherent DPSK OFDM system performance using the reference model and the SOC channel simulator designed with the MCM ($\tilde{P}_b$: realizations of $\hat{P}_b$ in (20)).

V. CONCLUSION

In this paper, the performance of the frequency-selective reference channel model and the corresponding SOC channel simulator have been analyzed w.r.t. the BEP

of DPSK OFDM systems. Analytical expressions for the BEP have been derived for both the coherent and noncoherent DPSK OFDM systems. From the derivations of the BEP, the relative error of the BEP has been studied, which allows to reduce the channel realization expenditure to a lower bound without causing any obvious BEP distortion. We have compared the best deterministic parameter design method (MEDS), the best stochastic one (R-MEDS), and the MCM by employing the relative error of the BEP as an appropriate criterion.

For coherent DPSK OFDM systems, it is shown by theory and confirmed by simulations that the SOC channel simulators designed by the MEDS, the R-MEDS, and the MCM are equivalent w.r.t. the BEP performance. When the number of cisoids tends to infinity, it has been proved that the BEP of the simulation system in the presence of a wideband SOC channel simulator converges to the reference BEP. The relative error of the BEP can be neglected if the channel simulator is designed using not less than 5 cisoids. For noncoherent DPSK OFDM systems, a closed-form expression has been derived for the relative error, which provides a powerful tool when discussing the performance of different parameter computation methods. From our results, we can conclude that the performance of the MEDS and the R-MEDS is almost the same w.r.t. the relative error of the BEP. However, both methods outperform the MCM.

F. A   Derivation of the envelope PDF $\hat{p}_\zeta(r)$

This appendix is devoted to the derivation of the PDF of the envelope $\hat{\zeta}(t) = |\hat{H}(f_0', t)|$. Suppose that $\hat{H}_{1,\ell}(f_0', t)$ and $\hat{H}_{2,\ell}(f_0', t)$ represent the real part and the imaginary part of the ℓth component $a_\ell \hat{\mu}_\ell(t) e^{-j2\pi f_0' \tau_\ell'}$ of $H(f_0', t)$, respectively. For fixed values of $t = t_0$, the joint characteristic function $\hat{\Psi}_{H_{1,\ell} H_{2,\ell}}(v_1, v_2)$ of $\hat{H}_{1,\ell}(f_0', t_0)$ and $\hat{H}_{2,\ell}(f_0', t_0)$ can be expressed by the relation [11]

$$\hat{\Psi}_{H_{1,\ell} H_{2,\ell}}(v_1, v_2) = \prod_{n=1}^{N_\ell} J_0 \left(2\pi a_\ell c_{n,\ell} \sqrt{v_1^2 + v_2^2} \right). \tag{A.1}$$

We denote the real and imaginary parts of $H(f', t)$ by $H_1(f', t)$ and $H_2(f', t)$, respectively. As mentioned before, the Doppler phases θ_n are i.i.d. random variables, which leads to the fact that the terms $\hat{H}_i(f_0', t_0) = \hat{H}_{i,1}(f_0', t_0) + \hat{H}_{i,2}(f_0', t_0) + \cdots + \hat{H}_{i,\mathscr{L}}(f_0', t_0)$ are also i.i.d. random variables ($i = 1, 2$). Thus, the joint characteristic function $\hat{\Psi}_{H_1 H_2}(v_1, v_2)$ of $\hat{H}_1(f_0', t_0)$ and $\hat{H}_2(f_0', t_0)$ can be formulated as the $\mathscr{L}$-fold product of the joint characteristic functions $\hat{\Psi}_{H_{1,\ell} H_{2,\ell}}(v_1, v_2)$, i.e.,

$$\hat{\Psi}_{H_1 H_2}(\nu_1, \nu_2) = \prod_{\ell=1}^{\mathscr{L}} \prod_{n=1}^{N_\ell} J_0(2\pi a_\ell c_{n,\ell} \sqrt{\nu_1^2 + \nu_2^2}). \qquad (A.2)$$

Then, the joint PDF $\hat{p}_{H_1 H_2}(x_1, x_2)$ is given by the inverse Fourier transform of $\hat{\Psi}_{H_{1,\ell} H_{2,\ell}}(\nu_1, \nu_2)$ [3, eq. (3.397-1,2)]

$$\hat{p}_{H_1 H_2}(x_1, x_2) = \int_{-\infty}^{\infty} \hat{\Psi}_{H_1 H_2}(\nu_1, \nu_2) e^{j2\pi(\nu_1 x_1 + \nu_2 x_2)} d\nu_1 d\nu_2$$

$$= 2\pi \int_0^{\infty} \left[\prod_{\ell=1}^{\mathscr{L}} \prod_{n=1}^{N_\ell} J_0(2\pi a_\ell c_{n,\ell} y) \right] \cdot J_0(2\pi y \sqrt{x_1^2 + x_2^2}) \, y \, dy. \qquad (A.3)$$

The transformation of the Cartesian coordinates (x_1, x_2) into polar coordinates (r, θ) with $x_1 = r\cos\theta$ and $x_2 = r\sin\theta$ allows us to calculate the joint PDF $\hat{p}_{\zeta\vartheta}(r, \theta)$ of the envelope $\hat{\zeta}(t) = |\hat{H}(f_0', t)|$ and the phase $\hat{\vartheta}(t) = \arg\{\hat{H}(f_0', t)\}$ as follows

$$\hat{p}_{\zeta\vartheta}(r, \theta) = r\,\hat{p}_{H_1 H_2}(r\cos\theta, r\sin\theta)$$

$$= 2\pi r \int_0^{\infty} \left[\prod_{\ell=1}^{\mathscr{L}} \prod_{n=1}^{N_\ell} J_0(2\pi a_\ell c_{n,\ell} y) \right] \cdot J_0(2\pi r y) \, y \, dy, \qquad (A.4)$$

for $z \geq 0$ and $|\theta| \leq \pi$. Integrating the joint PDF $\hat{p}_{\zeta\vartheta}(r, \theta)$ over θ results in

$$\hat{p}_\zeta(r) = (2\pi)^2 r \int_0^{\infty} \left[\prod_{\ell=1}^{\mathscr{L}} \prod_{n=1}^{N_\ell} J_0(2\pi a_\ell c_{n,\ell} y) \right] \cdot J_0(2\pi r y) \, y \, dy. \qquad (A.5)$$

F. B Proof of $\hat{p}_\zeta(r) \to p_\zeta(r)$ Holds If $N_\ell \to \infty$

In the following, we prove that the envelope PDF $\hat{p}_\zeta(r)$ of the SOC channel simulator converges to the Rayleigh distribution as $N_\ell \to \infty$. According to [7, p. 335], we have

$$\lim_{N_\ell \to \infty} \prod_{n=1}^{N_\ell} J_0(2\pi a_\ell c_{n,\ell} y) = e^{-2(\pi a_\ell \sigma_0 y)^2}. \qquad (B.1)$$

By using the result in (B.1) and considering the relation $\sum_{\ell=1}^{\mathscr{L}} a_\ell^2 = 1$, we obtain

$$\prod_{\ell=1}^{\mathscr{L}} \prod_{n=1}^{N_\ell} J_0(2\pi a_\ell c_{n,\ell} y) = e^{-2(\pi\sigma_0 y)^2 \sum_{\ell=1}^{\mathscr{L}} a_\ell^2} = e^{-2(\pi\sigma_0 y)^2} \qquad (B.2)$$

as $N_\ell \to \infty$. Thus, in the limit $N_\ell \to \infty$, the envelope PDF $\hat{p}_\zeta(r)$ in (A.5) tends to

$$\hat{p}_\zeta(r) = (2\pi)^2 r \int\limits_0^\infty e^{-2(\pi y \sigma_0)^2} \cdot J_0(2\pi ry)\, y\, dy$$

$$= \frac{r}{\sigma_0^2} e^{-\frac{r^2}{2\sigma_0^2}}, \quad r \geq 0, \tag{B.3}$$

which is known as the Rayleigh distribution.

F. C   Derivation of the BEP $\hat{P}_b$

Putting (11) and (14) into (13) results in the following twofold integral for the BEP

$$\hat{P}_b = 2\pi^2 \int\limits_0^\infty \int\limits_0^\infty r e^{-r^2 \frac{E_b}{N_0}} J_0(2\pi ry)\, dr \cdot \left[\prod_{\ell=1}^{\mathscr{L}} \prod_{n=1}^{N_\ell} J_0(2\pi a_\ell c_{n,\ell} y) \right] y\, dy. \tag{C.1}$$

The integral over r can be solved by using the relation [3, eq. (6.631.4)]

$$\int\limits_0^\infty r e^{-\alpha r^2} J_0(\beta r)\, dr = \frac{e^{-\frac{\beta^2}{4\alpha}}}{2\alpha}, \qquad \mathrm{Re}\{\alpha\} > 0, \beta > 0. \tag{C.2}$$

After some calculations, we finally obtain

$$\hat{P}_b = \frac{\pi^2}{E_b/N_0} \int\limits_0^\infty e^{-\frac{\pi^2 y^2}{E_b/N_0}} \left[\prod_{\ell=1}^{\mathscr{L}} \prod_{n=1}^{N_\ell} J_0(2\pi a_\ell c_{n,\ell} y) \right] y\, dy. \tag{C.3}$$

Next, we prove that $\hat{P}_b \to P_b$ holds if $N_\ell \to \infty$. If we substitute the result in (B.2) into the right-hand side of (B.3), we obtain

$$\hat{P}_b = \frac{\pi^2}{E_b/N_0} \int\limits_0^\infty e^{-\frac{\pi^2 y^2}{E_b/N_0}} e^{-2(\pi \sigma_0 y)^2} y\, dy$$

$$= \frac{1}{2(1 + 2\sigma_0^2 \frac{E_b}{N_0})}$$

$$= \frac{1}{2(1 + \overline{\gamma}_b)} \tag{C.4}$$

as $N_\ell \to \infty$.

REFERENCES

[1] P. A. Bello. Characterization of randomly time-variant linear channels. *IEEE Trans. Commun. Syst.*, 4:360–393, Dec. 1963.

[2] A. Goldsmith. *Wireless Communications*. Cambridge University Press, 2005.

[3] I. S. Gradshteyn and I. M. Ryzhik. *Tables of Integrals, Series, and Products*. Academic Press, 6th edition, 2000.

[4] C. A. Gutiérrez and M. Pätzold. Sum-of-sinusoids-based simulation of flat fading wireless propagation channels under non-isotropic scattering conditions. In *Proc. 50th Global Communication Conference, GLOBECOM 2007*, pages 3842–3846. Washington, D.C., USA, Nov. 2007.

[5] P. Höher. A statistical discrete-time model for the WSSUS multipath channel. *IEEE Trans. Veh. Technol.*, VT–41(4):461–468, Nov. 1992.

[6] Y. Ma and M. Pätzold. Wideband two-ring MIMO channel models for mobile-to-mobile communications. In *Proc. 10th International Symposium on Wireless Personal Multimedia Communications, WPMC 2007*, pages 380–384. Jaipur, India, Dec. 2007.

[7] M. Pätzold. *Mobile Fading Channels*. Chichester: John Wiley & Sons, 2002.

[8] M. Pätzold. System function and characteristic quantities of spatial deterministic Gaussian uncorrelated scattering processes. In *Proc. 57th Vehicular Technology Conference, VTC 2003-Spring*, pages 256–261. Jeju, Korea, Apr. 2003.

[9] M. Pätzold and C. A. Gutiérrez. Level-crossing rate and average duration of fades of the envelope of a sum-of-cisoids. In *Proc. 67th IEEE Vehicular Technology Conference, VTC 2008-Spring*, pages 488–494. Singapore, May 2008.

[10] M. Pätzold and F. Laue. The performance of deterministic Rayleigh fading channel simulators with respect to the bit error probability. In *Proc. 51st Vehicular Technology Conference, VTC 2000-Spring*. Tokyo, Japan, May 2000.

[11] M. Pätzold and B. Talha. On the statistical properties of sum-of-cisoids-based mobile radio channel models. In *Proc. 10th International Symposium on Wireless Personal Multimedia Communications, WPMC 2007*, pages 394–400. Jaipur, India, Dec. 2007.

[12] J. Proakis and S. Massoud. *Digital Communications*. New York: McGraw-Hill, 5th edition, 2007.

[13] S. O. Rice. Mathematical analysis of random noise. *Bell Syst. Tech. J.*, 23:282–332, Jul. 1944.

[14] S. O. Rice. Mathematical analysis of random noise. *Bell Syst. Tech. J.*, 24:46–156, Jan. 1945.

[15] Y. R. Zheng and C. Xiao. Simulation models with correct statistical properties for Rayleigh fading channels. *IEEE Trans. Commun.*, 51(6):920–928, Jun. 2003.

Appendix G

Paper VII

Title:	Performance Comparison of Space-Time Coded MIMO-OFDM Systems Using Different Wideband MIMO Channel Models
Authors:	**Yuanyuan Ma** and Matthias Pätzold
Affiliation:	University of Agder, Faculty of Engineering and Science, P. O. Box 509, NO-4898 Grimstad, Norway.
Conference:	*4th IEEE International Symposium on Wireless Communication Systems, ISWCS 2007*, Trondheim, Norway, Oct. 2007, pp. 762 – 766, DOI: 10.1109/ISWCS.2007.4392443.

Performance Comparison of Space-Time Coded MIMO-OFDM Systems Using Different Wideband MIMO Channel Models

Yuanyuan Ma and Matthias Pätzold

Department of Information and Communication Technology

Faculty of Engineering and Science, University of Agder

Servicebox 509, NO-4898 Grimstad, Norway

E-mails: {yuanyuan.ma, matthias.paetzold}@uia.no

Abstract — **This paper investigates the performance of multiple-input multiple-output orthogonal frequency division multiplexing (MIMO-OFDM) systems using different wideband MIMO channel models. The considered MIMO channel models are based on the geometrical elliptical model and the geometrical one-ring model. The spatial correlation effects due to the limited antenna spacings and the Doppler effect caused by the movement of the receiver are studied separately. It is shown that increasing the antenna spacings leads to a higher diversity gain. The relevant range of the antenna spacings that has a strong influence on the system performance is obtained through simulations. When the antenna spacings exceed the determined range, then the diversity gain does not increase significantly. Moreover, to achieve the same system performance, the MIMO-OFDM system employing the one-ring model requires larger antenna spacings than using the elliptical channel model. Furthermore, the influence of the maximum Doppler frequency has been studied under perfect and imperfect channel state information (CSI). It is demonstrated that system performance degradations occur if the maximum Doppler frequency increases, especially in case of imperfect CSI.**

I. Introduction

OFDM has been adopted in wireless local area networks (WLANs) and the IEEE 802.11a standard for its high spectral efficiency and ability to deal with frequency selective fading. The combination of MIMO techniques with OFDM is regarded as a promising solution for increasing data rates of future WLANs and 4th generation wireless communication systems. Most of the theoretical works in the past assumed simplified channel models such as frequency-flat fading channels. However, due to demands for high-speed communications, future communication systems are required to operate in much larger bandwidths than today's systems

[9]. The performance of practical receivers depends on the propagation conditions of the channel. Hence, for the design and realistic performance evaluation of space-time coded MIMO-OFDM systems, wideband MIMO channel models with accurate temporal, spatial, and frequency correlation properties are required.

The geometrical one-ring model [10], [5] and the two-ring model [1] have widely been accepted as proper narrowband MIMO channel models. To design, optimize, and test future mobile systems, wideband MIMO channel models based on the geometric elliptical model and the extended geometrical one-ring model were proposed [7], [8]. The performance of space-time coded MIMO-OFDM systems using a wideband MIMO one-ring channel simulator was investigated in [13]. Different geometrical channel models were proposed for different environments. The elliptical model was proposed for micro- and picocell environments, where multipath scattering exists at both the base station (BS) and the mobile station (MS). By contrast, the one-ring model is often used to model mobile radio channels in macrocell environments, such as rural and suburban areas. Hence, it is quite necessary and useful to investigate the system performance under realistic propagation conditions emulated by different geometrical-based MIMO channel simulators.

In this paper, we will focus on the performance comparison of MIMO-OFDM systems using the wideband MIMO elliptical channel model and the one-ring channel model. The comparison of the system performance will be made for transmission scenarios proposed in [2] for the high performance radio local area network (HiperLAN/2) standard. The main difference between the two channel models are the spatial correlation properties, which are determined by the antenna spacings [7], [8]. In this paper, we will first discuss the impact of the antenna spacings on the system performance assuming isotropic scattering conditions. Thereafter, the effect of the maximum Doppler frequency is studied under the assumption of both perfect CSI and imperfect CSI.

The rest of the paper is organized as follows. In Section II, we describe the wideband MIMO channel reference models derived from the geometric elliptical scattering model and the one-ring model. Section III briefly reviews the basic space-time coded MIMO-OFDM system. Its symbol error rate (SER) performance using different channel models is studied in Section IV. In this section, the impact of different channel parameters on the system performance is also discussed. Finally, the conclusions are drawn in Section V.

II. TWO WIDEBAND MIMO CHANNEL MODELS

A reference channel model consists of an infinite number of scatterers and is thus not realizable. However, reference channel models are important for the deriva-

tion of efficient MIMO channel simulators. According to the sum-of-sinusoids principle, a stochastic simulation model can easily be derived from a reference model by using a limited number of scatterers [4]. Finally, the resulting deterministic simulation model is obtained from the stochastic one by fixing all model parameters.

In this section, we will present two MIMO reference channel models obtained from the geometric elliptical model and the one-ring model.

A. The Geometric Elliptical Reference Model

In the narrowband elliptical reference model presented in [7], it is assumed that an infinite number of random scatterers is located on a single ellipse. The transmitter and the receiver are located at the focal points of the ellipse. To extend the narrowband channel model to a wideband model, we consider a propagation environment with scatterers located on more than one ellipse as shown in [7, Fig. 7]. All scatterers associated with a certain propagation delay τ'_ℓ are located on the ℓth ellipse. Assuming a MIMO system employing M_T transmit antennas at the BS and M_R receive antennas at the MS, the impulse response of the wideband reference channel model can be expressed as

$$h_{kl}(\tau',t) = \sum_{\ell=0}^{\mathscr{L}-1} a_\ell g_{kl,\ell}(t)\delta(\tau' - \tau'_\ell) \tag{1}$$

where $\delta(\cdot)$ is the delta function and $\mathscr{L}$ is the number of discrete propagation paths with different path gains a_ℓ. The complex channel gain associated with the ℓth path is denoted as $g_{kl,\ell}(t)$ and can be expressed by [7]

$$g_{kl,\ell}(t) = \lim_{N_\ell \to \infty} \frac{1}{\sqrt{N_\ell}} \sum_{n=1}^{N_\ell} a_{l,n,\ell} b_{k,n,\ell} e^{j(2\pi f_{n,\ell}t + \theta_{n,\ell})} \tag{2}$$

where

$$a_{l,n,\ell} = e^{j\pi(M_T - 2l + 1)\frac{\delta_T}{\lambda}\cos(\phi_T^{(n)} - \alpha_T)} \tag{3}$$

$$b_{k,n,\ell} = e^{j\pi(M_R - 2k + 1)\frac{\delta_R}{\lambda}\cos(\phi_R^{(n)} - \alpha_R)} \tag{4}$$

$$f_{n,\ell} = f_{\max}\cos(\phi_R^{(n)} - \alpha_V) \tag{5}$$

for $l = 1, 2, \ldots, M_T$ and $k = 1, 2, \ldots, M_R$. Let us denote N_ℓ as the number of scatterers located on the ℓth ellipse, then the total number of scatterers N is given by $N = \sum_{\ell=0}^{\mathscr{L}-1} N_\ell$. In the equations above, the symbol λ is referred to as the carrier's wavelength, α_V represents the angle of motion, and $f_{\max}$ is the maximum Doppler frequency. The phases $\theta_{n,\ell}$ are independent and identically distributed random variables, each with a uniform distribution over $[0, 2\pi)$. The quantities δ_T and δ_R repre-

sent the antenna spacings at the transmitter and receiver, respectively. The angle α_T describes the tilt angle of the antenna array at the transmitter. By analogy, the tilt angle at the receiver is denoted as α_R. The angle $\phi_T^{(n)}$ represents the angle of departure (AOD) of the nth incoming wave at the transmitter, while the angle of arrival (AOA) is described by $\phi_R^{(n)}$. In the reference model, the AOAs $\phi_R^{(n)}$ are independent random variables determined by the distribution of the local scatterers. The exact relation between the AOD $\phi_T^{(n)}$ and the AOA $\phi_R^{(n)}$ is given in [7].

B. The Geometrical One-Ring Reference Model

In the narrowband one-ring reference model, all scatterers are located on a ring around the MS [5, Fig. 1]. In order to incorporate frequency-selectivity in the one-ring model, we partition the ring of scatterers into $\mathcal{L}$ pairs of segments as described in [8], where each pair of segments is assigned to a single discrete propagation delay τ_ℓ' according to a fixed rule. Finally, we can obtain the impulse response of the one-ring reference model according to (1) when we replace $a_{l,n,\ell}$ and $b_{k,n,\ell}$ in (3) and (4) by

$$a_{l,n,\ell} = e^{j\pi(M_T-2l+1)\frac{\delta_T}{\lambda}[\cos(\alpha_T)+\phi_T^{\max}\sin(\alpha_T)\sin(\phi_R^{(n)})]} \tag{6}$$

$$b_{k,n,\ell} = e^{j\pi(M_R-2k+1)\frac{\delta_R}{\lambda}\cos(\phi_R^{(n)}-\alpha_R)} \tag{7}$$

respectively. In (6), $\phi_T^{\max}$ denotes one half of the maximum AOD seen at the BS.

C. Correlation Properties of Wideband Reference Models

The two-dimensional (2D) space cross-correlation function (CCF) of the reference model is defined as [7, 8]

$$\rho_{kl,k'l'}(\delta_T,\delta_R) = E\{g_{kl}(t)g_{k'l'}^*(t)\} \tag{8}$$

where $E\{\cdot\}$ denotes the expectation operator. The 2D space CCF of the elliptical (one-ring) model can be obtained by substituting the corresponding channel gains into (8). The results for the 2D space CCFs of the elliptical and the one-ring reference models are illustrated in Figs. G.1 and G.2, respectively. In the simulations, isotropic scattering is taken into account, where $\alpha_T = \alpha_R = \pi/2$, $\alpha_V = \pi$, $\phi_T^{\max} = 2°$, and $f_{\max} = 91\,\text{Hz}$.

The frequency-correlation function (FCF) of the wideband MIMO reference channel model is defined as [7, 8]

$$r_{\tau'}(v') = E\{H_{kl}(f',t)H_{kl}^*(f'+v',t)\} \tag{9}$$
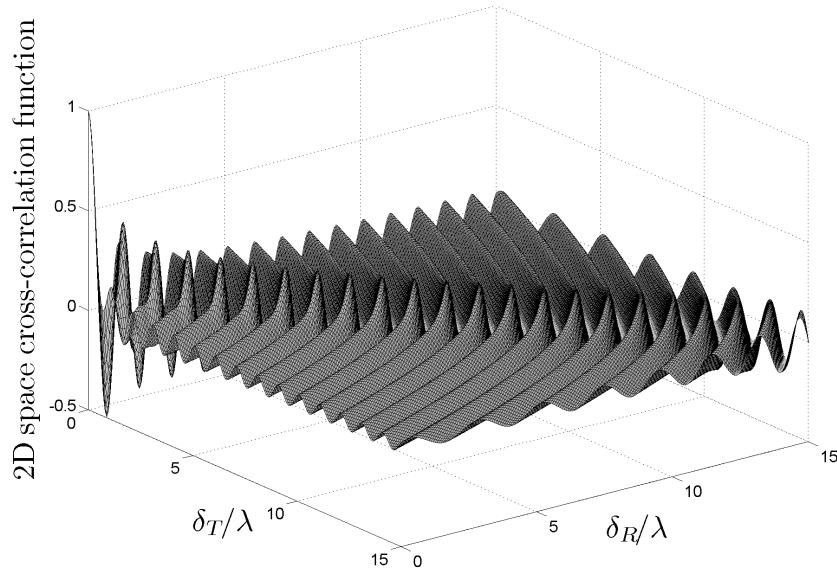
Figure G.1: The 2D space CCF $\rho_{kl,k'l'}(\delta_T, \delta_R)$ of the elliptical reference model.
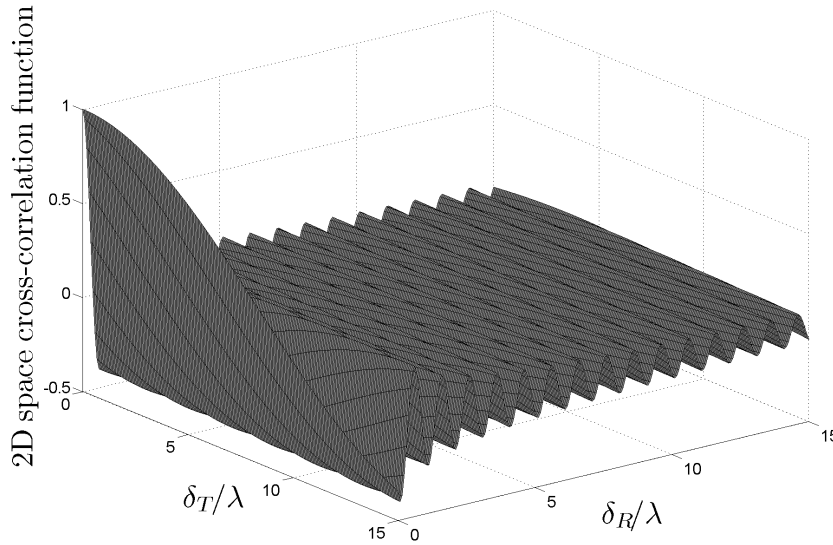
Figure G.2: The 2D space CCF $\rho_{kl,k'l'}(\delta_T, \delta_R)$ of the one-ring reference model.

where $H_{kl}(f',t)$ is the time-variant transfer function, which is the Fourier transform of the impulse response $h_{kl}(\tau',t)$ with respect to the propagation delay τ'. The absolute value of the FCFs of the elliptical model and the one-ring model according to the HiperLAN/2 model C is shown in Fig.G.3 [2].

III. SPACE-TIME CODED MIMO-OFDM SYSTEM

In this section, we consider the 2×2 space-time block coded MIMO-OFDM system shown in Fig.G.4. The serial data bits X_n are first passed through a serial-
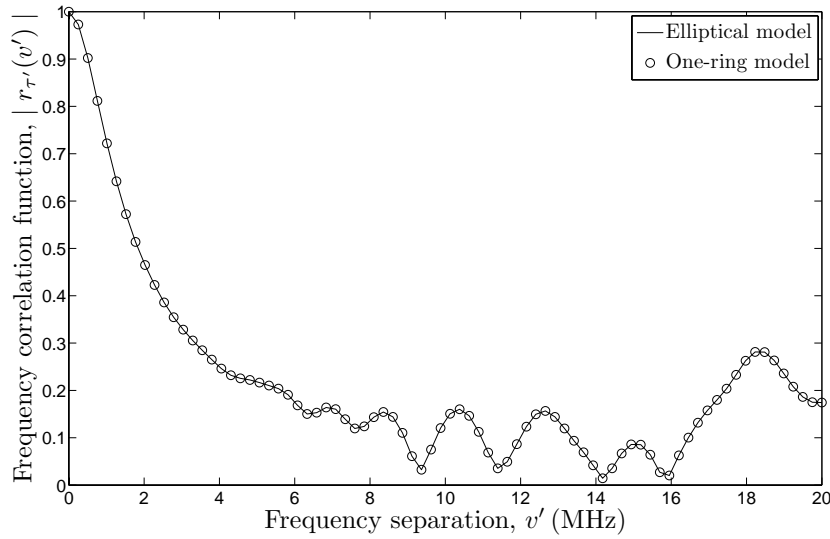
Figure G.3: Absolute value of the FCFs $|\, r_{\tau'}(v')\, |$ of the elliptical model and the one-ring model using the 18-path HiperLAN/2 model C [2].
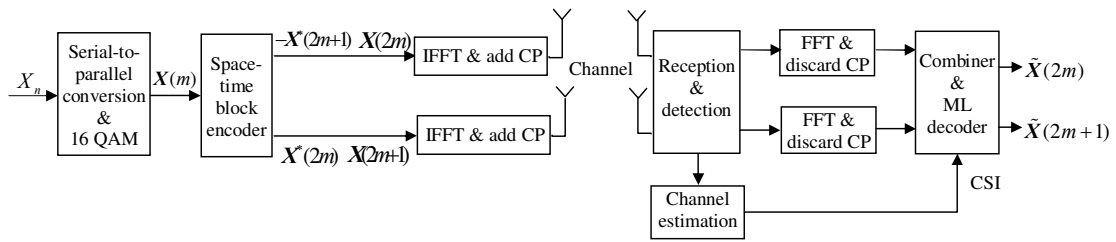
Figure G.4: Space-time block coded MIMO-OFDM system with two transmit and two receive antennas.

to-parallel converter. The resulting parallel data bits are modulated by a 16-QAM modulator, which produces a sequence of complex data symbols denoted by $\mathbf{X}(m)$ $(m = 0, 1, \ldots, M - 1)$. Then, two consecutive data symbols, $\mathbf{X}(2m)$ and $\mathbf{X}(2m+1)$, are coded together by using the Alamouti scheme[11]. After computing the inverse fast Fourier transform (IFFT), the cyclic prefix (CP) is added to each sequence. The baseband OFDM symbol sequences are then transmitted over the MIMO channel. The MIMO channel has been modeled as described in Section II. For each of the two MIMO reference channel models, a MIMO channel simulator has been derived by using the concept of deterministic channel modeling [4]. Moreover, we take into account that the time-variant transfer function $H_{kl}(f,t)$ changes during the transmission of two consecutive OFDM symbols due to fading.

At the receiver side, the demodulated symbol sequences are passed through a combiner. Finally, by using the CSI obtained from the channel estimator, all the symbols can be decoded as described in [11].

IV. SIMULATION RESULTS

In this section, we use the wideband MIMO channel simulators, obtained from the elliptical model and the one-ring model, to study the system performance of 2×2 and 4×4 MIMO-OFDM systems. We assume that there are 240 scatterers located on each ellipse in the deterministic elliptical model and 220 scatterers in the one-ring model. The generalized method of exact Doppler spread (GMEDS$_q$) [6] is used to compute the AOAs $\phi_R^{(n)}$ for both models. All other parameters of the deterministic simulation models are identical to the corresponding parameters of the reference models described in Section II. Moreover, we have employed the specified 18-path HiperLAN/2 model C [2] to describe the delay profile corresponding to typical large open areas.

Assuming perfect CSI at the receiver, we first present the symbol error rate (SER) performance for various antenna spacings without space-time block coding. The least square decoder described in [12] has been employed. Figure.G.5 shows the SER performance for various antenna spacings by employing the wideband elliptical model. From this figure, we can conclude that the system performance improves with increasing the antenna spacings. The reason is that the spatial correlation between sub-channels becomes smaller with increasing antenna spacings
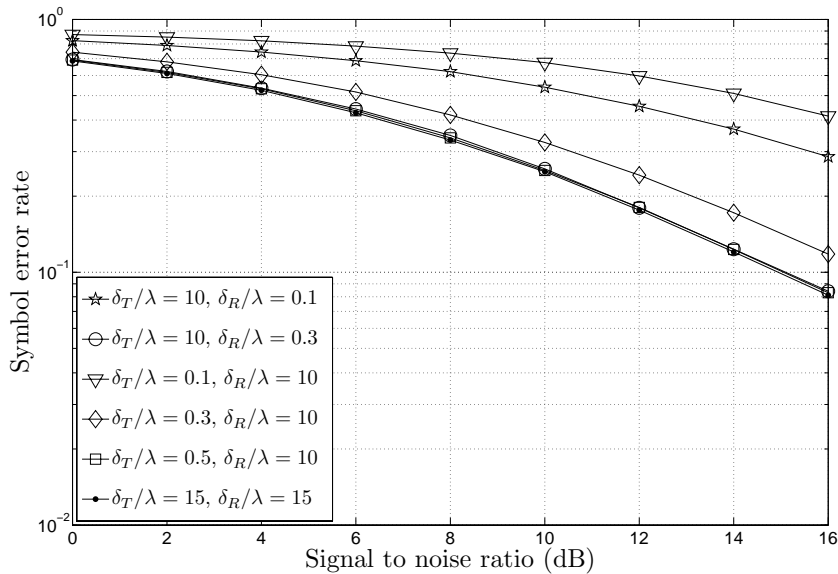
Figure G.5: SER performance of an uncoded MIMO-OFDM system with different antenna spacings using the elliptical 2×2 MIMO channel model.

(see Fig. G.1). Moreover, we can realize that a certain antenna spacing increment at the transmitter leads to a higher diversity gain than that of the same amount at the receiver. However, if $\delta_T > 0.5\lambda$ and $\delta_R > 0.3\lambda$, then no performance difference can be observed. In this case, the antenna spacings at the transmitter and the receiver have the same influence on the system performance.

The corresponding results for the one-ring model are shown in Fig. G.6, from which principally the same conclusions can be drawn. Here, no significant performance improvement can be observed if the $\delta_T > 10\lambda$ and $\delta_R > \lambda$.

We also investigated the SER performance of the space-time coded MIMO-OFDM system using the elliptical 2×2 and 4×4 MIMO channel models. The results are shown in Fig. G.7 for various antenna spacings. In the system simulations, the transmission matrices $\mathscr{G}_2$ and $\mathscr{H}_4$ described in [11] were chosen for the MIMO-OFDM systems with two and four transmit antennas, respectively. The diversity gain obtained by employing space-time codes can be observed clearly by comparing the performance with that of the uncoded MIMO-OFDM system (see Fig. G.5). Moreover, the same antenna spacing ranges can be obtained when space-time block codes are used. In addition, the simulation results demonstrate that significant diversity gains can be achieved by increasing the number of transmit antennas.

The SER performance for different antenna spacings using the one-ring 2×2 and 4×4 MIMO channel models is shown in Fig. G.8. The same conclusions can be drawn when using the elliptical model. From the SER performance depicted in
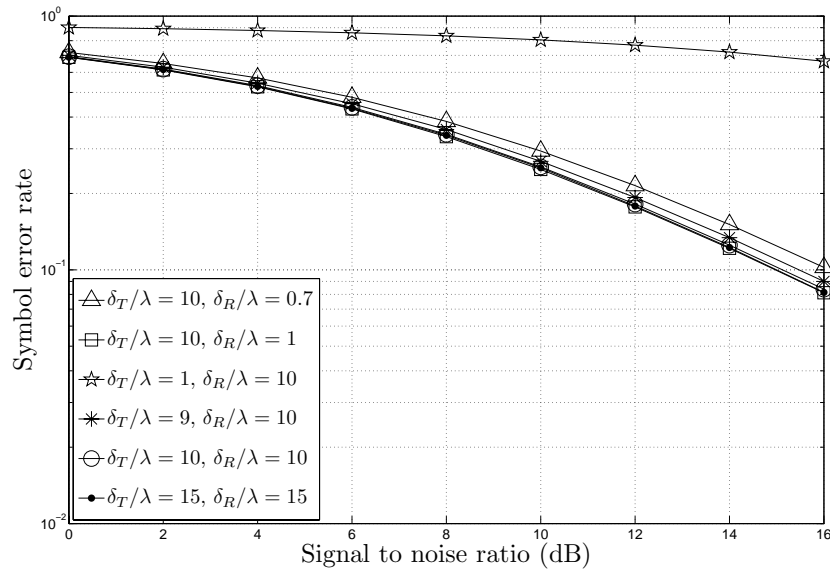
Figure G.6: SER performance of an uncoded MIMO-OFDM system with different antenna spacings using the one-ring 2×2 MIMO channel model.
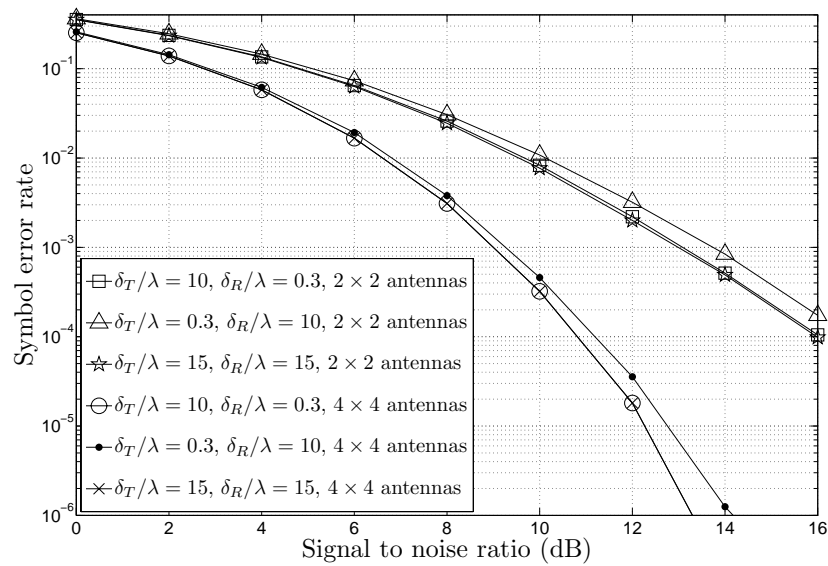
Figure G.7: SER performance of a space-time coded MIMO-OFDM system with different antenna spacings using the elliptical 2×2 and 4×4 MIMO channel models.
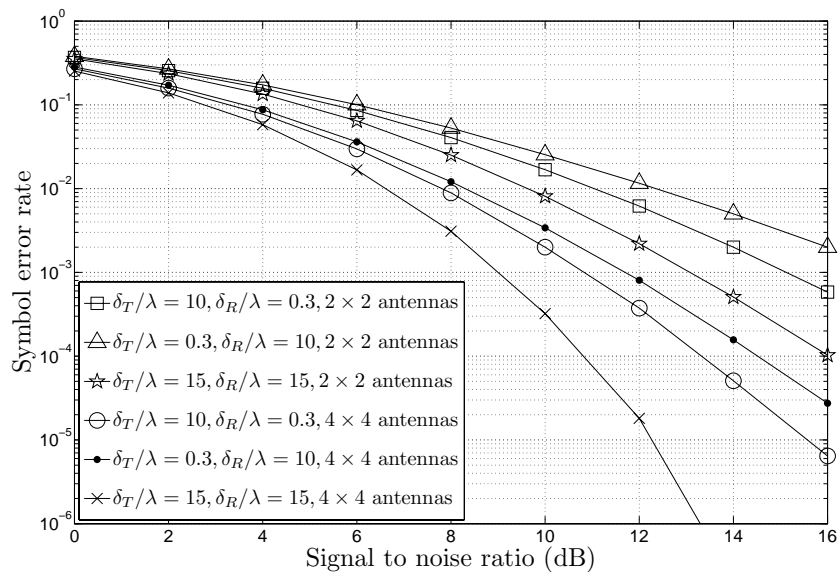
Figure G.8: SER performance of a space-time coded MIMO-OFDM system with different antenna spacings using the one-ring 2×2 and 4×4 MIMO channel models.

Figs. G.7 and G.8, it can be observed that the MIMO-OFDM system employing the elliptical channel model outperforms the one-ring model under the same conditions regarding the number of antennas and antenna spacings. The system using the elliptical 4×4 channel model with the antenna spacings $\delta_T = 10\lambda$ and $\delta_R = 0.3\lambda$ gains

about 3.7 dB against that using the one-ring channel model at the SER of 10^{-5}. The reason for this observation is that the spatial correlation function of the elliptical model decays faster with increasing antenna spacings than that of the one-ring model (compare Fig. G.1 and Fig. G.2).

The simulation results using the two channel models with different maximum Doppler frequencies are shown in Figs. G.9 and G.10, where we have assumed that the antenna spacings are given by $\delta_T = 15\lambda$ and $\delta_R = 15\lambda$. Both the perfect and imperfect CSI cases have been studied. For the latter case, the improved least square (LS) channel estimator described in [3] has been employed. It can be observed that the system performance degrades slightly under the assumption of perfect CSI if the maximum Doppler frequency $f_{\max}$ changes from 50 Hz to 500 Hz. However, severe degradations are obtained when $f_{\max}$ increases and imperfect CSI is assumed. It should be mentioned that the maximum Doppler frequency have an influence on the SER performance since the fading during two consecutive transmission time slots has been taken into account.

V. CONCLUSION

In this paper, different kinds of wideband MIMO channel simulators based on the geometric elliptical model and the one-ring model have been used to study the performance of space-time coded MIMO-OFDM systems. The influences of the antenna spacings and the maximum Doppler frequency have been discussed sepa-
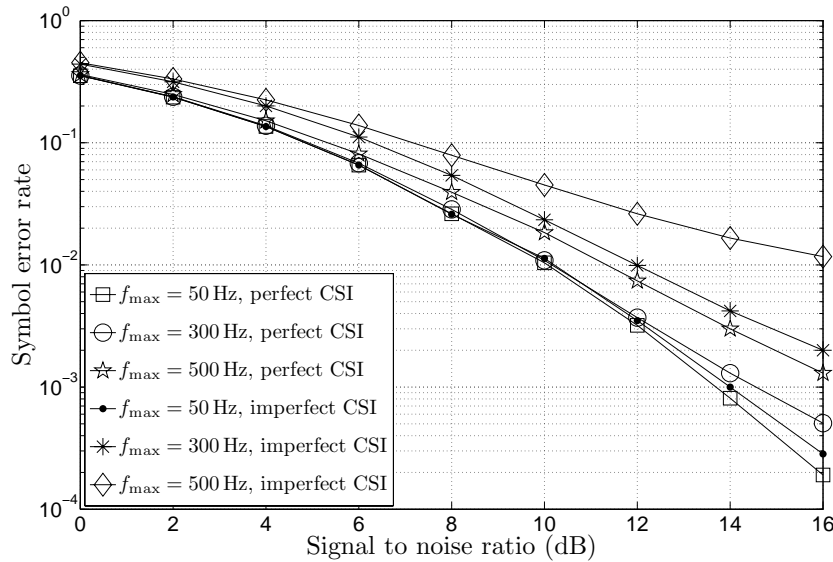
Figure G.9: SER performance of a space-time coded MIMO-OFDM system with different values for the maximum Doppler frequency $f_{\max}$ using the elliptical 2×2 MIMO channel model.
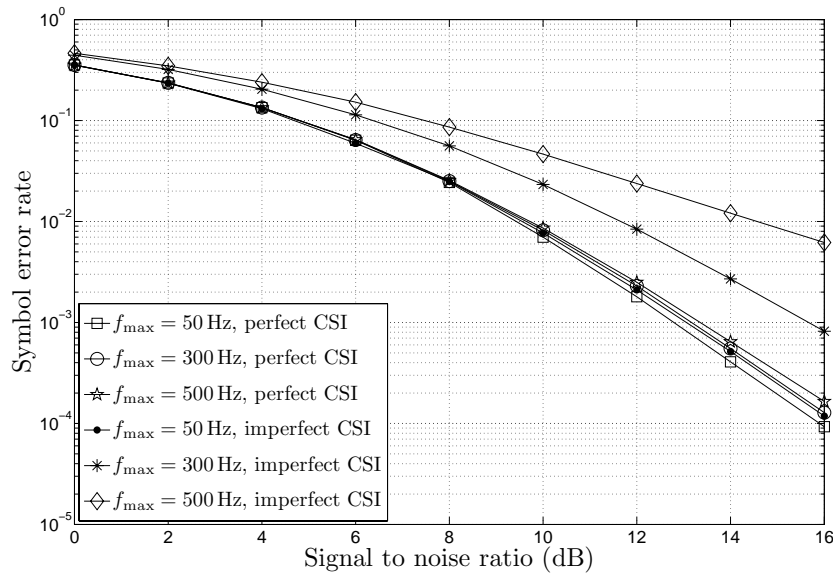
Figure G.10: SER performance of a space-time coded MIMO-OFDM system with different values for the maximum Doppler frequency f_{max} using the one-ring 2×2 MIMO channel model.

rately. We have determined the antenna spacing ranges, which are very helpful for the design of antenna arrays. If the antenna spacings exceed the determined values, then the diversity gain does not increase significantly with increasing antenna spacings. Furthermore, the MIMO-OFDM system employing the elliptical channel model can achieve a better performance than using the one-ring model with same antennas and antenna spacings. At the SER of 10^{-5}, it is observed that the MIMO-OFDM system with the 4×4 elliptical channel model gains about 3.7 dB against the one-ring channel model if the antenna spacings are $\delta_T = 10\lambda$ and $\delta_R = 0.3\lambda$. The reason is that the spatial correlation function of the elliptical model decays faster with increasing antenna spacings than that of the one-ring model. Moreover, our simulation results have also shown that the SER performance degrades with increasing maximum Doppler frequency, especially in case of imperfect CSI. Hence, accurate fast-tracking channel estimators are indispensable for mobile communication systems with high moving speed.

REFERENCES

[1] G. J. Byers and F. Takawira. Spatially and temporally correlated MIMO channels: modeling and capacity analysis. *IEEE Trans. on Veh. Technol.*, 53(3):634–643, May 2004.

[2] J. Medbo and P. Schramm. Channel models for HIPERLAN/2 in different indoor scenarios. Tech. Rep. 3ERI085B, ETSI EP, BRAN Meeting #3, Mar. 1998.

[3] V. D. Nguyen. Channel estimation for MIMO-OFDM systems in the case of insufficient guard interval length. In *Proc. International Conference on Communications and Electronics, IEEE ICCE 2006*, pages 229–233. Hanoi, Vietnam, Oct. 2006.

[4] M. Pätzold. *Mobile Fading Channels*. Chichester: John Wiley & Sons, 2002.

[5] M. Pätzold and B. O. Hogstad. A space-time channel simulator for MIMO channels based on the geometrical one-ring scattering model. *Wireless Communications and Mobile Computing, Special Issue on Multiple-input Multiple-output (MIMO) Communications*, 4(7):727–737, Nov. 2004.

[6] M. Pätzold and B. O. Hogstad. Two new methods for the generation of multiple uncorrelated Rayleigh fading waveforms. In *Proc. 63th Vehicular Technology Conference, VTC 2006-Spring*, volume 6, pages 2782–2786. Melbourne, Australia, May 2006.

[7] M. Pätzold and B. O. Hogstad. A wideband MIMO channel model derived from the geometric elliptical scattering model. In *Proc. 3rd International Symposium on Wireless Communication System, ISWCS 2006*, pages 138–144. Valencia, Spain, Sept. 2006.

[8] M. Pätzold and B. O. Hogstad. A wideband space-time MIMO channel simulator based on the geometrical one-ring model. In *Proc. 64th Vehicular Technology Conference, VTC 2006-Fall*. Montreal, Canada, Sept. 2006.

[9] M. Riback, H. Asplund, J. Medbo, and J. E. Berg. Statistical analysis of measured radio channels for future generation mobile communication systems. In *Proc. 61st IEEE Semiannual Vehicular Technology Conference, IEEE VTC 2005–Spring*, volume 1, pages 68–72. Stockholm, Sweden, May 2005.

[10] D. S. Shiu, G. J. Foschini, M. J. Gans, and J. M. Kahn. Fading correlation and its effect on the capacity of multielement antenna systems. *IEEE Trans. Commun.*, 48(3):502–513, Mar. 2000.

[11] V. Tarokh, H. Jafarkhani, and A. R. Calderbank. Space-time block coding for wireless communications: performance results. *IEEE J. Select. Areas Commun.*, 17(3):451–460, Mar. 1999.

[12] B. Vucetic and J. Yuan. *Space-Time Coding*. Chichester: John Wiley & Sons, 2003.

[13] H. Zhang, D. Yuan, M. Pätzold, and V. D. Nguyen. Performance of space-time coded transmitter diversity techniques in transmission scenarios of Hiper-LAN/2. In *Proc. International ITG/IEEE Workshop on Smart Antennas, WSA 2006*. Günzburg, Germany, Mar. 2006.

Appendix H

Paper VIII

Title:	Performance Analysis of STBC-OFDM Systems in Temporally or Spatially Correlated Fading Channels
Authors:	**Yuanyuan Ma** and Matthias Pätzold
Affiliation:	University of Agder, Faculty of Engineering and Science, P. O. Box 509, NO-4898 Grimstad, Norway.
Conference:	*IEEE Wireless Communications and Networking Conference, WCNC 2010*, Sydney, Australia, Apr. 2010, pp. 1 – 5. DOI: 10.1109/WCNC.2010.5506743.

Performance Analysis of STBC-OFDM Systems in Temporally or Spatially Correlated Fading Channels

Yuanyuan Ma and Matthias Pätzold

Department of Information and Communication Technology

Faculty of Engineering and Science, University of Agder

Servicebox 509, NO-4898 Grimstad, Norway

E-mails: {yuanyuan.ma, matthias.paetzold}@uia.no

Abstract — **This paper analyzes the performance of space-time block coded orthogonal frequency division multiplexing (OFDM) systems. In our analysis, we abandon the usually made assumption of quasi-static channel conditions. Instead of this, we consider the more general and realistic case that the channel envelope changes during two consecutive transmission time slots. In addition, we take the spatial correlation between sub-channels into account. We first present a general formal expression for the bit error probability (BEP), from which we find analytical solutions for the BEP not only for temporally fading channels but also for spatially correlated channels. The knowledge of the obtained analytical solutions makes the determination of the BEP less time-consuming compared with system simulations. Moreover, they give a deep insight into the impact of the Doppler effect and the antenna spacing on the system performance.**

I. INTRODUCTION

A space-time block coding (STBC) scheme was originally proposed by Alamouti as an effective method to achieve a transmit diversity gain [3]. Recently, increasing demands for high data rate wireless communication services necessitate data transmissions over wideband channels. The combination of STBC with OFDM is regarded as a promising solution for combating frequency-selective fading [8]. For both single-carrier and multi-carrier transmission systems, the Alamouti scheme works well if the channel is time-invariant over two consecutive symbol durations.

However, it is not realistic to assume that the channel remains constant during the period of the Alamouti codeword transmission, especially not under fast fading conditions. The impact of a time-varying fading channel on the performance of the Alamouti transmit scheme has been investigated in [13] for a single-carrier system and in [6] for an OFDM system. In both papers, the spatial correlation between the time-varying multipath Rayleigh fading sub-channels has not been considered.

However, it has been shown in [7] by simulations that the performance of a STBC-OFDM system depends not only on the temporal correlation but also on the spatial correlation.

In this paper, we study the performance of an Alamouti coded OFDM system in time-varying and spatially correlated Rayleigh fading channels. In our analysis, we take into account the channel variations during two consecutive transmission time slots. The zero-forcing (ZF) detector proposed in [13] has been used in this paper for the symbol detection. We first derive a general formal expression for the BEP. It is worth mentioning that the derived BEP expression is generally valid. It can be used to study the BEP performance for the more general and practical case, where the multipath channels can be arbitrarily correlated in either the temporal or the spatial domain or even in both domains. Starting from this relation, we derive analytical expressions for the BEP for (i) temporally correlated fading channels and (ii) spatially correlated channels. The derived theoretical expressions can be used to study the influence of the maximum Doppler frequency and the antenna spacing on the system performance. Although the temporal autocorrelation function (ACF) and the space cross-correlation function (CCF) have the same shape under isotropic scattering conditions, we find their influence on the system performance is different.

The remainder of this paper is organized as follows. In Section II, we first give a brief review of the Alamouti coded OFDM system as well as the wideband channel model. Considering that the channel changes within the duration of two neighboring symbols, a general expression for the BEP is derived in Section III. Section IV analyzes the performance of the Alamouti coded OFDM system in temporally correlated channels. Section V is devoted to the performance analysis in spatially correlated channels. Finally, the conclusions are drawn in Section VI.

II. A STBC-OFDM System

In this paper, we consider an OFDM system equipped with two transmit antennas and a single receive antenna. We assume that the complex data symbol pair (S_1, S_2) is encoded first by the Alamouti scheme [12] before it is transmitted over the multipath channel. The received symbols at time slots t_1 and t_2 are given by

$$Y_1 = H_{11}(f', x_1, t_1)S_1 + H_{21}(f', x_2, t_1)S_2 + N_1, \tag{1a}$$

$$Y_2 = -H_{11}(f', x_1, t_2)S_2^* + H_{21}(f', x_2, t_2)S_1^* + N_2, \tag{1b}$$

where N_i $(i = 1, 2)$ is the additive white Gaussian noise (AWGN) component and

$$H_{k1}(f', x_k, t_i) = \sum_{\ell=1}^{\mathcal{L}} a_\ell \mu_\ell(x_k, t_i) e^{-j2\pi f' \tau'_\ell}, \tag{2}$$

represents the space-time-variant transfer function in the time slot t_i of the transmission link from the kth transmitting antenna located at x_k ($k = 1, 2$) to the single receiving antenna. In the equation above, $\mathscr{L}$ is the number of discrete propagation paths. The quantities a_ℓ and τ'_ℓ denote the path gain and the propagation delay of the ℓth path, respectively. The processes $\mu_\ell(x_k, t_i)$ in (2) represent zero-mean complex Gaussian random processes. We further assume that the real and imaginary parts of $\mu_\ell(x_k, t_i)$ are uncorrelated, each having the variance $\sigma_0^2 = 1/2$. To ensure that the average power of the channel model is normalized to unity, the path gains a_ℓ have to fulfill the power constraint $\sum_{\ell=1}^{\mathscr{L}} a_\ell^2 = 1$.

Keeping in mind that mobile radio fading channels vary during two consecutive symbol slots, we use the combining strategy proposed in [13, 2] for symbol detection. Moveover, we assume that the knowledge of the channel state information is perfectly known at the receiver and no synchronization error exists. Therefore, the estimated symbols at the output of the ZF detector can be expressed as follows [13]

$$\hat{S}_1 = [H_{11}(f', x_1, t_1)H_{11}^*(f', x_1, t_2) + H_{21}(f', x_2, t_1)H_{21}^*(f', x_2, t_2)]S_1$$
$$+ H_{11}^*(f', x_1, t_2)N_1 + H_{21}(f', x_2, t_1)N_2^*, \tag{3a}$$

$$\hat{S}_2 = [H_{11}(f', x_1, t_1)H_{11}^*(f', x_1, t_2) + H_{21}(f', x_2, t_1)H_{21}^*(f', x_2, t_2)]S_2$$
$$+ H_{21}^*(f', x_2, t_2)N_1 + H_{11}(f', x_1, t_1)N_2^*. \tag{3b}$$

To facilitate the performance analysis, the complex space-time-variant transfer functions can be represented as

$$H_{11}(f', x_1, t_1) = R_1 e^{\Theta_1}, \qquad H_{11}(f', x_1, t_2) = R_2 e^{\Theta_2},$$
$$H_{21}(f', x_2, t_1) = R_3 e^{\Theta_3}, \qquad H_{21}(f', x_2, t_2) = R_4 e^{\Theta_4}. \tag{4}$$

Here, the envelope R_m represents the absolute value of the corresponding space-time-variant transfer function and Θ_m denotes the random phase ($m = 1, 2, 3, 4$). Moreover, studying the channel model described above, it becomes obvious that the random envelope R_m is Rayleigh distributed.

Since the system model is symmetrical, the BEP for S_1 is equal to the one for S_2. Therefore, in the following, we only concentrate on the BEP analysis for S_1. According to (3a), the instantaneous output signal-to-noise ratio (SNR) for $\hat{S}_1$ can be written as

$$\gamma_\Sigma = \frac{R_1^2 R_2^2 + R_3^2 R_4^2 + 2R_1 R_2 R_3 R_4 \cos(\Theta_1 - \Theta_2 + \Theta_4 - \Theta_3)}{(R_2^2 + R_3^2) \cdot 2\sigma_n^2}, \tag{5}$$

where $2\sigma_n^2$ is the variance of the AWGN noise. Note that if the channel is constant during the consecutive time slots t_1 and t_2, i.e., $H_{k1}(f',x_k,t_1) = H_{k1}(f',x_k,t_2)$ $(k = 1, 2)$, (5) reduces to the known instantaneous output SNR of the traditional maximum-likelihood detector described in [4].

III. GENERAL FORMAL BEP EXPRESSION

As seen from (5), the instantaneous output SNR depends not only on the envelopes (R_1, R_2, R_3, R_4) but also on the phases $(\Theta_1, \Theta_2, \Theta_3, \Theta_4)$. Even if the joint probability density function (PDF) of the envelopes and phases is known, it is still difficult to derive the theoretical expression for the PDF of the instantaneous output SNR.

For this purpose, we introduce in this paper an approximation for the instantaneous output SNR by neglecting the difference between the phase changes $\Theta_1 - \Theta_2$ and $\Theta_3 - \Theta_4$, i.e., $\Theta_1 - \Theta_2 - (\Theta_3 - \Theta_4) \approx 0$. Thus, the instantaneous output SNR γ_Σ in (5) can be approximated as

$$\gamma_\Sigma \approx \frac{R_1^2 R_2^2 + R_3^2 R_4^2 + 2R_1 R_2 R_3 R_4}{(R_2^2 + R_3^2) \cdot 2\sigma_n^2}. \tag{6}$$

Starting from the joint PDF of the envelopes R_1, R_2, R_3, and R_4, denoted by $p_{R_1 R_2 R_3 R_4}(r_1, r_2, r_3, r_4)$, an analytical expression for the PDF $p_{\gamma_\Sigma}(\gamma)$ of the approximate instantaneous output SNR is derived in the Appendix H.A [see (A.8)].

To verify its accuracy, we confirm the preceding theoretical PDF $p_{\gamma_\Sigma}(\gamma)$ [see (A.8)] by simulations. Figure H.1 presents the simulation results for the PDF of the approximate instantaneous output SNR as well as for the PDF of the exact instantaneous output SNR. Here, the exact instantaneous output SNR means the instantaneous output SNR without neglecting the overall phase contribution [see (5)]. In this figure, we measure both PDFs by considering different types of correlated channels, including (i) temporally correlated channels and (ii) spatially correlated channels. In all simulations, the typical 6-path Rural Area scenario specified according to COST 207 [1] has been considered. We assume that the average SNR $\bar{\gamma}$ is $5\,\text{dB}$, the symbol duration T_s equals $6.4\,\mu\text{s}$, the maximum Doppler frequency f_{max} is $500\,\text{Hz}$, and the transmit antenna spacing $\triangle x$ is $0.5\,\lambda$, where λ denotes the wavelength.

As seen from Fig. H.1, the simulation results match the theoretical results very well. Moreover, the difference between the PDF of the approximate instantaneous output SNR and the PDF of the exact instantaneous output SNR is indistinguishable. This means that both PDFs are almost equivalent. Thus, we can conclude that the overall phase contribution to the instantaneous output SNR is negligible. It should
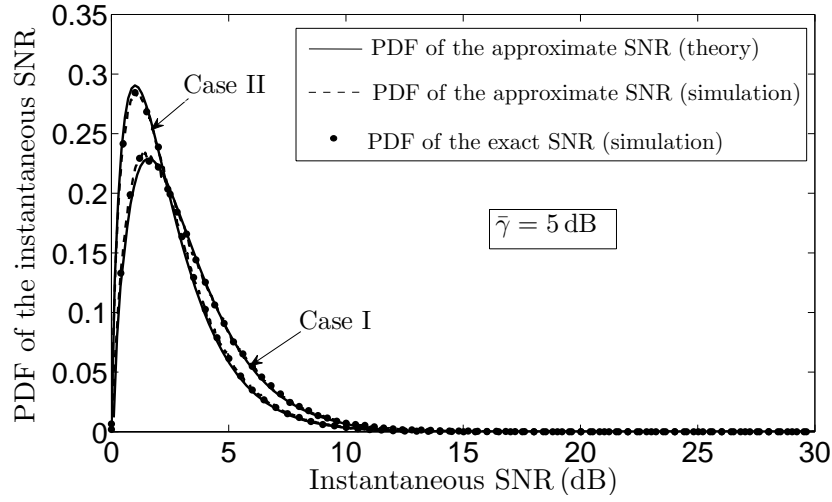
Figure H.1: Simulation results for the PDF of the instantaneous output SNR for (i) temporally correlated channels and (ii) spatially correlated channels.

be emphasized that in this paper, we have never neglected the phase change between Θ_1 and Θ_2 (or between Θ_3 and Θ_4), i.e., $\Theta_1 \neq \Theta_2$ and $\Theta_3 \neq \Theta_4$. Instead, we only assume that $(\Theta_1 - \Theta_2) - (\Theta_3 - \Theta_4) \approx 0$. The correctness of such an approximation has been confirmed by the excellent fitting between the theoretical and simulation results shown in Fig. H.1.

After substituting the obtained joint PDF $p_{\gamma_\Sigma}(\gamma)$ in the relation [4, Eq. (7.20)], we finally obtain the general formal expression for the BEP of the STBC-OFDM system, which has been presented in (7)

$$
P_b = \frac{2\sigma_0^2}{8\bar{\gamma}} \int_0^\infty \int_0^\infty \int_0^w \int_0^{z_2} P_{b|\gamma_\Sigma}(\gamma) \cdot \frac{z_2}{z_4(z_2 - z_4)w}
$$
$$
\cdot p_{R_1 R_2 R_3 R_4}\left(\frac{z_3}{\sqrt{z_2 - z_4}}, \sqrt{z_2 - z_4}, \sqrt{z_4}, \frac{w - z_3}{\sqrt{z_4}}\right) dz_4 dz_3 dz_2 d\gamma. \tag{7}
$$

In this equation, we have $w = \sqrt{2\sigma_0^2 \gamma z_2 / \bar{\gamma}}$ and $P_{b|\gamma_\Sigma}(\gamma)$ is the BEP conditioned on a specific value of the SNR γ, e.g., $P_{b|\gamma_\Sigma}(\gamma) = \mathrm{erfc}(\sqrt{\bar{\gamma}})/2$ for a binary phase-shift keying (BPSK) modulation scheme. Here, $\mathrm{erfc}(x) = \int_x^\infty \frac{2}{\sqrt{\pi}} e^{-y^2} dy$ represents the complementary error function.

It is worth mentioning that the result in (7) is generally valid. It can not only be used to study the BEP performance separately for temporally and spatially correlated fading channels, but also for channels that are correlated in both space and time.

So far, the joint PDF of four dependent Rayleigh variables is unknown in the literature. Thus, it is not straightforward to express the joint PDF $p_{R_1R_2R_3R_4}(r_1,r_2,r_3,r_4)$ of envelops when channels are spatially-temporally correlated. Since the derivation of the joint PDF of four Rayleigh variables is not the main interest of this paper, in the following, we will only be concerned with the first two cases to demonstrate the usefulness of (7).

IV. THE BEP PERFORMANCE OF STBC-OFDM SYSTEMS IN TEMPORALLY CORRELATED CHANNELS

In this section, we study the system performance in temporally correlated channels. We assume that the sub-channels are spatially uncorrelated.

According to [5], the temporal ACF of $H_{k1}(f',x_k,t_1)$ and $H_{k1}(f',x_k,t_2)$, defined by $r_{HH}(\tau) = E\{H_{k1}^*(f',x_k,t_1) \cdot H_{k1}(f',x_k,t_2)\}$, where $\tau = t_2 - t_1$, can be expressed as

$$r_{HH}(\tau) = 2\sigma_0^2 J_0(2\pi f_{\max}\tau) \tag{8}$$

for isotropic scattering environments. Here, $J_0(\cdot)$ is the zeroth-order Bessel function of the first kind. We further assume that there is no temporal correlation between $H_{k1}(f',x_k,t_1)$ and $H_{l1}(f',x_l,t_2)$ if $k \neq l$, so that the joint PDF $p_{R_1R_2R_3R_4}(r_1,r_2,r_3,r_4)$ of the envelopes R_1, R_2, R_3, and R_4 can be written as

$$p_{R_1R_2R_3R_4}(r_1,r_2,r_3,r_4) = p_{R_1R_2}(r_1,r_2) \cdot p_{R_3R_4}(r_3,r_4), \tag{9}$$

where $p_{R_1R_2}(r_1,r_2)$ denotes the joint PDF of the random variables R_1 and R_2, while $p_{R_3R_4}(r_3,r_4)$ is the joint PDF of R_3 and R_4. According to [5], the joint PDFs $p_{R_1R_2}(r_1,r_2)$ and $p_{R_3R_4}(r_3,r_4)$ are given by

$$p_{R_1R_2}(r_1,r_2) = \frac{r_1r_2}{\sigma_0^4 - \rho_T^2} \cdot e^{-\frac{\sigma_0^2(r_1^2+r_2^2)}{2(\sigma_0^4-\rho_T^2)}} \cdot I_0\left(\frac{r_1r_2\rho_T}{\sigma_0^4 - \rho_T^2}\right), \tag{10a}$$

$$p_{R_3R_4}(r_3,r_4) = \frac{r_3r_4}{\sigma_0^4 - \rho_T^2} \cdot e^{-\frac{\sigma_0^2(r_3^2+r_4^2)}{2(\sigma_0^4-\rho_T^2)}} \cdot I_0\left(\frac{r_3r_4\rho_T}{\sigma_0^4 - \rho_T^2}\right), \tag{10b}$$

where $I_0(\cdot)$ represents the zeroth-order modified Bessel function of the first kind, and $\rho_T = r_{HH}(\tau)/2$ denotes the temporal ACF of the real (imaginary) parts of $H_{k1}(f',x_k,t_1)$ and $H_{k1}(f',x_k,t_2)$ at $\tau = T_s$.

Submitting (9) into (7) and using (10a) and (10b) leads to the expression (11)

$$
P_b = \frac{2\sigma_0^2}{16(\sigma_0^4 - \rho_T^2)^2 \bar{\gamma}} \int\limits_0^\infty \int\limits_0^\infty \int\limits_0^w \int\limits_0^{z_2} \frac{z_2 z_3 (w - z_3)}{z_4 (z_2 - z_4) w} \cdot e^{-\frac{\sigma_0^2}{2(\sigma_0^4 - \rho_T^2)} \left[\frac{(w-z_3)^2}{z_4} + z_2 + \frac{z_3^2}{z_2 - z_4}\right]}
$$

$$
\cdot \operatorname{erfc}(\sqrt{\gamma}) \cdot I_0 \left(\frac{z_3 \rho_T}{\sigma_0^4 - \rho_T^2}\right) \cdot I_0 \left(\frac{(w - z_3)\rho_T}{\sigma_0^4 - \rho_T^2}\right) dz_4 dz_3 dz_2 d\gamma. \tag{11}
$$

This equation shows the BEP of the STBC-OFDM system in temporally correlated channels. Since there is no closed-form solution for the BEP in (11), the integrals have to be solved numerically.

The evaluation of the analytical expression for the BEP in (11) allows us to study the influence of the Doppler effect on the BEP. The analytical results are shown in Fig. H.2 for $f_{\max} = 100\,\text{Hz}$ and $f_{\max} = 500\,\text{Hz}$. This figure also presents the relevant simulation results. The simulation results are obtained by considering the real channel conditions, which means both the envelope change and the phase change during two consecutive transmission time slots have been taken into account. It can be seen from this figure that the simulation results match the analytical ones very well. The considered OFDM system consists of $K = 64$ subcarriers. All other parameters are the same as in Section II. It can be concluded from Fig. H.2 that the maximum Doppler frequency has an influence on the system performance, which can be attributed to the channel variations during two consecutive transmission time
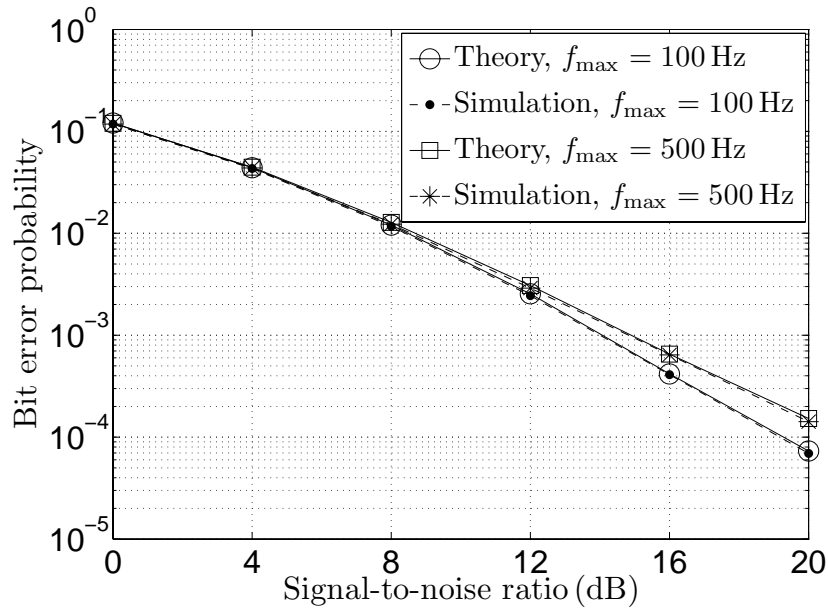
Figure H.2: BEP performance of STBC-OFDM systems in temporally correlated channels for $f_{\max} = 100\,\text{Hz}$ and $f_{\max} = 500\,\text{Hz}$.

slots. The performance deteriorates when $f_{\max}$ changes from $100\,\mathrm{Hz}$ to $500\,\mathrm{Hz}$ due to the lower temporal correlation.

V. THE BEP PERFORMANCE OF STBC-OFDM SYSTEMS IN SPATIALLY CORRELATED CHANNELS

This section deals with the analysis of the system performance in spatially correlated fading channels. We assume that the sub-channels are temporally uncorrelated.

The space CCF of $H_{11}(f', x_1, t_i)$ and $H_{21}(f', x_2, t_i)$, defined by $r_{HH}(\triangle x)$ $= E\{H_{11}^*(f', x_1, t_i) \cdot H_{21}(f', x_2, t_i)\}$, can be expressed as [10]

$$r_{HH}(\triangle x) = \sum_{\ell=1}^{\mathscr{L}} a_\ell^2 r_{\mu_\ell \mu_\ell}(\triangle x) \tag{12}$$

where $\triangle x = x_2 - x_1$. In (12), $r_{\mu_\ell \mu_\ell}(\triangle x)$ designates the space CCF of the $\mu_\ell(x_k, t_i)$ at $\triangle x = x_2 - x_1$. For the case of isotropic scattering, we have $r_{\mu_\ell \mu_\ell}(\triangle x) = 2\sigma_0^2 J_0(2\pi \triangle x/\lambda)$ [11].

We further assume that the space CCF between $H_{11}(f', x_1, t_i)$ and $H_{21}(f', x_2, t_j)$ is zero if $i \neq j$. Thus, again the joint PDF $p_{R_1 R_2 R_3 R_4}(r_1, r_2, r_3, r_4)$ of the envelopes R_1, R_2, R_3, and R_4 can be represented by the product of two joint PDFs as follows

$$p_{R_1 R_2 R_3 R_4}(r_1, r_2, r_3, r_4) = p_{R_1 R_3}(r_1, r_3) \cdot_{R_2 R_4}(r_2, r_4), \tag{13}$$

where $p_{R_1 R_3}(r_1, r_3)$ is the joint PDF of R_1 and R_3, while $p_{R_2 R_4}(r_2, r_4)$ is the joint PDF of R_2 and R_4. Since both $p_{R_1 R_3}(r_1, r_3)$ and $p_{R_2 R_4}(r_2, r_4)$ are given by the joint PDF of two dependent Rayleigh random variables, it follows that [5]

$$p_{R_1 R_3}(r_1, r_3) = \frac{r_1 r_3}{\sigma_0^4 - \rho_x^2} \cdot e^{-\frac{\sigma_0^2(r_1^2 + r_3^2)}{2(\sigma_0^4 - \rho_x^2)}} \cdot I_0 \left(\frac{r_1 r_3 \rho_x}{\sigma_0^4 - \rho_x^2} \right), \tag{14a}$$

$$p_{R_2 R_4}(r_2, r_4) = \frac{r_2 r_4}{\sigma_0^4 - \rho_x^2} \cdot e^{-\frac{\sigma_0^2(r_2^2 + r_4^2)}{2(\sigma_0^4 - \rho_x^2)}} \cdot I_0 \left(\frac{r_2 r_4 \rho_x}{\sigma_0^4 - \rho_x^2} \right). \tag{14b}$$

Substituting (13) into (7) and using (14a) and (14b) gives the BEP performance in spatially correlated channels. The analytical expression for the BEP is shown in (15)

$$P_b = \frac{2\sigma_0^2}{16(\sigma_0^4 - \rho_x^2)^2 \bar{\gamma}} \int_0^\infty \int_0^\infty \int_0^w \int_0^{z_2} \frac{z_2 z_3 (w - z_3)}{z_4 (z_2 - z_4) w} \cdot I_0 \left(\frac{z_3 \sqrt{z_4} \rho_x}{(\sigma_0^4 - \rho_x^2) \sqrt{z_2 - z_4}} \right)$$

$$\cdot I_0 \left(\frac{(w-z_3)\sqrt{z_2-z_4}\rho_x}{(\sigma_0^4-\rho_x^2)\sqrt{z_4}} \right) \cdot e^{-\frac{\sigma_0^2}{2(\sigma_0^4-\rho_x^2)}\left[\frac{(w-z_3)^2}{z_4}+z_2+\frac{z_3^2}{z_2-z_4}\right]} \cdot \mathrm{erfc}(\sqrt{\gamma})\, dz_4 dz_3 dz_2 d\gamma.$$

$$(15)$$

In this equation, $\rho_x = r_{HH}(\triangle x)/2$ is the space CCF of the real (imaginary) parts of $H_{11}(f', x_1, t_i)$ and $H_{21}(f', x_2, t_i)$ at $\triangle x = x_2 - x_1$.

The BEP calculated according to (15) is illustrated in Fig. H.3 for different antenna spacings $\triangle x = 0.1\lambda$ and $\triangle x = 3\lambda$. From this figure, we realize that system performance improvements can be achieved by increasing the antenna spacing. The reason is that the spatial correlation between sub-channels becomes smaller when the antenna spacing increases. Again, the theoretical curves in Fig. H.3 are validated by system simulations with the same parameters as described in Section III. Although the temporal ACF and the space CCF have the same shape, their influence on the system performance is different.

VI. CONCLUSION

In this paper, we have analyzed the performance of STBC-OFDM systems in correlated channels, where the statistical channel variations during two consecutive transmission time slots have been taken into consideration. We have pointed out that the instantaneous output SNR strongly depends on the statistics of the envelopes of the space-time-variant transfer functions, while the impact of the overall random phase
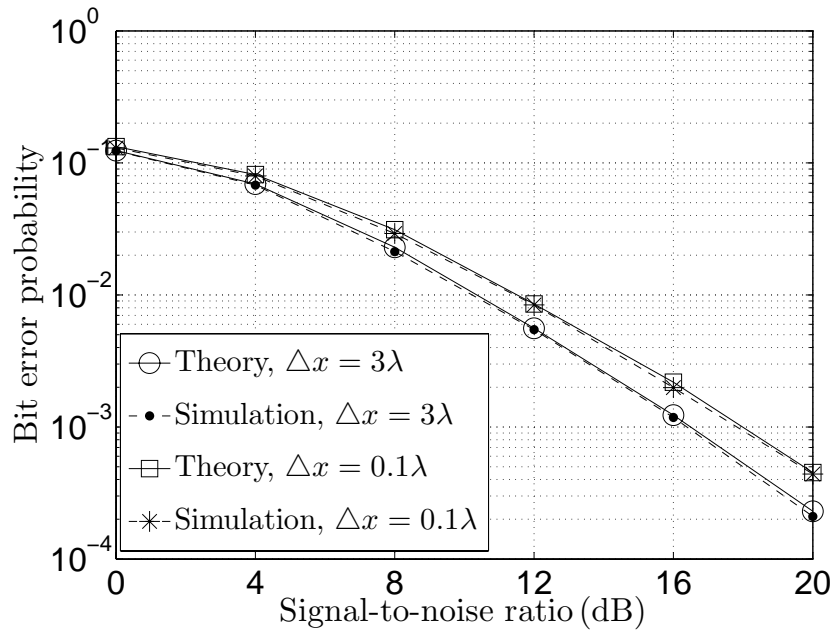
Figure H.3: BEP performance of STBC-OFDM systems in spatially correlated channels for $\triangle x = 0.1\lambda$ and $\triangle x = 3\lambda$.

contribution is negligible. A general equation for the BEP has been derived, which enables studying the system performance in different types of correlated channels. For instance, we have discussed the system performance separately for temporally and spatially correlated channels.

It has been shown that the system performance deteriorates when increasing the maximum Doppler frequency due to a lower temporal ACF. In contrast, the performance improves if reducing the space CCF, which can be implemented by increasing the antenna spacing. Therefore, we can conclude that the temporal ACF and the space CCF have inverse effect on the system performance. All the theoretical results in this paper have been validated by simulations. Even the overall random phase contribution has been neglected in our performance analysis, it has been shown the derived analytical results match the simulation results evaluated by considering this overall phase contribution.

H. A Derivation of the PDF of the instantaneous output SNR

This Appendix is devoted to express the PDF $p_{\gamma_\Sigma}(\gamma)$ of the instantaneous output SNR as a function of the joint PDF $p_{R_1R_2R_3R_4}(r_1, r_2, r_3, r_4)$ of the envelopes R_1, R_2, R_3, and R_4.

A starting point for the derivation of the joint PDF $p_{\gamma_\Sigma}(\gamma)$ is given by the PDF of the random variable Z, which is defined by

$$Z = \frac{R_1^2 R_2^2 + R_3^2 R_4^2 + 2R_1 R_2 R_3 R_4}{R_2^2 + R_3^2}. \tag{A.1}$$

For this purpose, we define the following system of equations

$$z_1 = (r_1 r_2 + r_3 r_4)^2, \quad z_2 = r_2^2 + r_3^2, \quad z_3 = r_1 r_2, \quad z_4 = r_3^2. \tag{A.2}$$

For $z_3 < \sqrt{z_1}$ and $z_4 < z_2$, the following solutions to the system of equations can be found

$$r_1 = \frac{z_3}{\sqrt{z_2 - z_4}}, \qquad r_2 = \sqrt{z_2 - z_4},$$

$$r_3 = \sqrt{z_4}, \qquad r_4 = \frac{\sqrt{z_1} - z_3}{\sqrt{z_4}}. \tag{A.3}$$

Applying the concept of transformation of random variables [9] leads to the join

PDF of the random variables Z_1, Z_2, Z_3, and Z_4

$$p_{Z_1 Z_2 Z_3 Z_4}(z_1, z_2, z_3, z_4) = |J(z_1, z_2, z_3, z_4)| \tag{A.4}$$

$$\cdot p_{R_1 R_2 R_3 R_4}\left(\frac{z_3}{\sqrt{z_2 - z_4}}, \sqrt{z_2 - z_4}, \sqrt{z_4}, \frac{\sqrt{z_1} - z_3}{\sqrt{z_4}}\right),$$

where

$$
J(z_1, z_2, z_3, z_4) = \begin{vmatrix}
\frac{\partial z_1}{\partial r_1} & \frac{\partial z_1}{\partial r_2} & \cdots & \frac{\partial z_1}{\partial r_4} \\
\frac{\partial z_2}{\partial r_1} & \frac{\partial z_2}{\partial r_2} & \cdots & \frac{\partial z_2}{\partial r_4} \\
\vdots & \vdots & \ddots & \vdots \\
\frac{\partial z_4}{\partial r_1} & \frac{\partial z_4}{\partial r_2} & \cdots & \frac{\partial z_4}{\partial r_4}
\end{vmatrix}^{-1}
$$

$$= -\frac{1}{8\sqrt{z_1}z_4(z_2 - z_4)} \tag{A.5}$$

denotes the Jacobian determinant. Furthermore, the joint PDF of the random variables Z_1 and Z_2 can be obtained by integrating the joint PDF $p_{Z_1 Z_2 Z_3 Z_4}(z_1, z_2, z_3, z_4)$ over z_3 and z_4 [9, p. 243], i.e.,

$$p_{Z_1 Z_2}(z_1, z_2) = \frac{1}{8\sqrt{z_1}} \int_0^{\sqrt{z_1}} \int_0^{z_2} \frac{1}{z_4(z_2 - z_4)} \tag{A.6}$$

$$\cdot p_{R_1 R_2 R_3 R_4}\left(\frac{z_3}{\sqrt{z_2 - z_4}}, \sqrt{z_2 - z_4}, \sqrt{z_4}, \frac{\sqrt{z_1} - z_3}{\sqrt{z_4}}\right) dz_4 dz_3.$$

The random variable Z can be written as the quotient of Z_1 over Z_2. Using the rule [9, Eq. (6–59)] enables us to calculate the PDF of Z, which is given by

$$p_Z(z) = \frac{1}{8} \int_0^{\infty} \int_0^{\sqrt{z z_2}} \int_0^{z_2} \frac{z_2}{z_4(z_2 - z_4)\sqrt{z z_2}} \tag{A.7}$$

$$\cdot p_{R_1 R_2 R_3 R_4}\left(\frac{z_3}{\sqrt{z_2 - z_4}}, \sqrt{z_2 - z_4}, \sqrt{z_4}, \frac{\sqrt{z z_2} - z_3}{\sqrt{z_4}}\right) dz_4 dz_3 dz_2.$$

Finally, we are in the position to express the desired PDF $p_{\gamma_{\Sigma}}(\gamma)$ of $\gamma_{\Sigma} = Z/2\sigma_n^2$ in the following form

$$p_{\gamma_{\Sigma}}(\gamma) = \frac{2\sigma_0^2}{8\bar{\gamma}} \int_0^{\infty} \int_0^{w} \int_0^{z_2} \frac{z_2}{z_4(z_2 - z_4)w} \tag{A.8}$$

$$\cdot p_{R_1 R_2 R_3 R_4}\left(\frac{z_3}{\sqrt{z_2 - z_4}}, \sqrt{z_2 - z_4}, \sqrt{z_4}, \frac{w - z_3}{\sqrt{z_4}}\right) dz_4 dz_3 dz_2,$$

where the upper limit w in the second integral represents $w = \sqrt{2\sigma_0^2 \gamma z_2 / \bar{\gamma}}$.

REFERENCES

[1] *Digital land mobile radio communications*. Office for Official Publications of the European Communities Std. Final report, 1989.

[2] G. Abreu and R. Kohno. Non-differential space-time transmission diversity in fast fading. In *Proc. 13th IEEE International Symposium on Personal, Indoor and Mobile Radio Communications*, volume 1, pages 74–78. Lisbon, Portugal, Sept. 2002.

[3] S. M. Alamouti. A simple transmit diversity technique for wireless communications. *IEEE Journal on Select Areas in Communications*, 16(8):1451–1458, Oct. 1998.

[4] A. Goldsmith. *Wireless Communications*. Cambridge University Press, 2005.

[5] W. C. Jakes. *Microwave Mobile Communications*. New Jersey: IEEE Press, 1994.

[6] D. B. Lin, P. H. Chiang, and H. J. Li. Performance analysis of two–branch transmit diversity block–coded OFDM systems in time–varying multipath Rayleigh–fading channels. *IEEE Trans. on Veh. Technol.*, 54(1):136–148, Jan. 2005.

[7] Y. Ma and M. Pätzold. Performance comparison of space-time coded MIMO–OFDM systems using different wideband MIMO channel models. In *Proc. 4th IEEE International Symposium on Wireless Communication Systems, ISWCS 2007*, pages 762–766. Trondheim, Norway, Oct. 2007.

[8] S. Mudulodu and A. Paulraj. A transmit diversity scheme for frequency selective fading channels. In *Proc. IEEE Global Telecommunications Conference 2000, GLOBECOM 2000*, volume 2, pages 1089–1093. San Francisco, USA, Nov. 2000.

[9] A. Papoulis and S. U. Pillai. *Probability, Random Variables and Stochastic Processes*. New York: McGraw-Hill, 4th edition, 2002.

[10] M. Pätzold. System function and characteristic quantities of spatial deterministic Gaussian uncorrelated scattering processes. In *Proc. 57th Vehicular*

Technology Conference, VTC 2003-Spring, pages 256–261. Jeju, Korea, Apr. 2003.

[11] M. Pätzold and B. O. Hogstad. Design and performance of MIMO channel simulators derived from the two-ring scattering model. In *Proc. 14th IST Mobile & Communications Summit, IST 2005*. Dresden, Germany, June 2005.

[12] V. Tarokh, H. Jafarkhani, and A. R. Calderbank. Space-time block coding for wireless communications: performance results. *IEEE J. Select. Areas Commun.*, 17(3):451–460, Mar. 1999.

[13] A. Vielmon, Y. Li, and J. R. Barry. Performance of Alamouti transmit diversity over time–varying Rayleigh–fading channels. *IEEE Trans. on Wire. Commun.*, 3(5):1369–1373, Sept. 2004.

Appendix I

Paper IX

Performance Analysis of Alamouti Coded OFDM Systems over Rayleigh Fading Channels Correlated in Space and Time

Yuanyuan Ma and Matthias Pätzold

Department of Information and Communication Technology

Faculty of Engineering and Science, University of Agder

Servicebox 509, NO-4898 Grimstad, Norway

E-mails: {yuanyuan.ma, matthias.paetzold}@uia.no

Abstract — **This paper deals with the performance analysis of Alamouti coded orthogonal frequency division multiplexing (OFDM) systems over time-varying multipath Rayleigh fading channels. In our analysis, we consider a physically more realistic channel, which can be correlated either in time or in space or even in both domains. We derive an analytical expression for the bit error probability (BEP), which describes the performance of an Alamouti coded OFDM system over fading channels correlated in space and time. It is shown that the derived BEP can be reduced to the known BEP obtained over fading channels correlated in time or space. The correctness of all theoretical results is validated by system simulations. The knowledge of the obtained theoretical results makes the BEP evaluation more straightforward and less time-consuming compared to simulations. Moreover, it allows us to discuss the effect of the maximum Doppler frequency and the antenna spacing on the system performance.**

I. INTRODUCTION

In the past two decades, space-time block coding (STBC) schemes have received considerable attention due to the fact that they can increase the transmission reliability over wireless fading channels [13]. One of the famous and simple STBCs is the Alamouti coding scheme [2], which has been proposed by Alamouti to achieve a transmit diversity gain. It has been shown in the literature, e.g., in [12], that the simple Alamouti scheme works well if the mobile fading channel remains constant over an Alamouti codeword period. Due to the increasing demand for high data rate wireless communication services, future communication systems are supposed to be operating in much larger bandwidth ranges than today's communication systems. To cope with the multipath fading problem faced by future wideband communication systems, one efficient solution is to combine the Alamouti scheme with OFDM techniques.

Since the symbol duration of an OFDM system is much longer than that of a single-carrier system, a channel which is quasi-static for a single-carrier system may not be quasi-static for an OFDM system. Therefore, when studying the performance of an Alamouti coded OFDM system, it is physically not realistic to consider the channel as time invariant over two consecutive symbol durations. The impact of a time-varying fading channel on the performance of Alamouti coded OFDM systems has been investigated in [6]. The drawback of this paper is that the spatial correlation between the Rayleigh fading subchannels has not been taken into account. However, it has been shown in [7] by simulations and in [5] by theory that the performance of an Alamouti coded OFDM system depends not only on the temporal correlation but also on the spatial correlation. Due to this fact, the authors in [8] have studied the impact of both the temporal and the spatial properties on the performance of Alamouti coded OFDM systems. However, in [8], the authors assumed that the subchannels cannot be correlated simultaneously in time and space. For example, they assumed that no spatial correlation exists when analyzing the system performance over channels correlated in time and vice versa. Thus, the results in [8] were not generally valid and they cannot be used for the realistic case where the subchannels are correlated in both time and space.

In this paper, we concentrate again on the performance analysis of Alamouti coded OFDM systems in time-varying multipath Rayleigh fading channels. In contrast to [6] and [8], we restrict our attention to the physically more realistic case that the channel can be arbitrarily correlated either in time or in space or even in both domains. In our analysis, we assume that the channel envelope changes during two consecutive transmission time slots. We derive an analytical expression for the BEP over channels correlated in space and time. We show that our derived BEP can be reduced to the BEP presented in [8] for channels correlated only in time or space. All theoretical results will be confirmed by system simulations. The obtained results allow us to study the influence of the Doppler effect and the antenna spacing on the system performance. It is shown that the system performance improvement can be achieved by increasing the antenna spacing, while the performance deteriorates if we increase the maximum Doppler frequency. It turns out that the temporal autocorrelation function (ACF) and the space cross-correlation function (CCF) have an inverse effect on the system performance though they have the same shape under isotropic scattering conditions.

The rest of the paper is organized as follows. In Section II, we briefly review the Alamouti coded OFDM system and the statistical properties of the considered wideband channel model. Section III analyzes the BEP performance over channels

correlated in space and time, where an analytical expression is derived for the BEP of Alamouti coded OFDM systems. Section IV confirms the correctness of the theory by simulation. Finally, we give the conclusions in Section V.

II. REVIEW OF THE ALAMOUTI CODED OFDM SYSTEM

In this paper, we consider an OFDM system equipped with two transmit antennas and a single receive antenna. The complex data symbol pair (S_1, S_2) is encoded first by the Alamouti scheme [12] before it is transmitted over a multipath fading channel. The symbols received at the time slots t_1 and t_2 can be expressed as

$$Y_1 = H_{11}(f', x_1, t_1)S_1 + H_{21}(f', x_2, t_1)S_2 + N_1, \tag{1a}$$

$$Y_2 = -H_{11}(f', x_1, t_2)S_2^* + H_{21}(f', x_2, t_2)S_1^* + N_2, \tag{1b}$$

where N_i denotes the additive white Gaussian noise (AWGN) component at the time slot t_i $(i = 1, 2)$ and

$$H_{k1}(f', x_k, t_i) = \sum_{\ell=1}^{\mathscr{L}} a_\ell \mu_\ell(x_k, t_i) e^{-j2\pi f' \tau'_\ell} \tag{2}$$

represents the space-time-variant transfer function of the transmission link from the kth transmit antenna located at x_k $(k = 1, 2)$ to the single receive antenna. Here, $\mathscr{L}$ is the number of discrete propagation paths. The quantities a_ℓ and τ'_ℓ denote the path gain and the propagation delay of the ℓth path, respectively. It is assumed that the average power of the channel model is normalized to unity, i.e., the power constraint $\sum_{\ell=1}^{\mathscr{L}} a_\ell^2 = 1$ holds. The processes $\mu_\ell(x_k, t_i)$ in (2) represent zero-mean complex Gaussian random processes. We assume that the real and imaginary parts of $\mu_\ell(x_k, t_i)$ are uncorrelated, each having the variance $\sigma_0^2 = 1/2$.

It is supposed that the receiver knows perfectly the channel state information, and we assume that no synchronization error exists. By applying the combining strategy proposed in [14, 1], the estimated symbols at the output of the detector can be expressed as

$$\begin{aligned}\hat{S}_1 &= [H_{11}(f', x_1, t_1)H_{11}^*(f', x_1, t_2) + H_{21}(f', x_2, t_1)H_{21}^*(f', x_2, t_2)]S_1 \\ &\quad + H_{11}^*(f', x_1, t_2)N_1 + H_{21}(f', x_2, t_1)N_2^*, \end{aligned} \tag{3a}$$

$$\begin{aligned}\hat{S}_2 &= [H_{11}(f', x_1, t_1)H_{11}^*(f', x_1, t_2) + H_{21}(f', x_2, t_1)H_{21}^*(f', x_2, t_2)]S_2 \\ &\quad + H_{21}^*(f', x_2, t_2)N_1 + H_{11}(f', x_1, t_1)N_2^*. \end{aligned} \tag{3b}$$

A. The Instantaneous Output Signal-to-Noise Ratio

For convenience, we express the complex space-time-variant transfer functions by

their envelopes $R_m = |H_{k1}(f', x_k, t_i)|$ and phases $\Theta_m = \arg\{H_{k1}(f', x_k, t_i)\}$ for $m = 1, 2, 3, 4$ as follows

$$H_{11}(f', x_1, t_1) = R_1 e^{\Theta_1}, \qquad H_{11}(f', x_1, t_2) = R_2 e^{\Theta_2},$$
$$H_{21}(f', x_2, t_1) = R_3 e^{\Theta_3}, \qquad H_{21}(f', x_2, t_2) = R_4 e^{\Theta_4}. \qquad (4)$$

Given the channel model described by (2), it turns out that the random envelope R_m follows the Rayleigh distribution.

Since the system model is symmetrical, the BEP of S_1 is equal to the one for S_2. Therefore, in the following, we only concentrate on the BEP analysis of S_1. For the instantaneous output signal-to-noise ratio (SNR) of $\hat{S}_1$, we find the following expression from (3a)

$$\gamma_\Sigma = \frac{R_1^2 R_2^2 + R_3^2 R_4^2 + 2R_1 R_2 R_3 R_4 \cos(\Theta_1 - \Theta_2 + \Theta_4 - \Theta_3)}{(R_2^2 + R_3^2) \cdot 2\sigma_n^2}, \qquad (5)$$

where $2\sigma_n^2$ denotes the variance of the AWGN noise. It should be mentioned that if the channel is constant during the consecutive time slots t_1 and t_2, i.e., $H_{k1}(f', x_k, t_1) = H_{k1}(f', x_k, t_2) \, (k = 1, 2)$, the instantaneous output SNR γ_Σ in (5) reduces to the one presented in [4, p. 214].

B. Statistical Properties of the Considered Channel Model

As shown in [7], the performance of an Alamouti coded OFDM system depends not only on the temporal correlation but also on the spatial correlation. For the purpose of performance analysis, we briefly review the main correlation functions of the considered channel, which is correlated in both spatial and temporal domains.

First, we consider the temporal ACF $r_{HH}(\tau)$ between the subchannels $H_{k1}(f', x_k, t_1)$ and $H_{k1}(f', x_k, t_2)$. By making use of the results in [11], we can express the temporal ACF $r_{HH}(\tau)$ as follows

$$r_{HH}(\tau) = E\{H_{k1}^*(f', x_k, t_1) \cdot H_{k1}(f', x_k, t_2)\}$$
$$= \sum_{\ell=1}^{\mathscr{L}} a_\ell^2 r_{\mu_\ell \mu_\ell}(\tau), \qquad (6)$$

where $\tau = t_2 - t_1$ and $r_{\mu_\ell \mu_\ell}(\tau)$ describes the temporal ACF between $\mu_\ell(x_k, t_1)$ and $\mu_\ell(x_k, t_2)$. Assuming isotropic scattering conditions, we have $r_{HH}(\tau) = 2\sigma_0^2 \cdot J_0(2\pi f_{\max} \tau)$. Here, $J_0(\cdot)$ is the zeroth-order Bessel function of the first kind and $f_{\max}$ represents the maximum Doppler frequency.

The space CCF $r_{HH}(\triangle x)$ between $H_{11}(f', x_1, t_i)$ and $H_{21}(f', x_2, t_i)$ can be computed via the definition $r_{HH}(\triangle x) = E\{H_{11}^*(f', x_1, t_i) \cdot H_{21}(f', x_2, t_i)\}$. Based on [11],

we have

$$r_{HH}(\triangle x) = \sum_{\ell=1}^{\mathscr{L}} a_\ell^2 r_{\mu_\ell \mu_\ell}(\triangle x), \tag{7}$$

where $\triangle x = x_2 - x_1$. In (7), $r_{\mu_\ell \mu_\ell}(\triangle x)$ designates the space CCF of the random processes $\mu_\ell(x_1, t_i)$ and $\mu_\ell(x_2, t_i)$. For the case of isotropic scattering, we have $r_{HH}(\triangle x) = 2\sigma_0^2 J_0(2\pi \triangle x / \lambda)$, where λ denotes the wavelength.

The space-time CCF between $H_{11}(f', x_1, t_i)$ and $H_{21}(f', x_2, t_j)$ is defined as

$$r_{HH}(\triangle x, \tau) = E\{H_{11}^*(f', x_1, t_i) \cdot H_{21}(f', x_2, t_j)\}, \tag{8}$$

for $i, j = 1, 2$ and $i \neq j$. Finally, we mention that the space-time CCF $r_{HH}(\triangle x, \tau)$ can be represented by the sum of the space-time CCFs of different propagation paths weighted by the path power a_ℓ^2.

III. THE BEP PERFORMANCE OF ALAMOUTI CODED OFDM SYSTEMS OVER FADING CHANNELS CORRELATED IN SPACE AND TIME

In the following, we will first derive an analytical expression for the joint PDF of the envelopes R_1, R_2, R_3, and R_4, denoted by $p_{R_1 R_2 R_3 R_4}(r_1, r_2, r_3, r_4)$. Thereafter, we will find a solution for the PDF of the instantaneous output SNR. At the end, the BEP can be easily derived by averaging the conditional BEP over the obtained PDF of the instantaneous output SNR [4].

A. The Derivation of the Joint PDF of Four Envelopes

We express the complex space-time-variant transfer functions by their real and imaginary parts in the following form

$$H_{11}(f', x_1, t_1) = X_1 + jY_1, \quad H_{11}(f', x_1, t_2) = X_2 + jY_2,$$
$$H_{21}(f', x_2, t_1) = X_3 + jY_3, \quad H_{21}(f', x_2, t_2) = X_4 + jY_4. \tag{9}$$

As already mentioned in Section II, X_m and Y_n are independent Gaussian random variables ($m, n = 1, 2, 3, 4$). Therefore, the joint PDF of the eight Gaussian random variables, i.e., $X_1, X_2, X_3, X_4, Y_1, Y_2, Y_3$, and Y_4, can be expressed by the product of two joint PDFs as follows

$$p_{X_1 X_2 X_3 X_4 Y_1 Y_2 Y_3 Y_4}(x_1, x_2, x_3, x_4, y_1, y_2, y_3, y_4) = p_{X_1 X_2 X_3 X_4}(x_1, x_2, x_3, x_4)$$
$$\cdot p_{Y_1 Y_2 Y_3 Y_4}(y_1, y_2, y_3, y_4). \tag{10}$$

Here, $p_{X_1 X_2 X_3 X_4}(x_1, x_2, x_3, x_4)$ denotes the joint PDF of the variables X_1, X_2, X_3, and X_4, while the joint PDF of Y_1, Y_2, Y_3, and Y_4 is described by $p_{Y_1 Y_2 Y_3 Y_4}(y_1, y_2, y_3, y_4)$.

Starting from the multivariate Gaussian distribution [10, Eq. (2.20)], we can compute the joint PDFs $p_{X_1 X_2 X_3 X_4}(x_1, x_2, x_3, x_4)$ and $p_{Y_1 Y_2 Y_3 Y_4}(y_1, y_2, y_3, y_4)$, which are presented in (11) and (12)

$$p_{X_1 X_2 X_3 X_4}(x_1, x_2, x_3, x_4) = \frac{1}{(2\pi)^2 \sqrt{E}} \tag{11}$$

$$\cdot e^{-\frac{1}{2E}[A(x_1^2 + x_2^2 + x_3^2 + x_4^2) + B(x_1 x_2 + x_3 x_4) + C(x_1 x_3 + x_2 x_4) + D(x_1 x_4 + x_2 x_3)]},$$

$$p_{Y_1 Y_2 Y_3 Y_4}(y_1, y_2, y_3, y_4) = \frac{1}{(2\pi)^2 \sqrt{E}} \tag{12}$$

$$\cdot e^{-\frac{1}{2E}[A(y_1^2 + y_2^2 + y_3^2 + y_4^2) + B(y_1 y_2 + y_3 y_4) + C(y_1 y_3 + y_2 y_4) + D(y_1 y_4 + y_2 y_3)]}.$$

The symbols A, B, C, D and E in (11) and (12) are given by

$$A = 2\rho_T \rho_x \rho_{x,T} + \sigma_0^2 (\sigma_0^4 - \rho_T^2 - \rho_x^2 - \rho_{x,T}^2), \tag{13a}$$

$$B = 2\sigma_0^2 \rho_x \rho_{x,T} - \rho_T (\sigma_0^4 - \rho_T^2 + \rho_x^2 + \rho_{x,T}^2), \tag{13b}$$

$$C = 2\sigma_0^2 \rho_T \rho_{x,T} - \rho_x (\sigma_0^4 + \rho_T^2 - \rho_x^2 + \rho_{x,T}^2), \tag{13c}$$

$$D = 2\sigma_0^2 \rho_T \rho_x - \rho_{x,T} (\sigma_0^4 + \rho_T^2 + \rho_x^2 - \rho_{x,T}^2), \tag{13d}$$

$$E = (\sigma_0^4 - \rho_T^2)^2 + (\rho_x^2 - \rho_{x,T}^2)^2 - 2(\sigma_0^4 + \rho_T^2)(\rho_x^2 + \rho_{x,T}^2) + 8\sigma_0^2 \rho_T \rho_x \rho_{x,T}, \tag{13e}$$

where $\rho_T = r_{HH}(T_s)/2$, $\rho_x = r_{HH}(\triangle x)/2$, and $\rho_{x,T} = r_{HH}(\triangle x, T_s)/2$.

Substituting (11) and (12) into (10), we obtain the analytical expression for the joint PDF $p_{X_1 X_2 X_3 X_4 Y_1 Y_2 Y_3 Y_4}(x_1, x_2, x_3, x_4, y_1, y_2, y_3, y_4)$. Then, after transforming the Cartesian coordinates (x_m, y_m) into the polar coordinates (r_m, θ_m), we can express the joint PDF $p_{R_1 R_2 R_3 R_4 \Theta_1 \Theta_2 \Theta_3 \Theta_4}(r_1, r_2, r_3, r_4, \theta_1, \theta_2, \theta_3, \theta_4)$ of the four envelopes $R_m = |X_m + jY_m|$ and the four phases $\Theta_m = \arg\{X_m + jY_m\}$ in the form shown at in (14)

$$p_{R_1 R_2 R_3 R_4 \Theta_1 \Theta_2 \Theta_3 \Theta_4}(r_1, r_2, r_3, r_4, \theta_1, \theta_2, \theta_3, \theta_4) = |J| \cdot p_{X_1 X_2 X_3 X_4 Y_1 Y_2 Y_3 Y_4}(r_1 \cos\theta_1,$$

$$r_2 \cos\theta_2, r_3 \cos\theta_3, r_4 \cos\theta_4, r_1 \sin\theta_1, r_2 \sin\theta_2, r_3 \sin\theta_3, r_4 \sin\theta_4), \tag{14}$$

In this equation,

$$J = \begin{vmatrix} \frac{\partial x_1}{\partial r_1} & \cdots & \frac{\partial x_1}{\partial r_4} & \frac{\partial x_1}{\partial \theta_1} & \cdots & \frac{\partial x_1}{\partial \theta_4} \\ \vdots & \ddots & \vdots & \vdots & \ddots & \vdots \\ \frac{\partial x_4}{\partial r_1} & \cdots & \frac{\partial x_4}{\partial r_4} & \frac{\partial x_4}{\partial \theta_1} & \cdots & \frac{\partial x_4}{\partial \theta_4} \\ \frac{\partial y_1}{\partial r_1} & \cdots & \frac{\partial y_1}{\partial r_4} & \frac{\partial y_1}{\partial \theta_1} & \cdots & \frac{\partial y_1}{\partial \theta_4} \\ \vdots & \ddots & \vdots & \vdots & \ddots & \vdots \\ \frac{\partial y_4}{\partial r_1} & \cdots & \frac{\partial y_4}{\partial r_4} & \frac{\partial y_4}{\partial \theta_1} & \cdots & \frac{\partial y_4}{\partial \theta_4} \end{vmatrix} = r_1 r_2 r_3 r_4 \tag{15}$$

denotes the Jacobian determinant. Now, the joint PDF $p_{R_1 R_2 R_3 R_4}(r_1, r_2, r_3, r_4)$ of the envelopes R_1, R_2, R_3, and R_4 can be computed by integrating (14) over the phases $\theta_1, \theta_2, \theta_3$, and θ_4, which results finally in the form presented in (16)

$$
\begin{aligned}
p_{R_1 R_2 R_3 R_4}(r_1, r_2, r_3, r_4) &= \frac{r_1 r_2 r_3 r_4}{(2\pi)^2 E} \cdot e^{\left[-\frac{A}{2E}(r_1^2 + r_2^2 + r_3^2 + r_4^2)\right]} \\
&\cdot \int_0^{2\pi}\int_0^{2\pi} e^{-\frac{1}{E}[B r_3 r_4 \cos(\varphi_2) + C r_2 r_4 \cos(\varphi_1 + \varphi_2) + D r_2 r_3 \cos(\varphi_1)]} \\
&\cdot I_0\left(\frac{1}{E}\sqrt{B^2 r_1^2 r_2^2 + C^2 r_1^2 r_3^2 + D^2 r_1^2 r_4^2 + 2 r_1 r_2 r_3 r_4 [BC\cos(\varphi_1) + BD\cos(\varphi_1 + \varphi_2) + CD\cos(\varphi_2)]}\right) d\varphi_1 d\varphi_2.
\end{aligned}
\tag{16}
$$

B. Derivation of the PDF of the Output Instantaneous SNR

This subsection is devoted to find an expression for the PDF $p_{\gamma_\Sigma}(\gamma)$ of the instantaneous output SNR. It is shown in (5) that the instantaneous output SNR is determined by the envelopes (R_1, R_2, R_3, R_4) and the phases $(\Theta_1, \Theta_2, \Theta_3, \Theta_4)$. Even if the joint probability density function (PDF) of the envelopes and phases is known in advance, it is mathematically complicated to find the theoretical expression for the PDF of the instantaneous output SNR.

For the purpose of performance analysis, we introduce an approximation for the instantaneous output SNR by neglecting the difference between the phase changes $\Theta_1 - \Theta_2$ and $\Theta_3 - \Theta_4$, i.e., $\Theta_1 - \Theta_2 - (\Theta_3 - \Theta_4) \approx 0$. Thus, the instantaneous output SNR γ_Σ in (5) can be approximated as

$$
\gamma_\Sigma \approx \frac{R_1^2 R_2^2 + R_3^2 R_4^2 + 2 R_1 R_2 R_3 R_4}{(R_2^2 + R_3^2) \cdot 2\sigma_n^2}.
\tag{17}
$$

To verify its accuracy, we compare the PDF of the exact instantaneous output SNR with that of the approximate one by means of simulations. Figure I.1 presents the simulation results for both PDFs by considering different types of correlated channels, including (i) channels correlated in time, (ii) channels correlated in space, and (iii) channels correlated in both domains. All simulation results presented in Fig. I.1 are obtained by considering a typical 6-path rural area propagation scenario [3]. It is assumed that the average SNR $\bar{\gamma}$ is 5 dB, the symbol duration T_s equals 6.4 μs, the maximum Doppler frequency $f_{\max}$ is 500 Hz, and the normalized transmit antenna spacing $\triangle x/\lambda$ is 0.5.

As illustrated in Fig. I.1, the difference between the two types of PDFs is indistinguishable. This means that the PDF of the approximate instantaneous output SNR is almost equivalent to that of the exact instantaneous output SNR. Thus, the
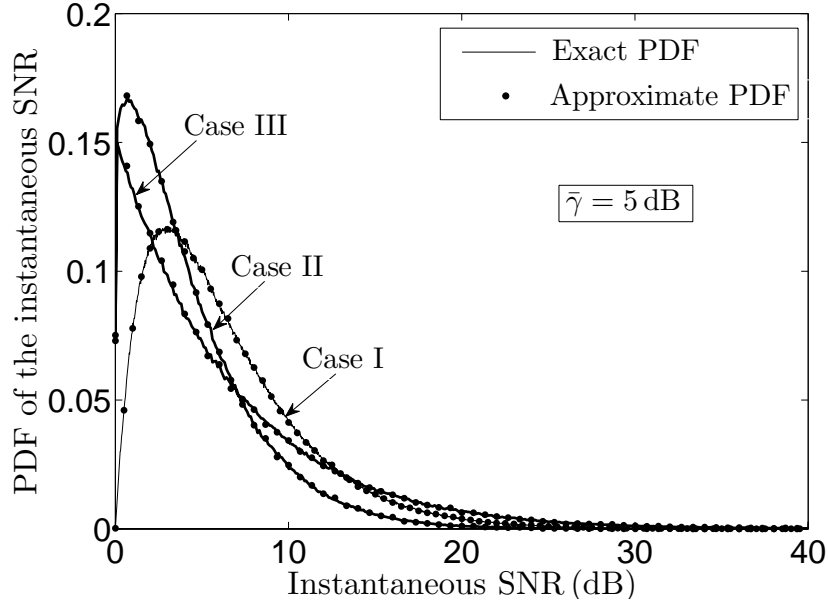
Figure I.1: Simulation results for the PDF of the instantaneous output SNR for channels correlated in time (case I), channels correlated in space (case II), and channels correlated in space and time (case III).

overall phase contribution to the instantaneous output SNR is negligible. It should be emphasized again that we have not neglected the phase difference between Θ_1 and Θ_2 (or between Θ_3 and Θ_4), i.e., $\Theta_1 \neq \Theta_2$ and $\Theta_3 \neq \Theta_4$. Instead of this, we only assume that $(\Theta_1 - \Theta_2) - (\Theta_3 - \Theta_4) \approx 0$. The accuracy of such an approximation has been confirmed by the excellent fitting between the PDF curves in Fig. I.1.

To obtain the PDF of the instantaneous output SNR, we start from deriving the PDF of the random variable Z defined by

$$Z = \frac{R_1^2 R_2^2 + R_3^2 R_4^2 + 2R_1 R_2 R_3 R_4}{R_2^2 + R_3^2}. \tag{18}$$

Let us define a system of equations as follows

$$z_1 = (r_1 r_2 + r_3 r_4)^2, \quad z_2 = r_2^2 + r_3^2, \quad z_3 = r_1 r_2, \quad z_4 = r_3^2, \tag{19}$$

from which we find the following real-valued solutions under the preconditions $z_3 < \sqrt{z_1}$ and $z_4 < z_2$

$$r_1 = \frac{z_3}{\sqrt{z_2 - z_4}}, \quad r_2 = \sqrt{z_2 - z_4}, \quad r_3 = \sqrt{z_4}, \quad r_4 = \frac{\sqrt{z_1} - z_3}{\sqrt{z_4}}. \tag{20}$$

With the concept of transformation of random variables [9], we can express the join PDF of the random variables Z_1, Z_2, Z_3, and Z_4 as follows

$$p_{Z_1 Z_2 Z_3 Z_4}(z_1, z_2, z_3, z_4) = |J(z_1, z_2, z_3, z_4)|$$
$$\cdot p_{R_1 R_2 R_3 R_4}\left(\frac{z_3}{\sqrt{z_2 - z_4}}, \sqrt{z_2 - z_4}, \sqrt{z_4}, \frac{\sqrt{z_1} - z_3}{\sqrt{z_4}}\right), \quad (21)$$

where the Jacobian determinant $J(z_1, z_2, z_3, z_4)$ equals $-1/[8\sqrt{z_1}z_4(z_2 - z_4)]$. Then, integrating the joint PDF $p_{Z_1 Z_2 Z_3 Z_4}(z_1, z_2, z_3, z_4)$ over z_3 and z_4 results in the joint PDF of the random variables Z_1 and Z_2, i.e.,

$$p_{Z_1 Z_2}(z_1, z_2) = \frac{1}{8\sqrt{z_1}} \int_0^{\sqrt{z_1}} \int_0^{z_2} \frac{1}{z_4(z_2 - z_4)}$$
$$\cdot p_{R_1 R_2 R_3 R_4}\left(\frac{z_3}{\sqrt{z_2 - z_4}}, \sqrt{z_2 - z_4}, \sqrt{z_4}, \frac{\sqrt{z_1} - z_3}{\sqrt{z_4}}\right) dz_4 dz_3. \quad (22)$$

Applying the rule presented in [9, Eq. (6–59)], we obtain the following expression for the PDF of the random variable $Z = Z_1/Z_2$

$$p_Z(z) = \frac{1}{8} \int_0^{\infty} \int_0^{\sqrt{zz_2}} \int_0^{z_2} \frac{z_2}{z_4(z_2 - z_4)\sqrt{zz_2}}$$
$$\cdot p_{R_1 R_2 R_3 R_4}\left(\frac{z_3}{\sqrt{z_2 - z_4}}, \sqrt{z_2 - z_4}, \sqrt{z_4}, \frac{\sqrt{zz_2} - z_3}{\sqrt{z_4}}\right) dz_4 dz_3 dz_2. \quad (23)$$

With [9, Eq. (5–3)], we can now express the desired PDF $p_{\gamma_{\Sigma}}(\gamma)$ of $\gamma_{\Sigma} = Z/2\sigma_n^2$ in terms of the joint PDF $p_{R_1 R_2 R_3 R_4}(r_1, r_2, r_3, r_4)$ as follows

$$p_{\gamma_{\Sigma}}(\gamma) = \frac{2\sigma_0^2}{8\bar{\gamma}} \int_0^{\infty} \int_0^{w} \int_0^{z_2} \frac{z_2}{z_4(z_2 - z_4)w} \quad (24)$$
$$\cdot p_{R_1 R_2 R_3 R_4}\left(\frac{z_3}{\sqrt{z_2 - z_4}}, \sqrt{z_2 - z_4}, \sqrt{z_4}, \frac{w - z_3}{\sqrt{z_4}}\right) dz_4 dz_3 dz_2,$$

where the upper limit w in the second integral represents $w = \sqrt{2\sigma_0^2 \gamma z_2/\bar{\gamma}}$.

C. Expression for the BEP

The BEP of the Alamouti coded OFDM system can be calculated by means of the relation [4, Eq. (7.20)]

$$P_b = \int_0^\infty p_{\gamma_\Sigma}(\gamma) \cdot P_{b|\gamma_\Sigma}(\gamma)\, d\gamma, \tag{25}$$

where $P_{b|\gamma_\Sigma}(\gamma)$ is the conditional BEP of a digital modulation scheme for a specific value of the SNR γ. For the binary phase-shift keying (BPSK) modulation scheme, e.g., $P_{b|\gamma_\Sigma}(\gamma) = \mathrm{erfc}(\sqrt{\gamma})/2$. Here, $\mathrm{erfc}(x) = \int_x^\infty \frac{2}{\sqrt{\pi}} e^{-y^2} dy$ represents the complementary error function.

Substituting the derived joint PDF $p_{\gamma_\Sigma}(\gamma)$ [see (24)] into (25) and taking (16) into account, we finally come to the result of the BEP of a BPSK Alamouti coded OFDM system as shown in (26).

$$P_b = \frac{2\sigma_0^2}{64\pi^2 \bar{\gamma} E} \int_0^\infty \int_0^\infty \int_0^w \int_0^{z_2} \frac{z_2 z_3 (w - z_3)}{z_4 (z_2 - z_4) w} \cdot e^{-\frac{A}{2E}\left[\frac{(w-z_3)^2}{z_4} + z_2 + \frac{z_3^2}{z_2 - z_4}\right]} \cdot \mathrm{erfc}(\sqrt{\gamma})$$

$$\cdot \int_0^{2\pi} \int_0^{2\pi} I_0 \left(\frac{1}{E} \sqrt{B^2 z_3^2 + C^2 \frac{z_4 z_3^2}{z_2 - z_4} + D^2 \frac{z_3^2 (w - z_3)^2}{z_4 (z_2 - z_4)} + 2 z_3 (w - z_3)[BC \cos\varphi_1 + BD \cos(\varphi_1 + \varphi_2) + CD \cos\varphi_1]} \right)$$

$$\cdot e^{-\frac{1}{E}\left[B(w - z_3)\cos\varphi_2 + C(w - z_3)\sqrt{\frac{(z_2 - z_4)}{z_4}}\cos(\varphi_1 + \varphi_2) + D\sqrt{z_4(z_2 - z_4)}\cos\varphi_1\right]} d\varphi_1 d\varphi_2 dz_4 dz_3 dz_2 d\gamma, \tag{26}$$

In the following, we will discuss two special cases. By considering $\rho_x = 0$ and $\rho_{x,T} = 0$, the BEP in (26) reduces to the BEP

$$P_b = \frac{2\sigma_0^2}{16(\sigma_0^4 - \rho_T^2)^2 \bar{\gamma}} \int_0^\infty \int_0^\infty \int_0^w \int_0^{z_2} \frac{z_2 z_3 (w - z_3)}{z_4 (z_2 - z_4) w} \cdot e^{-\frac{\sigma_0^2}{2(\sigma_0^4 - \rho_T^2)}\left[\frac{(w - z_3)^2}{z_4} + z_2 + \frac{z_3^2}{z_2 - z_4}\right]}$$

$$\cdot \mathrm{erfc}(\sqrt{\gamma}) \cdot I_0 \left(\frac{z_3 \rho_T}{\sigma_0^4 - \rho_T^2} \right) I_0 \left(\frac{(w - z_3)\rho_T}{\sigma_0^4 - \rho_T^2} \right) dz_4 dz_3 dz_2 d\gamma, \tag{27}$$

which has been presented in [8, Eq. (11)] describing the system performance over fading channels correlated in time.

For the case when $\rho_T = 0$ and $\rho_{x,T} = 0$, the BEP in (26) can be reduced to the result presented in [8, Eq. (15)]

$$P_b = \frac{2\sigma_0^2}{16(\sigma_0^4 - \rho_x^2)^2 \bar{\gamma}} \int_0^\infty \int_0^\infty \int_0^w \int_0^{z_2} \frac{z_2 z_3 (w - z_3)}{z_4 (z_2 - z_4) w} \cdot I_0 \left(\frac{z_3 \sqrt{z_4} \rho_x}{(\sigma_0^4 - \rho_x^2)\sqrt{z_2 - z_4}} \right)$$

$$\cdot I_0 \left(\frac{(w - z_3)\sqrt{z_2 - z_4}\rho_x}{(\sigma_0^4 - \rho_x^2)\sqrt{z_4}} \right) \cdot e^{-\frac{\sigma_0^2}{2(\sigma_0^4 - \rho_x^2)}\left[\frac{(w - z_3)^2}{z_4} + z_2 + \frac{z_3^2}{z_2 - z_4} \right]} \cdot \mathrm{erfc}(\sqrt{\gamma}) dz_4 dz_3 dz_2 d\gamma,$$

$$(28)$$

which represents the BEP performance of the Alamouti coded OFDM system over fading channels correlated in space.

IV. NUMERICAL RESULTS

This section is devoted to illustrate the theoretical BEP results given by (26), (27), and (28). To confirm their correctness, all derived theoretical results will be validated by system simulations. In all the simulations, we assume that the considered OFDM system consists of $K = 64$ subcarriers. All other parameters are the same as in Section II.

The BEP performance over fading channels correlated in spatial and temporal domains is presented in Fig. I.2 for different antenna spacings $\triangle x$ and different maximum Doppler frequencies $f_{\max}$. It is shown that the theoretical BEPs calculated by (26) match perfectly the ones obtained by system simulations. Moreover, we can observe that both the antenna spacing and the maximum Doppler frequency have an impact on the system performance.

In the following two figures, we present the BEP performance for the two special cases, where the channels are correlated either in the temporal or spatial domain.
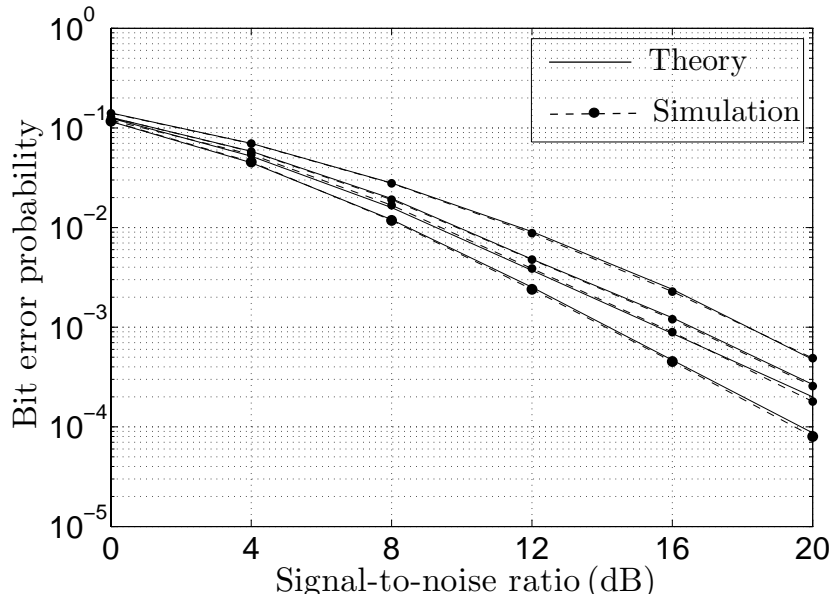
Figure I.2: BEP performance of Alamouti coded OFDM systems over fading channels correlated in space and time for different values of the maximum Doppler frequency $f_{\max}$ and the antenna spacing $\triangle x$.

Figure I.3 illustrates the BEP over channels correlated in the temporal domain for $f_{max} = 100\,\text{Hz}$ and $f_{max} = 500\,\text{Hz}$ [see (27)]. This figure also presents the relevant simulation results, which again confirm the correctness of the analytical ones. It turns out that the maximum Doppler frequency has an influence on the system performance, which can be attributed to the channel variations during two consecutive transmission time slots. The performance degrades when changing the maximum Doppler frequency f_{max} from $100\,\text{Hz}$ to $500\,\text{Hz}$.

The theoretical results of the BEP described by (28) are depicted in Fig. I.4 for different antenna spacings $\triangle x = 0.1\lambda$ and $\triangle x = 3\lambda$. It can be concluded from Fig. I.4 that the system performance can be improved by increasing the antenna spacing. This can be explained by the fact that the spatial correlation between subchannels becomes smaller when the antenna spacing increases. By comparing Fig. I.3 with Fig. I.4, we may conclude that though the temporal ACF and the space CCF have the same shape, their influence on the system performance is inverse.

V. CONCLUSION

In this paper, we have analyzed the performance of Alamouti coded OFDM systems over multipath Rayleigh fading channels correlated in space and time. In our analysis, we have considered the physically more realistic case that the channel envelope changes during two consecutive transmission time slots. It has been shown by simulations that the instantaneous output SNR strongly depends on the statistics
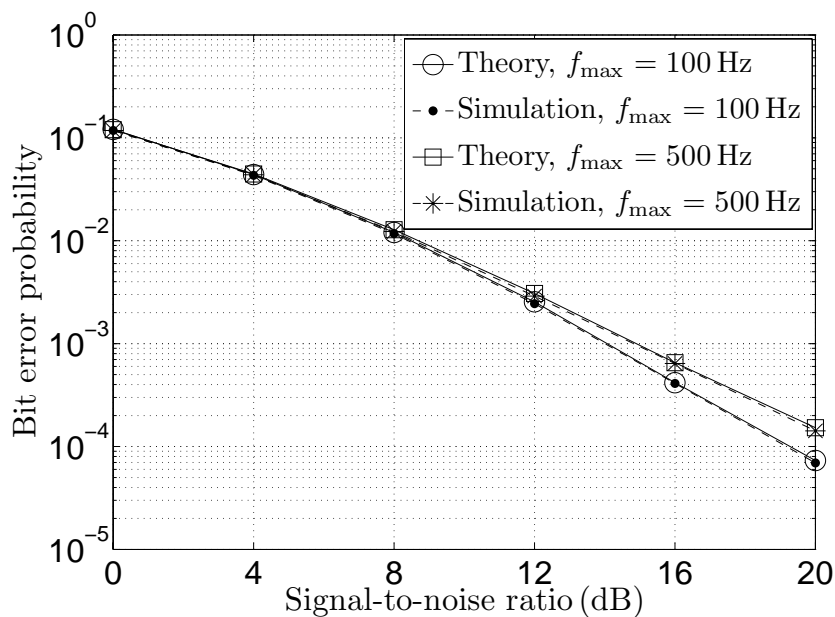
Figure I.3: BEP performance of Alamouti coded OFDM systems over fading channels correlated in time for $f_{max} = 100\,\text{Hz}$ and $f_{max} = 500\,\text{Hz}$.
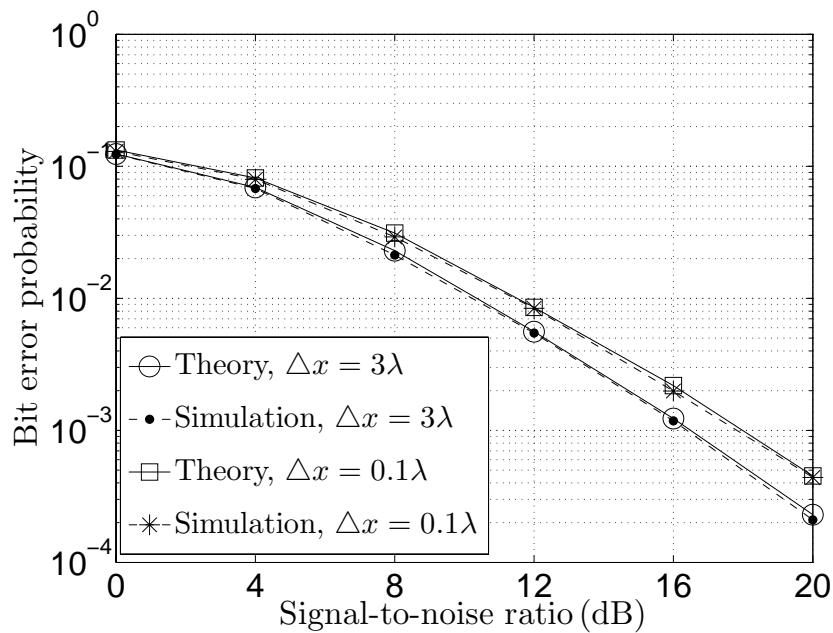
Figure I.4: BEP performance of Alamouti coded OFDM systems over fading channels correlated in space for $\triangle x = 0.1\lambda$ and $\triangle x = 3\lambda$.

of the envelopes of the space-time-variant transfer functions, while the impact of the overall random phase contribution is negligible. An analytical expression has been derived for the BEP of an Alamouti coded OFDM system over fading channels correlated both in temporal and spatial domains. The derived BEP includes the known BEPs for channels correlated in the temporal or spatial domain as special cases.

With the help of the derived BEP expressions, we have numerically evaluated the BEP performance for different types of correlated channels, where the impact of the maximum Doppler frequency and the antenna spacing on the system performance has been discussed. We found that the system performance deteriorates when increasing the maximum Doppler frequency due to a lower temporal ACF. In contrast, the performance improves if increasing the antenna spacing due to a lower space CCF. Therefore, it can be concluded that the temporal ACF and the space CCF have inverse effect on the system performance though they have the same shape under isotropic scattering conditions. In addition, we have confirmed all the theoretical results by system simulations.

REFERENCES

[1] G. Abreu and R. Kohno. Non-differential space-time transmission diversity in fast fading. In *Proc. 13th IEEE International Symposium on Personal, Indoor*

and Mobile Radio Communications, volume 1, pages 74–78. Lisbon, Portugal, Sept. 2002.

[2] S. M. Alamouti. A simple transmit diversity technique for wireless communications. *IEEE Journal on Select Areas in Communications*, 16(8):1451–1458, Oct. 1998.

[3] COST 207. *Digital land mobile radio communications*. Office for Official Publications of the European Communities, Final report, Luxembourg, 1989.

[4] A. Goldsmith. *Wireless Communications*. Cambridge University Press, 2005.

[5] E. Ko and D. Hong. A robust transmit diversity for OFDM systems in spatially correlated Rayleigh fading channels. In *Proc. 59th Vehicular Technology Conference, VTC 2004-Spring*, volume 4, pages 1840–1843. Milan, Italy, May 2004.

[6] D. B. Lin, P. H. Chiang, and H. J. Li. Performance analysis of two–branch transmit diversity block–coded OFDM systems in time–varying multipath Rayleigh–fading channels. *IEEE Trans. on Veh. Technol.*, 54(1):136–148, Jan. 2005.

[7] Y. Ma and M. Pätzold. Performance comparison of space-time coded MIMO–OFDM systems using different wideband MIMO channel models. In *Proc. 4th IEEE International Symposium on Wireless Communication Systems, ISWCS 2007*, pages 762–766. Trondheim, Norway, Oct. 2007.

[8] Y. Ma and M. Pätzold. Performance analysis of STBC-OFDM systems in temporally or spatially correlated fading channels. In *Proc. IEEE Wireless Communication and Network Conference, WCNC 2010*. Australia, Apr. 2010.

[9] A. Papoulis and S. U. Pillai. *Probability, Random Variables and Stochastic Processes*. New York: McGraw-Hill, 4th edition, 2002.

[10] M. Pätzold. *Mobile Fading Channels*. Chichester: John Wiley & Sons, 2002.

[11] M. Pätzold. System function and characteristic quantities of spatial deterministic Gaussian uncorrelated scattering processes. In *Proc. 57th Vehicular Technology Conference, VTC 2003-Spring*, pages 256–261. Jeju, Korea, Apr. 2003.

[12] V. Tarokh, H. Jafarkhani, and A. R. Calderbank. Space-time block coding for wireless communications: Performance results. *IEEE Journal on Selected Areas in Commun.*, 17(3):451–460, Mar. 1999.

[13] V. Tarokh, N. Seshadri, and A. R. Calderbank. Space-time codes for high data rate wireless communication: Performance criterion and code construction. *IEEE Trans. Inf. Theory*, 44(2):744–765, Mar. 1998.

[14] A. Vielmon, Y. Li, and J. R. Barry. Performance of Alamouti transmit diversity over time–varying Rayleigh–fading channels. *IEEE Trans. on Wire. Commun.*, 3(5):1369–1373, Sept. 2004.

Statement of figure mistakes: Fig. I.2 presented in the main text did not mark the values of the maximum Doppler frequency f_{max} and the antenna spacing $\triangle x$ under which the presented curves are plotted. The correction version of Fig. I.2 is given as follows.
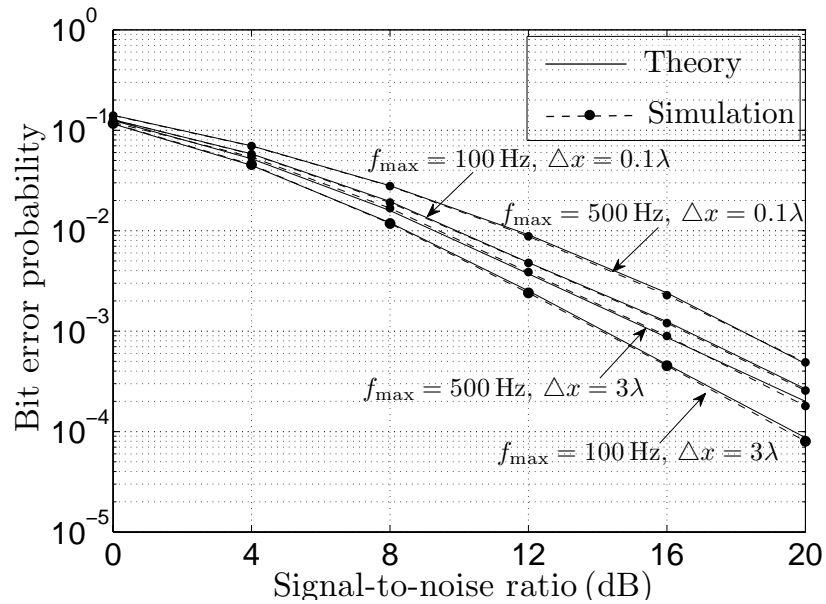
Figure I.5: Correction of Fig. I.2: BEP performance of Alamouti coded OFDM systems over fading channels correlated in space and time for different values of the maximum Doppler frequency f_{max} and the antenna spacing $\triangle x$.

Appendix J

Paper X

Authors:	Corneliu Eugen D. Sterian[1], **Yuanyuan Ma**[2], Matthias Pätzold[2], Ion Bănică[1], and Huaqiang He[2]
Affiliation:	[1]Department of Remote Control and Electronics for Transportation Systems, Polytechnic University of Bucharest, Bucharest, Romania [2]University of Agder, Faculty of Engineering and Science, P. O. Box 509, NO-4898 Grimstad, Norway

New Super-Orthogonal Space-Time Trellis Codes Using Differential M-PSK for Noncoherent Mobile Communication Systems with Two Transmit Antennas

Corneliu Eugen D. Sterian[1], Yuanyuan Ma[2], Matthias Pätzold[2],
Ion Bănică[1], and Huaqiang He[2]

[1]Department of Remote Control and Electronics for Transportation Systems,
Polytechnic University of Bucharest, Bucharest, Romania
E-mails: steriancorneliu@hotmail.com; ibanica@yahoo.com
[2]University of Agder, Faculty of Engineering and Science, P. O. Box 509,
NO-4898 Grimstad, Norway
Emails: yuanyuan.ma@uia.no; matthias.paetzold@uia.no; linzi_hust@163.com

Abstract — **In this paper, we develop super-orthogonal space-time trellis codes (SOSTTCs) using differential binary phase-shift keying (BPSK), quadriphase-shift keying (QPSK) and eight-phase shift keying (8PSK) for noncoherent communication systems with two transmit antennas without channel state information (CSI) at the receiver. Based on a differential encoding scheme proposed by Tarokh and Jafarkhani, we propose a new decoding algorithm with reduced decoding complexity. To evaluate the performance of the SOSTTCs by way of computer simulations, a geometric two-ring channel model is employed throughout. The simulation results show that the new decoding algorithm has the same decoding performance compared with the traditional decoding strategy, while it reduces significantly the overall computing complexity. As expected the system performance depends greatly on the antenna spacing and on the angular spread of the incoming waves. For fair comparison, we also design SOSTTCs for coherent detection of the same complexity as those demonstrated for the noncoherent case. As in the case of classical single antenna transmission systems, the coherent scheme outperforms the differential one by approximately 3 dB for SOSTTCs as well.**

I. INTRODUCTION

Space-time coding was introduced in the late 1990's as a promising technique to improve the reliability of mobile data links by using transmit antenna diversity [20, 3]. Those pioneering works and many others that soon followed were elaborated under

the assumption that the receiver can acquire perfect *channel state information* (CSI). Nevertheless, the known-channel assumption may not be realistic in a scenario of rapidly changing fading environments. In our paper, we propose space-time trellis codes to be used in noncoherent transmission systems where neither the transmitter nor the receiver knows the fading gains of the channel. For the single-input single-output (SISO) case, differential encoding coupled with trellis-coded modulation can provide a good solution to the problem [13, 5, 14, 23]. In the enlarged framework of multiple-input multiple-output (MIMO) systems, a new solution emerged as unitary space-time signals [7, 9, 2, 8]. Like Alamouti's scheme for coherent demodulation, these designs can provide diversity advantage, but no coding gain.

To obtain coding gains, trellis-coded unitary space-time modulation systems have been proposed in [16, 17, 4, 25, 18, 24]. To this end, the first prerequisite is a set of unitary matrices. To avoid this, Tarokh and Jafarkhani proposed a differential detection scheme for two transmit antennas in [19] and extended it to multiple transmit antennas in [11]. For the case when the receiver has CSI, super-orthogonal space-time trellis codes (SOSTTCs) have been introduced in [10]. Zhu and Jafarkhani presented in [26] two rather simple, fully-connected trellis sections for binary phase-shift keying (BPSK) and quadriphase-shift keying (QPSK). The case of eight-phase shift keying (8PSK) is not treated in [26]. In contradistinction to [26], we consider all the three signal constellations, BPSK, QPSK and 8PSK, and design differential super-orthogonal space-time trellis encoders based on non-fully connected trellises. Moreover, we use the differential scheme described in [19], while, as much as we understand, the authors of [26] prefer an older one, based on unitary matrices.

In [19], only differential BPSK modulation is described in detail for the case of two transmit antennas, while performance plots are also provided for QPSK and 8PSK. We made no attempt to consider 16PSK as well, since it has a rather small practical usefulness and the complexity grows unacceptably high, as the cardinality of the required matrix set is 256. Although we consider the differential scheme described in [19] as excellent, we propose a new decoding metric with exactly the same performance as that given in [19], but superior from the standpoint of the computing time.

The bit error rate (BER) performance of both coherent and noncoherent communication systems using SOSTTCs is evaluated by computer simulations based on a geometric two-ring channel model [12]. We take the opportunity of performing those simulations to study the impact of different channel parameters and transmission scenarios on the system performance. We compare the BER performance of

the SOSTTCs using both the differential and the coherent encoding schemes. As known from the theory and practice of single antenna communication systems, the SOSTTCs using the differential encoding scheme are approximately 3 dB worse than those using the coherent scheme, and this is the price paid for having no need of CSI at the receiver.

The rest of the paper is organized as follows. In Section II, we describe our channel model and develop the differential scheme for BPSK, QPSK and 8PSK. It will be clear that the matrix sets used for trellis-coding are quite different from those used for differential transmission. In Section III, for fair comparison, we first design SOSTTCs to be included in coherent transmission systems. In Section IV, we design SOSTTCs that work together with differential detection and therefore have no need of CSI. Receiver issues are treated in Section V, where the traditional decoding algorithm and the new decoding algorithm are presented. Simulation results and related comments are given in Section VI. Section VII contains our conclusions.

II. CHANNEL MODEL AND DIFFERENTIAL ENCODING

A. Channel Model

We consider a point-to-point noncoherent wireless communication link with two transmit antennas and one or two receive antennas, operating in a Rayleigh flat-fading environment like in [19]. The signal constellation used for transmission is M-PSK, with $M = 2^b$ and $b = 1, 2$, and 3, i.e., BPSK, QPSK and 8PSK. The average energy of the symbols transmitted from each antenna is normalized to be $1/2$, in order that the average power of the received signal at each receive antenna is 1. Therefore, the 2D signal constellation is a set

$$S = \left\{ \frac{e^{2\pi kj/M}}{\sqrt{2}} \,|k = 0, 1, \ldots, M-1 \right\} \tag{1}$$

where $j^2 = -1$.

In our method, we use a 4D signal constellation that is the Cartesian product of a 2D signal constellation by itself. Denote the 2D symbol interval by T. A 4D symbol is transmitted in two consecutive time intervals of duration T and thus its duration equals $2T$. We number the 4D symbol intervals by n, $n = 0, 1, 2, \ldots$, and the first and the second half of the generic 4D symbol interval are denoted as $2n$ and $2n + 1$, respectively. Note that actually BPSK is not 2D, but 1D.

In this paper, we assume that the fading is constant over a time interval whose duration is at least equal to $4T$. Furthermore, let us denote the path gain from the transmit antenna $q, q = 1, 2$, to the receive antenna p, by $h_n^{(p,q)}$. The path gains are

modelled as samples of independent complex Gaussian stochastic processes with variance 0.5 per real dimension.

B. Differential Encoding

We assume that the data transmission is being made by frames, where by *frame* we understand a block of N 4D consecutive symbols, or equivalently of $2N$ 2D consecutive QPSK or 8PSK symbols, and of N 2D consecutive symbols, or equivalently of $2N$ 1D consecutive BPSK symbols, that are maximum likelihood sequence decoded by the receiver using the Viterbi algorithm. For brevity of exposition, we consider 2D signal constellations, but the theory is the same for BPSK. We index the 4D symbols by $n, n = 0, 1, \ldots, N-1$. The nth 4D symbol comprises two consecutive 2D symbols denoted as s_{2n} and s_{2n+1} which are transmitted by the first antenna into two successive channel uses $2n$ and $2n+1$. The second antenna transmits the same information, but in a different order and form, i.e., $-a_n s_{2n+1}^*$ first and $a_n s_{2n}^*$ next, where the variable a_n can take the values $+1$ and -1 as it will be shown later. It is useful to consider these quantities as the entries of a 2×2 transmission matrix:

$$\mathbf{M}_n = \begin{pmatrix} s_{2n} & -a_n \cdot s_{2n+1}^* \\ s_{2n+1} & a_n \cdot s_{2n}^* \end{pmatrix}. \tag{2}$$

For a_n fixed as $+1$ or -1, we readily recognize in (2) the Alamouti matrix [3], which is also an orthogonal design, since the two columns, as well as the two rows, are orthogonal.

For coherent demodulation and a_n fixed, all the matrices that can be formed with symbols of a given signal constellation make up a signal set and a space-time trellis code can be designed by properly assigning a transmission matrix to each state transition of a topological trellis. Clearly, the data rate is determined by the cardinality of such a signal set. To increase the data rate by one bit per 4D symbol, the signal set is taken as the union of two families of matrices, one for $a_n = +1$ and the other one for $a_n = -1$. With this enlarged set of matrices, an SOSTTC can be built [10].

When no CSI is available at the receiver, only noncoherent demodulation can be used. As in [19], we consider the two orthogonal vectors $(s_{2n}, -a_n \cdot s_{2n+1}^*)$ and $(s_{2n+1}, a_n \cdot s_{2n}^*)$ having unit length. Then, any 2D vector $(s_{2n+2}, -a_n \cdot s_{2n+3}^*)$ can be uniquely represented in the orthonormal basis given by these vectors. Assuming that the fading is constant at least over two consecutive 4D symbols, the information to be transmitted in the $(n+1)$th 4D symbol interval is differentially encoded as

follows:

$$
\begin{pmatrix}
s_{2n+2} & -a_{n+1} \cdot s_{2n+3}^* \\
s_{2n+3} & a_{n+1} \cdot s_{2n+2}^*
\end{pmatrix}
=
\begin{pmatrix}
u_{2n+2} & u_{2n+3} \\
-a_n \cdot a_{n+1} \cdot u_{2n+3}^* & a_n \cdot a_{n+1} \cdot u_{2n+2}^*
\end{pmatrix}
$$
$$
\cdot
\begin{pmatrix}
s_{2n} & -a_n \cdot s_{2n+1}^* \\
s_{2n+1} & a_n \cdot s_{2n}^*
\end{pmatrix}
\tag{3}
$$

where

$$
u_{2n+2} = s_{2n}^* \cdot s_{2n+2} + a_n \cdot a_{n+1} \cdot s_{2n+1} \cdot s_{2n+3}^* \tag{4}
$$

and

$$
u_{2n+3} = s_{2n+2} \cdot s_{2n+1}^* - a_n \cdot a_{n+1} \cdot s_{2n} \cdot s_{2n+3}^* . \tag{5}
$$

From (3), we also have that

$$
s_{2n+2} = u_{2n+2} \cdot s_{2n} + u_{2n+3} \cdot s_{2n+1} \tag{6}
$$

$$
s_{2n+3} = a_n \cdot a_{n+1} \left(u_{2n+2}^* \cdot s_{2n+1} - u_{2n+3}^* \cdot s_{2n} \right) . \tag{7}
$$

We call *transmission matrix* a matrix whose entries, denoted by the letter *s*, are transmitted from the two transmit antennas, and *encoding matrix*, a matrix whose entries are denoted by the letter *u*. The encoding matrices are used to label the state transitions of the trellis diagram. Define the encoding matrix as

$$
\mathbf{ME}_{n+1} =
\begin{pmatrix}
u_{2n+2} & -a_n \cdot a_{n+1} \cdot u_{2n+3}^* \\
u_{2n+3} & a_n \cdot a_{n+1} \cdot u_{2n+2}^*
\end{pmatrix} . \tag{8}
$$

Then, the encoding equation (3) can be written as

$$
\mathbf{M}_{n+1} = \mathbf{ME}_{n+1}^T \cdot \mathbf{M}_n . \tag{9}
$$

It is easy to see that, if the entries of the transmission matrices are signal points from an *M*-PSK constellation, unfortunately, the entries of the encoding matrices are *not*.

The general structure of our transmission system is depicted in Fig. J.1.

C. Signal Constellations for Trellis Coding

In trellis-coded modulation, the signal constellation, which is double-sized compared to the one used by the uncoded system, is partitioned into two equal-sized subsets called families and denoted as F_0 and F_1 [21, 22]. In our paper, the family F_0 comprises all encoding matrices with $a_n a_{n+1} = 1$, while the family F_1 comprises all encoding matrices with $a_n a_{n+1} = -1$. For each matrix belonging to F_0, there is
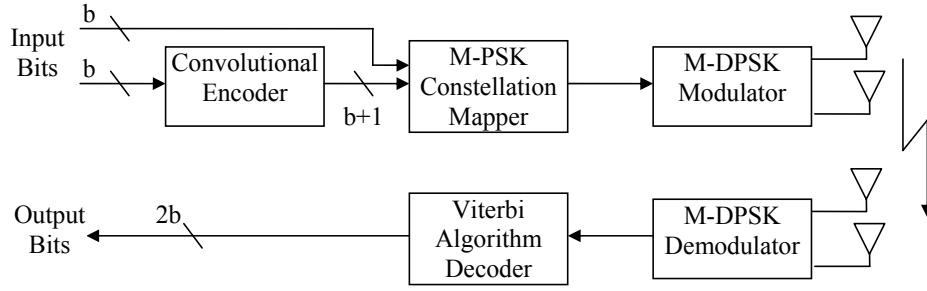
Figure J.1: Transceiver structure of super-orthogonal space-time trellis encoded M-DPSK for fading channels.

a matrix in F_1 having the same first column, but a different second one. The two matrices are selected by blocks of bits at the output of a systematic feedback convolutional encoder differing only in the least significant bit, i.e., $c0_{n+1} = 0$ for F_0 and $c0_{n+1} = 1$ for F_1. The differential encoding according to (4) and (5) depends on both (s_{2n}, s_{2n+1}) and (s_{2n+2}, s_{2n+3}). To select the corresponding 4D symbol (u_{2n+2}, u_{2n+3}), only $2b$ input bits are available, while twice as much bits would have been necessary to select an 8D symbol $(s_{2n}, s_{2n+1}, s_{2n+2}, s_{2n+3})$. The $2b$ input bits can select one out of 2^{2b} vectors (u_{2n+2}, u_{2n+3}) that transform a given 4D signal point (s_{2n}, s_{2n+1}) into the next one (s_{2n+2}, s_{2n+3}). To establish a bijection, a possibility is to fix a point (for instance, $s_{2n} = s_{2n+1} = 1/\sqrt{2}$ as in [19]) and use it for all other 4D signal points (s_{2n}, s_{2n+1}).

Consider first BPSK, which uses a 1D signal constellation and is equivalent to binary amplitude shift keying (BASK). In the $(n+1)$th 2D symbol interval, two consecutive source bits, denoted as $b1_{2n+2}$ and $b1_{2n+3}$, are presented at the input of a systematic convolutional encoder whose output comprises three bits: $c0_{n+1}$, $c1_{n+1} = b1_{2n+2}$ and $c2_{n+1} = b1_{2n+3}$. There must be a bijective mapping of the set of dibits $\{c1_{n+1}, c2_{n+1}\}$ onto the set of encoding symbols $\{u_{2n+2}, u_{2n+3}\}$. Following [19], we fix $s_{2n} = s_{2n+1} = 1/\sqrt{2}$ in (3) and (4). For this particular case, we have

$$u_{2n+2} = \left(s_{2n+2} + a_n \cdot a_{n+1} \cdot s_{2n+3}^*\right)/\sqrt{2} \tag{10}$$

$$u_{2n+3} = \left(s_{2n+2} - a_n \cdot a_{n+1} \cdot s_{2n+3}^*\right)/\sqrt{2}. \tag{11}$$

The signal points, computed with (4) and (5), are listed in Table J.1. Note that, in contradistinction to the 1D signal constellation constituent of the 2D signal constellation used for transmission, which has only two points $-1/\sqrt{2}$ and $+1/\sqrt{2}$, that one used for trellis encoding comprises three points: $+1, -1$, and 0.

Next, we consider QPSK. In the $(n+1)$th 4D symbol interval, four consecutive source bits, denoted as $b1_{2n+2}$, $b2_{2n+2}$, $b1_{2n+3}$ and $b2_{2n+3}$, are fed to a systematic

Table J.1: Mapping of selection bits into 2D BPSK signal points

Subset	$c2_{n+1}$	$c1_{n+1}$	u_{2n+2}	u_{2n+3}
SD_0	0	0	1	0
	1		-1	0
SD_1	0	1	0	-1
	1		0	1

convolutional encoder whose output comprises five bits: $c0_{n+1}$, $c1_{n+1} = b1_{2n+2}$, $c2_{n+1} = b2_{2n+2}$, $c3_{n+1} = b1_{2n+3}$, and $c4_{n+1} = b2_{2n+3}$. When fixing $s_{2n} = s_{2n+1} = 1/\sqrt{2}$ as for BPSK, the result of the computation using (8) and (9) is given in Table J.2. Note that, with this mapping, (6) and (7) will result into QPSK symbols only if the product $s_{2n} \cdot s_{2n+1}$ is a real number. However, when this product is an imaginary number, it is easy to verify that some of the symbols computed with (6) and (7) do not belong to QPSK.

Table J.2: Mapping of selection bits into 4D QPSK signal points

Subset	$c4_{n+1}$	$c3_{n+1}$	$c2_{n+1}$	$c1_{n+1}$	u_{2n+2}	u_{2n+3}
SD_0	0	0	0	0	1	0
	0	1			0	j
	1	0			0	$-j$
	1	1			-1	0
SD_1	0	0	0	1	$(1-j)/2$	$(1+j)/2$
	0	1			$-(1-j)/2$	$(1+j)/2$
	1	0			$(1-j)/2$	$-(1+j)/2$
	1	1			$-(1-j)/2$	$-(1+j)/2$
SD_2	0	0	1	0	$(1+j)/2$	$(1-j)/2$
	0	1			$(1+j)/2$	$-(1-j)/2$
	1	0			$-(1+j)/2$	$(1-j)/2$
	1	1			$-(1+j)/2$	$-(1-j)/2$
SD_3	0	0	1	1	0	1
	0	1			j	0
	1	0			$-j$	0
	1	1			0	-1

Finally, we consider 8PSK. In the $(n+1)$th 4D symbol interval, six consecutive source bits, denoted as $b1_{2n+2}$, $b2_{2n+2}$, $b3_{2n+2}$, $b1_{2n+3}$, $b2_{2n+3}$ and $b3_{2n+3}$, are fed to a systematic convolutional encoder whose output comprises seven bits: $c0_{n+1}$, $c1_{n+1} = b1_{2n+2}$, $c2_{n+1} = b2_{2n+2}$, $c3_{n+1} = b3_{2n+2}$, $c4_{n+1} = b1_{2n+3}$, $c5_{n+1} = b2_{2n+3}$ and $c6_{n+1} = b3_{2n+3}$. The mapping of the selection bits onto the encoding symbols is given in Table J.3. Note that, for convenience, the shorthand notation $a = a_n \cdot a_{n+1}$ was used.

We make here the same comment as in the case of QPSK: when the product $s_{2n} \cdot s_{2n+1}$ is complex-valued, using (6) and (7) results into some symbols that do not belong to 8PSK. Fortunately, this has no detrimental effect on the receiver, since the carrier phase is not recovered.

Table J.3: Mapping of selection bits into 4D 8PSK signal points

Subset	$c6_{n+1}$	$c5_{n+1}$	$c4_{n+1}$	$c3_{n+1}$	$c2_{n+1}$	$c1_{n+1}$	u_{2n+2}	u_{2n+3}
SD_0	0	0	0	0	0	0	1	0
	0	0	1				$\frac{\sqrt{2}}{2}$	$\frac{j\sqrt{2}}{2}$
	0	1	0				$-\frac{\sqrt{2}}{2}$	$\frac{j\sqrt{2}}{2}$
	0	1	1				$\frac{j(1-a)}{2}$	$\frac{j(1+a)}{2}$
	1	0	0				$\frac{\sqrt{2}}{2}$	$-\frac{j\sqrt{2}}{2}$
	1	0	1				0	$-j$
	1	1	0				-1	0
	1	1	1				$-\frac{\sqrt{2}}{2}$	$-\frac{j\sqrt{2}}{2}$
SD_1	0	0	0	0	0	1	$\frac{2+\sqrt{2}-j\sqrt{2}}{4}$	$\frac{2-\sqrt{2}+j\sqrt{2}}{4}$
	0	0	1				$\frac{\sqrt{2}-j(2-\sqrt{2})}{4}$	$\frac{\sqrt{2}+j(2+\sqrt{2})}{4}$
	0	1	0				$-\frac{2+\sqrt{2}-j\sqrt{2}}{4}$	$\frac{2-\sqrt{2}+j\sqrt{2}}{4}$
	0	1	1				$-\frac{\sqrt{2}-j(2-\sqrt{2})}{4}$	$\frac{\sqrt{2}+j(2+\sqrt{2})}{4}$
	1	0	0				$\frac{2+\sqrt{2}-j\sqrt{2}}{4}$	$-\frac{2-\sqrt{2}+j\sqrt{2}}{4}$
	1	0	1				$\frac{\sqrt{2}-j(2-\sqrt{2})}{4}$	$-\frac{\sqrt{2}+j(2+\sqrt{2})}{4}$
	1	1	0				$-\frac{2+\sqrt{2}-j\sqrt{2}}{4}$	$-\frac{2-\sqrt{2}+j\sqrt{2}}{4}$
	1	1	1				$-\frac{\sqrt{2}-j(2-\sqrt{2})}{4}$	$-\frac{\sqrt{2}+j(2+\sqrt{2})}{4}$
SD_2	0	0	0	0	1	0	$\frac{2-\sqrt{2}-j\sqrt{2}}{4}$	$\frac{2+\sqrt{2}+j\sqrt{2}}{4}$
	0	0	1				$\frac{\sqrt{2}-2+j\sqrt{2}}{4}$	$\frac{2+\sqrt{2}+j\sqrt{2}}{4}$
	0	1	0				$-\frac{\sqrt{2}-j(2+\sqrt{2})}{4}$	$-\frac{\sqrt{2}+j(2-\sqrt{2})}{4}$
	0	1	1				$-\frac{\sqrt{2}-j(2+\sqrt{2})}{4}$	$\frac{\sqrt{2}+j(2-\sqrt{2})}{4}$
	1	0	0				$\frac{\sqrt{2}-j(2+\sqrt{2})}{4}$	$\frac{\sqrt{2}+j(2-\sqrt{2})}{4}$
	1	0	1				$\frac{\sqrt{2}-j(2+\sqrt{2})}{4}$	$-\frac{\sqrt{2}-j(2-\sqrt{2})}{4}$
	1	1	0				$-\frac{2-\sqrt{2}-j\sqrt{2}}{4}$	$-\frac{2+\sqrt{2}+j\sqrt{2}}{4}$
	1	1	1				$\frac{2-\sqrt{2}+j\sqrt{2}}{4}$	$-\frac{2+\sqrt{2}-j\sqrt{2}}{4}$

Subset	$c6_{n+1}$	$c5_{n+1}$	$c4_{n+1}$	$c3_{n+1}$	$c2_{n+1}$	$c1_{n+1}$	u_{2n+2}	u_{2n+3}
SD_3	0	0	0	0	1	1	$\frac{1-j}{2}$	$\frac{1+j}{2}$
	0	0	1				0	$\frac{\sqrt{2}(1+j)}{2}$
	0	1	0				$-\frac{\sqrt{2}(1-j)}{2}$	0
	0	1	1				$-\frac{1-j}{2}$	$\frac{1+j}{2}$
	1	0	0				$\frac{\sqrt{2}(1-j)}{2}$	0
	1	0	1				$\frac{1-j}{2}$	$-\frac{1+j}{2}$
	1	1	0				$-\frac{1-j}{2}$	$-\frac{1+j}{2}$
	1	1	1				0	$-\frac{\sqrt{2}(1+j)}{2}$
SD_4	0	0	0	1	0	0	$\frac{2+\sqrt{2}+j\sqrt{2}}{4}$	$\frac{2-\sqrt{2}-j\sqrt{2}}{4}$
	0	0	1				$\frac{2+\sqrt{2}+j\sqrt{2}}{4}$	$\frac{\sqrt{2}-2+j\sqrt{2}}{4}$
	0	1	0				$-\frac{\sqrt{2}+j(2-\sqrt{2})}{4}$	$-\frac{\sqrt{2}-j(2+\sqrt{2})}{4}$
	0	1	1				$\frac{\sqrt{2}+j(2-\sqrt{2})}{4}$	$\frac{-\sqrt{2}+j(2+\sqrt{2})}{4}$
	1	0	0				$\frac{\sqrt{2}+j(2-\sqrt{2})}{4}$	$\frac{\sqrt{2}-j(2+\sqrt{2})}{4}$
	1	0	1				$-\frac{\sqrt{2}+j(2-\sqrt{2})}{4}$	$\frac{\sqrt{2}-j(2+\sqrt{2})}{4}$
	1	1	0				$-\frac{2+\sqrt{2}+j\sqrt{2}}{4}$	$-\frac{2-\sqrt{2}-j\sqrt{2}}{4}$
	1	1	1				$-\frac{2+\sqrt{2}+j\sqrt{2}}{4}$	$\frac{2-\sqrt{2}-j\sqrt{2}}{4}$
SD_5	0	0	0	1	0	1	$\frac{1+j}{2}$	$\frac{1-j}{2}$
	0	0	1				$\frac{\sqrt{2}(1+j)}{2}$	0
	0	1	0				0	$-\frac{\sqrt{2}(1-j)}{2}$
	0	1	1				$\frac{1+j}{2}$	$-\frac{1-j}{2}$
	1	0	0				0	$\frac{\sqrt{2}(1-j)}{2}$
	1	0	1				$-\frac{1+j}{2}$	$\frac{1-j}{2}$
	1	1	0				$-\frac{1+j}{2}$	$-\frac{1-j}{2}$
	1	1	1				$-\frac{\sqrt{2}(1+j)}{2}$	0
SD_6	0	0	0	1	1	0	0	1
	0	0	1				$\frac{j\sqrt{2}}{2}$	$\sqrt{2}/2$
	0	1	0				$\frac{j\sqrt{2}}{2}$	$-\sqrt{2}/2$
	0	1	1				j	0
	1	0	0				$-\frac{j\sqrt{2}}{2}$	$\sqrt{2}/2$
	1	0	1				$-j$	0
	1	1	0				0	-1
	1	1	1				$-\frac{\sqrt{2}}{2}$	$-\frac{\sqrt{2}}{2}$
SD7	0	0	0	1	1	1	$\frac{2-\sqrt{2}+j\sqrt{2}}{4}$	$\frac{2+\sqrt{2}-j\sqrt{2}}{4}$
	0	0	1				$\frac{\sqrt{2}+j(2+\sqrt{2})}{4}$	$\frac{\sqrt{2}-j(2-\sqrt{2})}{4}$
	0	1	0				$\frac{2-\sqrt{2}+j\sqrt{2}}{4}$	$-\frac{2+\sqrt{2}-j\sqrt{2}}{4}$
	0	1	1				$\frac{\sqrt{2}+j(2+\sqrt{2})}{4}$	$-\frac{\sqrt{2}-j(2-\sqrt{2})}{4}$
	1	0	0				$-\frac{2-\sqrt{2}+j\sqrt{2}}{4}$	$\frac{2+\sqrt{2}-j\sqrt{2}}{4}$
	1	0	1				$-\frac{\sqrt{2}+j(2+\sqrt{2})}{4}$	$\frac{\sqrt{2}-j(2-\sqrt{2})}{4}$
	1	1	0				$-\frac{2-\sqrt{2}+j\sqrt{2}}{4}$	$-\frac{2+\sqrt{2}-j\sqrt{2}}{4}$
	1	1	1				$-\frac{\sqrt{2}+j(2+\sqrt{2})}{4}$	$-\frac{\sqrt{2}-j(2-\sqrt{2})}{4}$

III. SUPER-ORTHOGONAL SPACE-TIME TRELLIS CODES
FOR COHERENT DETECTION

In this section, we present SOSTTCs for coherent detection that are used as references for the new codes, designed for noncoherent communications systems. We do this in a somewhat expedite manner, since such codes are rather well known [10, 15].

It is useful to see a signal point s of coordinates (x,y) as a complex number $x+jy$. To measure the difference between two transmission matrices $\mathbf{M}_n^{(1)}$ and $\mathbf{M}_n^{(2)}$ as defined by (2), we use the *coding gain distance* (CGD), defined in [10] as follows. Define $\mathbf{B}_n = \mathbf{M}_n^{(1)} - \mathbf{M}_n^{(2)}$ and form the matrix $\mathbf{A}_n = \mathbf{B}_n \cdot \mathbf{B}_n^H$, where $\mathbf{B}_n^H$ is the Hermitian (complex conjugate and transpose) of $\mathbf{B}_n$. Then, $d^2 = \det(\mathbf{A}_n)$. Note that this is actually the squared Euclidian distance between two 4D signal points $\left(x_{2n}^{(1)}, y_{2n}^{(1)}, x_{2n+1}^{(1)}, y_{2n+1}^{(1)} \right)$ and $\left(x_{2n}^{(2)}, y_{2n}^{(2)}, x_{2n+1}^{(2)}, y_{2n+1}^{(2)} \right)$:

$$d^2 = \sum_{i=0}^{1} \left[\left(x_{2n+i}^{(1)} - x_{2n+i}^{(2)} \right)^2 + \left(y_{2n+i}^{(1)} - y_{2n+i}^{(2)} \right)^2 \right] . \tag{12}$$

Obviously, the larger the difference of the respective coordinates, the larger is the CGD. Following [10], we define the parameter $\omega = 2\pi/M$. Assuming a circle of radius $1/\sqrt{2}$ centred in the origin, we then express the coordinates x_{2n+i} and y_{2n+i}, $i = 0,1$, as

$$x_{2n+i} = \frac{1}{\sqrt{2}} \cos k_{2n+i}\,\omega \tag{13}$$

and

$$y_{2n+i} = \frac{1}{\sqrt{2}} \sin k_{2n+i}\,\omega . \tag{14}$$

Inserting (13) and (14) into (12), we easily obtain:

$$d^2 = \sum_{i=0}^{1} \left[1 - \cos\left(k_{2n+i}^{(1)} - k_{2n+i}^{(2)} \right) \omega \right]^2 . \tag{15}$$

A. SOSTTCs for BPSK

The BPSK signal constellation is illustrated in Fig.J.2. The two 1D signal points are labelled as 0 and 1. In this very particular case, the natural and the Gray mapping coincide, and BPSK is equivalent to BASK: a bit 0 is transmitted as the amplitude $1/\sqrt{2}$, while a bit 1 is transmitted as the amplitude $-1/\sqrt{2}$. Grouping the 1D points into 2D points, we obtain four 2D points: $(0,0)$, $(0,1)$, $(1,0)$, and $(1,1)$. We partition this set into two subsets S_0 and S_1 such that the intrasubset Hamming
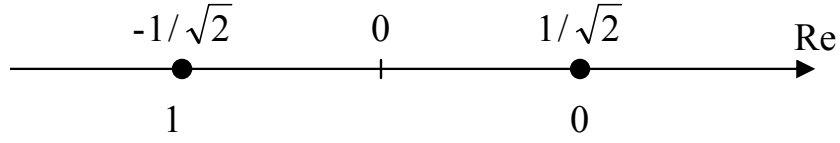
Figure J.2: BPSK signal constellation.

distance is maximized to 2:

$$S_0 = \{(0,0),\ (1,1)\} \tag{16}$$

$$S_1 = \{(0,1),\ (1,0)\}. \tag{17}$$

In two consecutive signalling intervals $2n$ and $2n+1$, two bits are gathered at the input of the transmitter, denoted by $b1_{2n}$ and $b1_{2n+1}$. A 2D signal point is the concatenation of two 1D points that are transmitted by BPSK in two consecutive signalling periods. The bit $b1_{2n}$ is encoded by a rate-1/2 systematic convolutional encoder, while the bit $b1_{2n+1}$ remains uncoded and, for convenience, is denoted as $c2_n$ at the input of the BPSK mapper. The rate-1/2 convolutional encoder outputs two bits, denoted by $c0_n$ and $c1_n$ such that $c1_n = b1_{2n}$.

Consider the orthogonal matrices defined by (2). They form two families F_0 (with $a_n = +1$) and F_1 (with $a_n = -1$), selected by $c0_n = 0$ and $c0_n = 1$, respectively. Moreover, each family is further partitioned in subsets of matrices and denoted as $\mathbf{SM}_p$, such that the index of a matrix subset SM_p is given by

$$p = 2c1_n + c0_n. \tag{18}$$

The first antenna transmits consecutively the symbols s_{2n} and s_{2n+1} from the BPSK signal constellation. However, for $c0_n = 0$ and $c0_n = 1$, the second antenna will transmit data symbols according to the matrix pattern with $a_n = +1$ and $a_n = -1$, respectively.

To select a point from a 1D BPSK constellation, constituent of a 2D constellation, a bit is required, denoted by $z1_i$, where $i \in \{2n,\ 2n+1\}$. The convolutionally encoded bit $c1_n$ (actually, the input bit $b1_{2n}$) selects a 2D subset that is the set of all 2D points for which the following relation holds true:

$$z1_{2n+1} = c1_n \oplus z1_{2n}. \tag{19}$$

Then, the index m of the subset S_m, $m = 0, 1$, is given by $m = z1_{2n} \oplus z1_{2n+1}$.

The uncoded input bit $b1_{2n+1}$ determines the 2D signal point within the already selected 2D subset to be transmitted by the first antenna in two consecutive signalling intervals $2n$ and $2n+1$ such that $z1_{2n} = b1_{2n+1}$.

In the context of space-time trellis coding, the TCM rules given by Ungerboeck [21, 22, 23] sound as follows:

1. The state transitions originating in even-numbered states are assigned transmission matrices belonging to the family F_0, and the state transitions originating in odd-numbered states are assigned transmission matrices belonging to the family F_1.

2. The state transitions reaching the same next state are assigned transmission matrices from the same family, be it F_0 or F_1.

Define two binary state variables $\sigma1_n$ and $\sigma2_n$ such that the decimal value of the current state is written as $\sigma_n = 2\sigma2_n + \sigma1_n$. Using Ungerboeck's rules to assign orthogonal matrices to the state transitions of a 4-state topological trellis [21], we derive the block diagram of the SOSTTC encoder given in Fig. J.3. SOSTTCs with a larger number of states can be built in a similar way.

B. SOSTTCs for QPSK

The QPSK signal constellation, with natural and, in parentheses, Gray mapping, is illustrated in Fig. J.4. For coherent demodulation, the natural mapping will do. The four 2D signal points are labelled as $0, 1, 2$, and 3. By grouping them into 4D points, we obtain 16 points from $(0,0)$ to $(3,3)$. With those points, we then form the following 4D subsets:

$$
\begin{aligned}
S_0 &= \{(0,0),(1,1),(2,2),(3,3)\} & (20)\\
S_1 &= \{(0,1),(1,2),(2,3),(3,0)\} & (21)\\
S_2 &= \{(0,2),(1,3),(2,0),(3,1)\} & (22)\\
S_3 &= \{(0,3),(1,0),(2,1),(3,2)\}. & (23)
\end{aligned}
$$

To select one out of four subsets S_m, $m = 0,\dots,3$, two bits are required, say, $c1_n$ and $c2_n$, such that the index m can be written as $m = 2c2_n + c1_n$.

In two consecutive signalling intervals $2n$ and $2n+1$, four bits are gathered at the input of the transmitter, denoted by $b1_{2n}$, $b2_{2n}$, $b1_{2n+1}$, $b2_{2n+1}$. The first two bits, $b1_{2n}$ and $b2_{2n}$, are encoded by a rate-2/3 systematic convolutional encoder, while the next two bits, $b1_{2n+1}$ and $b2_{2n+1}$, remain uncoded. The rate-2/3 convolutional encoder outputs three bits, denoted by $c0_n$, $c1_n$, and $c2_n$, such that $c1_n = b1_{2n}$ and $c2_n = b2_{2n}$.
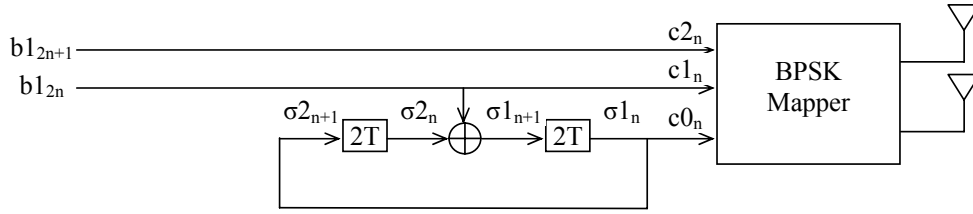
Figure J.3: Super-orthogonal space-time trellis encoder for BPSK signal constellation.
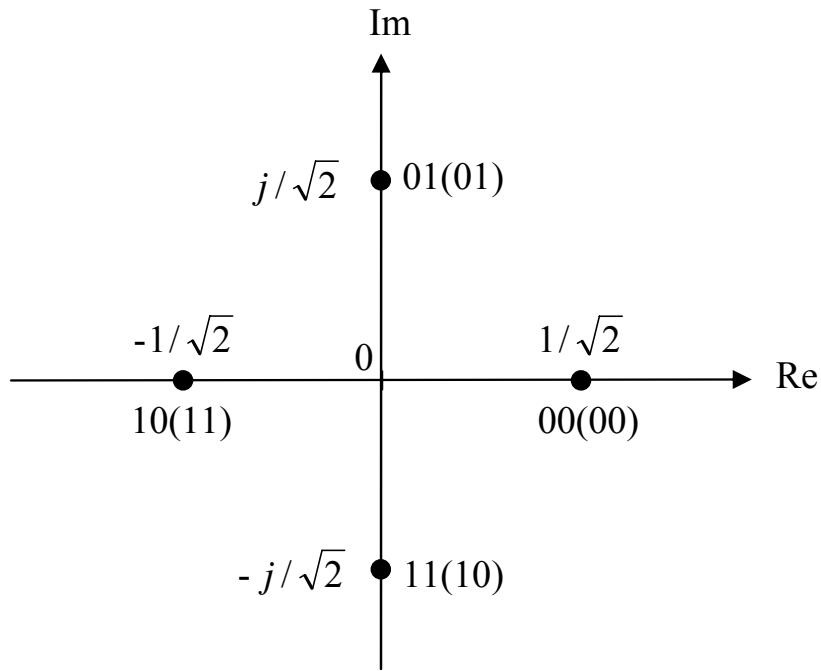

Figure J.4: QPSK signal constellation with natural mapping and, in parentheses, Gray mapping.

For QPSK, the index of a matrix subset SM_p is given by

$$p = 4c2_n + 2c1_n + c0_n .\tag{24}$$

To select a point from a 2D QPSK constellation, constituent of a 4D constellation, two bits are required, denoted by $z1_i$, $z2_i$, where $i \in \{2n, 2n+1\}$. The two bits $(z2_i\, z1_i)$ select a 2D signal point as shown in Fig. J.4.

The two convolutionally encoded bits $c1_n$ and $c2_n$ (actually, the input bits $b1_{2n}$ and $b2_{2n}$) select a 4D subset that is the set of all 4D signal points for which (19) and (25) below hold true:

$$z2_{2n+1} = c2_n \oplus z2_{2n} \oplus (c1_n \cdot z1_{2n}) .\tag{25}$$

The two uncoded input bits, $b1_{2n+1}$ and $b2_{2n+1}$, determine the 4D signal point within the already selected 4D subset to be transmitted by the first antenna in two consecutive signalling intervals $2n$ and $2n+1$ such that $z1_{2n} = b1_{2n+1}$ and $z2_{2n} = b2_{2n+1}$.

Define three binary state variables $\sigma1_n$, $\sigma2_n$, and $\sigma3_n$ such that the decimal value of the current state is written as $\sigma_n = 4\sigma3_n + 2\sigma2_n + \sigma1_n$. Using the same TCM rules as before, we derive the logic diagram given in Fig. J.5.

C. SOSTTCs for 8PSK

The 8PSK signal constellation, with natural and, in parentheses, Gray mapping, is illustrated in Fig. J.6. The eight 2D points are labelled from 0 to 7. Grouping them into 4D points, we get 64 4D points from $(0,0)$ to $(7,7)$. With those points, we form the following 4D subsets:

$$S_0 = \{(0,0),(1,1),(2,2),(3,3),(4,4),(5,5),(6,6),(7,7)\} \tag{26}$$

$$S_1 = \{(0,1),(1,2),(2,3),(3,4),(4,5),(5,6),(6,7),(7,0)\} \tag{27}$$

$$S_2 = \{(0,2),(1,3),(2,4),(3,5),(4,6),(5,7),(6,0),(7,1)\} \tag{28}$$

$$S_3 = \{(0,3),(1,4),(2,5),(3,6),(4,7),(5,0),(6,1),(7,2)\} \tag{29}$$

$$S_4 = \{(0,4),(1,5),(2,6),(3,7),(4,0),(5,1),(6,2),(7,3)\} \tag{30}$$

$$S_5 = \{(0,5),(1,6),(2,7),(3,0),(4,1),(5,2),(6,3),(7,4)\} \tag{31}$$

$$S_6 = \{(0,6),(1,7),(2,0),(3,1),(4,2),(5,3),(6,4),(7,5)\} \tag{32}$$

$$S_7 = \{(0,7),(1,0),(2,1),(3,2),(4,3),(5,4),(6,5),(7,6)\}. \tag{33}$$

To select one out of eight subsets S_m, $m = 0, \cdots, 7$, three bits are required, say, $c1_n$, $c2_n$, and $c3_n$ such that the index m can be written as $m = 4c3_n + 2c2_n + c1_n$.

In two consecutive signalling intervals $2n$ and $2n+1$, six bits are gathered at the input of the transmitter, denoted by $b1_{2n}$, $b2_{2n}$, $b3_{2n}$, $b1_{2n+1}$, $b2_{2n+1}$, $b3_{2n+1}$. The
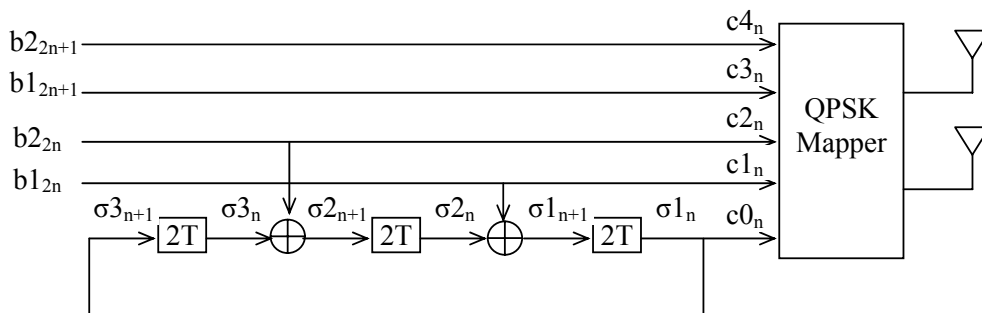

Figure J.5: Super-orthogonal space-time trellis encoder for QPSK signal constellation.
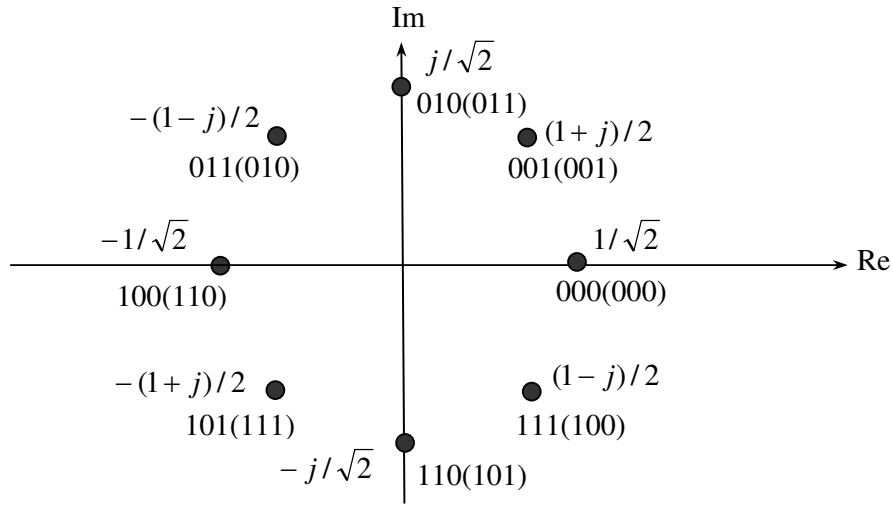
Figure J.6: 8PSK signal constellation with natural mapping and, in parenthesis, Gray mapping.

first three bits are encoded by a rate-3/4 systematic convolutional encoder, while the other three bits remain uncoded. The rate-3/4 convolutional encoder outputs four bits, denoted by $c0_n$, $c1_n$, $c2_n$, and $c3_n$, such that $c1_n = b1_{2n}$, $c2_n = b2_{2n}$, and $c3_n = b3_{2n}$.

For 8PSK, the index p of a matrix subset SM_p is given by

$$p = 8c3_n + 4c2_n + 2c1_n + c0_n. \tag{34}$$

To select a point from a 2D 8PSK constellation, constituent of a 4D constellation, three bits are required, denoted by $z1_i$, $z2_i$, and $z3_i$, where $i \in \{2n, 2n+1\}$. These three bits select a 2D signal point according to the natural mapping as shown in Fig. J.6.

The three convolutionally encoded bits $c1_n$, $c2_n$ and $c3_n$ (actually, the input bits $b1_{2n}$, $b2_{2n}$ and $b3_{2n}$) select a 4D subset that is the set of all 4D signal points for which (19), (25) and (35) below hold true:

$$z3_{2n+1} = c3_n \oplus z3_{2n} \oplus [c2_n \cdot z2_{2n} + (c2_n \oplus z2_{2n}) \cdot (c1_n \cdot z1_{2n})] . \tag{35}$$

The three uncoded input bits $b1_{2n+1}$, $b2_{2n+1}$, and $b3_{2n+1}$, determine the 4D signal point within the already selected 4D subset to be transmitted by the first antenna in two consecutive signalling intervals $2n$ and $2n+1$ such that $z1_{2n} = b1_{2n+1}$, $z2_{2n} = b2_{2n+1}$ and $z3_{2n} = b3_{2n+1}$.

Define four binary state variables $\sigma1_n$, $\sigma2_n$, $\sigma3_n$, and $\sigma4_n$ such that the decimal value of the current state is written as $\sigma_n = 8\sigma4_n + 4\sigma3_n + 2\sigma_n + \sigma1_n$. The

resulting logic diagram is given in Fig. J.7. The easy way of selection, as reflected in (19), (25) and (35), is explained by the clever partition of the 4D signal constellation into $M = 2^b$ subsets: the generic subset S_m contains the points $\{(0, m), (1, m+1), \dots, (M-1, M+m-1 \mod M)\}$. We claim that any other partition would require a rather complex look-up table, with no special advantage. This is also well explained in [15].

IV. SUPER-ORTHOGONAL SPACE-TIME TRELLIS CODES FOR NONCOHERENT DETECTION

In this section, we present the main contribution of our paper, i.e., SOSTTCs for communication systems having no knowledge of CSI. To this end, the differential encoding scheme developed in Section II is added to the SOSTTCs designed for coherent demodulation as explained in the following. To reflect the differential encoding, we now consider $n+1$ as the time index of the 4D (2D in case of BPSK) current symbol and, accordingly, $2n+2$ and $2n+3$ as the time indices of the two consecutive 2D (1D in case of BPSK) signal symbols. The signal constellation is the collection of all two-tuples (u_{2n+2}, u_{2n+3}) as given in Tables J.1I, J.2, and J.3. Using the TCM rules, those symbols are assigned to state transitions of a topological trellis. Having in view that the mappings given in the said tables are bijective, this is equivalent to assigning vectors of selection bits to the state transitions.

For BPSK, the mapping of selection bits into 2D signal points (u_{2n+2}, u_{2n+3}) is shown in Table J.1, where we also group the four 2D signal points into two subsets SD_0 and SD_1. Two bits are required to select a 2D point, $c1_{n+1}$ to select the subset and $c2_{n+1}$ to select the point within the selected subset. The input bit $b1_{2n+2}$ is encoded by a rate-1/2 systematic convolutional encoder just as in the coherent case and is denoted by $c1_{n+1}$ at the output.
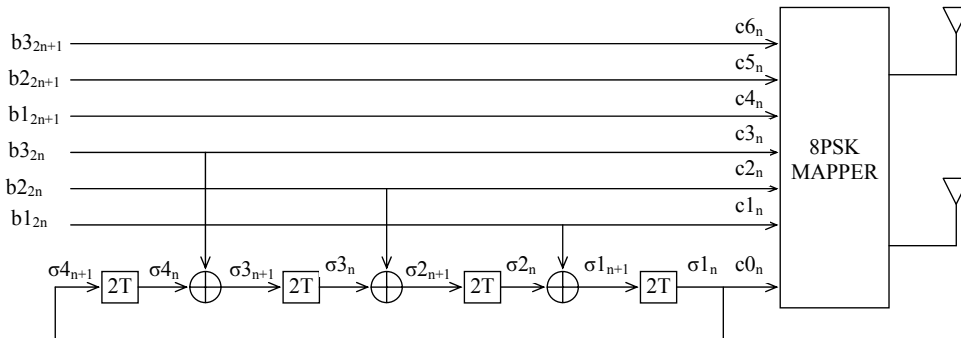

Figure J.7: Super-orthogonal space-time trellis encoder for 8-PSK signal constellation.

The mapping of selection bits into 4D QPSK signal points (u_{2n+2}, u_{2n+3}) is given in Table J.2, where the 16 4D signal points are grouped into four subsets SD_0, SD_1, SD_2, and SD_3. Table J.3 shows how to map selection bits into 4D 8PSK signal points and subsets. The block diagrams of the SOSTTC encoder for BPSK signal constellation, QPSK constellation, and 8PSK signal constellation look similar to those given in Figs.J.3, J.5, and J.7, respectively, but the mapping includes the differential encoding as well.

The main contradistinction to the coherent case is that the output of the convolutional encoder does not select the 4D signal point to be transmitted by the first antenna in two consecutive signalling intervals as well as the pattern of the Alamouti transmission matrix, but the complex-valued two-tuple (u_{2n+2}, u_{2n+3}) as well as the pattern of the differential encoding matrix, as given in (3). The 4D (2D in case of BPSK) signal constellations used for differential encoding are 2^{2b}-point sets, where a 4D (2D in case of BPSK) signal point is a two-tuple (u_{2n+2}, u_{2n+3}) of complex-valued symbols. It seems not very useful to consider such a 4D signal constellation as the Cartesian product of a 2D signal constellation by itself. Therefore, the selection procedure is somewhat different from that used for coherent detection. Another important contradistinction to the coherent case is that the convolutionally encoded bit $c0_{n+1}$ selects the encoding matrix family as follows: when $c0_{n+1} = 0$, then $a_n \cdot a_{n+1} = +1$, and when $c0_{n+1} = 1$, then $a_n \cdot a_{n+1} = -1$. Note that, for each originating state at time $n+1$, the value of a_n is known because of the second TCM rule, stating that all state transitions arriving in the same next state are assigned matrices from the same family, and thus, having the same a_n.

V. RECEIVER ISSUES

A. Channel Model for Simulations

For the convenience of the reader, we insert here a short description of the MIMO channel simulator developed from a two-ring reference channel model that was employed to evaluate the performance of the SOSTTCs. In this model, it is assumed that local scatterers are located on two individual rings around the transmitter and the receiver. Homogeneous plane waves emitted from the transmitter are bounced only by the scatterers around the receiver. Assuming that the transmitter and the receiver are equipped with M_T transmit antennas and M_R receive antennas, the complex channel gains of the channel simulator can be expressed as [12]

$$h_{kl}(t) = \frac{1}{\sqrt{2M_s}} \sum_{m=1}^{M_s} a_{l,m} b_{k,m} e^{j(2\pi f_{1,m}t + \theta_{1,m})} + \frac{1}{\sqrt{2N_s}} \sum_{n=1}^{N_s} c_{l,n} d_{k,n} e^{j(2\pi f_{2,n}t + \theta_{2,n})} \quad (36)$$

for $l = 1, 2, \ldots, M_T$ and $k = 1, 2, \ldots, M_R$. In (36), M_s and N_s denote the number of local scatterers placed around the transmitter and the receiver, respectively. The quantities $f_{1,m}$ and $f_{2,n}$ represent the Doppler frequencies, as defined in [12]. The phases $\theta_{1,m}$ and $\theta_{2,n}$ are considered as outcomes from a random generator uniformly distributed over $(0, 2\pi]$. Furthermore, we have

$$a_{l,m} = e^{j\pi(M_T - 2l + 1)\frac{\delta_T}{\lambda}\cos\left(\phi_{T_1}^{(m)} - \beta_T\right)} \tag{37a}$$

$$b_{k,m} = e^{j\pi(M_R - 2k + 1)\frac{\delta_R}{\lambda}\left[\phi_R^{\max}\sin\phi_{T_1}^{(m)}\sin\beta_R - \cos\beta_R\right]} \tag{37b}$$

$$c_{l,m} = e^{j\pi(M_T - 2l + 1)\frac{\delta_T}{\lambda}\left[\phi_T^{\max}\sin\phi_{R_2}^{(n)}\sin\beta_T + \cos\beta_T\right]} \tag{37c}$$

$$d_{k,m} = e^{j\pi(M_R - 2k + 1)\frac{\delta_R}{\lambda}\cos\left(\phi_{R_2}^{(n)} - \beta_R\right)}. \tag{37d}$$

In the equations presented above, the antenna spacings at the transmitter and the receiver are denoted by δ_T and δ_R, respectively, and the orientations of the antenna arrays are described by β_T and β_R. The carrier's wavelength is denoted by λ. The angle $\phi_{T_1}^{(m)}$ represents the angle of departure (AOD), while the angle of arrival is described by $\phi_{R_2}^{(n)}$. The angle $\phi_R^{\max}$ describes one half of the maximum angle of arrival (AOA) observed at the receiver, while $\phi_T^{\max}$ is one half of the maximum AOD observed at the transmitter.

In this paper, we employ the von Mises distribution [1] to characterize the distribution of the AODs and the AOAs. For the channel simulator, both the AODs and the AOAs are determined by the modified method of equal area (MMEA) [6].

B. Decoding of SOSTTCs for Known CSI at the Receiver

Consider first the case of a single receive antenna. Denote the channel gains from the two transmit antennas to the receive antenna as h_1 and h_2. Denote by r_{2n} and r_{2n+1} the complex-valued signals received in two consecutive symbol periods. For $a_n = +1$, these are:

$$r_{2n} = h_1 \cdot s_{2n} - h_2 \cdot s_{2n+1}^* + \eta_{2n} \tag{38}$$

$$r_{2n+1} = h_1 \cdot s_{2n+1} + h_2 \cdot s_{2n}^* + \eta_{2n+1} \tag{39}$$

where η_{2n} and η_{2n+1} are noise components. Using (38) and (39), form the following decision variables:

$$\tilde{s}_{2n}^{(+1)} = h_1^* \cdot r_{2n} + h_2 \cdot r_{2n+1}^* = \left(|h_1|^2 + |h_2|^2\right)s_{2n} + h_1^* \cdot \eta_{2n} + h_2 \cdot \eta_{2n+1}^* \tag{40}$$

$$\tilde{s}_{2n+1}^{(+1)} = h_1^* \cdot r_{2n+1} - h_2 \cdot r_{2n}^* = \left(|h_1|^2 + |h_2|^2\right)s_{2n+1} + h_1^* \cdot \eta_{2n+1} - h_2 \cdot \eta_{2n}^*. \tag{41}$$

For $a_n = -1$, the received signals are:

$$r_{2n} = h_1 \cdot s_{2n} + h_2 \cdot s_{2n+1}^* + \eta_{2n} \tag{42}$$

$$r_{2n+1} = h_1 \cdot s_{2n+1} - h_2 \cdot s_{2n}^* + \eta_{2n+1}. \tag{43}$$

Form the following two decision variables:

$$\tilde{s}_{2n}^{(-1)} = h_1^* \cdot r_{2n} - h_2 \cdot r_{2n+1}^* = \left(|h_1|^2 + |h_2|^2\right) s_{2n} + h_1^* \cdot \eta_{2n} - h_2 \cdot \eta_{2n+1}^* \tag{44}$$

$$\tilde{s}_{2n+1}^{(-1)} = h_1^* \cdot r_{2n+1} + h_2 \cdot r_{2n}^* = \left(|h_1|^2 + |h_2|^2\right) s_{2n+1} + h_1^* \cdot \eta_{2n+1} + h_2 \cdot \eta_{2n}^*. \tag{45}$$

Suppose that a matrix with $a_n = +1$ was transmitted, but instead of (40) and (41), (44) and (45) were used. The result would be:

$$\tilde{s}_{2n}^{(+1/-1)} = \left(|h_1|^2 - |h_2|^2\right) s_{2n} - 2h_1^* \cdot h_2 \cdot s_{2n+1}^* + h_1^* \cdot \eta_{2n} - h_2 \cdot \eta_{2n+1}^* \tag{46}$$

$$\tilde{s}_{2n+1}^{(+1/-1)} = \left(|h_1|^2 - |h_2|^2\right) s_{2n+1} + 2h_1^* \cdot h_2 \cdot s_{2n}^* + h_1^* \cdot \eta_{2n+1} + h_2 \cdot \eta_{2n}^*. \tag{47}$$

On the other hand, if a matrix with $a_n = -1$ was transmitted, but instead of (44) and (45), (40) and (41) were used, the result would be:

$$\tilde{s}_{2n}^{(-1/+1)} = \left(|h_1|^2 - |h_2|^2\right) s_{2n} + 2h_1^* \cdot h_2 \cdot s_{2n+1}^* + h_1^* \cdot \eta_{2n} + h_2 \cdot \eta_{2n+1}^* \tag{48}$$

$$\tilde{s}_{2n+1}^{(-1/+1)} = \left(|h_1|^2 - |h_2|^2\right) s_{2n+1} - 2h_1^* \cdot h_2 \cdot s_{2n}^* + h_1^* \cdot \eta_{2n+1} - h_2 \cdot \eta_{2n}^*. \tag{49}$$

It is thus clear that the simple maximum likelihood decision rule proposed by Alamouti in [3] is possible only if there is certainty on the family to which the transmitted matrix belongs.

The sequence decoding of SOSTTCs is performed using the Viterbi algorithm. The observations are the complex-valued output signals of a PSK demodulator, which will be denoted as $r_{2n} = R_{2n} \cdot e^{j\varphi_{2n}}$ and $r_{2n+1} = R_{2n+1} \cdot e^{j\varphi_{2n+1}}$. Let us express the path gains from the first and the second transmit antenna to the receiver as $h_1 = H_1 \cdot e^{j\gamma_1}$ and $h_2 = H_2 \cdot e^{j\gamma_2}$. Then, for maximum likelihood sequence decoding with perfect CSI at the receiver, a suitable branch metric is given as

$$BM_n = \left| r_{2n} - h_1 \cdot s_{2n} + a_n \cdot h_2 \cdot s_{2n+1}^* \right|^2 + \left| r_{2n+1} - h_1 \cdot s_{2n+1} - a_n \cdot h_2 \cdot s_{2n}^* \right|^2. \tag{50}$$

After some simple algebra and trigonometry, we obtain:

$$\begin{aligned} BM_n = {} & R_{2n}^2 + R_{2n+1}^2 + H_1^2 + H_2^2 \\ & - \sqrt{2} H_1 \left[R_{2n} \cdot \cos(\varphi_{2n} - \gamma_1 - k_{2n} \cdot \omega) \right. \end{aligned} \tag{51}$$

$$+R_{2n+1} \cdot \cos(\varphi_{2n+1} - \gamma_1 - k_{2n+1} \cdot \omega)]$$
$$+\sqrt{2}a_n \cdot H_2 \left[R_{2n} \cdot \cos(\varphi_{2n} - \gamma_2 + k_{2n+1} \cdot \omega) \right.$$
$$\left. -R_{2n+1} \cdot \cos(\varphi_{2n+1} - \gamma_2 - k_{2n} \cdot \omega) \right].$$

The branch metric is used to reduce the number of transitions in the trellis diagram reaching the same state to a single one, called *survivor*. The branch metric with $a_n = +1$ and $a_n = -1$ is used for those transitions originating in even and odd numbered states, respectively.

When it is possible to equip the receiver with two antennas, the branch metric is simply the sum of two branch metrics as derived for a single receive antenna:

$$BM_n = BM_n^{(1)} + BM_n^{(2)}. \tag{52}$$

The path gains are denoted by $h^{(1,q)}$ and $h^{(2,q)}$, $q = 1, 2$, for the first and the second receive antenna, respectively.

C. Decoding of SOSTTCs for Unknown CSI at the Receiver
We have two alternative strategies.
C.1. First decoding strategy
The first decoding strategy is essentially the method applied in [19]. Consider first a single receive antenna. For differential decoding, the receiver is based on the following measured quantities:

$$r_{2n} = h_1 \cdot s_{2n} - h_2 \cdot a_n \cdot s_{2n+1}^* + \eta_{2n} \tag{53}$$
$$r_{2n+1} = h_1 \cdot s_{2n+1} + h_2 \cdot a_n \cdot s_{2n}^* + \eta_{2n+1} \tag{54}$$
$$r_{2n+2} = h_1 \cdot s_{2n+2} - h_2 \cdot a_{n+1} \cdot s_{2n+3}^* + \eta_{2n+2} \tag{55}$$
$$r_{2n+3} = h_1 \cdot s_{2n+3} + h_2 \cdot a_{n+1} \cdot s_{2n+2}^* + \eta_{2n+3} \tag{56}$$

where η_{2n}, η_{2n+1}, η_{2n+2}, and η_{2n+3} are noise components. The symbols r_{2n+2} in (55) and r_{2n+3} in (56) denote the complex-valued signals received in the two consecutive symbol periods $2n+2$ and $2n+3$. We need some derived quantities upon which to base our estimation on u_{2n+2} and u_{2n+3} as given in (4) and (5), respectively. Define

$$R_1 = r_{2n}^* \cdot r_{2n+2} + a_n \cdot a_{n+1} \cdot r_{2n+1} \cdot r_{2n+3}^*. \tag{57}$$

Introducing (52)-(56) in this expression, we obtain:

$$R_1 = \left(|h_1|^2 + |h_2|^2 \right) u_{2n+2} + \text{noise terms}.$$ (58)

Define also

$$R_2 = r_{2n+1}^* \cdot r_{2n+2} - a_n \cdot a_{n+1} \cdot r_{2n} \cdot r_{2n+3}^*.$$ (59)

Proceeding as before, we get:

$$R_2 = \left(|h_1|^2 + |h_2|^2 \right) u_{2n+3} + \text{noise terms}.$$ (60)

It is assumed that a_n is known. For both $a_{n+1} = +1$ and $a_{n+1} = -1$, the receiver computes the closest vector $(u_{2n+2} \ u_{2n+3})$ to $(R_1 \ R_2)$. If hard decision is used, by inverse mapping, the bits used further in the Viterbi algorithm are obtained. However, if soft decision is applied, the quantized version of $(R_1 \ R_2)$ is used in the Viterbi algorithm.

When the receiver is equipped with two antennas, using the same method, we compute $R_1^{(1)}$ and $R_2^{(1)}$ for the first antenna and $R_1^{(2)}$ and $R_2^{(2)}$ for the second antenna. Then, the closest vector $(u_{2n+2} \ u_{2n+3})$ to $\left(R_1^{(1)} + R_1^{(2)} \ R_2^{(1)} + R_2^{(2)} \right)$ is computed. The rest of the procedure is the same as explained for a single receive antenna.

C.2. Second decoding strategy

The transmission matrix at the discrete time $n + 1$, according to (2), is:

$$\mathbf{M}_{n+1} = \begin{pmatrix} s_{2n+2} & -a_{n+1} \cdot s_{sn+3}^* \\ s_{2n+3} & a_{n+1} \cdot s_{sn+2}^* \end{pmatrix}.$$ (61)

We can write the branch metric as

$$BM_{n+1} = \left| r_{2n+2} - h_1 \cdot s_{2n+2} + h_2 \cdot s_{2n+3}^* \right|^2 + \left| r_{2n+3} - h_1 \cdot s_{2n+3} - h_2 \cdot s_{2n+2}^* \right|^2.$$ (62)

From (62), we obtain:

$$
\begin{aligned}
BM_{n+1} = \ & |r_{2n+2}|^2 + |r_{2n+3}|^2 + \left(|h_1|^2 + |h_2|^2 \right) \left(\left| s_{2n+2}^2 \right|^2 + \left| s_{2n+3}^2 \right|^2 \right) \\
& + 2Re \left\{ r_{2n+2} \left(-h_1^* \cdot s_{2n+2}^* + h_2^* \cdot a_{n+1} \cdot s_{2n+3} \right) \right. \\
& \left. + r_{2n+3} \left(-h_1^* \cdot s_{2n+3}^* - h_2^* \cdot a_{n+1} \cdot s_{2n+2} \right) \right\}.
\end{aligned}
$$ (63)

The first terms are positive and common to all state transitions of a trellis section. Only the last term depends on the signal being actually transmitted. Define thus the

reduced metric

$$
\begin{aligned}
RM_{n+1} \;=\; & 2Re\left\{ r_{2n+2}\left(-h_1^*\cdot s_{2n+2}^* + h_2^*\cdot a_{n+1}\cdot s_{2n+3}\right)\right. \\
& \left.+ r_{2n+3}\left(-h_1^*\cdot s_{2n+3}^* - h_2^*\cdot a_{n+1}\cdot s_{2n+2}\right)\right\}.
\end{aligned}
\tag{64}
$$

The branch metric BM_{n+1} is minimized by the most negative value of the reduced metric RM_{n+1}. Using the differential encoding, we have:

$$
\begin{aligned}
RM_{n+1} \;=\; & 2Re\left\{ u_{2n+2}\left[r_{2n+2}^*\left(-h_1\cdot s_{2n} + h_2\cdot a_n\cdot s_{2n+1}^*\right)\right]\right. \\
& + r_{2n+3}\left(-h_1^*\cdot a_n\cdot s_{2n+1}^* - h_2^*\cdot s_{2n}\right)a_{n+1}\big] \\
& + u_{2n+3}\left[r_{2n+2}^*\left(-h_1\cdot s_{2n+1} - h_2\cdot a_n\cdot s_{2n}^*\right)\right. \\
& \left.\left.+ r_{2n+3}\left(h_1^*\cdot a_n\cdot s_{2n}^* - h_2^*\cdot s_{2n+1}\right)a_{n+1}\right]\right\}.
\end{aligned}
\tag{65}
$$

By neglecting the noise term, we can write:

$$
r_{2n} \;=\; h_1\cdot s_{2n} - h_2\cdot a_n\cdot s_{2n+1}^*
\tag{66}
$$

$$
r_{2n+1} \;=\; h_1\cdot s_{2n+1} + h_2\cdot a_n\cdot s_{2n}^*.
\tag{67}
$$

Finally, we obtain:

$$
\begin{aligned}
RM_{n+1} \;=\; & -2Re\left\{\left(r_{2n}\cdot r_{2n+2}^* + a_n\cdot a_{n+1}\cdot r_{2n+1}^*\cdot r_{2n+3}\right)u_{2n+2}\right. \\
& \left.+ \left(r_{2n+1}\cdot r_{2n+2}^* - a_n\cdot a_{n+1}\cdot r_{2n}^*\cdot r_{2n+3}\right)u_{2n+3}\right\}.
\end{aligned}
\tag{68}
$$

For each state transition, the receiver knows all the quantities from this expression. The survivor is selected as that transition entering a given next state that makes RM_{n+1} to be the most negative one. The knowledge of h_1 and h_2 is obviously not required.

VI. SIMULATION RESULTS

In this section, we first compare the performance of the differential SOSTTCs decoded by the two algorithms described in Section V. All the three signal constellations, i.e., BPSK, QPSK, and 8PSK, have been considered. For comparison, we also present simulation results for SOSTTCs using the coherent encoding scheme. Moreover, we study the effect of the antenna spacing and the angular spread of scatterers on the BER performance of the differential SOSTTCs.

In all simulations, the AODs and the AOAs were determined by using the MMEA with $M_s = 40$ and $N_s = 50$, $\beta_T = \beta_R = \pi/2$ and $\phi_T^{\max} = \phi_R^{\max} = 2°$. The transmitter and the receiver moved in the direction determined by the angles of motion

$\alpha_T = 60°$ and $\alpha_R = 60°$. The maximum Doppler frequencies at both sides were equal to 91 Hz. The chosen value 91 Hz is for the case when the carrier frequency is 900 MHz and the speed of the mobile unit is 110 km/h. If not mentioned otherwise, we assume that the scatterers were located uniformly on the two rings, i.e., the parameter κ controlling the angular spread in the von Mises distribution equals zero.

The performance comparison between the differential SOSTTCs using the proposed decoding algorithm and the conventional decoding algorithm is depicted in Fig. J.8 for BPSK. The comparison between the two aforementioned decoding algorithms is presented in Fig. J.9 for QPSK and in Fig. J.10 for 8PSK. In these three figures, we also present the simulation results for the cases in which the receiver is equipped with one antenna and two antennas. It is seen from Figs. J.8–J.10 that the proposed algorithm has the same decoding performance as the conventional algorithm. For the sake of comparison, Figs. J.8–J.10 also present the BER performance of the coherent SOSTTC. It can be concluded from the three figures that a loss of 3 dB occurs when differential SOSTTCs are used instead of coherent SOSTTCs, what fully agrees with [19].

In addition, we compare the simulation time of the differential SOSTTCs using both decoding algorithms for the case $M_T = 2$ and $M_R = 1$. The Tables J.4, J.5, and J.6 show the simulation time required for the differential SOSTTC using the BPSK, QPSK, and 8PSK constellation, respectively. The quantity L in these three tables denotes the number of symbols used in the simulation runs. According to
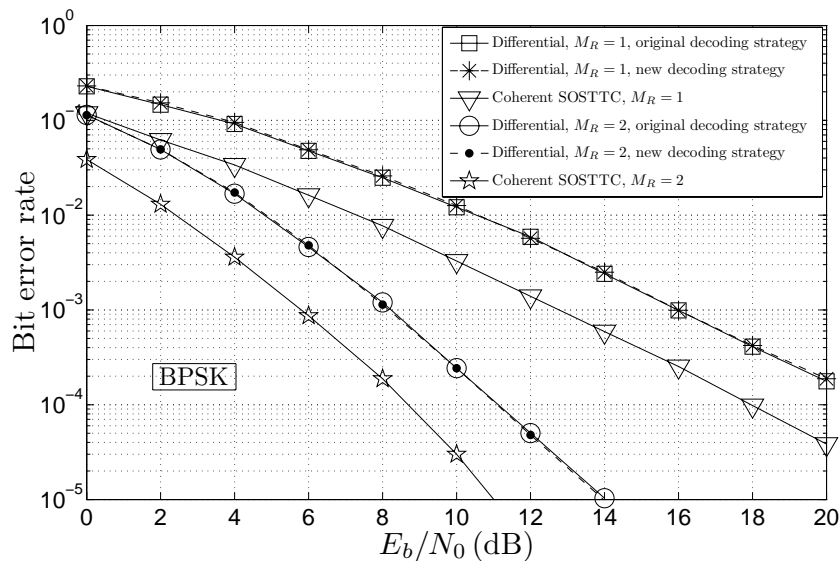

Figure J.8: Performance of differential SOSTTC and coherent SOSTTC BPSK for one ($M_R =$1) receive antenna and two ($M_R =$2) antennas.
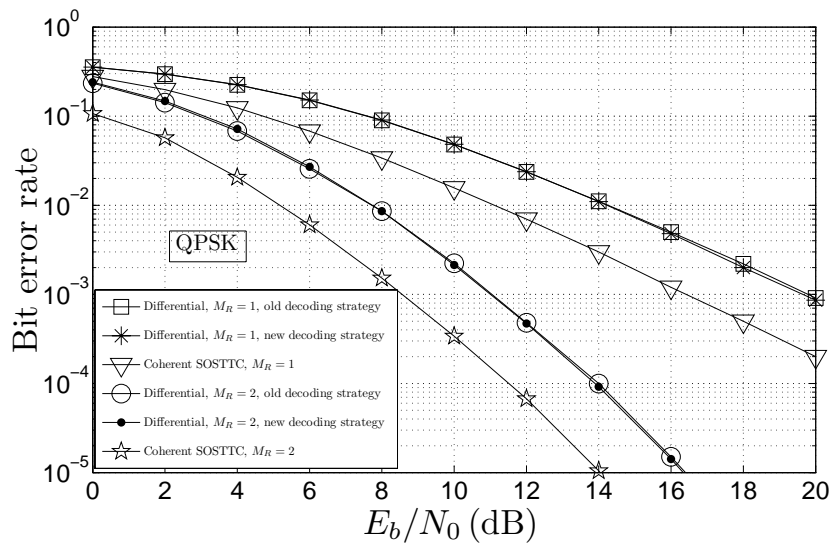
Figure J.9: Performance of differential SOSTTC and coherent SOSTTC QPSK for one ($M_R = 1$) receive antenna and two ($M_R = 2$) antennas.
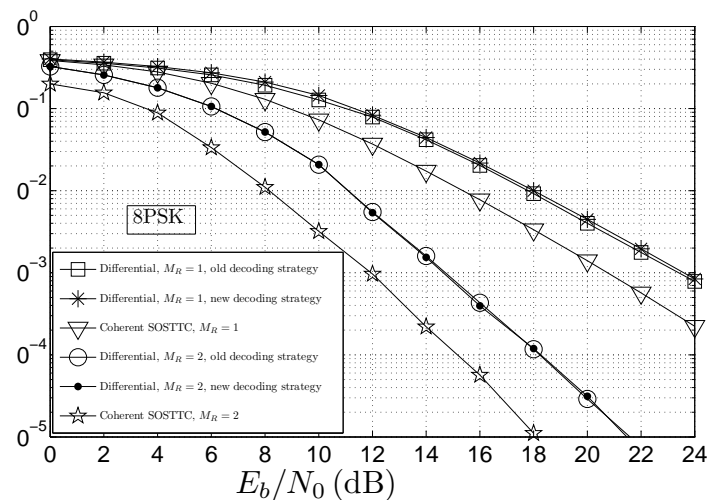

Figure J.10: Performance of differential SOSTTC and coherent SOSTTC SOSTTC 8PSK for one ($M_R = 1$) receive antenna and two ($M_R = 2$) antennas.

Tables J.4 – J.6, we find that, for the differential BPSK, QPSK and 8PSK scheme, the simulation time using the new decoding algorithm is approximately 70%, 68%, and 58% of that using the traditional one, from which we may conclude that the proposed decoding algorithm has a lower complexity. Moreover, the new decoding algorithm works more efficiently for differential SOSTTCs having a larger size of signal constellation.

In the following, we study the effect of the antenna spacing and the angular spread of the incoming waves on the performance of the differential SOSTTC with

Table J.4: Comparison of the required simulation time for the BPSK constellation

	10^4	10^5	10^6	10^7
Traditional decoding strategy	0.80 s	7.92 s	78.84 s	792.98 s
New decoding strategy	0.61 s	5.54 s	55.52 s	554.13 s

Table J.5: Comparison of the required simulation time for the QPSK constellation

	10^4	10^5	10^6	10^7
Traditional decoding strategy	1.75 s	16.62 s	165.66 s	1651.60 s
New decoding strategy	1.30 s	11.24 s	112.50 s	1125.41 s

Table J.6: Comparison of the required simulation time for the 8PSK constellation

	10^4	10^5	10^6	10^7
Traditional decoding strategy	4.63 s	45.87 s	459.68 s	4546.00 s
New decoding strategy	2.71 s	26.56 s	260.38 s	2643.62 s

BPSK. Here, we only focus on the differential SOSTTC using the new decoding algorithm. Moreover, we assume that the transmitter and the receiver are equipped with two antennas.

Figure J.11 illustrates the impact of the antenna spacing on the BER performance. As expected, the BER performance improves with increasing antenna spacings, while the performance deteriorates if the antennas become close to each other. The reason for this behavior is that the spatial correlation between the channel gains decreases as the antenna spacing becomes larger. It seems that the transmitter and the receiver have almost equivalent influence on the BER performance. This can be explained on account of the symmetry of the geometrical two-ring scattering model and the equal values set for the main parameters of the transmitter and the receiver.

Figure J.12 shows the impact of the angular spread of the incoming waves on the BER performance. The considered propagation scenarios include both isotropic ($\kappa = 0$) and nonisotropic ($\kappa \neq 0$) scattering. In simulations, we assume that the scatterers are clustered around the mean AOA $\mu = \pi$ and the antenna spacings are fixed to $\delta_T = 10\lambda$ and $\delta_R = 3\lambda$. It is shown that increasing the value of κ leads to performance degradations. However, when the scatterers are highly centralized, e.g., when $\kappa = 20$, no significant performance difference can be observed if we further increase the value of κ.

VII. CONCLUSIONS

In this paper, a differential encoding scheme has been applied to design new and better SOSTTCs for noncoherent mobile communication systems for which CSI is
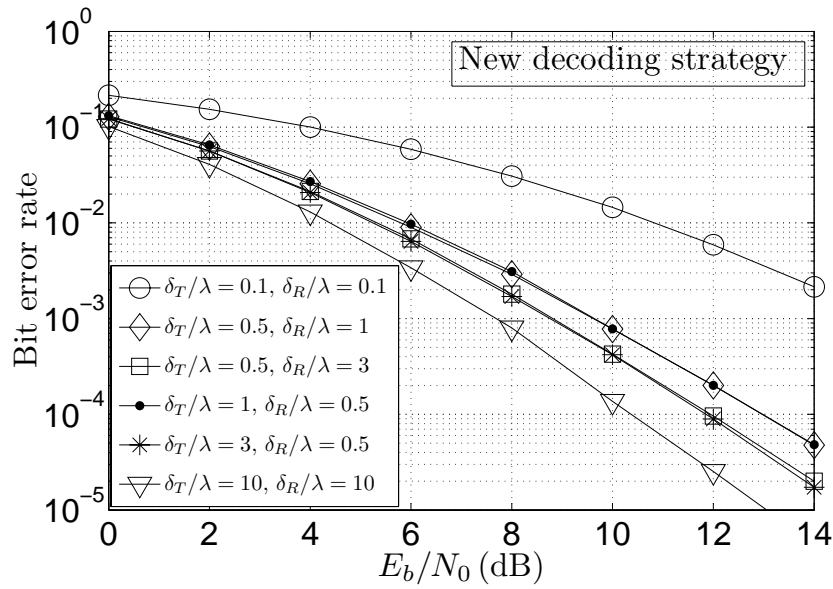
Figure J.11: The effect of the antenna spacings on the BER performance of differential BPSK SOSTTC under isotropic scattering conditions ($\kappa = 0$, $M_T = 2$, $M_R = 2$).
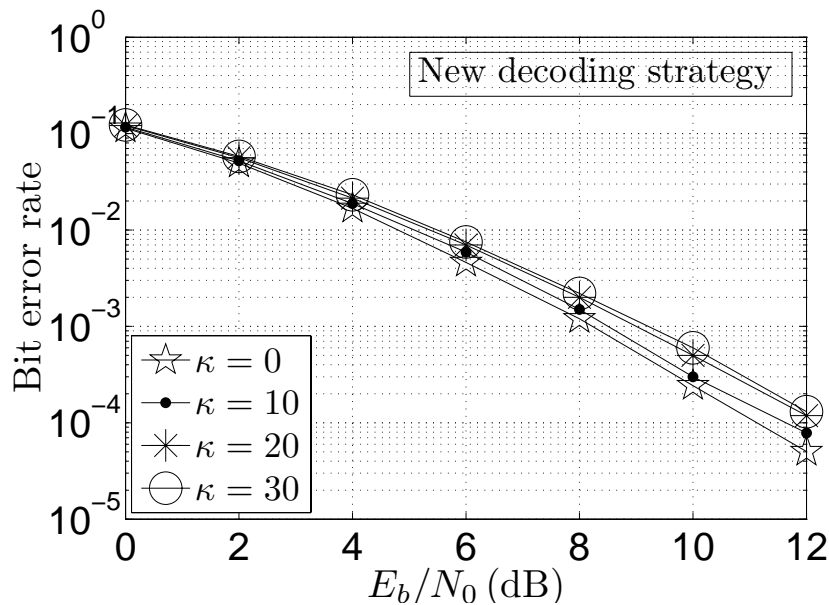

Figure J.12: The effect of the angular spread ($\approx 2/\sqrt{\kappa}$) on the BER performance of differential BPSK SOSTTC under isotropic ($\kappa = 0$) and non-isotropic ($\kappa \neq 0$) scattering conditions ($\delta_T = 10\lambda$, $\delta_R = 3\lambda$, $M_T = 2$, $M_R = 2$).

not available at both the transmitter and the receiver. A two-ring MIMO channel simulator has been used to study the performance of the differential SOSTTCs for BPSK, QPSK and 8PSK. Moreover, we have proposed a new decoding algorithm. It has been shown by simulations that the proposed decoding algorithm can provide the same performance compared with the traditional strategy, while it reduces

the decoding complexity by approximately 30 %. The proposed decoding algorithm works more efficiently for a larger size of signal constellation. For example, for differential 8PSK scheme, the new algorithm can save around 42% decoding time compared with the traditional algorithm. Our simulations have confirmed the engineering intuition that the system performance depends greatly on the antenna spacing as well as on the angular spread of the incoming waves. Moreover, we have compared the BER performance of the differential SOSTTCs with that of the coherent SOSTTCs. As expected, the coherent scheme outperforms the differential one by a coding gain of approximately 3 dB.

REFERENCES

[1] A. Abdi, J. A. Barger, and M. Kaveh. A parametric model for the distribution of the angle and the associated correlation function and power spectrum at the mobile station. *IEEE Trans. Veh. Technol.*, 51(3):425–434, May 2002.

[2] D. Agrawal, T. L. Richardson, and R. L. Urbanke. Multiple-antenna signal constellations for fading channels. *IEEE Trans. Inform. Theory*, 47(6):2618–2626, September 2001.

[3] S. M. Alamouti. A simple transmit diversity technique for wireless communications. *IEEE J. Select. Areas Commun.*, 16(8):1451–1458, October 1998.

[4] I. Bahceci and T. M. Duman. Trellis-coded unitary space-time modulation. *IEEE Trans. Wireless Commun.*, 3(6):2005–2012, November 2004.

[5] F. Edbauer. Performance of interleaved trellis-coded differential 8-PSK modulation over fading channels. *IEEE J. Select. Areas Commun.*, 7:1340–1346, December 1989.

[6] C. A. Gutiérrez and M. Pätzold. Sum-of-sinusoids-based simulation of flat fading wireless propagation channels under non-isotropic scattering conditions. In *Proc. 50th Global Communication Conference, GLOBECOM 2007*, pages 3842–3846. Washington, D.C., USA, Nov. 2007.

[7] B. M. Hochwald and T. L. Marzetta. Unitary space-time modulation for multiple-antenna communications in Rayleigh flat fading. *IEEE Trans. Inform. Theory*, 46:543–564, March 2000.

[8] B. M. Hochwald, T. L. Marzetta, T. J. Richardson, W. Sweldens, and R. Urbanke. Systematic design of unitary space-time constellations. *IEEE Trans. Inform. Theory*, 46(6):1962–1973, September 2000.

[9] B. L. Hughes. Differential space-time modulation. *IEEE Trans. Inform. Theory*, 46:2567–2578, November 2000.

[10] H. Jafarkhani and N. Seshadri. Super-orthogonal space-time trellis codes. *IEEE Trans. Inform. Theory*, 49:937–950, April 2003.

[11] H. Jafarkhani and V. Tarokh. Multiple transmit antenna differential detection from generalized orthogonal designs. *IEEE Trans. Inform. Theory*, 47(6):2626–2631, September 2001.

[12] Y. Ma and M. Pätzold. Wideband two-ring MIMO channel models for mobile-to-mobile communications. In *Proc. 10th International Symposium on Wireless Personal Multimedia Communications, WPMC 2007*, pages 380–384. Jaipur, India, December 2007.

[13] P. J. McLane et al. PSK and DPSK trellis codes for fast fading, shadowed mobile satellite communication channels. *IEEE Trans. Commun.*, 36:1242–1246, November 1988.

[14] C. Schlegel and D. J. Costello, Jr. Bandwidth efficient coding for fading channels: Code construction and performance analysis. *IEEE J. Select. Areas Commun.*, 7:1356–1368, December 1989.

[15] C. E. D. Sterian, A. A. Enescu, and I. Bănică. Super-orthogonal space-time trellis codes with eight dimensional phase-shift keying signal constellations. 62(3/4):486–512, March/April 2007.

[16] Z. Sun and T. T. Tjhung. On the performance analysis and design criteria for trellis coded unitary space-time modulation. *IEEE Communications Letters*, 7(4):156–158, April 2003.

[17] Z. Sun and T. T. Tjhung. Multiple-trellis-coded unitary space-time modulation in Rayleigh flat fading. *IEEE Trans. Wireless Commun.*, 3(6):2335–2334, November 2004.

[18] M. Tao and R. S. Cheng. Trellis-coded differential unitary space-time modulation over flat fading channels. *IEEE Trans. Commun.*, 51(4):587–596, April 2003.

[19] V. Tarokh and H. Jafarkhani. A differential detection scheme for transmit diversity. *IEEE J. Select. Areas Commun.*, 18(7):1169–1174, July 2000.

[20] V. Tarokh, N. Seshadri, and A. R. Calderbank. Space-time codes for high data rate wireless communication: performance criterion and code construction. *IEEE Trans. Inform. Theory*, 44(2):744–765, March 1998.

[21] G. Ungerboeck. Channel coding with multilevel/phase signals. *IEEE Trans. Inform. Theory*, IT-28:55–67, January 1982.

[22] L. F. Wei. Rotationally invariant convolutional channel coding with expanded signal space - Part I: 180° and Part II: Nonlinear codes. *IEEE J. Select. Areas Commun.*, 2:659–686, September 1984.

[23] L. F. Wei. Coded M-PSK with built-in time diversity for fading channels. *IEEE Trans. Inform. Theory*, 39(6):1820–1839, November 1993.

[24] Y. Wu, V. K. N. Lau, and M. Pätzold. Constellation design for trellis-coded unitary space-time modulation systems. *IEEE Trans. Commun.*, 54(11):1948–1959, November 2006.

[25] W. Zhao, G. Leus, and G. B. Giannakis. Orthogonal design of unitary constellations for uncoded and trellis-coded noncoherent space-time systems. *IEEE Trans. Inform. Theory*, 50(6):1319–1327, June 2004.

[26] Y. Zhu and H. Jafarkhani. Differential super-orthogonal space-time trellis codes. *IEEE Trans. Wireless Commun.*, 5(12):3634–3643, December 2006.